

TUNL LII  
PROGRESS REPORT

1 SEPTEMBER 2012 – 30 NOVEMBER 2013

TRIANGLE UNIVERSITIES NUCLEAR LABORATORY

DUKE UNIVERSITY  
NORTH CAROLINA STATE UNIVERSITY  
UNIVERSITY OF NORTH CAROLINA AT CHAPEL HILL  
Box 90308, DURHAM, NORTH CAROLINA 27708-0308, USA

Work described in this Progress Report is supported by the United States Department of Energy, Office of High Energy and Nuclear Physics, under:

Grant No. DE-FG02-97ER41033 (Duke University),

Grant No. DE-FG02-97ER41042 (North Carolina State University), and

Grant No. DE-FG02-97ER41041 (University of North Carolina).

# Contents

<b>Introduction</b>	<b>vii</b>
<b>Personnel</b>	<b>xxv</b>
<b>1 Fundamental Symmetries in the Nucleus</b>	<b>1</b>
1.1 The Neutron Electric Dipole Moment . . . . .	2
1.1.1 Search for the Neutron Electric Dipole Moment . . . . .	2
1.1.2 Geometric Phase Effects . . . . .	4
1.1.3 Development of a Systematic-Studies Apparatus for the nEDM Experiment . . . . .	6
1.1.4 Cryogenic Design and Testing for the nEDM Project . . . . .	8
1.1.5 Superfluid Helium Film Flow and Vapor Reflux . . . . .	10
1.1.6 Measurement-Cell Development for the nEDM Experiment . . . . .	12
1.2 Fundamental Coupling Constants . . . . .	14
1.2.1 The UCNA Experiment . . . . .	14
1.2.2 Determination of the Neutron Lifetime Using Magnetically Trapped Neutrons . . . . .	16
1.2.3 Lanthanum Isotopes and the Neutron Fluence at the Oklo Natural Nuclear Reactors . . . . .	18
<b>2 Neutrino Physics</b>	<b>21</b>
2.1 $\beta\beta$ -Decay Experiments . . . . .	22
2.1.1 Construction Update for the MAJORANA DEMONSTRATOR Project . . . . .	22
2.1.2 Parts Database for the MAJORANA DEMONSTRATOR . . . . .	24
2.1.3 Detector-String Testing for the MAJORANA DEMONSTRATOR . . . . .	26
2.1.4 Waveform Simulation for Pulse-Shape-Analysis Validation in the MAJORANA DEMONSTRATOR . . . . .	28
2.1.5 The MALBEK Detector: Low-Energy Analysis Update . . . . .	30
2.1.6 Characterization of $^{76}\text{Ge}$ Detectors for the MAJORANA DEMONSTRATOR using an Azimuthal Scanning Table . . . . .	32
2.1.7 Simulations of an Azimuthal Scanning Table . . . . .	34
2.1.8 Investigation of Pulse-Tube Refrigerators for Germanium-Detector-Array Cooling . . . . .	36
2.1.9 Underground Low-Background Assay at KURF . . . . .	38
2.1.10 Neutron-Capture Cross-Section Measurements of $^{136}\text{Xe}$ in the Energy Region 0.4-14.8 MeV . . . . .	40
2.1.11 The $^{40}\text{Ar}(n,\gamma)^{41}\text{Ar}$ Cross Section between 0.4 and 14.8 MeV . . . . .	42
2.1.12 Measurements of the Neutron-Capture Cross-Sections of $^{74}\text{Ge}$ and $^{76}\text{Ge}$ from 0.4 to 14.8 MeV for $0\nu\beta\beta$ -Decay Applications . . . . .	44
2.1.13 $2\nu\beta\beta$ Decay of $^{96}\text{Zr}$ to the First Excited $0^+$ State . . . . .	46
2.1.14 Search for Resonant Double-Electron Capture of $^{156}\text{Dy}$ . . . . .	48
2.1.15 TUNL's KamLAND Effort . . . . .	50
2.2 Tritium $\beta$ Decay . . . . .	52
2.2.1 Commissioning of the KATRIN Main Spectrometer . . . . .	52
2.2.2 Comparison of Field Calculations to Commissioning Measurements for the KATRIN Experiment . . . . .	54

2.2.3	Characterization of the Muon Veto for the KATRIN Experiment . . . . .	56
<b>3</b>	<b>Nuclear Astrophysics</b>	<b>59</b>
3.1	Nucleosynthesis in Hydrostatic and Explosive Environments . . . . .	60
3.1.1	The $^{14}\text{N}(p,\gamma)^{15}\text{O}$ Reaction at Low Stellar Energies . . . . .	60
3.1.2	The $^{23}\text{Na}(p,\gamma)^{24}\text{Mg}$ Reaction and Sodium in AGB Stars . . . . .	62
3.1.3	Nuclear Mixing Meters for Classical Novae . . . . .	64
3.2	Thermonuclear Reaction Rates . . . . .	66
3.2.1	Relative Monte Carlo Reaction-Rate Contributions . . . . .	66
3.2.2	Mean Proton and $\alpha$ -Particle Reduced Widths of the Porter-Thomas Distribution and Astrophysical Applications . . . . .	68
<b>4</b>	<b>Nuclear Structure and Reactions</b>	<b>71</b>
4.1	Reaction Dynamics of Light Nuclei . . . . .	72
4.1.1	Measurement of the $^{10}\text{B}(p,\alpha)^7\text{Be}$ Reaction Cross Section between 2.1 and 6.0 MeV . . . . .	72
4.1.2	Cross-Section Measurements of the $^{10}\text{B}(p,\gamma)^{11}\text{C}$ Reaction between 2.0 and 6.0 MeV . . . . .	74
4.2	Preequilibrium Nuclear Reactions . . . . .	76
4.2.1	Preequilibrium Reaction Phenomenology . . . . .	76
4.3	Neutron-Induced Reactions . . . . .	78
4.3.1	Neutron-Capture Experiments . . . . .	78
<b>5</b>	<b>Photonuclear Reactions at HI<math>\gamma</math>S</b>	<b>81</b>
5.1	Nuclear Astrophysics . . . . .	82
5.1.1	Further Measurement of the $2_2^+$ State in $^{12}\text{C}$ with the HI $\gamma$ S OTPC . . . . .	82
5.1.2	New Triple- $\alpha$ Reaction Rates from the $2_2^+$ State in $^{12}\text{C}$ . . . . .	84
5.2	Few-Body Interactions . . . . .	86
5.2.1	Three- and Two-Body Photodisintegration of $^3\text{He}$ with Double Polarizations . . . . .	86
5.2.2	Differential Cross-Section Measurements of Three-Body Photodisintegration of the Triton . . . . .	88
5.3	Study of Many-Body Systems . . . . .	90
5.3.1	Measurement of the Isovector Giant Quadrupole Resonance in $^{124}\text{Sn}$ via Polarized Compton Scattering at HI $\gamma$ S . . . . .	90
5.3.2	Beam Test of Compton Scattering from Unpolarized $^3\text{He}$ . . . . .	92
<b>6</b>	<b>Applied Research</b>	<b>95</b>
6.1	Homeland and National Nuclear Security . . . . .	96
6.1.1	Dipole Transitions in $^{240}\text{Pu}$ . . . . .	96
6.1.2	Fission-Product Yields of $^{235}\text{U}$ , $^{238}\text{U}$ , and $^{239}\text{Pu}$ at Incident Neutron Energies of 1.4, 2.4 and 14.8 MeV . . . . .	98
6.2	National Ignition Facility Activities . . . . .	100
6.2.1	Study of the $^{169}\text{Tm}(n,2n)^{168}\text{Tm}$ and $^{169}\text{Tm}(n,3n)^{167}\text{Tm}$ Reactions and the National Ignition Facility . . . . .	100
6.2.2	The $^{124}\text{Xe}(n,\gamma)^{125}\text{Xe}$ and $^{124}\text{Xe}(n,2n)^{123}\text{Xe}$ Reactions and NIF . . . . .	102
6.2.3	Neutron Capture Cross Section of $^{181}\text{Ta}$ and $^{197}\text{Au}$ in Relation to NIF . . . . .	104
6.3	Public Health Research . . . . .	106
6.3.1	Degradation Studies of Water Purification Membranes Using Rutherford Backscattering Spectrometry . . . . .	106
6.4	Plant Physiology Research . . . . .	108
6.4.1	Production of $^{52}\text{Fe}$ for Plant Physiology Studies . . . . .	108
6.4.2	Simulation of Sugar Allocation and Translocation in Grasses . . . . .	110
6.5	Nuclear Data Evaluation . . . . .	112
6.5.1	Nuclear Data Evaluation Activities . . . . .	112

<b>7</b>	<b>Accelerator Physics</b>	<b>115</b>
7.1	The High-Intensity $\gamma$ -Ray Source (HI $\gamma$ S) . . . . .	116
7.1.1	Operation of the HI $\gamma$ S Facility – Beamtime Summary . . . . .	116
7.1.2	Operation of the HI $\gamma$ S Facility – Accelerator Reliability . . . . .	118
7.1.3	Commissioning and Operation of the FEL Wiggler Switchyard . . . . .	120
7.1.4	Design of a Soft Orbit Bump for FEL Mirror Protection at the Duke FEL/HI $\gamma$ S Facility . . . . .	122
7.1.5	Protection of VUV FEL Mirrors Using a Soft Orbit Bump at the Duke FEL/HI $\gamma$ S Facility . . . . .	124
7.1.6	Electron-Bunch Cleaning with a Transverse Feedback System . . . . .	126
7.1.7	Wiggler Field Compensation at the Duke FEL Storage Ring . . . . .	128
7.1.8	Implementation of Magnetic Lattice and Magnetic Field Compensation Schemes for FEL Wiggler Operation . . . . .	130
7.1.9	Developing New Capabilities for the Storage-Ring Injection System . . . . .	132
7.2	The FN Tandem Accelerator and Ion Sources . . . . .	134
7.2.1	Tandem Accelerator Operation . . . . .	134
7.2.2	A $^3\text{He}$ Gas-Recirculation System for the Helium Ion Source . . . . .	136
7.3	The LENA Accelerator and Ion Sources . . . . .	138
7.3.1	The LENA JN Van de Graaff Accelerator . . . . .	138
7.3.2	A Proposed Upgrade of the Acceleration Column of LENA’s ECR Source . . . . .	140
<b>8</b>	<b>Nuclear Instrumentation and Methods</b>	<b>143</b>
8.1	Targets . . . . .	144
8.1.1	Status Report for the HI $\gamma$ S Frozen-Spin Target . . . . .	144
8.1.2	Beam Test of the Dilution Refrigerator for HIFROST . . . . .	146
8.1.3	Cool-Down Tests of HIFROST at HI $\gamma$ S . . . . .	148
8.1.4	A Cryogenic Target for Photonuclear Experiments at HI $\gamma$ S . . . . .	150
8.1.5	Development of a Tritium Gas Target for a Three-Body Photodisintegration Experiment . . . . .	152
8.2	Detector Development and Characterization . . . . .	154
8.2.1	A Recirculation System for Isotopically Enriched Gas Used in the HI $\gamma$ S OTPC . . . . .	154
8.2.2	An Optical Time Projection Chamber for Primordial Deuterium Abundance Studies . . . . .	156
8.2.3	Monte Carlo Simulation of the LENA Detector System . . . . .	158
8.2.4	Development of a Para-Ortho Deuterium Converter and Raman Spectrometer . . . . .	160
8.2.5	Detector Characterization and Simulation for a Neutron-Antineutron Oscillation Search . . . . .	162
8.2.6	Characterization of $^{10}\text{B}$ -Lined Proportional Counters and Moderator Design . . . . .	164
8.2.7	Measurement of the Nab/UCNB Silicon-Detector Response to 15 to 40 keV Protons and Deuterons . . . . .	166
8.2.8	Measurement of the Response Matrix of a Large Volume $\text{LaBr}_3\text{:Ce}$ Detector at the HI $\gamma$ S Facility . . . . .	168
8.3	Facilities . . . . .	170
8.3.1	Construction of an Ultracold-Neutron-Source Facility at the NC State PULSTAR Reactor . . . . .	170
8.3.2	Beamline and Target Chamber for Studies of the ( $^3\text{He},n$ ) Reaction . . . . .	172
8.4	Data Acquisition Hardware and Software Development . . . . .	174
8.4.1	Status of the ORCA Data-Acquisition Software . . . . .	174
8.4.2	Addition of 3D Displays in ORCA . . . . .	176
<b>A</b>	<b>Appendices</b>	<b>179</b>
A.1	Graduate Degrees Awarded . . . . .	180
A.2	Publications . . . . .	182
A.3	Invited Talks, Seminars, and Colloquia . . . . .	190
A.4	Professional Service Activities . . . . .	197

<b>Glossary of Acronyms</b>	<b>200</b>
<b>Index</b>	<b>202</b>

# Introduction

## Who We Are

The primary mission of the Triangle Universities Nuclear Laboratory (TUNL) is to advance the frontiers of nuclear physics and to educate students and young scientists to work at the forefront of the field. This mission is carried out by a consortium of three major universities in North Carolina's Research Triangle area: Duke University, North Carolina State University (NCSU), and the University of North Carolina at Chapel Hill (UNC). There are currently 19 faculty members along with approximately 50 graduate students and 15 postdoctoral fellows in the consortium. Their research covers a wide range of topics in nuclear physics that broadly include fundamental symmetries, neutrino physics, nuclear astrophysics, and strong interaction physics (hadron structure, light nuclei, and many-body systems). Progress in basic scientific research often requires technological advances, so TUNL groups are conducting R&D on particle detectors, signal processing electronics, data acquisition systems, production and evaluation of ultra-low-radioactivity materials, and particle accelerator systems. In addition to the basic nuclear physics research program, groups at TUNL are applying nuclear-physics techniques in areas of national nuclear security, homeland security, and plant biology.

In addition to consortium members, long-term collaborators contribute substantially to the research and education activities at TUNL. These collaborators participate in and lead research projects at the laboratory, thus significantly expanding the opportunities for undergraduate students and students from under-represented ethnic groups to participate in nuclear research. The collaborators include groups from two local historically black universities (North Carolina Central University and North Carolina A&T State University) plus several primarily undergraduate-serving institutions (James Madison University, North Georgia College and State University, University of Connecticut at Avery Point, and Tennessee Technological University). In addition, there are long-term international collaborations with groups from the Istituto Nazionale di Fisica Nucleare (Pisa), the Jagiellonian University (Cracow), the Joint Institute for Nuclear Research (Dubna), the Technische Hochschule Darmstadt, the University of Cologne, and the University of Mainz. In our applications and interdisciplinary research programs, we collaborate with scientists from several national laboratories, including Lawrence Livermore National Laboratory, Jefferson Laboratory, and Los Alamos National Laboratory. Many of the collaborators from the above institutions are listed as co-authors of the reports in this document.

## Our Research Program

The research program at TUNL is a mixture of experiments conducted at our local research facilities and large-scale collaborative projects that are carried out at national user laboratories and facilities. The latter include the neutron electric dipole moment (nEDM) experiment and the MAJORANA DEMONSTRATOR. Both parts of the program use TUNL's research infrastructure. This includes our engineering, technical, and administrative support; our research facilities; our materials and supplies; and our equipment. The capabilities at the local accelerator facilities enable TUNL groups to conduct world-class research programs in low-energy QCD, nuclear structure, and nuclear astrophysics. The coordination of effort by the research groups and the strategic use of technical resources enable groups at TUNL to take on major responsibilities in the nEDM and MAJORANA DEMONSTRATOR projects.

The Low-Energy program in the Office of Nuclear Physics (ONP) at the Department of Energy (DOE) supports the collaborative research at TUNL through three grants, one to each consortium university. The grants to NCSU and UNC support the activities of the research groups at these institutions. The budgets for these awards include support for student and post-doctoral fellows, salaries for senior investigators, and travel, plus modest funding for research instrumentation and for laboratory materials and supplies. The UNC grant includes support for one research scientist staff position for the neutrino physics research. The Duke grant has two components: (1) support for the shared research infrastructure at TUNL (including the operation of accelerator facilities, technical and engineering support, special research facilities, materials, supplies, and equipment) and (2) support for the Duke research group (personnel and student support plus travel funds).

## Our Facilities and Support Staff

TUNL operates three accelerator facilities: the High Intensity Gamma-Ray Source (HI $\gamma$ S), the Laboratory for Experimental Nuclear Astrophysics (LENA) and the tandem Van de Graaff accelerator laboratory.

Of the three facilities, HI $\gamma$ S has the largest user community and supports the broadest research program. HI $\gamma$ S is a Compton-backscattering  $\gamma$ -ray source that produces  $\gamma$ -ray beams by colliding photons inside the optical cavity of a free-electron laser with electrons circulating in a storage ring. This source delivers nearly mono-energetic and highly polarized  $\gamma$ -ray beams on target with the highest spectral intensity of all accelerator-driven  $\gamma$ -ray beam sources worldwide. The capabilities of HI $\gamma$ S are in large part due to its intrinsic design advantages over other sources plus the innovativeness of the accelerator physics group that supports HI $\gamma$ S operations and conducts research focused on advancing the  $\gamma$ -ray beam capabilities at this unique facility.

LENA is a light-ion, low-energy accelerator facility with beam capabilities optimized for nuclear astrophysics experiments. This laboratory has two low-energy electrostatic accelerators capable of delivering high-current charged-particle beams to experiments. One is an electron-cyclotron-resonance source on a 200-kV isolated potential platform; the other is a 1-MV JN Van de Graaff accelerator.

The main accelerator in the tandem laboratory is an FN tandem Van de Graaff that has a maximum terminal voltage of 10 MV. The beams from this facility support a nuclear physics research program that uses light-ions and neutrons to study nuclear structure and the strong interaction at low energies. The special beam capabilities include nearly mono-energetic unpolarized and polarized fast neutron beams (pulsed and dc), pulsed light-ion beams, and polarized proton and unpolarized deuteron beams.

The accelerators at LENA and the tandem laboratory are operated by the research groups using the facilities and are maintained by technicians. R&D to create new capabilities is carried out by the research groups in collaboration with the technical staff.

In addition to the accelerator facilities, the local research infrastructure includes non-accelerator research facilities. These include project R&D laboratories at Duke, NC State, and UNC; a low-background counting facility at Duke and a low-radioactivity fabrication and assembly facility at UNC. TUNL also has several research laboratories at the Kimballton Underground Research Facility (KURF) in Kimballton, VA, which is a regional facility operated by Virginia Tech in an active limestone mine.

The technical and administrative staffs at TUNL are vital to carrying out the research program. The engineering expertise of the technical staff includes mechanical engineering, high vacuum systems, cryogenics, optical systems, high-power electrical systems, electron guns, and RF accelerator systems). We also have technicians trained in mechanical equipment, high-power electrical systems, vacuum systems, light-ion sources, electrostatic accelerator systems, and electronics. Finally, we have staff trained in accelerator physics and engineering. The technical staff provides research support, maintains the accelerators and research facilities, and supports accelerator operations. Groups at TUNL have access to laboratory materials, supplies, and a pool of research equipment.

## Research Highlights

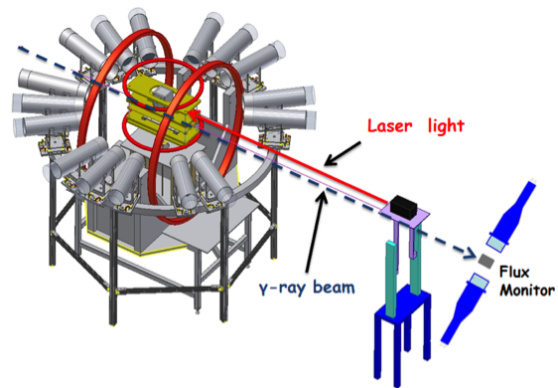
This section showcases highlights from the overall TUNL research program during the reporting period. A more comprehensive summary of our current research effort is given in a later section of this introduction, and a description of individual projects constitutes the main body of the Progress Report.

### 1. First Measurements of the Spin-Dependent Cross Section for Photodisintegration of $^3\text{He}$

The study of three-nucleon systems has long been of fundamental importance in developing descriptions of nuclear systems that evolve in a coherent way across the different degrees of freedom used to formulate the theory of strongly interacting matter. To this end, high-accuracy few-nucleon data on a wide variety of observables at low energies are essential for advancing *ab initio* nuclear-reaction and nuclear-structure calculations. It is therefore significant that *the double polarization (polarized beam and polarized target) cross section for photodisintegration of  $^3\text{He}$  was measured for the first time.*

These new data provide stringent tests of state-of-the-art three-nucleon calculations that use realistic nucleon-nucleon and three-nucleon interactions. The measurements were performed at HI $\gamma$ S using a  $^3\text{He}$  target polarized by the spin-exchange optical-pumping technique and a beam of circularly polarized mono-energetic  $\gamma$  rays with energies of 12.8 and 14.7 MeV. A schematic of the experimental apparatus is shown in Fig. 1.

**Figure 1:** (Color online) Schematic of the experimental apparatus: The movable  $^3\text{He}$  target system is surrounded by 16 liquid-scintillator detectors placed inside mu-metal tubes, one meter away from the center of the target at neutron laboratory angles varying from  $30^\circ$  to  $165^\circ$ . The mu-metal tubes are used to shield the detectors from the magnetic field produced by the Helmholtz coils (big red rings in the drawing).



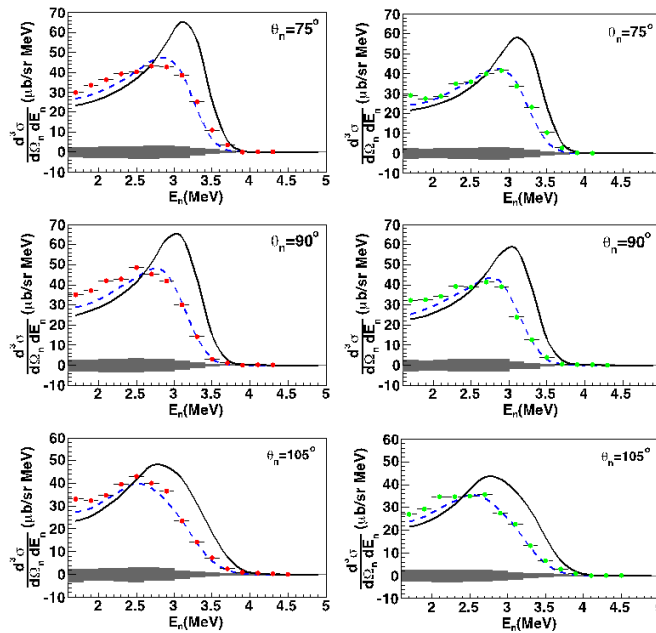
The measured spin-dependent double-differential cross sections are compared to the state-of-the-art three-body calculations in Fig. 2. The good agreement between the data and calculations gives confidence in the theoretical treatment of this reaction and clearly illustrates the importance of the inclusion of the Coulomb interaction in the calculations. Furthermore, these data are used to determine the integrand for the Gerasimov-Drell-Hearn (GDH) sum rule on  $^3\text{He}$ . The sum rule relates the dynamics of the photoabsorption process to the static magnetic moment of the nucleus. The value of the integrand for the GDH sum rule is computed as the energy-weighted difference of the spin-dependent total photoabsorption cross sections for target spin and beam helicity parallel and antiparallel to one another. These results were published in G. Laskaris *et al.*, Phys. Rev. Lett. **110**, 202501 (2013).

### 2. Fine Structure of the Giant M1 Resonance in $^{90}\text{Zr}$

Understanding the magnetic-dipole and Gamow-Teller responses in nuclei is a long-standing challenge in nuclear physics. Due to the close relationship between the M1 excitation and neutrino-nucleus processes, knowledge of the M1 excitation is particularly important for estimating neutral-current cross sections for supernova explosions and for terrestrial detection of supernova neutrinos.

As a general observation, measurements find considerably less magnetic strength than theoretically expected. This is known as the quenching phenomenon of the nuclear spin-flip magnetic

**Figure 2:** (Color online) Spin-dependent double-differential cross sections for parallel (left-hand panels) and antiparallel (right-hand panels) states as a function of the neutron energy at the incident photon energy of 12.8 MeV. The data are compared with two theoretical calculations, one made with the Coulomb interaction (dashed curves) and one without it (solid curves). The band at the bottom shows the systematic uncertainties.



response. Explaining the dynamics of quenching means understanding the coupling of the two-quasiparticle doorway states to many-quasiparticle configurations.

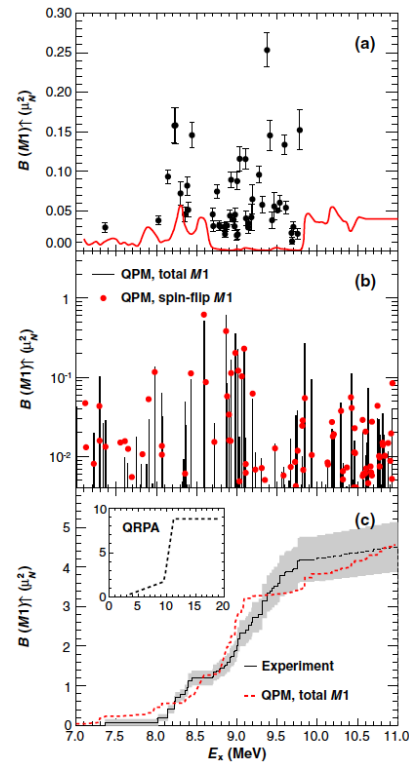
We studied the M1 excitations in  $^{90}\text{Zr}$  in a photon-scattering experiment with mono-energetic and 100% linearly polarized beams from 7 to 11 MeV. Results are shown in Fig. 3. More than forty  $J_\pi = 1^+$  states have been identified from observed ground-state transitions. These data reveal the fine structure of the giant M1 resonance for the first time. The concentration of M1 strength around 9 MeV is further confirmed in three-phonon quasi-phonon model calculations and are explained as fragmented spin-flip excitations. The observed strongly fragmented M1 strength and its absolute value can be explained only if excitations more complex than the single particle-hole ones are taken into account. These results were published in G. Rusev *et al.*, Phys. Rev. Lett. **110**, 022503 (2013).

### 3. Unambiguous Identification of the Second $2^+$ State in $^{12}\text{C}$

Late-stage red giant stars produce energy in their interiors via helium ( $\alpha$ ) burning. The outcome of helium burning in red giant stars is the formation of the two elements, carbon and oxygen. The ratio of carbon to oxygen at the end of helium burning has been identified as one of the key open questions in nuclear astrophysics. Helium burning proceeds through the  $3\alpha$  (three  $^4\text{He}$  nuclei) process to produce carbon, which eventually burns to oxygen via the  $^{12}\text{C}(\alpha,\gamma)^{16}\text{O}$  reaction. An excited state in  $^{12}\text{C}$ , named the Hoyle State after Fred Hoyle who predicted its existence, plays a central role in determining the rate of the  $3\alpha$  process. This prediction was the first, and quite possibly still the best, example of an application of the anthropic principle in physics. Soon after the discovery of this excited state in  $^{12}\text{C}$ , predictions of the rotational band structure of the Hoyle state led to a fifty-year search for an excited state built on the Hoyle state. *An excited state having the properties of the Hoyle-state excitation was unambiguously identified at HI $\gamma$ S.* This result was reported recently in W.R. Zimmerman *et al.*, Phys. Rev. Lett. **110**, 152502 (2013).

The state was identified using the  $^{12}\text{C}(\gamma,\alpha)^8\text{Be}$  reaction. The alpha particles produced by the photodisintegration of  $^{12}\text{C}$  were detected using an optical time-projection chamber (OTPC). Data were collected at beam energies between 9.1 and 10.7 MeV using the intense, nearly monoenergetic  $\gamma$ -ray beams at the HI $\gamma$ S facility. The measured angular distributions determine the cross sections and the E1-E2 relative phases as a function of energy, leading to an unambiguous identification of the second  $2^+$  state in  $^{12}\text{C}$  at 10.13(60) MeV. This work was a collaborative effort which includes TUNL, the University of Connecticut, Yale University, Physikalisch-Technische Bundesanstalt, Germany, and the Weizmann Institute of Science, Israel. In Fig. 4, a  $\gamma$  ray of 9.5 MeV, not seen in the image, breaks a carbon nucleus into a helium fragment and a  $^8\text{Be}$  fragment. The  $^8\text{Be}$  immediately

Figure 3: (Color online) Results for (a) the measured  $B(M1)$  strength of discrete levels in  $^{90}\text{Zr}$  compared with the detection limits (red solid line) and (b) predictions from the quasiparticle phonon model. A comparison of the measured and calculated QPM cumulative  $M1$  strength is shown in panel (c). The shaded area gives the uncertainty of the experimental values.



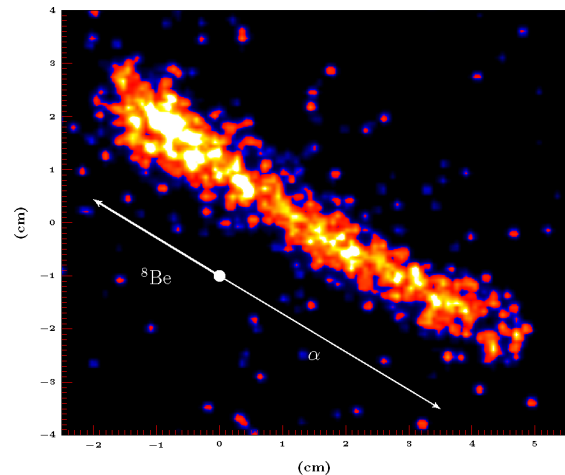
decays into two  $\alpha$ -particles and appears as two tracks merged into each other. A fast, high-resolution, and image-intensified camera created this image. Other components of the OTPC gather information on the energy of these fragments and the angles at which they are ejected, thus providing a complete picture of the reaction.

#### 4. MAJORANA DEMONSTRATOR Highlights

Construction of the MAJORANA DEMONSTRATOR (MJD) has advanced significantly this past year. The MJD is being assembled 4850 feet underground in special clean laboratories established at the Sanford Underground Research Facility in Lead, SD. Over 85% of the ultra-clean, low-activity electroformed copper required for the array's cryostats, string components, and inner shielding has been electroformed and machined underground.

Two "strings" of high purity germanium (HPGe) detectors grown from natural germanium have

Figure 4: (Color online) A typical image recorded by the charge-coupled-device camera of three alpha particles from the reaction  $^{12}\text{C}(\gamma, \alpha_0)^8\text{Be} \rightarrow \alpha + \alpha$ . The two  $\alpha$  particles from the disintegration of  $^8\text{Be}$  are in the upper left of the figure and the third  $\alpha$  particle is in the lower right.



been fabricated, assembled, and operated (see Fig. 5). An operating prototype cryostat, identical to the MJD cryostats with the exception of using standard commercial copper has allowed us to acquire commissioning data from strings and to refine the components and assembly procedures that will be used to assemble the final ultra-clean modules.



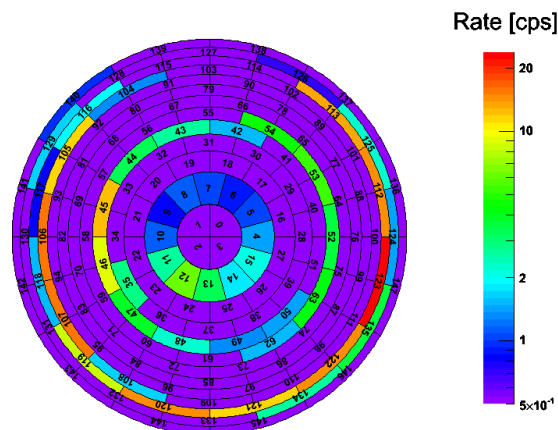
Figure 5: (Color online) Majorana collaborators work inside of a special low-radon, class-10 glove box to install a string of natural HPGe detectors in the prototype cryostat. The associated vacuum system is to the left in this photograph.

## 5. KATRIN Highlights

The first commissioning of the KATRIN main spectrometer and detector system was successfully carried out from May to September 2013. A detailed series of measurements on the spectrometer transmission characteristics and backgrounds was completed. The ORCA data acquisition system collected high quality data and operated continuously over the entire 120-day commissioning period. During the commissioning, TUNL/UNC researchers provided 9% of the relative total on-site shifts. Results from an early commissioning run are shown in Fig. 6.

A five-million-element GPU-based fully three-dimensional electromagnetic model (KEMField) for the main spectrometer and detector region has been developed for KATRIN. This code has been used extensively by the groups involved in commissioning measurements and has become a vital tool for understanding the commissioning data. The calculated electric potential of the main spectrometer is shown in Fig. 7.

Figure 6: (Color online) Observed rates in the segmented KATRIN focal plane detector during one of the early commissioning measurements. The observed “ring” structure corresponds to the wire electrode, in agreement with predictions from simulations.



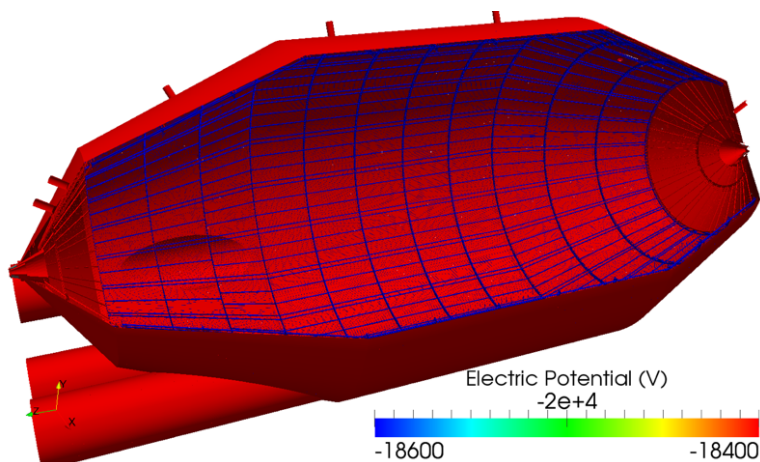


**Figure 7:** (Color online) The electric potential of the main spectrometer and its inner electrode system calculated using KEMField 3-dimensional model.

## Our Education Program

Because TUNL is a consortium with faculty from the three major universities in the Research Triangle area, one of our important contributions to the nuclear physics community is the education and training of a significant number of graduate students and post-doctoral fellows, many of whom go on to make important contributions to the field. Our educational program, however, does not end there. It includes other activities that benefit a broader range of personnel, both from within the TUNL consortium and from other institutions.

### Research Experience for Undergraduates

TUNL runs an NSF-supported Research Experience for Undergraduates (REU) program in nuclear physics. This year twelve students participated in this ten-week summer program; ten of them were supported by the NSF REU grant, and the other two by grants to TUNL faculty. Two of the students conducted research with the Duke High-Energy group and spent the second half of their summer at the CERN Large Hadron Collider. The inclusion of students wishing a research experience in experimental high-energy physics was a pilot for designing an international component to the TUNL REU program.

### Seminars

The TUNL seminar program continues with characteristic vigor, with 35 invited speakers. A full list of the titles and speakers from this year's seminars is given in the appendix to the progress report. The seminar series is augmented by the TUNL Informal Lunch Talks (TILTs), where graduate students and postdoctoral fellows present their research projects. A related series of talks, the Triangle Nuclear Theory Colloquia, is also beneficial to TUNL faculty and students.

### Orientation and Training Classes

Another component to our educational effort is a special lecture series given by local speakers on Advances in Physics as part of the REU program during the summer. These are supplemented by classes on some of the basic experimental and theoretical techniques used in nuclear physics as well as classes on scientific writing. These are primarily for the REU students and entering graduate students.

## Summary of Research Results

The main body of this progress report is a compilation of status reports of research projects conducted by TUNL groups during the period **September 1, 2012 to November 30, 2013**. It covers the second half of the first year (March 1, 2012 to February 28, 2013) and the first half of the second year (March 1, 2013 to February 28, 2014) of the current three-year grants (March 1, 2012 to February 28, 2015) to the three consortium universities from the DOE ONP Low-Energy Program.

During this reporting period research groups at TUNL published thirty-five papers in refereed journals of which five were letter articles. Consortium members delivered more than 450 invited talks at APS meetings, conferences, and workshops, plus department colloquia and seminars. In addition, the consortium groups published sixteen papers in conference proceedings. About 50% of the journal papers were based on work done at the on-site accelerator and research facilities. The balance of this introduction contains summaries of the accomplishments made during this reporting period in nuclear physics and accelerator physics research. Selected instrumentation and equipment R&D associated with research projects at TUNL is reported toward the end of this section.

The summary for each research area lists the faculty who devote more than 25% of their effort in that area. The graduate students listed are either conducting their thesis research in that field or, if they have not yet committed to a thesis project, have this as the area of their main research contribution. The number in parenthesis is the number of students involved, and only students enrolled at one of the consortium universities are listed.

In addition, the number of journal papers published during this reporting period is given for each area.

## 1. Fundamental Symmetries in the Nucleus

The main experiments in this research area include a search for violation of time-reversal invariance via measurement of the neutron electric dipole moment (nEDM), a test of the long-term stability of coupling constants, non-unitarity tests of the CKM matrix, and measurement of the neutron lifetime. Progress on the nEDM project, interaction coupling constant experiments and the neutron lifetime measurements are summarized below.

*Faculty:* Gao, Golub, Gould, Haase, Huffman, and Young

*Graduate Students (9):* Dees (NCSU), Gooden (NCSU), Huffer (NCSU), Medlin (NCSU), Palmquist (NCSU), Reid (NCSU), VornDick (NCSU), Zeck (NCSU), and Zhang (Duke)

*Ph.D. Degrees Awarded:* Pattie (NCSU), Kendellen (NCSU), and Schelhammer (NCSU)

*Number of Journal Articles:* 7

- **nEDM experiment**

The nEDM collaboration has successfully completed its two-year R&D phase and is transitioning into what is called the critical-component-demonstration (CCD) phase. The collaboration has shifted its focus to the development of the key components of the large-scale nEDM apparatus. TUNL's primary activity is the development of a small-scale test apparatus to be used at the PULSTAR ultracold neutron (UCN) source to explore UCN- $^3\text{He}$  interactions. During the past year, we have developed the engineering design of this apparatus, including tests of many individual design components. Concurrent to this work, the construction of the UCN source at the PULSTAR reactor at NCSU is proceeding on a schedule to produce its first beam early in 2014. The NC State group has also built and tested a general-purpose cryogenic testing facility that is presently being used to test seals and composite materials for the larger nEDM experiment. Further details are given in Sects. 1.1.3, 8.3.1, and 1.1.4.

- **UCNA  $\beta$ -asymmetry measurement**

The UCNA collaboration has made significant progress in reducing systematic errors in their polarization and energy calibrations. These improvements make possible  $\beta$ -asymmetry measurements with a precision better than 0.5 %. In particular, polarimetry uncertainties have been reduced to the 0.2 % level, with further reduction in the uncertainty expected. The journal articles published during this period describe the analysis of the 2010 run (a 0.94 % measurement of the  $\beta$ -asymmetry), the UCN source at Los Alamos, two material-scattering experiments, and new analysis approaches to place limits on tensor couplings from neutron decay. Further details are given in Sect. 1.2.1.

- **Nab and UCNB experiments**

During the last year, a paper analyzing the proton detection sensitivity of the thick, highly

segmented, large area silicon detectors for the Nab (and UCNB) experiments was published. Further details are given in Sect. 8.2.7.

- **Underground studies of double beta-decay and astroparticle physics**

Over the past year the NC State group essentially completed commitments for the detector acceptance procedures and evaluation of the SEGA detector. This was part of the MAJORANA neutrinoless double  $\beta$ -decay experiment.

- **Oklo natural reactor**

A key parameter for all studies of the Oklo natural nuclear reactors is the total neutron fluence during reactor operation. We have explored whether lanthanum isotopic data can provide confirmation of values traditionally derived from neodymium analyses. If the starting lanthanum elemental abundance can be reliably inferred, the answer is yes. And if not, the problem can be inverted to determine elemental abundances—an issue of geophysical interest in uraninite formation and the incorporation of rare earth elements in primordial mineralization. Further details are given in Sect. 1.2.3.

- **HI $\gamma$ S studies using nuclear resonance fluorescence**

Nuclear resonance fluorescence (NRF) is used to study collective excitations in nuclei at energies below the giant dipole resonance. The new  $\gamma^3$  array, comprised of HPGe and LaBr<sub>3</sub>:Ce detectors, was commissioned this year. This new array gives access to observation of both ground-state and cascade transitions in the de-excitation of excited nuclei.

- **High precision measurement of the <sup>19</sup>Ne Lifetime**

Measurements of the lifetime for superallowed  $0^+ \rightarrow 0^+$  Fermi decays in nuclei provide the most precise determination of the weak-mixing parameter  $V_{ud}$  between the up and down quarks in the CKM matrix. Analysis of mirror decays, such as the decay of <sup>19</sup>Ne to <sup>19</sup>F, provide a powerful cross-check of the nuclear-structure-dependent corrections required to extract  $V_{ud}$  from the superallowed decays. Analysis of <sup>19</sup>Ne lifetime data recently measured at KVI by a TUNL group was completed at the 0.5 % level, and a paper was submitted. The results of this measurement suggest that systematic errors may not yet be properly assessed for the lifetime data in this system.

- **Neutron lifetime**

The NIST neutron lifetime experiment has finalized analysis of its neutron trapping data. Efforts to understand a key systematic effect have focused on determining the isotopic purity of the <sup>4</sup>He. Direct measurements of the <sup>3</sup>He/<sup>4</sup>He ratio, performed in collaboration with both Argonne National Laboratory and CalTech, have yielded consistent values of the purity levels at the few  $\times 10^{-12}$  level. Details are given in Sect. 1.2.2.

## 2. Neutrino Physics

A major theme in this research area is the search for violation of lepton-number conservation through the observation of neutrinoless double-beta ( $0\nu\beta\beta$ ) decay. The MAJORANA DEMONSTRATOR (MJD) is the main project at TUNL in this pursuit. The MJD project uses p-type point-contact high-purity germanium crystals, isotopically enriched in <sup>76</sup>Ge, as the sample and detector in the search for  $0\nu\beta\beta$  decay. The MJD experiment is located at the 4850-foot level in the Sanford Underground Research Facility (SURF) in Lead, SD. Other activities in this research area include KATRIN (determination of the absolute mass of neutrinos via high-resolution measurement of the energy spectrum of the emitted betas in tritium decay),  $\beta\beta$  decay to excited  $0^+$  states, measurements of nuclear reaction data important for guiding calculations of nuclear matrix elements for  $0\nu\beta\beta$  decay and for modeling neutron-induced backgrounds in  $0\nu\beta\beta$  decay and dark-matter detection experiments. Progress on projects in this area is summarized below.

*Faculty:* Henning, Howell, Karwowski, Tornow, Wilkerson, and Young

*Graduate Students (13):* Combs (NCSU), Corona (UNC), Finch (Duke), Giovanetti (UNC), Leviner (NCSU), Rager (UNC), Rich (UNC/Duke), Shanks (UNC), Snavely (UNC), Strain (UNC), Ticehurst (UNC/Duke), Vorren (UNC), and Wierman (UNC)

*Ph.D. Degrees Awarded:* MacMullin (UNC) and Finnerty (UNC)

*Number of journal papers:* 7

## Majorana Demonstrator (MJD) Project

### • Construction of the MJD

Construction of the MJD experiment at SURF is proceeding well. Major achievements were made on the underground fabrication, assembly, and testing of systems for which TUNL has responsibility. See Sect. 2.1.1 for details. The accomplishments include:

- All the copper materials needed to construct two cryostats for the MJD experiment have been electroformed. Machining of the copper components is proceeding as scheduled.
- The vacuum and cryogenics systems for the prototype module have been assembled and tested.
- The fabrication of the prototype cryostat has been completed and the cryostat is operating successfully.
- The first two strings of un-enriched detectors have been assembled and are being tested inside the prototype cryostat.
- Underground testing of enriched detector modules for cryostat-1 is underway at SURF.
- The machining and initial electron-beam welding of cryostat-1 at PNNL has been completed.
- The assembly of the shield has started, and significant progress has been made on installing the muon veto, and the copper and lead shields.

### • Materials and parts characterization

Characterizing the radioactivity of all materials and components used in the construction of the MJD experiment is essential for minimizing backgrounds and for accurately simulating the signal-to-background ratio in the energy region of interest for the neutrinoless double-beta decay process. The web-based software interface to the MJD Parts Tracking Database (PTDB) was brought online this year for access by members of the MJD collaboration involved in component fabrication, systems assembly, and experiment simulations. See Sect. 2.1.2 for details.

### • Detector testing

Before a detector string is installed in its cryostat it is characterized in a String Test Cryostat (STC). There are seven STCs, each with its own Dewar equipped with an IR shield and a cold plate that are cooled by a two-piece cold finger. The cold finger can be separated to allow the STC to fit into the glove box for string mounting and dismounting without exposing the detector to the room air. Two detector strings were tested in the STC this year. One is currently in operation in the prototype cryostat. See Sect. 2.1.3 for details.

### • Automated scanning table

An automated scanning table was built at UNC and put into service this year. The scanning table is used to characterize the detector properties over the volume of the detector and to calibrate the position sensitivity of the detector by moving and recording the position a  $\gamma$ -ray source azimuthally and vertically about the String Test Cryostat. This device is especially important for characterizing the surface features of each detector module. See Sect. 2.1.6 for details.

## Other Low-Background Counting Activities

### • MALBEK

The Majorana Low-Background Broad-Energy Germanium Detector at KURF (MALBEK) is part of the R&D program for the MJD project. MALBEK is a 465 g p-type point-contact (PPC) high-purity germanium detector manufactured by Canberra Industries. This detector was deployed at KURF in January 2010. The goals of the work with MALBEK were to study the

performance and backgrounds of a PPC detector and to perform a search for weakly interacting massive particles (WIMPs) with masses below  $10 \text{ GeV}/c^2$ . An analysis of data accumulated over 288 collection-days does not show evidence for signals from light WIMP interactions in the detector. See Sect. 2.1.5 for details.

- **Two-neutrino double-beta decay**

Measurements of  $2\nu\beta\beta$  decay to excited states provide information important for assessing calculations of nuclear matrix elements for  $0\nu\beta\beta$  decay. Last year a new setup was installed at KURF to measure the half-life for  $2\nu\beta\beta$  of  $^{96}\text{Zr}$  to the first excited state. The experiment has collected about 23.5 g-years of data. Preliminary analysis of these data provides a limit on the half-life that is about a factor two more precise than the previous limit. See Sect. 2.1.13 for details.

- **Neutrinoless double-electron capture**

Resonance double-electron capture is a possible alternative to  $0\nu\beta\beta$  decay for searching for lepton-number violation and for determining whether the neutrino is a Majorana particle. An experiment to search for neutrinoless double-electron capture in  $^{156}\text{Dy}$  was installed and commissioned at KURF this year. The sample used in this experiment is  $\text{Dy}_2\text{O}_3$  enriched to about 21% in  $^{156}\text{Dy}$  and containing a total of 213 mg of  $^{156}\text{Dy}$ . The target is sandwiched between two clover HPGe detectors. About 18.3 g-days of data were collected this year, and data collection continues. See Sect. 2.1.14 for details.

- **KATRIN**

The Karlsruhe Tritium Neutrino (KATRIN) experiment is a measurement of the kinematic mass of the electron antineutrino through the analysis of the spectral shape in the endpoint region of the electron energy spectrum from tritium  $\beta$ -decay. Commissioning of the main spectrometer was started this year. A series of measurements on the spectrometer transmission characteristics and backgrounds was carried out from May through September 2013. The TUNL group reports significant contributions to the commissioning. The ORCA data acquisition system, which is the responsibility of the TUNL/UNC group, was used continuously during the 120 days of the commissioning run. The group covered about 10% of the on-site shifts for the spectrometer commissioning. Their other contributions to the commissioning and to the overall experiment include developing and performing large-scale three-dimensional electromagnetic simulations that model the main spectrometer and detector region. These simulations are carried out using the graphics-processing-unit sub-cluster on the "Killdevil" computing system at UNC. See sections 2.2.1 and 2.2.2 for details.

## Nuclear Reactions Important for Low-Background Counting Measurements

- **Possible sources of neutron-induced backgrounds**

Neutron-induced reactions are a source of backgrounds in low-background counting experiments searching either for  $0\nu\beta\beta$  decay or for dark-matter particles. Groups at TUNL are measuring cross sections of nuclear reactions important for modeling the neutron-induced backgrounds in  $0\nu\beta\beta$  decay experiments and dark-matter particle detectors. These reactions include  $^{136}\text{Xe}(n,2n)^{135}\text{Xe}$ ,  $^{136}\text{Xe}(n,n'\gamma)^{136}\text{Xe}$ ,  $^{40}\text{Ar}(n,n'\gamma)^{40}\text{Ar}$ ,  $^{20}\text{Ne}(n,n'\gamma)^{20}\text{Ne}$ ,  $\text{Ge}(n,x\gamma)$ ,  $\text{Cu}(n,x\gamma)$ ,  $^{40}\text{Ar}(n,p)^{40}\text{Cl}$ , and neutron elastic scattering on Ne and Ar. This year cross-section measurements were made on the neutron-capture reaction for  $^{136}\text{Xe}$ ,  $^{40}\text{Ar}$ , and  $^{74,76}\text{Ge}$  in the energy range from 0.4 to 14.8 MeV. See Sects. 2.1.10, 2.1.11, and 2.1.12 for details.

- **Two-nucleon transfer reactions**

Two-nucleon transfer reactions provide a mechanism for validating assumptions made in QRPA calculations about the ground-state configuration of nuclei involved in  $0\nu\beta\beta$  decay. To this end, TUNL groups are constructing an experiment to perform  $(^3\text{He},n)$  two-proton transfer reactions on nuclei used in  $0\nu\beta\beta$  decay searches. This year the beam line and the scattering chamber for this experiment were installed and tested, the design of the helium-gas recirculation system for the helium ion source was finalized, and all the components have been procured. Details can be found in Sects. 8.3.2 and 7.2.2 of this report.

### 3. Nuclear Astrophysics

The research at TUNL in this area focuses on measurements and data evaluations that are important for resolving element-abundance anomalies in globular clusters and for modeling stellar evolution, nucleosynthesis, and classical novae. Key parts of this program are the measurement of reactions relevant to the evolution of massive stars (e.g. the  $^{12}\text{C}(\alpha,\gamma)^{16}\text{O}$  reaction) and the reactions that govern energy production in stars (e.g. the  $^{14}\text{N}(p,\gamma)^{15}\text{O}$  reaction in the carbon-nitrogen cycle). This research is primarily carried out at LENA and HI $\gamma$ S. The nuclear astrophysics experiments done at HI $\gamma$ S are reported in the Photonuclear Reactions section of this introduction. Highlights of the accomplishments made this year in the research program at LENA are given below.

*Faculty:* Champagne, Iliadis, and Kelley

*Graduate Students (6):* Buckner(UNC), Cooper(UNC), Dermigny (UNC), Downen(UNC), Hunt(UNC) and Kelly (UNC)

*Ph.D. Degrees Awarded:* Daigle (UNC)

*Number of journal papers:* 2

#### Nucleosynthesis in Hydrostatic and Explosive Environments

- **The  $^{14}\text{N}(p,\gamma)^{15}\text{O}$  reaction**

The  $^{14}\text{N}(p,\gamma)^{15}\text{O}$  reaction regulates energy production in the CN cycle and therefore impacts nucleosynthesis in red giants and novae. The ground-state transition in the reaction accounts for between 9% and 25% of the S-factor at zero energy but is poorly constrained by experiment. A new experiment to reduce the uncertainties in the S-factor for this reaction is being developed at LENA. This year a proof-of-principle measurement was carried out using the proton beam from the JN accelerator and the APEX NaI detector. The approach looks promising. The counting rate and signal-to-background ratio can be increased by using the high-current beam from the ECR source. See Sect. 3.1.1 for details.

- **The  $^{23}\text{Na}(p,\gamma)^{24}\text{Mg}$  reaction and sodium abundance**

Understanding the abundance of sodium in globular clusters may reveal information about the history of star formation in the cluster. Element-abundance data for globular clusters show star-to-star variations for light elements such as carbon, nitrogen, oxygen, sodium, magnesium and aluminum. One possible source of these variations is the massive asymptotic giant branch stars. A group conducting research at LENA has developed a new computational tool for determining the sensitivity of element production in a particular stellar environment to specific nuclear reaction rates. The method is based on random sampling of the values of the reaction rates used in network calculations that produce the elements of interest. The sampling is done over the uncertainties in all reaction rates in the network using the Monte-Carlo technique. This computational technique was applied to determine the sensitivity of the new cross-section measurements of the  $^{23}\text{Na}(p,\gamma)^{24}\text{Mg}$  reaction made at LENA to the abundance of  $^{23}\text{Na}$  in AGB stars. See Sect. 3.1.2 for details.

- **Nuclear mixing meters for classical novae**

Observations of novae indicate that material at the surface of a white dwarf mixes with the matter accreted from the companion star in the burning region prior to thermonuclear runaway. However, the mechanism for this mixing is not understood. This year a TUNL group performed Monte-Carlo simulations that model the nuclear-reaction network of ONE nova. The purpose of this work was to identify elemental ratios of ejected materials from a novae that vary strongly with the mixing fraction and therefore could serve as a metric for quantifying material-mixing in nova. Five such element ratios were identified in this work. Details are in Sect. 3.1.3.

#### Thermonuclear Reaction Rates

- **Monte-Carlo reaction-rate contributions**

Computational tools that are based on Monte-Carlo techniques and use evaluated nuclear reaction rate libraries, such as STARLIB or NACRE, have been developed to aid in the identification

of the most important nuclear reactions in a particular stellar process. In addition, the software enables researchers to estimate the accuracy required of new measurements if they are to make a significant contribution to the field. See Sect. 3.2.1 for details.

- **Astrophysical applications of the Porter-Thomas distribution**

The Porter-Thomas distribution is essential for estimating thermonuclear reaction rates in cases where unobserved resonances contribute to the total rate. This year the mean-reduced widths of proton and  $\alpha$ -particle resonances in compound nuclei in the  $A = 28$  to 67 mass range were derived and then used to improve the estimation of reaction rates used to model stellar processes. See Sect. 3.2.2 for details.

## 4. Nuclear Structure and Reactions

This area broadly includes the topics of few-nucleon systems and many-body physics of strongly interacting particles. The main aim of the few-nucleon experiments is to provide data that are important for refining few-nucleon calculations and developing theoretical frameworks that have the structure and symmetries of QCD. An example is effective field theories, for describing low-energy systems of strongly interacting hadrons. In the area of many-nucleon systems, research groups at TUNL study the collective responses of nuclei to electromagnetic waves and the structure of nuclei by analyzing reaction data with statistical models. The on-site accelerator facilities used for this research are the tandem lab and HI $\gamma$ S. Some of this work is also done at the Los Alamos Neutron Science Center. The experiments in this area done at HI $\gamma$ S are reported in the Photonuclear Reactions section of the introduction. Work not conducted at HI $\gamma$ S is summarized here.

*Faculty:* Ahmed, Howell, Karwowski, Kelley, Mitchell, Tornow, and Weller

*Graduate Students (3):* Gooden (NCSU), Kafkarkou (Duke), and Malone (Duke)

*Ph.D. Degrees Awarded:* Walker (NCSU)

*Number of journal papers:* 6

- **The neutron-neutron strong force**

The neutron-neutron ( $nn$ ) strong force is one of the three basic two-nucleon strong interactions required in ab-initio few-nucleon calculations, and the fundamental coupling constants for this interaction are parameters that can be predicted in lattice-QCD calculations. Because the  $nn$  interaction cannot be directly characterized over the energy and angular-momentum ranges relevant for low-energy nuclear systems, this interaction is modeled by applying charge symmetry to the nuclear part of the proton-proton ( $pp$ ) interaction. Comparison of the  $pp$  and  $nn$   $^1S_0$  scattering lengths strongly suggests that charge symmetry is valid to within a few percent for angular momentum  $l = 0$  near zero energy. However, recent measurements of the cross section for  $nn$  quasi-free scattering (QFS) in neutron-deuteron ( $nd$ ) breakup suggest that charge symmetry is violated by more than 10% for  $l = 0$  and  $E > 0$ . This year we conducted proof-of-principle measurements to evaluate one of our experimental techniques for measuring the cross section for  $nn$  QFS in  $nd$  breakup below 20 MeV. The tests indicate that the technique has a sufficiently high signal-to-background ratio to produce reliable values for the cross section.

- **The  $^{11}\text{B}(p,\alpha)\alpha\alpha$  reaction**

The  $^{11}\text{B}(p,\alpha)\alpha\alpha$  reaction is a candidate energy source for aneutronic fusion power reactors. Because natural boron contains about 20%  $^{10}\text{B}$ , it is important to study the reactions involving  $^{10}\text{B}$  that produce radioactive nuclei. This year, two reactions that could produce radioactive contaminants in a boron-fueled reactor were studied:  $^{10}\text{B}(p,\alpha)^7\text{Be}$  and  $^{10}\text{B}(p,\gamma)^{11}\text{C}$ . Cross sections were measured over the energy range most relevant to nuclear-fusion reactor design. The measurements were carried out in the tandem laboratory. Details are given in Sects. 4.1.1 and 4.1.2.

- **Projectile breakup reactions**

The TUNL pre-equilibrium reaction model code, PRECO, has the ability to treat light complex particles (mass numbers of two to four) as well as nucleons in the reaction entrance and exit

channels. However, like virtually all pre-equilibrium codes, it has lacked a module to include the effects of the breakup of complex projectiles. A model for such processes has been developed at TUNL and was programmed into what will eventually be a subroutine in PRECO. The validity of the breakup model was previously verified by comparing model calculations to data for deuteron and  $^3\text{He}$  projectiles and has now also been tested for  $\alpha$ -particle breakup channels. The comparisons for all three projectiles indicate that the projectile-breakup contribution to the total reaction cross section increases with incident energy and accounts for up to about two-thirds of the total reaction cross section. Details are given in Sect. 4.2.1.

- **Neutron-capture cross sections at DANCE**

Neutron-capture cross sections provide information about low-energy collective excitations in nuclei. Examples are the scissors mode and pygmy resonances. Such excitations are important for applications in fields such as nuclear astrophysics, stewardship science, and advanced-fuel-cycle calculations. The DANCE collaboration at LANSCE uses  $\gamma$ -ray cascade measurements of isolated neutron resonances to determine resonance properties and the photon strength function. This year, the work of the DANCE collaboration included a study of the resonances in the  $^{155}\text{Gd}(n,\gamma)$  reaction and of the strength of the scissors mode in odd-mass Gd isotopes. Analyses of data on several nuclei were completed. Finally, a new method for determining resonance spins from the multiplicity distributions of  $\gamma$ -ray cascade data was developed. See Sect. 4.3.1 for details.

## 5. Photonuclear Reactions at HI $\gamma$ S

The HI $\gamma$ S facility provides polarized beams for a broad research program in nuclear physics, including nuclear structure, nuclear astrophysics, and nucleon structure. The main focus of the nuclear structure program is the study of collective responses of nuclei to electromagnetic excitation, thus providing data for developing and testing ab-initio few-nucleon calculations and low-energy effective-field theories. Collective modes are studied both at excitation energies below the Giant Dipole Resonance (GDR), using nuclear resonance fluorescence (NRF) with linearly polarized  $\gamma$ -rays, and at energies above the onset of the GDR, using polarized Compton scattering. An example of a collective nuclear phenomenon that can be probed using polarized Compton scattering is the isovector giant quadrupole resonance. Most of the few-nucleon research at HI $\gamma$ S involves measurements of the photodisintegration process with the purpose of testing ab-initio calculations and investigating the Gerasimov-Drell-Hearn (GDH) sum rule. Internal degrees of freedom of nucleons are probed using Compton scattering from unpolarized and polarized targets at energies above about 70 MeV by measuring the collective electromagnetic responses of the proton or of nucleons inside few-nucleon systems.

Specific goals of the nuclear physics program at HI $\gamma$ S include: (1) measuring the astrophysical S-factor for the  $^{12}\text{C}(\alpha,\gamma)^{16}\text{O}$  reaction at energies important to astrophysics; (2) studying collective nuclear excitations using NRF and Compton scattering; (3) providing data for developing effective field theory descriptions of few-nucleon systems; (4) determining the electric and magnetic polarizabilities of the nucleons; and (5) measuring the nucleon spin polarizabilities.

Proposals for nuclear-physics experiments requesting beam time at HI $\gamma$ S are reviewed by a Program Advisory Committee (PAC) consisting of members external to the TUNL consortium. The HI $\gamma$ S PAC meets once a year. During this reporting period it met on June 4–5, 2013. Progress on PAC approved experiments is summarized below.

*Faculty:* Ahmed, Clegg, Gao, Howell, Karwowski, Kelley, Iliadis, Tornow, and Weller

*Graduate Students (6):* Friesen (Duke), Han (Duke), Huang (Duke), Laskaris (Duke), Peng (Duke), and Ye (Duke)

*Ph.D. Degrees Awarded:* Tompkins (UNC), Zimmerman (UConn), and Mueller (Duke)

*Number of journal papers:* 10

### Nuclear Astrophysics

- **Characterization of the second 2+ state in  $^{12}\text{C}$**

The OTPC (optical time-projection chamber) collaboration completed analysis of their cross-

section data for the  $^{12}\text{C}(\gamma, 3\alpha)$  reaction that were measured at HI $\gamma$ S last year. This photodisintegration reaction enabled direct observation and characterization of the second  $2^+$  state in  $^{12}\text{C}$ . The results were reported in Zimmerman *et al.*, Phys. Rev. Lett., **110**, 152502 (2013). Preparation of a longer paper on the experimental techniques and full results is underway. The implications of this state for nuclear astrophysics are being considered. See sections 5.1.1 and 5.1.2 for details.

- **The  $^{16}\text{O}(\gamma, \alpha)$  reaction**

The OTPC collaboration performed measurements of the  $^{16}\text{O}(\gamma, \alpha)$  reaction using high-purity  $\text{N}_2\text{O}$  as the counter gas instead of  $\text{CO}_2$ . This change was made to eliminate the background from the photodisintegration of carbon. Analysis of these data is underway. The full angular coverage of these data enabled the most precise determination of the E1-E2 mixing at the resonance energy around 9.45 MeV  $\gamma$ -ray energy. This year the collaboration started an upgrade of the OTPC gas-handling system that will allow us to use isotopically pure  $^{13}\text{CO}_2$  gas. This will optimize the signal-to-background ratio, as measurements are pushed to lower energies. Details of the system for handling high-purity gas on the OTPC are given in Sect. 8.2.1.

### Few-nucleon Systems

- **Photodisintegration of  $^3\text{He}$  with double polarization**

HI $\gamma$ S experiments P-03-09 and P-14-11 provide double-polarization (beam and target) data for three-body and two-body photodisintegration of  $^3\text{He}$ . These data are important in developing ab-initio calculations for the GDH sum rule and for determining the forward-angle spin-polarizability parameter. Measurements on three-body photodisintegration were made this year at  $\gamma$ -ray beam energies of 12.8 and 14.7 MeV. The measurements were carried out using circularly polarized  $\gamma$  rays on a high-pressure, optically-pumped, polarized  $^3\text{He}$  gas target. The results of these measurements were published in G. Laskaris *et al.*, Phys. Rev. Lett. **110**, 202501 (2013). For details see Sect. 5.2.1.

- **Photodisintegration of the triton**

The development of an experiment to make the first differential cross-section measurements of two and three-body photodisintegration of the triton is underway. These measurements will be carried out at HI $\gamma$ S using  $\gamma$ -ray beam energies of 15 and 25 MeV. The resulting data will be used to determine the neutron-neutron  $^1\text{S}_0$  scattering length for the first time using this reaction. The HI $\gamma$ S PAC approved the proposal for this experiment (P-02-13) in June 2013 with an excellent science rating. This year substantial progress was made on developing the tritium gas targets and the position-sensitive charged-particle full-energy detector. This project will bring hardware and software technologies for highly segmented detectors to TUNL. For details see sections 5.2.2 and 8.1.5.

- **Compton scattering from unpolarized  $^3\text{He}$**

The goal of HI $\gamma$ S experiment P-07-10 is to measure the spin polarizabilities of the neutron using a polarized  $^3\text{He}$  target. The experiment will be carried out by measuring Compton-scattering of circularly polarized  $\gamma$  rays from a high-pressure, polarized- $^3\text{He}$ , optically-pumped gas target. The scattered  $\gamma$  rays will be detected with the HINDA array. About 60 hours of beam was delivered to this experiment this year to study backgrounds and other experimental design issues. The results of this test indicate that the current beam intensity at HI $\gamma$ S is about a factor ten too low to perform this measurement. See Sect. 5.3.2 for details.

### Nuclear Structure

- **The IVGQR in  $^{124}\text{Sn}$**

The isovector giant quadrupole resonance (IVGQR) is a general feature of the collective modes of motion of heavy nuclei and is related to the symmetry energy in the macroscopic equation of state for nuclear matter. Because of the scarcity of data sensitive to this nuclear excitation mode, the energy dependence of where the maximum amplitude occurs is not well characterized as a function of atomic mass number  $A$ . A TUNL and George Washington University collaboration is

using a technique based on Compton scattering to characterize the IVGQR of nuclei strategically selected to verify the  $A$ -dependence of the resonance centroid energy. This year the collaboration performed measurements of the energy, width, and cross section of the IVGQR in  $^{124}\text{Sn}$  (HI $\gamma$ S experiment P-11-2012). The results are being prepared for publication. For details see Sect. 5.3.1.

- **Nuclear resonance fluorescence measurements**

The  $\gamma^3$   $\gamma$ -ray spectroscopy setup for NRF measurements was installed at HI $\gamma$ S in August 2012, and the first set of experiments with this system were conducted that fall. This setup consists of four 60% HPGe detectors and an array of LaBr scintillation detectors to provide wide angular coverage and the ability to perform  $\gamma$ - $\gamma$  coincidence measurements. This instrumentation is the main detector system of the  $\gamma^3$  collaboration, which consists of groups from TUNL and GSI. This year the collaboration published results of NRF measurements used to study the dipole collective response of  $^{142}\text{Nd}$ ,  $^{86}\text{Kr}$ ,  $^{90}\text{Zr}$ , and  $^{76}\text{Se}$ . These publications are listed in the appendix. The collaboration also performed NRF measurements on  $^{76}\text{Ge}$ ,  $^{92,94}\text{Zr}$ ,  $^{124}\text{Sn}$ ,  $^{128}\text{Te}$ ,  $^{140}\text{Ce}$ ,  $^{152,156}\text{Gd}$ ,  $^{162,164}\text{Dy}$ ,  $^{181}\text{Ta}$ , and  $^{206}\text{Pb}$  during fall of 2012 and 2013. This year a TUNL group performed NRF measurements on  $^{154}\text{Sm}$  to determine the  $\gamma$ -ray dipole strength below the giant dipole resonance. Data analysis is underway.

## 6. Applied Research

In addition to the above research in the frontier areas of nuclear physics, we run a nuclear data program and are conducting research important for applications of nuclear physics in national nuclear security, homeland security, and biology. Some highlights of these activities are given below.

*Faculty:* Ahmed, Howell, Karwowski, Kelley, Mitchell, Tornow, and Weller

*Graduate Students (3):* Cumberbatch (Duke), Fallin (Duke), and Gooden (NCSSU)

*Ph.D. Degrees Awarded:* none

*Number of journal papers:* 4

- **Nuclear data program**

The nuclear data evaluation at TUNL is part of the United States Nuclear Data Program and the International Nuclear Structure and Decay Data network. Its varied activities, which are summarized in Sect. 6.5.1, include:

- Work to update the ENSDF files for  $A = 2, 3,$  and  $12$  is underway.
- The TUNL group is responsible for creating the  $A = 2$  to  $20$  data sets for the Experimental Un-evaluated Nuclear Data List (XUNDL). The TUNL group updates an average of about five data sets each month.
- In May 2013 TUNL hosted a workshop on the future organization of the XUNDL compilation effort.

- **Applications**

The research activities that are focused on applied topics include:

- $\gamma$ -ray-induced reactions for homeland security and national nuclear security (NRF measurements and polarized photofission on actinides at HI $\gamma$ S)
- Neutron-induced reactions for national nuclear security, including reactions important for neutron flux diagnostics at the National Ignition Facility
- Plant physiology studies using accelerator-produced  $^{11}\text{CO}_2$ ,  $^{13}\text{NO}_3$  and  $^{52}\text{Fe}$ . Details are given in Sect. 6.4.1
- Studies of membranes used for water purification using Rutherford backscattering. Details are given in Sect. 6.3.1

## 7. Accelerator Physics

TUNL operates three accelerator facilities: the High Intensity Gamma-Ray Source (HI $\gamma$ S), the Laboratory for Experimental Nuclear Astrophysics (LENA) and the tandem accelerator laboratory. The main R&D activities for the TUNL accelerators are summarize here.

*Faculty:* Champagne, Clegg and Wu

*Graduate Students (3):* Yan (Duke) and Zhou (Duke)

*Ph.D. Degrees Awarded:* none

*Number of journal papers:* none

- **HI $\gamma$ S**

- The FEL wiggler switchyard system was commissioned this year. This new system provides the capabilities required to carry out the Compton-scattering program at HI $\gamma$ S. In February through March 2013 the switchyard was used to deliver an intense and circularly polarized  $\gamma$ -ray beam at about 87 MeV to Compton-scattering experiments. The switchyard can be reconfigured (i.e., changed from four helical wigglers to a mixture of two helical and two dipole wigglers) in about six days. The configuration with four helical wigglers provides a higher intensity of circular polarized  $\gamma$ -ray beams. Details are given in Sect. 7.1.3.
- Production of high-intensity, high-energy  $\gamma$ -ray beams in the energy range of 60 to 158 MeV requires a high-current electron beam at energies of 0.9 to 1.2 GeV. At these energies, the edge radiation from the end-of-arc dipole is the dominant cause of a rapid degradation of the down-stream FEL mirror. A soft orbit bump has been studied with beam calculations, and implementation is being developed with the goal of significantly reducing the impact of the radiation from this dipole. Development of the soft orbit bump and cooled mirror holders are parts of the strategy for increasing the lifetime of the FEL mirrors used to produce  $\gamma$ -ray beams with energies greater than about 100 MeV. Details are given in Sect. 7.1.5.
- The mirror development program to produce radiation-resistant, high-reflectivity 175 nm mirrors continues. These mirrors are needed to reliably produce  $\gamma$ -ray beams in the energy range of 110 to 120 MeV. In the coming year, work will continue to develop new mirror holders that will allow the use of mirrors with different sizes and provide improved cooling of the mirrors.

- **LENA:**

The ECR source provides the primary beam for experiments at LENA. Since 2011, it has had the capability of delivering up to 1.5 mA of direct current H<sup>+</sup> beam on target at energies between 90 and 200 keV. This source is being upgraded to increase the beam current and to provide pulsed-beam capability with about a 10% duty factor. This is part of the strategy to increase the signal-to-background ratio in reaction measurements at LENA. The standard operating parameters at LENA are beam currents of about 20 to 30 mA at energies between 90 and 240 keV. The upgrade is being carried out in two steps: (1) developing the pulsed ECR source and (2) developing the acceleration column with high-current and high transport-efficiency capabilities. This year a remotely controllable microwave system to excite the ECR source plasma was installed. This new system provides the capability of pulsing the plasma off and on, in order to produce a pulsed beam with about a 10% duty factor. This beam structure will contribute substantially to reducing the beam-uncorrelated backgrounds in the nuclear reaction measurements at LENA. The design of the accelerator column is underway. The Hyperion ion source design of the accelerator tube by Twin Creeks Technologies is being considered.

## 8. Nuclear Instrumentation and Methods

Developments in technology and instrumentation are vital to our research and training program. The current instrumentation development activities include development of the following capabilities:

- Liquid hydrogen target for photonuclear measurements at HI $\gamma$ S
- Cryogenic polarized target for research at HI $\gamma$ S (HIFROST)
- Tritium gas targets for research at HI $\gamma$ S
- Detectors for  $\gamma$ -ray measurements, spectroscopy of low-energy charged particles, low-energy neutron counting, time projection chambers, and rare-event counting.
- Infrastructure facilities needed for research with ultra-cold neutrons.
- Rare-gas handling systems for using  $^3\text{He}$  in the helium ion source in the tandem laboratory and  $^{13}\text{CO}_2$  in the OTPC used in the  $^{16}\text{O}(\gamma, \alpha)$  measurement.

# Personnel

Department of Physics, Box 90308, Duke University,  
Durham, NC 27708-0308

Department of Physics, Box 8202, North Carolina State University,  
Raleigh, NC 27695-8202

Department of Physics and Astronomy, University of North Carolina,  
Chapel Hill, NC 27599-3255

## *Faculty*

Ahmed, M. W. (Adjunct Associate Professor)	NCCU/Duke
Barbeau, P. S. <sup>1</sup> (Assistant Professor)	Duke
Bilpuch, E. G. <sup>2</sup> (Professor Emeritus)	Duke
Champagne, A. E. (Professor)	UNC
Clegg, T. B. (Professor)	UNC
Gao, H. (Professor)	Duke
Golub, R. (Professor)	NCSU
Gould, C. R. (Professor)	NCSU
Haase, D. G. (Professor)	NCSU
Henning, R. (Assistant Professor)	UNC
Howell, C. R. (Director, Professor)	Duke
Huffman, P. R. (Associate Director, Professor)	NCSU
Iliadis, C. (Professor)	UNC
Karwowski, H. J. (Professor)	UNC
Kelley, J. H. (Research Associate Professor)	NCSU
Ludwig, E. J. (Professor Emeritus)	UNC
Merzbacher, E. <sup>3</sup> (Professor Emeritus)	UNC
Mitchell, G. E. (Professor Emeritus)	NCSU
Roberson, N. R. (Professor Emeritus)	Duke
Tilley, D. R. (Professor Emeritus)	NCSU
Tonchev, A. P. (Adjunct Associate Professor)	LLNL/Duke
Tornow, W. (Professor Emeritus)	Duke
Walter, R. L. (Professor Emeritus)	Duke
Weller, H. R. (Assoc. Dir. for Nuclear Physics at HI $\gamma$ S, Professor Emeritus)	Duke
Wilkerson, J. F. (Associate Director, Professor)	UNC
Wu, Y. K. (Associate Director for Light Sources, Associate Professor)	Duke
Young, A. R. (Professor)	NCSU

---

<sup>1</sup>As of 8/13

<sup>2</sup>Deceased 9/12

<sup>3</sup>Deceased 6/13

*TUNL Advisory Committee*

Aprahamian, A.	University of Notre Dame
Balantekin, A. B.	University of Wisconsin
Garvey, G. T.	Los Alamos National Laboratory
Vigdor, S. E.	Brookhaven National Laboratory
Wiescher, M. C.	University of Notre Dame

*HI $\gamma$ S Program Advisory Committee*

Beise, E. J.	University of Maryland
Garvey, G. T. (Chair)	Los Alamos National Laboratory
Griesshammer, H.	George Washington University
Rehm, K. E.	Argonne National Laboratory
Sherrill, B. M.	National Superconducting Cyclotron Laboratory
Chen, J. P.	Thomas Jefferson National Laboratory
Donnelly, T. W.	Massachusetts Institute of Technology

*Associated Faculty*

Crawford, B. E.	Gettysburg College
Crowe, B. J.	North Carolina Central University
Dutta, D.	Mississippi State University
Engel, J.	University of North Carolina
Gai, M.	University of Connecticut at Avery Point
Keeter, K. J.	Idaho State University
Korobkina, E.	North Carolina State University
Markoff, D. M.	North Carolina Central University
McLaughlin, G. C.	North Carolina State University
Norum, B.	University of Virginia
Pedroni, R. S.	North Carolina A&T State University
Prior, R. M.	North Georgia College and State University
Purcell, J. E.	Georgia State University
Shriner, J. F.	Tennessee Technological University
Spraker, M. C.	North Georgia College and State University
Stephenson, S. L.	Gettysburg College
Weisel, G. J.	Penn State Altoona

*Accelerator Physics Staff for Operations*

Li, J. <sup>1</sup>	Senior Research Scientist (at HI $\gamma$ S)
Mikhailov, S. F.	Senior Research Scientist (at HI $\gamma$ S)
Popov, V. G.	Senior Research Scientist (at HI $\gamma$ S)
Westerfeldt, C. R.	Research Scientist (low energy accel.) & Rad. Safety Manager

---

<sup>1</sup>On leave 3/13

*Research Staff*

Baramsai, B. <sup>1</sup> (Research Associate)	NCSU
Bhike, M. (Research Associate)	Duke
Broussard, L. J. (Research Associate)	NCSU
Chu, P. (Research Associate)	Duke
Crowell, A. S. (Research Scientist)	Duke
Dashdorj, D. <sup>1</sup> (Research Associate)	NCSU
Esterline, J. H. <sup>2</sup> (Research Associate)	Duke
Fränkle, F. M. <sup>3</sup> (Research Associate)	UNC
Green, M. P. <sup>2</sup> (Research Associate)	UNC
Hao, H. (Research Associate)	Duke
Howard, C. <sup>4</sup> (Research Associate)	UNC
Howe, M. A. (Senior Research Scientist)	UNC
Jawalkar, S. <sup>3</sup> (Research Associate)	Duke
Kalbach Walker, C. (Senior Research Scientist)	Duke
Kendellen, D. P. <sup>5</sup> (Research Associate)	Duke
Krishichayan <sup>6</sup> (Research Associate)	Duke
Leung, K. (Research Associate)	NCSU
Longland, R. <sup>6</sup> (Research Associate)	UNC
Mazumdar, I. <sup>7</sup> (Senior Visiting Research Scientist)	Duke
Mehta, V. <sup>8</sup> (Research Associate, part time)	NCSU
Meziane, M. (Research Associate)	Duke
Myers, L. S. <sup>3</sup> (Research Associate)	Duke
O'Shaugnessy, C. (Research Associate) <sup>5</sup>	UNC
Pattie, R. W. (Research Associate)	NCSU
Phillips II, D. G. (Research Associate)	NCSU
Sallaska, A. (Research Associate) <sup>9</sup>	UNC
Seo, P.-N. (Research Associate)	UVA
Sikora, M. H. (Research Associate)	GWU
Swank, C. A. (Research Associate)	NCSU
Wu, W. (Research Associate)	Duke
Ye, Z. (Research Associate)	Duke

*Technical and Nuclear Data Support Staff*

Busch, M.	Mechanical Engineer
Carlin, B. P.	Electronics Supervisor
Carter, E. P. <sup>10</sup>	Accelerator Technician
Dunham, J. D.	Accelerator Technician
Emamian, M.	Mechanical Engineer (at HI $\gamma$ S)
Faircloth, J.	Project and Building Maint. Coordinator (at HI $\gamma$ S)
Johnson, M.	Vacuum Technician (at HI $\gamma$ S)
Mulkey, P. H. <sup>10</sup>	Electronics Technician
Oakley, O. <sup>10</sup>	Electronics Technician (at HI $\gamma$ S)
O'Quinn, R. M.	Accelerator Supervisor
Pentico, M.	Accelerator Technician (at HI $\gamma$ S)

<sup>1</sup>Supported by NNSA/DOE<sup>2</sup>Departed 9/13<sup>3</sup>Departed 8/13<sup>4</sup>Departed 7/13<sup>5</sup>As of 11/12<sup>6</sup>As of 8/13<sup>7</sup>Departed 2/13<sup>8</sup>Supported by NSF/DOE<sup>9</sup>Departed 4/13<sup>10</sup>Departed 5/13<sup>11</sup>Supported by DHS

Rathbone, V.  
Sheu, G.  
Swift, G.<sup>11</sup>  
Wallace, P.<sup>11</sup>  
Walsh, B.  
Wang, P.

Accelerator Technician (at HI $\gamma$ S)  
Project Coordinator, Nuclear Data  
Vacuum Engineer (at HI $\gamma$ S)  
Electrical Engineer and Safety Manager (at HI $\gamma$ S)  
Accelerator Technician  
RF Engineer (at HI $\gamma$ S)

*Graduate Students*

Buckner, M. <sup>2</sup>	UNC	Medlin, G. <sup>5</sup>	NCSU
Combs, D.	NCSU	Mueller, J. M. <sup>1</sup>	Duke
Cooper, A.L.	UNC	Palmquist, G.	NCSU
Corona, T. J.	UNC	Peng, C.	Duke
Cumberbatch, L. C.	Duke	Powell, J.	UNC
Daigle, S. <sup>1</sup>	UNC	Rager, J.	UNC
Dees, E.	NCSU	Reid, A.	NCSU
Dermigny, J.	UNC	Rich, G.	UNC
Downen, L. N.	UNC	Schelhammer, K. <sup>1</sup>	NCSU
Esan, I.	NCCU	Shanks, B.	UNC
Fallin, B. A.	Duke	Silano, J.	UNC
Finch, S. W.	Duke	Strain MacMullin, J.	UNC
Finnerty, P. <sup>1</sup>	UNC	Snavely, K.	UNC
Friesen, F. Q.	Duke	Swindell, A. G.	U. Conn
Gooden, M. E.	NCSU	Ticehurst, D. R.	UNC
Giovanetti, G. K. <sup>3</sup>	UNC	Tompkins, J. R. <sup>1</sup>	UNC
Huang, M.	Duke	Vorren, K.	UNC
Hunt, S.	UNC	VornDick, B. <sup>4</sup>	NCSU
Huffer, C.	NCSU	Walker, C. <sup>1,6</sup>	NCSU
Kafkarkou, A.	Duke	Wierman, K.	UNC
Kelly, K.	UNC	Xiong, W.	Duke
Kendellen, D. P. <sup>1</sup>	NCSU	Yan, J.	Duke
Laskaris, G.	Duke	Yan, X.	Duke
Leviner, L.	NCSU	Ye, Q. J. <sup>1</sup>	Duke
Li, W.	Duke	Zeck, B. <sup>7</sup>	NCSU
Lin, L.	UNC	Zhang, Y.	Duke
MacMullin, S. <sup>1</sup>	UNC	Zhou, W.	Duke
Malone, R.	Duke	Zimmerman, W. R. <sup>1</sup>	U. Conn

*Visiting Scientists*

Witala, H.	7/13 - 8/13	Jagiellonian University, Cracow, Poland
------------	-------------	---

*Administrative Support Personnel*

Strope, J. <sup>8</sup>	Staff Assistant
West, B.	Staff Assistant

<sup>1</sup>Graduated with Ph.D. Degree between 9/12 and 11/13<sup>2</sup>Supported by DOE NSSA Fellowship<sup>3</sup>Supported by DOE Office of Science Fellowship<sup>4</sup>Supported by NSF/DOE<sup>5</sup>Supported in part by a GAANN Fellowship<sup>6</sup>Supported by NNSA/DOE<sup>7</sup>Supported in part by LANL<sup>8</sup>Partially supported by the Duke University Physics Department

*Undergraduates*

<i>Student</i>	<i>Institution</i>	<i>Faculty Advisor</i>
Ahrendsen, K. <sup>1</sup>	Buena Vista University	K. Scholberg (Duke)
Bai, V.	Duke University	C. R. Howell
Binter, E. <sup>1</sup>	Beloit College	A. V. Kotwal (Duke)
Daniel, Q.	Florida A&M University	C. R. Howell
Epland, M. <sup>1</sup>	U. Minnesota Twin Cities	M. C. Kruse and A. T. Arce (Duke)
Esposito, C. <sup>1</sup>	St. Joseph's University	K. Scholberg (Duke)
Fetiha, I.	NCCU	M. W. Ahmed
Gray, I. <sup>1</sup>	U. Minnesota Twin Cities	C. R. Howell
Harrison, H.	NCCU	M. W. Ahmed
Horyn, L. <sup>1</sup>	Tufts University	A. T. Goshaw (Duke)
Lieberman, S. <sup>1</sup>	NJ Institute of Technology	A. T. Arce (Duke)
Ludin, N. <sup>1</sup>	University of Denver	W. Tornow
Makhanov, A. <sup>1</sup>	High Point University	A. R. Young
Martin, J.	NCCU	M. W. Ahmed
Payette, D. <sup>1</sup>	North Georgia University	H. R. Weller
Petersburg, R.	UNC	J. F. Wilkerson
Shuman, J. <sup>1</sup>	Rose Hulman Inst. of Tech.	J. H. Kelley
Thomas, B.	NCCU	M. W. Ahmed
Wright, A. <sup>1</sup>	University of Texas Austin	C. R. Howell
Zitin, A.	UNC	J. F. Wilkerson

---

<sup>1</sup>Supported by the TUNL NSF REU Program





# Fundamental Symmetries in the Nucleus

---

Chapter 1

- **The Neutron Electric Dipole Moment**
- **Fundamental Coupling Constants**

In the Nuclear Physics Long Range Plan, NSAC laid out a decadal program to discover components of what was termed the “New Standard Model.” This major initiative in nuclear science aims to answer questions such as *What is the nature of the neutrinos, what are their masses, and how have they shaped the evolution of the cosmos?* and *Why is there now more visible matter than antimatter in the universe?* and *What are the unseen forces that were present at the dawn of the universe but disappeared from view as it evolved?* TUNL has major initiatives directed towards this New-Standard-Model initiative. They are discussed in this section and the following one.

The discovery of a non-zero permanent neutron electric dipole moment (nEDM) would imply violation of the time reversal symmetry and thus help explain the matter/antimatter asymmetry in the universe. TUNL plays a major role in the neutron EDM experiment based at ORNL. This experiment offers the promise of up to two orders of magnitude improvement in sensitivity over existing measurements. Such an improvement would provide new and powerful constraints on possible sources of time-reversal violation within the Standard Model and beyond it.

Precision measurements of  $\beta$ -decay parameters continue to be an integral part of a comprehensive strategy to test electroweak interactions. These measurements are important to astrophysics, where uncertainties in the axial-vector coupling  $G_A$  influence predictions of the  $p$ - $p$  solar neutrino flux, and to Beyond the Standard Model physics, where new scalar or tensor interactions could be revealed through  $\beta$ -decay correlation studies. In Big Bang nucleosynthesis, the neutron-to-proton conversion rate set by the neutron lifetime, competes with the Hubble rate to determine the primordial  ${}^4\text{He}$  abundance. TUNL has active programs in neutron decay as well as in heavier nuclei.

## 1.1 The Neutron Electric Dipole Moment

---

### 1.1.1 Search for the Neutron Electric Dipole Moment

---

M.W. AHMED, P. CHU, H. GAO, R. GOLUB, C.R. GOULD, D.G. HAASE, P.R. HUFFMAN, E. KOROBKINA, K. LEUNG, A.R. REID, C.M. SWANK, A.R. YOUNG, *TUNL*; THE nEDM COLLABORATION

**TUNL plays a major role in the ORNL-based nEDM experimental program. We are developing a new technique that holds promise of improving sensitivity by up to two orders of magnitude over existing measurements. During the past year, TUNL researchers have continued efforts on geometric-phase-effect studies; published heat-flow measurements in superfluid films; collaborated on efforts to measure the scintillation efficiencies in liquid helium; developed measurement-cell coating and assembly techniques; analyzed UCN-storage data in acrylic measurement cells, and are developing an apparatus to study systematic effects using polarized  $^3\text{He}$  and ultracold neutrons.**

The discovery of a neutron electric dipole moment above the Standard Model background—currently about five orders of magnitude below the present limits—would be the first evidence for a new type of time-reversal violation, and hence CP-violation via the CPT theorem. The known CP-violation in the Standard Model remains insufficient by many orders of magnitude to explain the baryon asymmetry of the universe, leaving a window of discovery for non-Standard-Model CP-violation and making the search for new sources of CP-violation essential.

The 2011 DOE/NSF Nuclear Science Advisory Committee’s Fundamental Neutron Physics report reiterated the scientific motivation for EDM searches, saying they remain as compelling as ever. The nEDM experiment was thus deemed to be the initiative with the highest scientific priority in the US neutron science program [Abe11]. The goal of the nEDM experiment is to achieve a sensitivity of  $< 5 \times 10^{-28}$  e-cm. A conceptual design is shown in Fig. 1.1. A value (or limit) for the neutron EDM will be extracted from the difference between neutron spin-precession frequencies for parallel and anti-parallel magnetic fields of about 30 mGauss and electric fields of about 75 kV/cm. This experiment, based on the proposal by Golub and Lamoreaux [Gol94], uses a novel polarized  $^3\text{He}$  co-magnetometer and will detect the neutron precession via spin-dependent neutron capture on  $^3\text{He}$ . A high density of trapped ultracold neutrons is produced via

phonon production in superfluid  $^4\text{He}$ , which can also support large electric fields.

The experiment has several characteristics that distinguish it from the others being planned by reducing potential systematic effects, or allowing us to understand them better. These characteristics include: directly loading the neutron trap with UCNs that are produced in liquid He via the phonon recoil process [Gol77]; using superfluid  $^4\text{He}$  as a working medium for the very high electric field; using a dilute mixture of polarized  $^3\text{He}$  in superfluid  $^4\text{He}$  as a co-magnetometer; using a sensitive SQUID measurement of the precession frequency of the  $^3\text{He}$  magnetic dipoles; using a superconducting shield to isolate the measurement region from external magnetic field fluctuations; determining the difference between the neutron and  $^3\text{He}$  precession frequencies from the spin-dependent absorption cross section and the subsequent variations in light intensity from scintillations in the  $^4\text{He}$ ; allowing two techniques for measuring the nEDM, either the free precession method with SQUIDS or a dressed-spin method that uses a high-frequency magnetic field to modify the effective magnetic moments of the two polarized species [Gol94]; providing a comparison measurement of changes in the precession frequency of the two species under  $E$  and/or  $B$  field reversal in two measurement cells; and using the temperature dependence of the geometric phase for the  $^3\text{He}$  to measure this important systematic [Pen04].

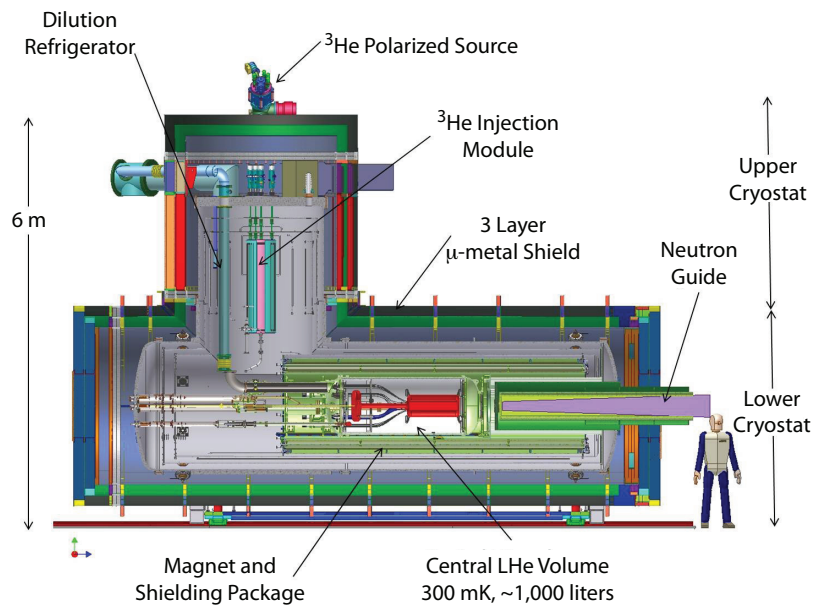


**Figure 1.1:** (Color online) Cross sectional view of the nEDM apparatus, which is approximately 7.5 m long and 2.2 m wide. The neutron beam enters from the right and is down-scattered in liquid helium to produce ultracold neutrons that are confined within the measurement cells. The cells are positioned within a strong electric field and weak magnetic field. The cells are surrounded by about 1,000 l of liquid helium housed in a composite vessel. The  $^3\text{He}$  system and central volume are cooled to below 500 mK with a  $^3\text{He}/^4\text{He}$  dilution refrigerator.

Presently, the collaboration is focused on a number of critical R&D developments. Key issues being addressed include: the maximum electric field strength for electrodes made of appropriate materials in superfluid helium below a temperature of 1 K; magnetic field uniformity for a large-scale magnetic coil and a lead superconducting magnetic shield; estimation of the detected light signal from scintillation in superfluid helium; development of coated measurement cells that preserve neutron and  $^3\text{He}$  polarization along with neutron storage time; understanding polarized  $^3\text{He}$  injection and transport in the superfluid; and exploring the systematics of the dressed-spin technique, including polarized ultracold neutrons and  $^3\text{He}$ . TUNL is playing a major role in three of these efforts—light collection, measurement cells, and systematic studies.

TUNL faculty also serve in leadership roles in the project. Golub serves as a principal scientist; Golub and Huffman co-chair the internal technical committee; Gao, Golub, and Huffman serve on the project’s executive committee;

Haase and Huffman serve as subsystem managers for the construction of the cryovessel and for the assembly and commissioning of the subsystems, respectively; and Huffman serves on the federal project team as the project’s technical coordinator and deputy project manager. Several others serve as work-package managers for components of the subsystems.

- 
- [Abe11] H. Abele *et al.*, *Report to the Nuclear Science Advisory Committee, Submitted by the Subcommittee on Fundamental Physics with Neutrons*, Technical report, 2011.
- [Gol77] R. Golub and J. Pendlebury, *Phys. Lett.*, **A62**, 337 (1977).
- [Gol94] R. Golub and S. K. Lamoreaux, *Phys. Reports*, **237**, 1 (1994).
- [Pen04] J. M. Pendlebury *et al.*, *Phys. Rev. A*, **70**, 032102 (2004).

### 1.1.2 Geometric Phase Effects

R. GOLUB, A. REID, C.M. SWANK, *TUNL*; A. DIPERT, *Arizona State University, Tempe, AZ*;

**In order to achieve the targeted precision of the nEDM experiment, it is necessary to deal with the systematic error associated with the interaction of the well known  $\vec{v} \times \vec{E}$  field with magnetic field gradients. This systematic effect was studied theoretically for a number of operating conditions and is being investigated experimentally in a newly constructed apparatus at TUNL.**

In the neutron electric dipole moment (nEDM) apparatus, the interaction of the field  $\vec{B}_{\text{eff}} \sim \vec{v} \times \vec{E}$  with magnetic field gradients will produce a frequency shift linearly proportional to the electric field. Known as the geometric phase effect and mimicking a true EDM, this effect has recently emerged as a primary systematic error limiting the precision of the next generation of neutron EDM searches.

In the context of neutron EDM experiments, this effect was first investigated experimentally and theoretically by Pendelbury *et al.* [Pen04] and later by Lamoreaux and Golub [Lam05]. In our published work [Bar06], we introduced an analytic form for the correlation function that determines the behavior of the frequency shift, and we showed in detail how it depends on the operating conditions of the experiment. A recently published theory formulates correlation functions for two and three dimensions valid for all mean free paths [C.M12]. Further progress implies it is necessary to include gas collisions that change the velocity of the  $^3\text{He}$ . The validity of this modification to the theory is being checked, while its predicted ramifications are being examined with Monte-Carlo simulations and experiments.

All models that have been proposed indicate that it may be possible to fine-tune the effect to a high degree by an appropriate choice of operating temperature and frequency. The size of the effect at the expected operating parameters is shown in Fig. 1.2. This is a plot of the frequency shift  $\delta\omega$  (which is linear in  $E$ ) as a function of the Larmor frequency  $f_0$ . Values are calculated for particles with values of  $v$  chosen according to the Maxwell-Boltzmann distribution for the chosen operating temperature of 400 mK. The geometry is a rectangular cell of dimensions equal to the nEDM experiment. The model predicts an acceptable

shift that is linear in  $E$  for  $^3\text{He}$  in the nEDM experiment.

Models of the geometric phase effect rely on theoretical calculations of the correlation function. The same correlation function can be determined by measuring the  $T_1$  relaxation rate of the  $^3\text{He}$  polarization in a magnetic field gradient. Thus it is not necessary to measure directly the geometric frequency shift, which is linear in  $E$ .

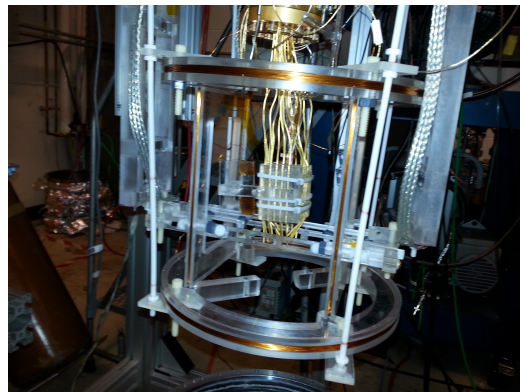


**Figure 1.3: (Color online) The TUNL dilution refrigerator, sample volume, and NMR coils.**

The apparatus to make these gradient measurements uses a dilution refrigerator with a non-magnetic Dewar containing NMR coils and a sample volume. The open Dewar is shown in Fig. 1.3. Data were analyzed for measurements completed at a molar concentration ratio  $^3\text{He}:^4\text{He}$  of  $1 \times 10^{-6}$  at a temperature of 420 mK, and results agree with known theories. For a better understanding of the correlation function, it is desirable to make measurements with a larger mean free path. This is achieved by lowering the temperature or decreasing the concentration. An

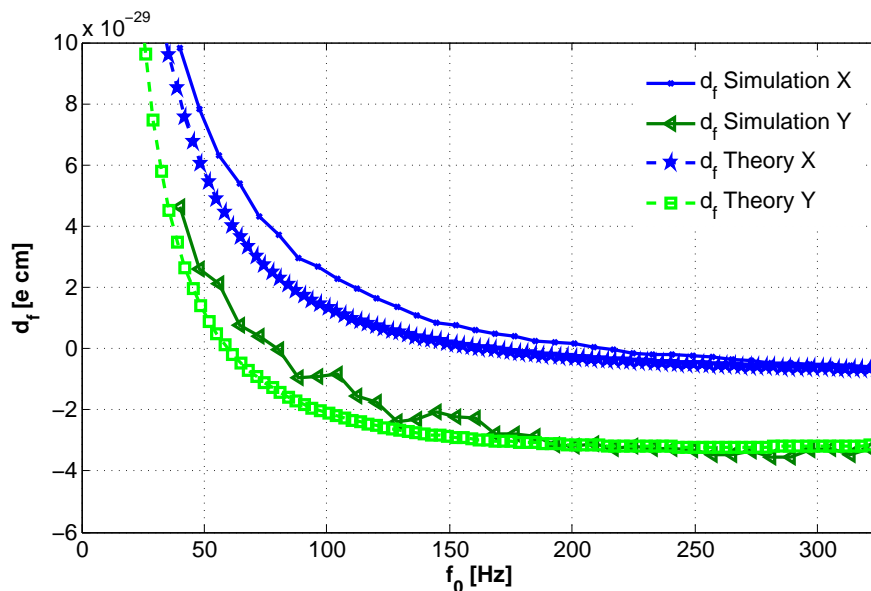


Figure 1.2: (Color online) Simulations compared with theory for the frequency shift induced by the geometric phase effect for  $^3\text{He}$  at the expected operating conditions. The results are separated into the contributions of the  $x$  and  $y$  dimensions of a three dimensional rectangular cell of dimensions  $x = 10.2$  cm,  $y = 40$  cm and  $z = 7.6$  cm, where  $z$  is the direction of the holding field and thus does not contribute to the linear-in- $E$  frequency shift.

apparatus upgraded with a SQUID is being prepared for taking data. Calculations indicate that a SQUID can measure relaxation rates for molar concentration ratios of  $5 \times 10^{-8}$ , which is twenty times smaller than previous measurements, but the noise must be reduced by the same factor of twenty.

In order to reduce noise, we have implemented a unique superconducting shield. Finite-element-method simulations show that a holding field can be generated outside the apparatus and passed through a superconducting cylinder if the cylinder has a vertical slit. This is achieved while still blocking a majority of the RF noise and increasing overall uniformity. To avoid distortion to the

gradient field, the gradient coils must be repositioned inside the superconducting shield.

- 
- [Bar06] A. L. Barabanov, R. Golub, and S. K. Lamoreaux, Phys. Rev. A, **74**, 052115 (2006).
- [C.M12] C.M. Swank, A.K. Petukhov and R. Golub, Phys. Lett., **A376**, 2319 (2012).
- [Lam05] S. K. Lamoreaux and R. Golub, Phys. Rev. A, **71**, 032104 (2005).
- [Pen04] J. M. Pendlebury *et al.*, Phys. Rev. A, **70**, 032102 (2004).

---

### 1.1.3 Development of a Systematic-Studies Apparatus for the nEDM Experiment

---

P. CHU, H. GAO, R. GOLUB, D.G. HAASE, P.R. HUFFMAN, K. LEUNG, A.R. REID, C.M. SWANK, TUNL; A. HAWARI, E. KOROBKINA, *North Carolina State University, Raleigh, NC*; THE NEDM COLLABORATION

**An apparatus is being designed to allow key systematic effects in the neutron electric-dipole-moment (nEDM) experiment to be explored. The apparatus will initially allow one to measure the neutron and/or  $^3\text{He}$  storage lifetimes in a full-size measurement cell. The ultimate goal is to permit the testing of five key scientific areas identified as essential for the larger nEDM project. This work is a natural extension to our on-going  $^3\text{He}$ -depolarization and geometric-phase work.**

The nEDM project team has identified a new opportunity that will significantly reduce the risk to the nEDM project while shortening the time to a physics measurement. The PULSTAR ultracold-neutron (UCN) source will soon come online and become a world-class source of UCNs, comparable in intensity to existing sources at both the Institut Laue Langevin and Los Alamos National Laboratory. This source, coupled with the existing polarized  $^3\text{He}$  capabilities at TUNL, will enable development of an ideal setup for investigating many UCN- $^3\text{He}$  interactions at cryogenic temperatures.

The development will be carried out in two phases. Phase I will involve modifying an existing apparatus in order to allow one to measure the storage time of ultracold neutrons and the depolarization lifetime of  $^3\text{He}$  in a full-size measurement cell at cryogenic temperatures. In addition, studies of  $^3\text{He}$  insertion and removal from liquid  $^4\text{He}$  will be possible. Phase II will include the addition of a uniform magnetic field around the measurement cell.

During the past year, we have focused on the design of the apparatus. A schematic is shown in Fig. 1.4. We will modify an existing Dewar so that it can house this apparatus. This will include modifications to the outer vacuum can, construction of cryogenic shields and an inner vacuum can, integration of an existing  $^3\text{He}$ - $^4\text{He}$  dilution refrigerator into the Dewar, and procurement and installation of all ancillary equipment.

The basic idea of the apparatus is that a measurement cell filled with liquid  $^4\text{He}$  at a temperature of about 450 mK will be placed within

a uniform magnetic field, denoted as the  $B_0$  coil. Cryogenic conventional and superconducting magnetic shields will surround this geometry, as will thermal-radiation shields and, finally, a series of additional external conventional magnetic shields. UCNs from the PULSTAR source will be transported to the cell through a series of guides and then introduced into the cell through the vestibule region shown in Fig. 1.5. Polarized  $^3\text{He}$  will be produced using an external system and will be introduced into the cells alongside the polarized UCNs.

Interactions of the UCNs with the  $^3\text{He}$  will be monitored using the spin-dependent neutron-capture rate. Light from neutron capture produces scintillations in the liquid helium and will be wavelength shifted to visible wavelengths using deuterated fluors. It will then be transported away from the cell through acrylic light-guides for detection by photomultiplier tubes. Pulses will be digitized and analyzed offline. At the end of a measurement cycle, the unpolarized  $^3\text{He}$  must then be removed from the liquid. This will be performed using the heat-flush technique to concentrate the  $^3\text{He}$  into a small volume that can be removed from the cryostat.

The areas where studies at TUNL will provide significant advances to the development and implementation of the nEDM project are as follows:

*Measurement of scintillations due to the relative UCN and  $^3\text{He}$  precession and demonstration of the critical-dressing technique.* The motion of a spin under the application of static and non-resonant oscillating magnetic fields is quite com-

licated. Without the new apparatus, the measurements necessary to establish working parameters for the double resonance of UCNs and  $^3\text{He}$  must occur on the project's critical path during the commissioning phase. The proposed apparatus will allow the critical-dressing parameters to be established and the techniques for providing the critical dressing to be experimentally vetted in parallel with the construction and commissioning of the main apparatus. This will reduce both the time to data collection and the overall risk to the project.

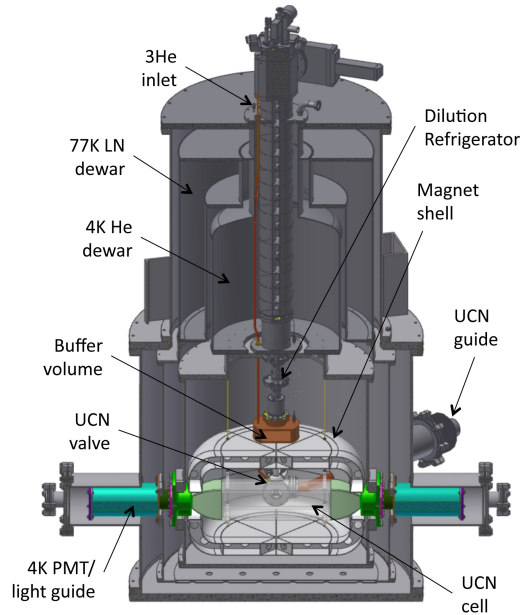


**Figure 1.4:** (Color online) Engineering cross-sectional schematic of the nEDM systematic-studies apparatus. UCNs from the external source enter the apparatus through a horizontal port via a vestibule attached to the side of the cell. Polarized  $^3\text{He}$  enters through a tube (not shown) extending vertically alongside the dilution refrigerator and through the same vestibule.

*Measurement of the trajectory correlation function for systematic-error quantification.* Differences between the actual trajectory correlation function in the measurement cells and those predicted by theory may result in a mishandling of the geometric-phase systematic error, leading to a false nEDM result. The proposed apparatus will allow these functions to be measured in order to establish, for example, the effect of wall collisions on the correlation function prior to performing measurements in the main apparatus.

*Detection of the  $^3\text{He}$  pseudomagnetic field in search of possible double-resonance effects.* This

field results from the spin-dependent coherent-scattering cross section, which leads to an energy shift for the UCNs that is spin-dependent and thus appears as a magnetic field. The pseudomagnetic field is not directly affected by the application of an electric field, but can be the source of fluctuations in the precession frequency and hence extra noise in the system. The magnitude of the pseudomagnetic field can be reduced by ensuring that the  $^3\text{He}$  spins have no component along the static magnetic field. This is possible by careful control of the spin flip pulses.

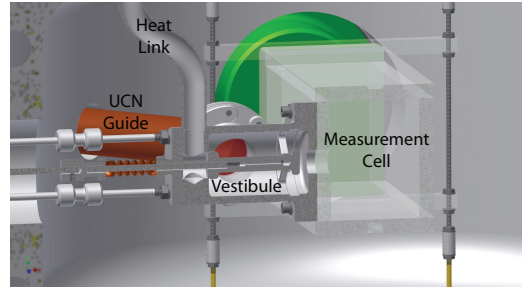


**Figure 1.5:** (Color online) Engineering cross-sectional schematic of the vestibule and measurement cell. The valve will allow UCNs and polarized  $^3\text{He}$  to enter the measurement cell.

*Development of techniques for NMR imaging of  $^3\text{He}$ .* Inhomogeneities in the  $^3\text{He}$  distribution can couple with field gradients and/or detection non-uniformities to produce a false nEDM signal. The proposed apparatus will enable us to develop imaging techniques to map the uniformity of the  $^3\text{He}$  distribution and to study inhomogeneities that might arise as a result of polarity-dependent heat currents, for example, that drive the  $^3\text{He}$  distribution in different directions.

*Study techniques for reversing  $\sigma_{^3\text{He}}$ ,  $\sigma_{\text{UCN}}$  and  $B_0$ .* Establishing the experimental parameters for reversing the spins and magnetic fields will take a considerable length of time during the commissioning phase of the apparatus. Developing these techniques in parallel in the new apparatus will provide an environment where a more complete study of these reversals can be performed without the external time constraints imposed by the critical path. This will reduce both the risk to the project and the time to data collection.

This program of studies will occur in parallel with the construction and commissioning of the main nEDM apparatus. We estimate that the entire program will last four to five years.

---

### 1.1.4 Cryogenic Design and Testing for the nEDM Project

---

D.G. HAASE, P.R. HUFFMAN, D.P. FRAME, J.R. ROWLAND, *TUNL*

**TUNL has played a major role in the cryogenic design and construction issues related to the larger neutron EDM project and in the design of a new nEDM test facility at the PULSTAR reactor. This effort involves the development of (1) a closed cycle refrigerator which cools below the helium lambda point for the testing of components and (2) strategies for the removal of  $^3\text{He}$  from liquid  $^4\text{He}$  during the PULSTAR measurement cycle.**

#### Construction and Operation of the Cryocooler Test Facility

We have built a chamber in which pieces of equipment up to 20 inches diameter and 18 inches high can be cooled to 4 K for vacuum leak testing. The chamber is cooled by a Sumitomo RDK-415D cryocooler that has reached 3.5 K. Because several nEDM components must be leak tight to superfluid helium we have added a closed helium recirculation cycle to the cryocooler, in order to provide continuous cooling and operation below the helium lambda point,  $T_\lambda = 2.17$  K.

The superfluid cooling stage is based on the design of a device meant to liquefy helium for a neutron scattering target [SW06]. We have made several modifications. Specifically, the heat exchanger which pre-cools incoming helium gas was constructed from seven 16-cm-long segments of thin copper tubing connected by 10 cm long brass tubes. The inner and outer diameters (ID and OD) of the copper tubing are 1.67 mm and 2.38 mm, respectively. The same quantities for the brass tubing are 0.866 mm and 1.57 mm. The segments were hard soldered in series and wrapped as a spiral around the second stage regenerator tube of the cryocooler. The copper segments were then clamped to the regenerator tube with stainless-steel hose clamps.

The lower end of the heat exchanger was measured as about 9 K during the recirculation process, in reasonable agreement with a viscous-flow calculation of the exchanger geometry. The heat exchanger feeds a 100-cm-long liquefier made of the same copper tubing hard soldered to a copper flange that was greased and bolted to the second stage. The liquid at about 4.5 K is then fed through a flow impedance (18 cm of 0.010-in. ID

stainless steel tube) into a container pumped by a small, unsealed mechanical pump. In tests, the pumped section cooled to 1.75 K, as measured by a  $^4\text{He}$  vapor-pressure thermometer.

Having noticed large oscillations in temperature, we inserted a 10 cm<sup>3</sup> copper “phase separator” volume into the reflow circuit bolted to the second stage of the cryocooler. In operation, this volume greatly improved the stability of the refrigerator, although filling the separator increased the time for cooling to 1.75 K. The helium gas pumped from the evaporator was passed through a liquid N<sub>2</sub>-cooled charcoal filter and then fed back to the liquefier through a single-head, Air Dimensions Dia Vac R221 diaphragm pump at a pressure of 15 to 20 psig, making this a closed-cycle refrigerator.

#### Fabrication and Testing of Etched Silicon Superfluid Helium Film Suppressors

The nEDM PULSTAR test facility it is planned to have  $^3\text{He}$  injected into a 2.8-liter volume of liquid  $^4\text{He}$  and then removed, either through a heat flush technique or through evaporation of the  $^3\text{He}$ . The intent is to decrease the  $^3\text{He}$  concentration from  $3 \times 10^{-10}$  to  $3 \times 10^{-12}$  in about 16 hours, while keeping the liquid below 1.0 K. Because the vapor pressure of  $^3\text{He}$  is much greater than that of  $^4\text{He}$  at low temperatures, the vapor removal is conceptually possible if one could construct an efficient vapor pump and/or minimize the effects of superfluid  $^4\text{He}$  film flow [DuB09]. A superfluid  $^4\text{He}$  film can crawl up the pumping tube and evaporate at higher temperatures, thereby reducing the effective gas-pumping speed. The low-vapor-pressure requirement suggests a charcoal adsorption pump located near the sample

volume at  $T = 4$  K [Sal89]. The film flow could be limited by a small orifice on the pumping line, possibly including an etched silicon wafer as a “film pinner” of a type that has been used on two earth satellites that are cooled by superfluid helium [Shi98, Ish10].

We have designed a set of such pinner which were then fabricated at the North Carolina State University Nanofabrication Facility (see Figs. 1.6 and 1.7). The pinner are made from 200-micron-thick silicon wafers cut into squares measuring 12.7 mm to 25.4 mm on a side. Each square includes a central pumping orifice, 0.5 mm to 18.0 mm in diameter, surrounded by seven to ten etched barrier ridges with a nominal width of 200 microns. The edges of the ridges are smaller than the 10 nm resolution of the atomic force microscope measurement, as shown in Fig. 1.7. The superfluid must bend as it flows over an atomically sharp ridge. The surface-tension component of the chemical potential increases and causes film thinning. A film of less than about 10 nm thickness cannot support superfluid film flow.

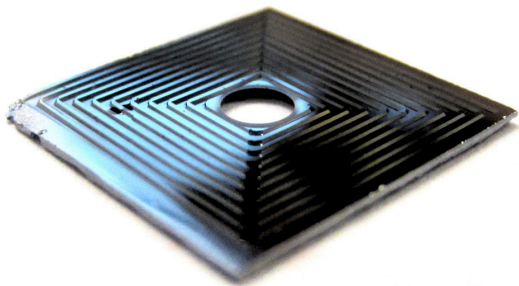


**Figure 1.6:** (Color online) Photo of an etched silicon film-pinner showing central pumping orifice and ridges. This particular pinner is a 12.5-mm square, and the central pumping orifice is 2.0 mm in diameter.

The effectiveness of the film pinner will be tested on the superfluid helium stage of the cryocooler. The silicon pinner is mounted with A12 epoxy to an Invar flange inserted into the pumping line of the 1.7 K helium volume. Two 100 k $\Omega$

ruthenium oxide resistors are hanging in the vapor above and below the pinner. Such resistors are highly temperature dependent below 4 K. Sending a current pulse to the resistor burns off the superfluid film. The presence or absence of the film is seen in the change in resistance of the bolometer. In the process of building the film pinner, we have developed a theoretical model of the helium film flow and heat exchange through the pinner, as well as a model of the bolometric detection of the superfluid film.

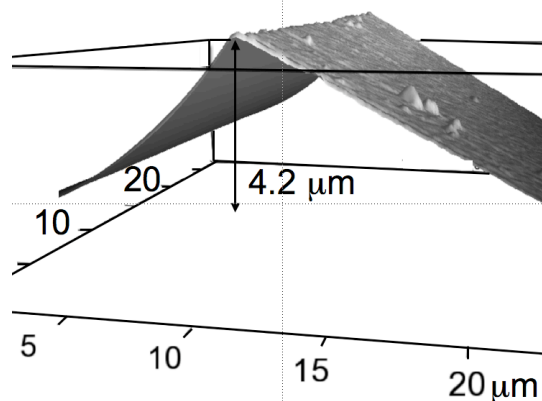


**Figure 1.7:** Atomic force microscope scan of one of the ridges on a patterned silicon wafer showing the sharpness of the ridge. The resolution of the probe was about 10 nanometers.

[DuB09] F. H. DuBose, Ph.D. thesis, North Carolina State University, 2009.

[Ish10] K. Ishikawa *et al.*, *Cryogenics*, **50**, 507 (2010).

[Sal89] R. Salmelin *et al.*, *J. Low Temp. Phys.*, **76**, 83 (1989).

[Shi98] P. J. Shirron and M. J. DiPirro, *Adv. Cryogenic Eng.*, **43**, 949 (1998).

[SW06] P. Schmidt-Wellenburg and O. Zimmer, *Cryogenics*, **46**, 799 (2006).

### 1.1.5 Superfluid Helium Film Flow and Vapor Reflux

D.P. KENDELLEN, D.G. HAASE, *TUNL*

In the last year we completed analysis of measurements of superfluid helium film flow and vapor reflux in a closed container, and the final results were published. We measured this effect at 0.3 K in a closed thermal column in order to validate an existing model at the operating temperature for the nEDM experiment and to guide the design of heat sinks in the apparatus.

In the nEDM apparatus, a series of liquid helium volumes and connecting tubes will move polarized  $^3\text{He}$  into the measurement cells and remove the depolarized  $^3\text{He}$ . In each volume, there is a free surface of liquid at about 0.3 K and a tube leading to warmer parts of the apparatus. A superfluid film flows up the walls in response to the temperature gradient. The film eventually vaporizes, creating a pressure gradient that drives the warm vapor back to the liquid, where it recondenses. This reflux effect efficiently transports heat to the low temperature end.

Heat transport from the refluxing vapor has been modeled [Nac94] with a cold volume of liquid helium at the base, connected by a thin-walled tube to an upper heated volume. All heat is assumed to be transported by refluxing vapor. We have extended this model to include conduction through the walls of the tube. Combining Poiseuille's equation, which describes the pressure gradient in a tube with diameter  $d$  and wall cross-sectional area  $A$ , with the chemical potential of an ideal gas, the model gives the thermal impedance of the cell as

$$\frac{\dot{Q}}{\nabla_z T} = (k_{\text{tube}}A) + \left( \frac{1}{\left(\frac{5}{2} - \frac{\mu_4}{kT}\right)} \frac{128\eta R T^2}{\pi d^4 L P^2} \right)^{-1}, \quad (1.1)$$

where  $\eta$  is the viscosity of the helium gas,  $k$  is Boltzmann's constant,  $\mu_4$  the chemical potential,  $R$  the gas constant,  $L$  the latent heat of the bulk liquid,  $k_{\text{tube}}$  is the conductance of the tube walls, and  $\dot{Q}$  is the heater power applied to the top of the cell. At temperatures above 0.8 K, the gas has a high thermal conductance, and temperature gradients are small. Below 0.5 K, however, the rapidly decreasing saturated vapor pressure has become small enough that the thermal con-

ductance is dominated by conduction through the tube wall.

We have now tested the model down to 0.3 K using a cell with  $d = 6.53$  mm to match the lower temperatures and larger tubes in the proposed nEDM apparatus. Our apparatus is a series of stainless steel tubes with 0.79-mm-thick walls, separated by copper flanges. A resistive heater was attached at the top, and  $\text{RuO}_2$  thermometers were placed at five points along the cell. The thermal conductivity of the empty tube was measured and found comparable to published data on stainless steel.

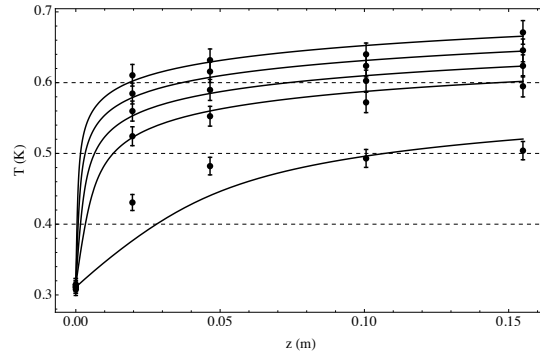


**Figure 1.8:** Temperature profiles measured with liquid in the cell. The measured points at each  $z$ -value correspond, from top to bottom, to heater powers of  $\dot{Q} = 200, 100, 50, 25,$  and  $0 \mu\text{W}$ . The solid lines are reflux model curves. The bottom curve is calculated for  $\dot{Q} = 3 \mu\text{W}$  for comparison with the background heating profile.

Figure 1.8 shows measured profiles of the cell filled with sufficient liquid to form a saturated film. The curves for each heater power were calculated from the reflux model. The bottom curve has  $\dot{Q}$  set to  $3 \mu\text{W}$  in the model to match the tem-

peratures measured with the heater turned off (i.e.  $\dot{Q} = 0$ ), suggesting that the background heat is on the order of a few microwatts. The measured points should not match the model curve precisely since all of the background heat is not deposited at the top of the cell, as the model assumes. The profiles for 25 to 200  $\mu\text{W}$  agree with the reflux model. Thus we have confirmed that the model, including the tube thermal conductance, accurately describes heat transport due to the reflux effect in a larger diameter tube at  $T = 0.3$  K.

We also measured the breakdown of reflux in the cell when the base is at 0.75 K. As the heater power is increased, more film will evaporate in the top of the tube than can be replenished by film flowing up the walls. At this critical heater power, the temperature at the top of the cell rose rapidly, as reported in past experiments on unsaturated films [Bow51].

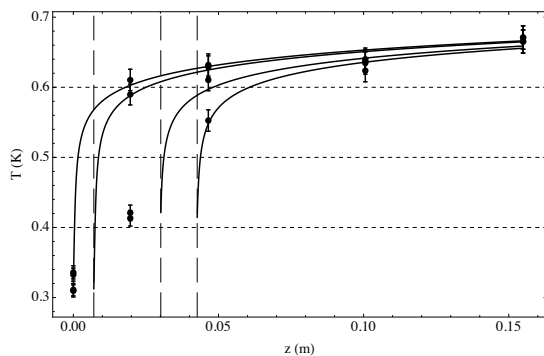


**Figure 1.9:** Profiles at four liquid levels for  $\dot{Q} = 200 \mu\text{W}$ . The dashed vertical lines indicate liquid levels determined from room temperature pressure measurements. These levels were used as starting  $z$ -values in the reflux calculations

Because the bulk superfluid is a good thermal conductor, adding liquid to the cell should alter the cell temperature profile. Figure 1.9 shows measured temperature profiles for  $\dot{Q} = 200 \mu\text{W}$

at four liquid levels: the first small amount of liquid and three additional portions. The liquid-level-heights set the starting  $z$ -value of the reflux-model calculations. The model curves reproduce the measured temperature profiles, indicating agreement with the liquid levels determined from measurements of pressure changes in the room-temperature storage volumes. We have calculated that these differences in temperature are consistent with Kapitza resistance between the liquid helium and the copper base.

In summary, we have verified the modified Nacher, Cornut, and Hayden reflux model over the temperature range from 0.3 to 0.8 K in a cell with  $d = 6.5$  mm. Conduction through the tube walls competed with the reflux effect over a short section at the base of the cell for the lowest heater powers and base temperatures. Condensing a small amount of liquid into the cell greatly increased the thermal conductance, altered the measured temperature profiles, and matched predictions from the reflux model. Results of the work have been published in Ref. [Ken13].

The reflux model will be applied to heat-sinking tubes in the nEDM apparatus. As described above, several volumes in the nEDM experiment connect through a vapor-filled tube to warmer parts of the apparatus. A properly designed small-diameter orifice in such a tube could limit film flow to the upper section of the tube (since the volume flow rate is proportional to the orifice diameter) while restricting the flow of warm refluxing vapor.

---

[Bow51] R. Bowers, D. F. Brewer, and K. Mendelssohn, *Philos. Mag. Series 7*, **42**, 1445 (1951).

[Ken13] D. P. Kendellen and D. G. Haase, *Cryogenics*, **57**, 134 (2013).

[Nac94] P. J. Nacher, M. Cornut, and M. E. Hayden, *J. Low Temp. Phys.*, **97**, 417 (1994).

---

### 1.1.6 Measurement-Cell Development for the nEDM Experiment

---

K. LEUNG, R. GOLUB, P.R. HUFFMAN, A. REID, C.M. SWANK, *TUNL*; THE nEDM COLLABORATION

**A measurement cell exhibiting a long storage time for ultra-cold neutrons (UCNs) is crucial for attaining the target sensitivity in the nEDM experiment. The cell has to be coated on the inside with a low-loss UCN reflective material and has to satisfy stringent cryogenic, magnetic, and optical requirements. Primary development activities have now shifted to TUNL, where a new dispensing machine has been commissioned and where other new techniques are being developed.**

The nEDM experiment will employ the Golub and Lamoreaux scheme [Gol94], where polarized ultracold neutrons (UCNs) are stored in a measurement cell along with a polarized  $^3\text{He}$  co-magnetometer. The EDM signal is detected by using a strong external electric field of about 75 kV/cm to shift the precession frequency of the neutrons in a weak magnetic field of about 30 mG. This technique aims to improve upon the current limit on the nEDM [Bak06] by two orders of magnitude.

An advantage of using UCNs is the long interaction time of the neutron with the electric field. The sensitivity of an experiment increases with the characteristic storage time of UCNs in the measurement cell as  $\sqrt{\tau_{\text{tot}}}$ . However, the primary trade-off with UCNs is the limited statistics due to the low density of UCNs in experiments. For instance, previous experiments had a useful density of only about  $1 \text{ UCN cm}^{-3}$ .

To address this, our measurement cell will be filled with superfluid  $^4\text{He}$ . UCNs are produced directly inside the cell via down-scattering of cold neutrons (CNs) from excitations in the superfluid [Gol75]. This removes the losses from source-to-measurement-cell transport. Furthermore, since the neutron- $^4\text{He}$  capture cross-section is zero and the up-scattering process can be made negligible if the converter is kept at a temperature below about 0.4 K, a density of UCNs can be accumulated in the measurement cell. The attainable density is given by  $\rho_{\text{UCN}} = P \tau_{\text{tot}}$ , where  $P$  is the volumetric UCN production rate, which for our CN beam is about  $0.26 \text{ UCN cm}^{-3} \text{ s}^{-1}$ . The target  $\tau_{\text{tot}}$  is around 500 s, which equates to a  $\rho_{\text{UCN}}$  of about  $130 \text{ UCN cm}^{-3}$ .

One can see that the statistical sensitivity to

an EDM depends linearly on  $\tau_{\text{tot}}$ , making improvements of the cell storage-time a critical part of the experiment. The cell walls must be coated with a material that has a low UCN loss rate, a low UCN depolarization rate, and a low  $^3\text{He}$  depolarization rate. Additionally, since the precession frequency of the UCNs relative to the co-magnetometer is measured from the scintillation light produced in the superfluid after spin-dependent UCN- $^3\text{He}$  capture, other requirements of the cell are that the cell walls serve as a wavelength shifter for the hard UV scintillated light at about 80 nm; that the bulk material of the walls be transparent to visible light, as they will guide this light to a set of photo-multiplier tubes for detection; and that the cell be superfluid tight and satisfy cryogenic and magnetic requirements.

The design of the cell has walls made from UV-transparent acrylic and coated with deuterated polystyrene (PS), which has a neutron optical potential  $V_{\text{opt}} = 165 \text{ neV}$ , so that UCNs with energies up to this energy are stored. It is doped with the deuterated wavelength-shifter tetraphenyl butadiene (TPB) [Huf13]. Since the quality of the coating is significantly improved when using flat plates, four side-plates and two end-plates are glued together to form the cell, which has inner dimensions of 7 cm in width, 10 cm in height, and 40 cm in length.

The last set of cells was produced at LANL, and storage data were measured at a UCN source at the Los Alamos Neutron Science Center. The cells demonstrated a  $\tau_{\text{tot}}$  of about 500 s, but only for about 30% of the UCNs; the rest had a  $\tau_{\text{tot}}$  of only 80 s. These data were re-analyzed with a model developed by us in which UCN transport through the pre-polarizer magnet/foil and guides

are taken into account. This led to an improved description of the UCN spectrum and provided a better fit to the data. This analysis confirmed that a suspected patch of material with a weak  $V_{\text{opt}}$  of around 70 to 90 neV and an area of 0.2 to 0.5 cm<sup>2</sup> was causing the shorter storage times. The primary cause of this is either that the glue used for the plates (MC Bond<sup>TM</sup>, an acrylic cement) seeped into the volume or that there was a contaminant such as dust on the surface of the plates.

The primary efforts of cell production have now shifted to NCSU. To address the above issues in future cells, an automated-process dispensing machine (S-820B from Asymtek) has been installed and commissioned in a “class 1000” clean room (see Fig. 1.10). The goal is to have a controlled and reproducible way of depositing the glue. Acrylic plates with a groove-feature that catches excess glue before it flows into the interior of the cell have also been designed.

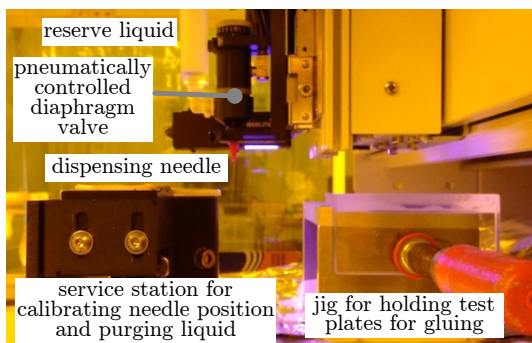


**Figure 1.10:** (Color online) The commissioning of the dispensing machine in the clean room at NCSU.

Batches of protonated PS and TPB solutions have been produced for the tests, and recently a set of full-sized plates were produced and sent to ORNL for their light collection studies (see Fig. 1.11). Other studies, such as atomic-force-microscope imaging of the coatings surface roughness (which allows quantification of the <sup>3</sup>He depolarization time) have also been performed.

Further effort will be required for us to learn how to use the dispensing machine effectively. We are currently actively pursuing this. We aim to produce several improved cells for the next set of storage experiments, currently scheduled for spring 2014, and will continue to provide samples to the collaboration for other various diagnostic measurements.



**Figure 1.11:** (Color online) An acrylic plate swing-coated with protonated PS and TPB for the ORNL light-collection measurements. A UV lamp is used to cause the observed fluorescence.

- 
- [Bak06] C. A. Baker *et al.*, Phys. Rev. Lett., **97**, 131801 (2006).
  - [Gol75] R. Golub and J. M. Pendlebury, Phys. Lett., **A53**, 133 (1975).
  - [Gol94] R. Golub and S. K. Lamoreaux, Phys. Rep., **237**, 1 (1994).
  - [Huf13] P. R. Huffman and D. N. McKinsey, J. Instrum., **8**, C09008 (2013).

## 1.2 Fundamental Coupling Constants

### 1.2.1 The UCNA Experiment

L.J. BROUSSARD, E.B. DEES, A.T. HOLLEY, R.W. PATTIE, JR., D.G. PHILLIPS II, B.M. VORNDICK, A.R. YOUNG, B.A. ZECK, *TUNL*

The UCNA collaboration published a 0.92% measurement of the  $\beta$ -asymmetry in polarized neutron decay during the 2010 run period at the Los Alamos National Laboratory. During the 2011/2012 run period, additional data were obtained which should lead to a precision of better than 0.6%. Analysis of these results is ongoing. Several key systems, including one designed and produced at TUNL, have been upgraded to reduce systematic uncertainties.

Measurements of neutron decay provide fundamental information on parameters, such as the axial form factor for the charged weak current, that characterize the weak interaction of the nucleon. These parameters impact predictions of the solar neutrino flux, Big-Bang nucleosynthesis, and the spin content of the nucleon. They also can be used to place constraints on standard-model extensions such as supersymmetry and left-right symmetric models.

The UCNA experiment is the first attempt to utilize ultracold neutrons (UCNs) for an angular correlation measurement in neutron decay. The use of UCNs for angular-correlation measurements provides a different and powerful approach to the systematic errors characteristic of traditional cold- or thermal-neutron-beam experiments. In particular, UCNs provide significant advantages for determining the neutron polarization and for controlling neutron-generated backgrounds. UCNs are generated using a solid deuterium source developed for this project at the Los Alamos Neutron Science Center. The source is described in detail by Saunders *et al.* [Sau13]. Historically, the neutron density in cold neutron beams has been much higher than available UCN densities, making beam experiments the favored method to perform angular correlations, but systematic errors have increasingly driven the ultimate uncertainty of angular-correlation measurements, thus providing impetus to explore the use of UCNs.

The  $\beta$ -asymmetry measures the angular correlation between the emitted electron's momentum and the direction of the neutron spin. This correlation is parameterized by the  $A$  coefficient,

with the Particle Data Group's world average being  $A_0 = -0.1176(11)$ .

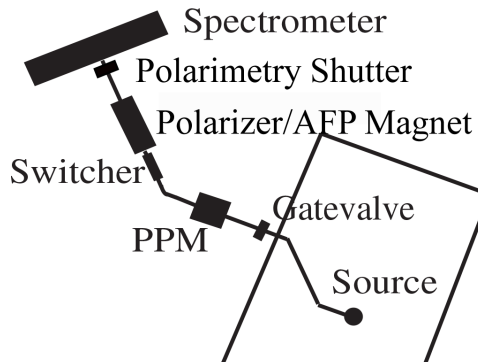


Figure 1.12: A schematic diagram of the layout of the UCNA experiment, showing the installation position of the new polarimetry shutter.

The  $\mu \cdot \mathbf{B}$  interaction of the neutron with magnetic fields produces an energy change of  $\pm 60$  neV/T, depending on whether the neutron spin is parallel or antiparallel to the applied field. The extremely low kinetic energy of UCNs—below 180 neV for our experiment—makes possible a method unique to UCNs for producing highly polarized neutron samples. The  $\mu \cdot \mathbf{B}$  interaction produces a 420 neV barrier to the neutrons with spin parallel to the field in our 7 T polarizer magnet (see Fig. 1.12), completely blocking the transmission of this spin state through the high-field system. There is therefore an essentially 100% polarized sample of UCNs after traversing this region. The UCNs then pass through a high-power, radio-frequency adiabatic spin-flipper which permits the prepa-

ration of a UCN sample polarized either parallel or antiparallel to the field. The spin-flipper region is then coupled by our guide system to a decay volume within the uniform 1 T field of the  $\beta$ -spectrometer.

At present, the UCNA collaboration is analyzing data accumulated in the 2011/2012 accelerator cycle with the expected precision below 0.6%. Also during this period, analysis was completed on the 2010 run period, and the results were published by Mendenhall *et al.* [Men13]. Improvements to the UCN source prior to the 2010 run resulted in a maximum decay rate of about  $55 \text{ s}^{-1}$  and an improvement of roughly a factor of two over the average decay rate in 2008/2009. The run cycle included 60 min of  $\beta$ -decay measurement, followed by an approximately 4 min measurement of the depolarized UCN fraction which accumulated in our decay volume during the  $\beta$ -decay measurement, and about an 8 min measurement of the background. The UCN spin-flipper was set either “on” or “off” in an eight cycle sequence designed to measure decay rates with the neutron spin parallel and antiparallel to the field axis, and to cancel, up to second order, drifts in the backgrounds.

The UCNs were confined to a 12.5-cm-diameter, 3-m-long Cu decay trap, coaxial with a 1 T uniform field at the center of the spectrometer. The inner surface of the decay trap is coated with diamond-like carbon. The ends of the decay trap were sealed with Be-coated Mylar windows.  $\beta$ -particles were recorded in detector assemblies situated at either end of the solenoidal spectrometer, where the field has fallen to 0.6 T. Each detector assembly is composed of a position-sensitive multi-wire proportional counter (MWPC) with aluminum-coated mylar entrance and exit windows. It is backed by a plastic scintillator to measure the full energy of the  $\beta$  particles. Backgrounds were reduced by requiring a coincidence between the scintillator and MWPC, and by a cosmic ray veto. Over  $32 \times 10^6$  decays were observed in an analysis window between 225 and 675 keV, yielding a  $\beta$ -spectrum in good agreement with expectations (see Fig. 1.13).

The emphasis of the 2010 run period was to refine our  $\beta$ -spectrometry. To this end, we replaced and improved the photomultiplier-tube (PMT) bases, added pulsers to the light guides to each PMT to improve our gain monitoring, added variable attenuation to the pulser already coupled directly to the scintillator to provide con-

tinuous linearity monitoring, and additional magnetic field monitors for the spectrometer to characterize the stability of the spectrometer fields over the course of the run period. These improvements resulted in better than a factor-of-two reduction in the energy-calibration-related systematic uncertainties in the experiment. The final result of the 2010 run was a 0.92% determination of the  $\beta$ -asymmetry parameter  $A_0 = -0.11952(110)$  [Men13].

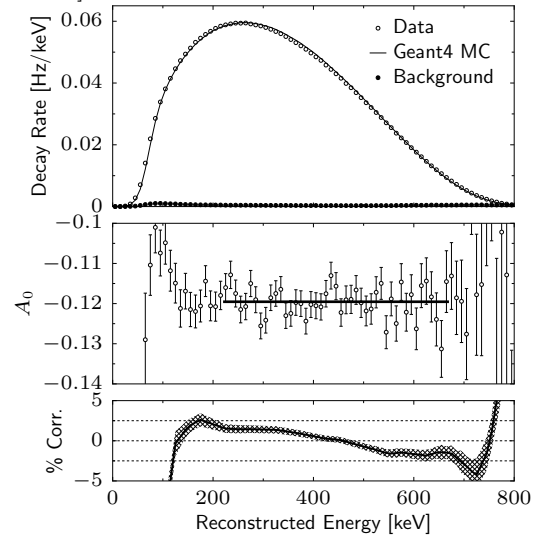


**Figure 1.13:** Top panel: The measured  $\beta$ -decay energy spectrum, averaged over neutron spin state, is compared to Monte Carlo results. Middle Panel: The measured asymmetry, after the application of energy-dependent corrections, is fit from 225–675 keV to determine  $A_0$ . Bottom Panel: Combined scattering corrections to the asymmetry (black line) are shown with their estimated uncertainty (hatching).

The 2011–2013 run periods featured significant improvements to polarimetry and energy reconstruction. Polarimetry was improved using a UCN shutter (see Fig. 1.12) that was designed and constructed at TUNL. The installation of a scanning LED system will allow for offline tracking of time-dependent drifts in detector linearity and is projected to reduce the energy reconstruction uncertainty to below 0.2%.

[Men13] M. P. Mendenhall *et al.*, Phys. Rev. C, **87**, 032501 (2013).

[Sau13] A. Saunders *et al.*, Rev. Sci. Instrum., **84**, 013304 (2013).

---

## 1.2.2 Determination of the Neutron Lifetime Using Magnetically Trapped Neutrons

---

C.R. HUFFER, P.R. HUFFMAN, K. SCHELHAMMER, *TUNL*; M.S. DEWEY, M. HUBER, H.P. MUMM, A.K. THOMPSON, A. YUE, *National Institute of Standards and Technology, Gaithersburg, MD*; K.J. COAKLEY, *National Institute of Standards and Technology, Boulder, CO*;

**We present progress on an experiment to measure the neutron lifetime using a technique with a different set of systematic uncertainties from those of previous measurements. Progress during the past year involves improved measurements of the isotopic purity of the superfluid helium used in the technique, construction of a helium purification system, and refined data analysis.**

The goal of this work is to measure the neutron lifetime in an experiment having a different set of systematic uncertainties from those of previous measurements [Doy94]. In our approach, ultracold neutrons (UCNs) are produced by inelastic scattering of cold (0.89 nm) neutrons in a reservoir of superfluid  $^4\text{He}$  [Gol75]. These neutrons are then confined using a three-dimensional magnetic trap. As the trapped neutrons  $\beta$  decay, the energetic electrons produced in the decay generate scintillations in the liquid helium [McK03, McK99], and each decay is detectable with nearly 100 % efficiency. The neutron lifetime can thus be directly determined by measuring the scintillation rate as a function of time. An overview of the experimental apparatus and technique can be found in Refs. [Bro01, Sch13].

As previously reported, we have completed and fully commissioned an upgrade to our apparatus that allows us to trap about twenty times more neutrons than before. We collected several months' worth of neutron-trapping data using this apparatus at the National Institute of Standards and Technology reactor facility and have been working to analyze these data, along with many of their systematic effects.

Events are digitized, and a timestamp is recorded for each. Corrections are made to the data for dead time arising during readout of the digitizing cards and due to the hardware event-veto. Corrections are applied to the pulse area and pulse height in response to the gain monitoring system. Several cuts are applied to remove background events. Initially, our electronics require a coincidence between events in both photomultiplier tubes of the primary detector, so

that all digitized data have events that pass a low-level voltage discrimination threshold in both primary detector channels. Next, events are corrected for gain changes using a separate gain-monitoring system. More restrictive upper and lower level software cuts are then applied to the pulse area to remove both uncorrelated events related to neutron-induced luminescence (upper level) and pulse-shape distortion due to the limited digitizer dynamic range (lower level). The resulting data are then analyzed in terms of pulse shape.

A technique that utilizes the kurtosis—a Gaussian parameter related to the fourth moment of the distribution—is used to separate different classes of events. This corresponds to events that occur in either the helium itself (lower value of kurtosis) or in the acrylic light guides (higher value of kurtosis).

The remaining backgrounds are removed by taking the difference between data from trapping and non-trapping runs. Neutron-trapping runs are where the magnetic field remains energized during both the trapping and observation periods, and non-trapping runs are where the magnetic field is energized only during the observation period, so that neutrons are not trapped during the loading phase. A sample set of trapping and non-trapping data with the result of this subtraction is shown in Fig. 1.14. These data are then directly fit to an exponential decay to extract the neutron lifetime.

The neutron decay curves extracted from 300-mK data collected using our new apparatus exhibit a trap lifetime that has a significant shift due to some, as yet, unexplained systematic ef-

fect, suggesting that there are neutron trap-loss mechanisms other than  $\beta$  decay. Runs where the magnetic fields are ramped to remove marginally trapped neutrons have not been able to explain this discrepancy. However, based on recent results from accelerator mass spectrometry (AMS) measurements on the isotopically-pure helium produced by McClintock, we believe that losses due to the presence of small amounts of  $^3\text{He}$  in our isotopically purified  $^4\text{He}$  is a likely candidate. A significant benefit of the new apparatus is that the increased count rates give us time to perform systematic checks such as the measurement of the neutron loss due to phonon up-scattering, the elimination of above-threshold neutrons, and a careful characterization of imperfect background subtraction. Going forward, we intend to purify a new sample of isotopically-pure helium and use this sample to continue our systematic studies of marginally trapped neutrons.

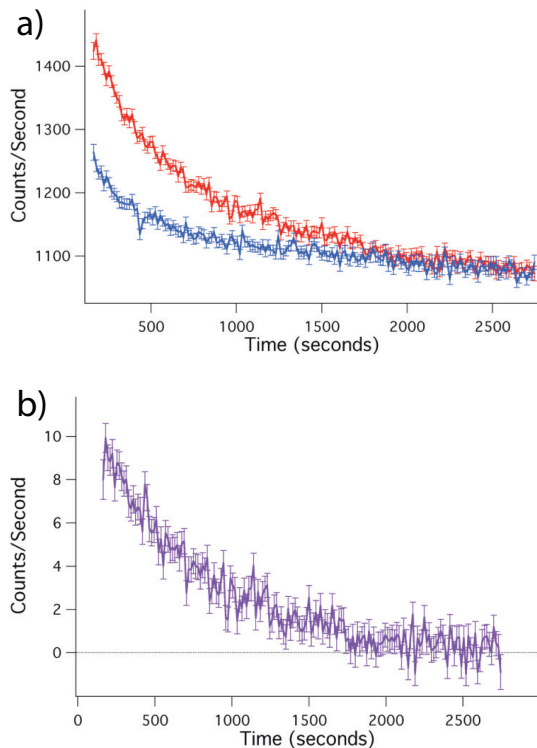


**Figure 1.14:** (Color online) (a) Neutron trapping (upper) and non-trapping (lower) data after all background cuts, summed over twenty runs; (b) the neutron decay signal extracted by subtraction of the trapping and non-trapping data runs in (a) but averaged (not summed) over twenty run pairs. These data correspond to approximately one week of data collection.

For the lifetime experiment, an isotopic helium purity of  $R_{34} < 10^{-15}$  is required to re-

duce the correction from the  $^3\text{He}$  absorption to  $< 2 \times 10^{-5} \tau_n$ . The quantity  $R_{34}$  is the ratio of  $^3\text{He}$  to  $^4\text{He}$  in the sample. Such purities have been previously demonstrated [McC78]. In order to verify the required purity with a direct measurement, we have been collaborating with the AMS group at the Argonne Tandem Linac Accelerator System facility at ANL to further refine AMS techniques for making low-mass measurements. We believe that the results from our latest series of runs show that the facility will be capable of making AMS measurements with sufficient sensitivity for our needs. We measured a set of isotopically-pure samples from the apparatus and from a small quantity of gas from the original purification. While data analysis is still underway, both samples show contamination at the few  $\times 10^{-12}$  level. For reference, a purity of  $5 \times 10^{-12}$  would lead to a shift in the measured neutron lifetime of 90 s. In addition, we are finalizing the construction of a helium purifier based on the work in Ref. [McC78] that will allow on-site purification of the helium using an all-metal system. This should significantly increase the purity of the helium used in the measurements.

Assuming our apparatus operates as it has previously, we anticipate that, by taking advantage of several opportunities for improvement, we will be able to perform a 0.5 % lifetime measurement in 18 days, or, equivalently, a measurement with a statistical uncertainty corresponding to less than 3 s in a 40-day reactor cycle. Such a measurement would yet play an important role in clarifying the current uncertainty surrounding the neutron lifetime, as the systematic uncertainties will be very different from those of other experiments.

- 
- [Bro01] C. R. Brome *et al.*, Phys. Rev. C, **63**, 055502 (2001).
- [Doy94] J. M. Doyle and S. K. Lamoreaux, Europhys. Lett., **26**, 253 (1994).
- [Gol75] R. Golub and J. Pendlebury, Phys. Lett., **A53**, 133 (1975).
- [McC78] P. McClintock, Cryogenics, **18**, 201 (1978).
- [McK99] D. N. McKinsey *et al.*, Phys. Rev. A, **59**, 200 (1999).
- [McK03] D. N. McKinsey *et al.*, Phys. Rev. A, **67**, 062716 (2003).
- [Sch13] K. Schelhammer, Ph.D. thesis, North Carolina State University, 2013.

### 1.2.3 Lanthanum Isotopes and the Neutron Fluence at the Oklo Natural Nuclear Reactors

C.R. GOULD, *TUNL*; E.I. SHARAPOV, *Joint Institute for Nuclear Reactions, Dubna, Russia*

**Data from the Oklo natural nuclear reactors have enabled some of the most sensitive terrestrial tests of time variation of dimensionless fundamental constants. A key parameter in all these analyses is the total neutron fluence over the time the reactors operated. We have explored whether lanthanum isotopic data can provide an alternate fluence estimate. We find the answer is yes, if the starting lanthanum elemental abundance can be reliably inferred from other data.**

The Oklo natural nuclear reactors in Gabon, West Africa were discovered in 1972 and have continued to generate scientific interest across many disciplines to this day. The basic facts are well established: two billion years ago the natural percentage of  $^{235}\text{U}$  was 3.7%, comparable to today's power reactors, and sufficient to allow a chain reaction to proceed in ordinary water. The power was low—tens of kilowatts. However, the reactors maintained operation over tens or hundreds of thousands of years, apparently in a cycling operation with reactor-on periods of around 0.5 hr, separated by dormant reactor-off periods of around 2.5 hr. Remarkably, the fission products remained undisturbed after the reactors ceased operation, allowing for detailed analyses of elemental abundances and isotopic ratios in these products.

All Oklo analyses to date have relied on neutron fluence calculations based on neodymium isotopic abundances in the residual ores. We recently explored whether lanthanum abundances could also be used to estimate fluences [Gou12], or conversely, whether primordial lanthanum abundances could be determined if the fluences were known from neodymium data. The terrestrial abundances for the lanthanum isotopes are 0.088% for  $^{138}\text{La}$  and 99.91% for  $^{139}\text{La}$ . However in the Oklo reactor-zone core RZ10 the  $^{138}\text{La}$  was found to be present in two samples at only the 0.0129% level. This is due to a large cumulative production of  $^{139}\text{La}$  in the fission of  $^{235}\text{U}$  by thermal neutrons (cumulative fission yield  $Y_{235,139} = 0.063$ ), while  $^{138}\text{La}$  production is negligible ( $Y_{235,138} = 3 \cdot 10^{-7}$ ), because this isotope is shielded by stable precursors in the beta-decay

chains of fission products. We found [Gou12] that the ratio  $^{138}\text{La}/^{139}\text{La}$  can indeed be a good predictor of the neutron flux. However, the result is dependent on knowing the primordial abundance of lanthanum at the time the reactor began operating. Considerable variation in elemental concentrations from place to place is expected, in contrast to isotopic abundance data, which tend to show less fluctuation and can be more reliably averaged inside or outside the reactor core.

Turning the problem around, however, we can estimate the starting lanthanum concentration taking the neodymium fluence as known. Figure 1.15 shows our estimate for the RZ10 core based on the meta-sample fluence  $0.65 \pm 0.19 \text{ kb}^{-1}$ , which we used in our earlier work.

Determining starting elemental concentrations in the Oklo cores may be of value since there is evidence that the Oklo phenomenon is potentially complicated by hints of selective retention of rare earth elements depending on whether they are of fissionogenic or non-fissionogenic origin [Hid00]. There are also indications that uraninite in Oklo incorporated lower amounts of rare-earth elements during primordial mineralization [Hid00]. Our result for lanthanum concentrations may therefore be of interest with respect to the study of uraninite formation processes.

---

[Gou12] C. R. Gould and E. I. Sharapov, *Phys. Rev. C*, **86**, 027601 (2012).

[Hid00] H. Hidaka and F. Gauthier-Lafaye, *Geochimica et Cosmochimica Acta*, **64**, 2093 (2000).

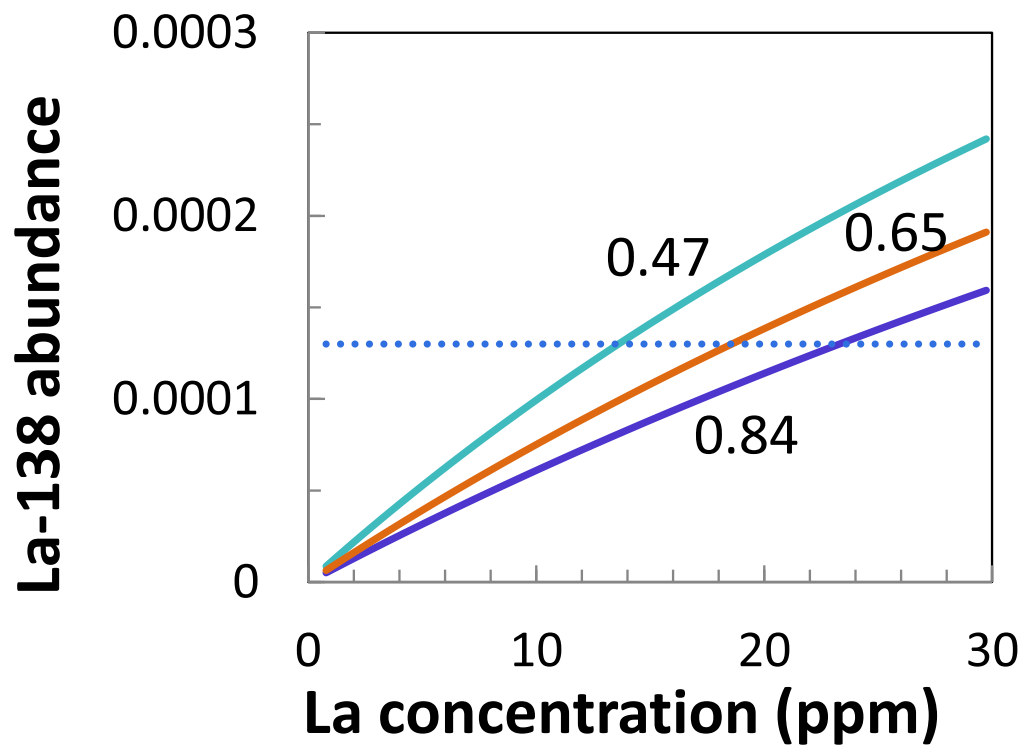


Figure 1.15: (Color online). The  $^{138}\text{La}$  abundance versus primordial elemental lanthanum abundance for Oklo active core RZ10. The three curves correspond to the indicated fluences. A fluence of  $0.65 \pm 0.19 \text{ kb}^{-1}$ , leads to a lanthanum concentration of  $18.6 \pm 4.9 \text{ ppm}$ .



# Neutrino Physics

---

Chapter 2

- $\beta\beta$ -Decay Experiments
- Tritium  $\beta$  Decay

## 2.1 $\beta\beta$ -Decay Experiments

### 2.1.1 Construction Update for the MAJORANA DEMONSTRATOR Project

M. BUSCH, M.P. GREEN, R. HENNING, J.F. WILKERSON *TUNL*

We report on progress on the construction of the MJD at the 4850-foot level of the Sanford Underground Research Facility. TUNL has played a leading role in many of the construction activities and provided a significant on-site workforce. During the reporting period, we have achieved many important goals relating to TUNL's work on the vacuum systems, parts fabrication, shield assembly, and string assembly.

During the reporting period, significant progress has been made in the construction of the MJD experiment at the Sanford Underground Research Facility in Lead, SD. Most of the work reported here occurred at the laboratory on the 4850-foot level of the mine. At the start of the reporting period, we had just received occupancy of the laboratory and started initial deployment of equipment underground. We had also been operating an underground clean machine shop to fabricate parts for MJD for about three months. Our main efforts since then have been geared towards the assembly of the prototype module of unenriched detectors and the fabrication of parts for cryostat 1, which will be loaded with enriched detectors.

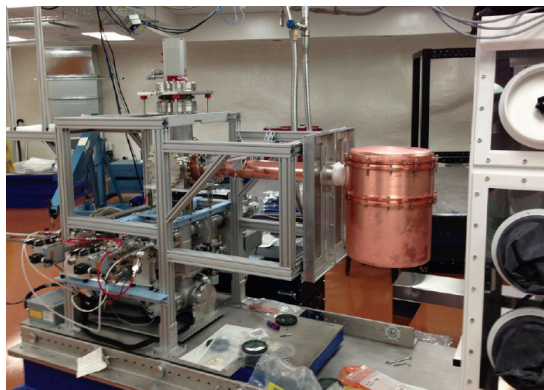


**Figure 2.1:** (Color online) On the left is the vacuum system for the prototype module after it was assembled underground. Attached on the right is the copper cryostat for the prototype module

Major achievements during the reporting period include:

1. The vacuum and cryogenics systems for the prototype module have been assembled and tested underground (see Figs. 2.1 and 2.2). This effort was led by TUNL.



**Figure 2.2:** (Color online) Custom liquid-nitrogen Dewar that is part of the cryogenics system that will cool the detector arrays.

2. The fabrication of the prototype cryostat has been completed, and the cryostat has been assembled and vacuum tested successfully underground (see Fig. 2.1). This effort was led by TUNL.
3. The first two strings of unenriched detectors have been assembled and are being tested inside the prototype cryostat (see Fig. 2.3). Numerous TUNL post-docs and graduate students were trained in the string assembly procedure and later participated in the assembly.
4. We have received and tested numerous enriched

detectors underground for cryostat 1. Students from TUNL have participated in this activity and helped with the data analysis.



**Figure 2.3:** (Color online) A string of broad-energy germanium detectors for the prototype module that were assembled underground.

5. The machining and initial electron-beam welding of cryostat 1 at PNNL has been completed (see Figs. 2.4 and 2.5). This effort was lead by TUNL.
6. The underground chemical laboratory is operational, and numerous parts have been cleaned and etched, based on procedures developed at TUNL.
7. The assembly of the shield has started, and significant progress has been made with the installation of the muon veto, copper and lead

shields, and support structures. The poly-shield fabrication has also started at the surface.

8. During this time the underground laboratory and machine shop have been in operation continuously. Fabrication activities at the machine shop are coordinated by TUNL engineers.



**Figure 2.4:** (Color online) Cryostat 1 being machined from electroformed copper at the underground machine shop.



**Figure 2.5:** (Color online) Cryostat 1 parts during welding at PNNL.

Our main focus for the next year will be the deployment and commissioning of the prototype module and the construction of the first enriched detector module, cryostat 1.

---

### 2.1.2 Parts Database for the MAJORANA DEMONSTRATOR

---

R. PETERSBURG, K. SNAVELY, M. GREEN, R. HENNING, J.F. WILKERSON, *TUNL*

**The MAJORANA parts-tracking database is an application that tracks the entire fabrication and transportation histories of the radio-pure components required in the construction of the MAJORANA DEMONSTRATOR, allowing for detailed radio-background simulations of the DEMONSTRATOR. Users can modify the tracking history through a web application. A radiation-exposure calculator estimates the cosmogenic activation of the parts during shipping and storage.**

The MAJORANA DEMONSTRATOR is an ultra-low-background experiment designed to search for the neutrinoless double-beta decay of  $^{76}\text{Ge}$ . In order to achieve a background of less than three counts per tonne-year within a 4-keV region around 2039 keV, the DEMONSTRATOR requires that all components (primarily copper, but also steel, teflon, and other plastics) be radio-pure. Therefore, the MAJORANA parts-tracking database (PTDB) has been developed to store relevant information about each part in one virtual location, allowing for simple reference during construction, to ensure that quality requirements are met.

When a part is created for the DEMONSTRATOR, it is given a unique serial number in the PTDB. This number is then labeled on the part itself by laser engraving or metal stamp. It is also associated with its parent stock and inherited material type. Throughout the part's lifetime, its record will be updated with specific history entries including storage, transportation, cleaning, etching, machining, and assembling. When multiple parts undergo the same process simultaneously, a single history entry is created and linked to by each of the processed parts, maintaining this relationship. Each part can also be red-flagged for any chemical impurities or excessive radioactivity during any of these processes.

Parts are organized in the PTDB hierarchically, with a strict parent-to-child relationship: parents can connect to multiple children, but children can only connect to a single parent. An object that is constructed of multiple parts is designated as an assembly. Assemblies are given their own unique serial numbers and monitored for the same processes during their lifetimes, but all updates are also pushed to their constituent parts. The assemblies are also or-

ganized in parent-child relationships, where each part can only link to one assembly and each assembly may be a component of only one other assembly.

The PTDB was developed using CouchDB, a database accessible through any web browser and customizable for web applications [And]. CouchDB stores information in JavaScript object notation (JSON) [Sev12], a data model that is represented by object literals: keys (stored as strings) are linked to values (stored as strings), numbers, arrays, or other object literals. Therefore, JSON is human-readable, naturally parses into JavaScript objects, and can be parsed by other programming languages, such as Python. Each part, assembly, and history entry is represented by a JSON document, where relationships between these entries are represented by storing serial numbers of linked records within the appropriate fields. CouchDB also utilizes the MapReduce paradigm [Dea08], optimizing queries for parallel/cluster computing, and multi-version concurrency control, allowing for database interactions to scale to large numbers of concurrent readers and writers.

The MAJORANA PTDB provides a graphical interface for entry updates and inspection through a password-protected web application. This application uses a model-view-controller (MVC) decomposition [Kra88] to separate the user inputs (controller) from the logic and data structures (model) and the resultant visual representation (view) which is, in this case, output as HTML and CSS. An MVC framework known as Backbone.js [Bac] provides base Model, View, and Collection (lacking an explicit controller class) objects that are designed to interact. Backbone Models are representations of the CouchDB part, assembly, and history en-

tries. The Backbone View listens for changes to these models and for user inputs, altering the HTML output or model representations accordingly. Backbone's Collections are containers for the model objects and act as mediators for any interactions, passing messages between the models and the view. For a visual example of the logical structure, see Fig. 2.6.

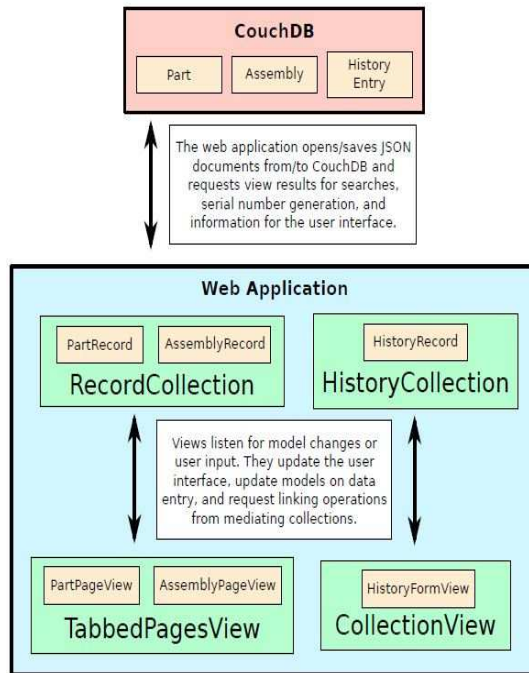


**Figure 2.6:** (Color online). Simple representation of Backbone's organizational structure and relation to CouchDB

A Python script has also been written to calculate activation rates based on the above-ground storage and transportation entries within the MAJORANA PTDB. This exposure calculator crawls the database sequentially, without interacting, and pulls all relevant data, street addresses and lengths of time, in a usable form. These addresses are converted to latitude, longitude, and elevation geo-codes using the Google Maps application programming interface (API) [Goo], and any transportation entries are approximated along the preferred route offered by the API. The resulting collections of elevation and time data can then be used to calculate expected activation rates along the entire history of each part, and the exposure value (along with a time stamp) is stored within the respective part record. The script is run interactively in a server mode, using the Twisted Python library [Twi], allowing for greater efficiency during calculation.

In order to fully understand background

events detected in the MAJORANA DEMONSTRATOR, a full suite of simulations was performed using MAGE [Bos11], a simulation application built on GEANT4 [Gea] developed jointly by the MAJORANA and GERDA Collaborations. For simulations of the DEMONSTRATOR, a highly detailed geometric model of the detector was constructed, allowing a detailed study of the detector's efficiency for detecting simulated events generated in individual components. The MAJORANA PTDB, by maintaining relationships to assays performed on the parent material, tracking above-ground exposure of cosmogenically sensitive materials, and recording the final locations of parts within the larger detector assembly, provides a map of activations that can be combined with simulated efficiencies to produce a complete estimate of background rates and spectra expected in the DEMONSTRATOR.

The PTDB is currently in full use by the MAJORANA Collaboration. The web application is the primary form of interaction with the PTDB and has been shown to be stable enough for consistent use. The exposure calculator is not currently being utilized, though it has proven successful on test databases. We are expecting to implement a passive version of the script that listens for changes to each part history and only updates the exposure value when a storage or transportation entry is added.

- [And] J. C. Anderson, J. Lehnardt, and N. Slater, *Couchdb the Definitive Guide*, <http://guide.couchdb.org/index.html>.
- [Bac] <https://backbonejs.org/>.
- [Bau06] M. Bauer *et al.*, *J. Phys.: Conf. Ser.*, **39** (2006).
- [Dea08] J. Dean and S. Ghemawat, *Commun. ACM*, **51**, 107 (2008).
- [Gea] <https://geant4.org/geant4/support>.
- [Goo] Google, *Google Maps API Developer's Guide*, <https://developers.google.com/maps/documentation/javascript/tutorial>.
- [Kra88] G. E. Krasner *et al.*, *J. Object-Oriented Programming*, **1**, 26 (1988).
- [Sev12] C. Severance, *Computer*, **45**, 6 (2012).
- [Twi] <https://twistedmatrix.com/trac>.

### 2.1.3 Detector-String Testing for the MAJORANA DEMONSTRATOR

J. MACMULLIN, M. BUSCH, D. COMBS, P. FINNERTY, F.M. FRÄNKLE, G.K. GIOVANETTI, M.P. GREEN, R. HENNING, M.A. HOWE, L. LEVINER, C. O'SHAUGHNESSY, B. SHANKS, K. SNAVELY, G. SWIFT, W. TORNOW, K. VORREN, J.F. WILKERSON, A.R. YOUNG, *TUNL*

**The MAJORANA DEMONSTRATOR is composed of two independent cryostats, with each cryostat containing an array of strings and capable of housing up to 20 kg of HPGe detectors. Before a string is installed in its cryostat, it is characterized in a string test cryostat (STC). The details of the STC and the status of the detector string tests are discussed.**

The MAJORANA DEMONSTRATOR contains two independent vacuum cryostats, cryostats 1 and 2 (see Sect. 2.1.1), each capable of holding up to seven strings of germanium detectors. All but two of the natural detectors in the MAJORANA DEMONSTRATOR are broad-energy germanium (BEGe) detectors commercially available through Canberra. Two of the natural detectors and all of the enriched detectors are processed by ORTEC for MAJORANA. These p-type point-contact (PPC) detectors are larger in size than the BEGe detectors (see Fig. 2.7).

The MAJORANA string design is low mass and is flexible enough to accommodate the two different detector geometries. In the MAJORANA DEMONSTRATOR, each component of the string is made of either underground-electro-formed copper or NXT-85, a Teflon that is manufactured in a cleanroom.

To date, a prototype cryostat has been constructed. Its strings are made of high-purity commercial copper, rather than underground electro-formed copper. It contains two strings of natural PPC detectors: one with five BEGe detectors and the other with two BEGe detectors plus the two natural ORTEC detectors. The latter is depicted in Fig. 2.7.

#### 2.1.3.1 String-Test Cryostat Design

Before a string is installed in its cryostat it is characterized in a string-test cryostat (STC). There are seven STCs, each with its own Dewar. Infrared (IR) radiation can cause an increase in a detector's leakage current, so each string is surrounded by an IR shield in the STC. The IR shield and string are attached to a cold-plate. Both the cold-plate and IR shield are in thermal

contact with the cold finger and cool the string (see Fig. 2.8). The cold finger is composed of two separate pieces, and the bottom piece can be unscrewed from the top piece. This allows the STC to fit into the MAJORANA glove-box, so that the strings can be mounted in and dismantled from the STC without being exposed to the air in the laboratory, thus limiting the detectors' exposure to  $^{222}\text{Rn}$ .

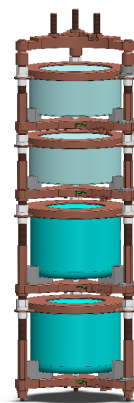


**Figure 2.7: (Color online) A model of one of the two strings in the prototype cryostat. The top two detectors are representative of the BEGe detectors. The bottom two are representative of the PPC detectors.**

The vacuum system for the STC is constructed from all-metal ultra-high-vacuum components. The STC pump-cart is able to connect to two STCs at a time (see Fig. 2.9). Each STC is equipped with a non-evaporable getter pump to help maintain vacuum in the STC while it is disconnected from the pump-cart during string testing. Every STC has its own vacuum gauge which

is remotely monitored via ORCA (see Sect. 8.4.1).

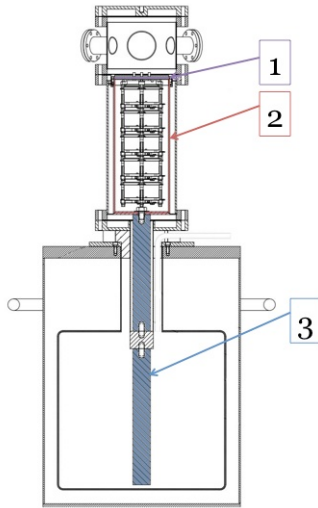


Figure 2.8: (Color online) A cross-section of the assembly drawing for an STC. Label 1 (purple) is the cold-plate, label 2 (red) is the IR shield, and label 3 (blue) is the cold finger.



Figure 2.9: (Color online). The STC pump-cart connected to two STCs.

### 2.1.3.2 String Characterization

One of the main goals of the STC is to determine the health of the detectors after they have been installed in their MAJORANA string and to determine each detector's optimal operating voltage. Bias scans are done for each detector in the STC to determine the leakage current and capacitance as a function of bias voltage.

Another main goal of the STC is to understand the performance of the string detectors in the energy range of neutrinoless double-beta decay for  $^{76}\text{Ge}$ . Data are taken for several hours with a thoriated ( $^{232}\text{Th}$ ) welding rod and a  $^{60}\text{Co}$

source. With the two sources, a number of  $\gamma$ -ray peaks are observed throughout a wide range of energy. Thus one can obtain the energy resolution as a function of energy and investigate the linearity of the DAQ system.

The MAJORANA DEMONSTRATOR will also be sensitive to light weakly-interacting massive particles, a dark-matter candidate (see Sect. 2.1.5). This requires understanding the performance of the detectors at low energy. With an  $^{241}\text{Am}$  source, the electronic noise, low-energy resolution, and low-energy linearity can be investigated. When specific tests are not being done on a string in the STC, background runs are taken to help understand the stability of the system and look for any abnormal backgrounds (see Fig. 2.10).

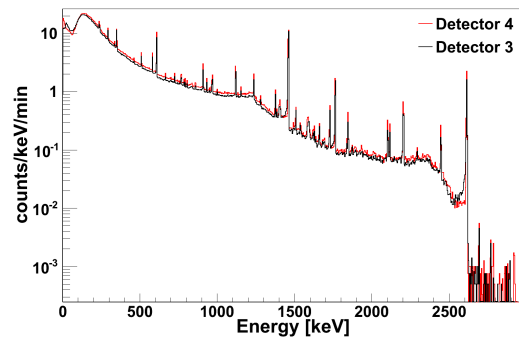


Figure 2.10: (Color online). A 17-hour background run for two detectors in an STC. This string is now currently installed in the prototype cryostat and is pictured in Fig. 2.7. Detector 4 is the bottom-most detector in the string, with detector 3 directly above it. Detector 3's overall background is slightly lower than detector 4's due to greater shielding from the other detectors in the string.

### 2.1.3.3 Current Status

The two strings for the prototype cryostat have both been tested in an STC, and one of them is currently installed in the prototype cryostat. This cryostat has proven to be successful in allowing the collaboration to identify what modifications can be made in refining the design and hardware before the installation of strings in cryostats 1 and 2. The second string will undergo these modifications, be re-tested in an STC, and then be installed in the prototype cryostat. Once both of the strings have been successfully tested and installed, work will begin on assembling the strings for cryostat 1.

### 2.1.4 Waveform Simulation for Pulse-Shape-Analysis Validation in the MAJORANA DEMONSTRATOR

B. SHANKS, C. O'SHAUGHNESSY, *TUNL*

**We describe ongoing simulation efforts to verify the efficiency of background-suppression cuts used in the MAJORANA DEMONSTRATOR and based on pulse-shape analysis.**

In order to show sensitivity to neutrino-less double-beta decay ( $0\nu\beta\beta$ ), the MAJORANA DEMONSTRATOR aims to achieve a background rate of less than three counts/tonne-year in the 4-keV-wide region of interest (ROI) around the  $^{76}\text{Ge}$   $0\nu\beta\beta$   $Q$  value. The primary source of background events in the ROI is expected to originate from  $\gamma$  rays, which often deposit energy through Compton scattering at multiple sites inside a detector. Events corresponding to a  $0\nu\beta\beta$  signal, by contrast, deposit energy in a narrowly-localized volume. The p-type point contact (PPC) germanium detectors used in the DEMONSTRATOR allow pulse-shape-analysis (PSA) algorithms to distinguish between multi- and single-site waveforms for background reduction. Current work is focused on employing pulse-shape-simulation (PSS) techniques to validate the efficiency of candidate PSA algorithms.

Standard germanium detectors are manufactured in a coaxial configuration that collects electron holes on a long electrode extending through the center of the bulk material. PPC detectors collect charge on a shallow contact at the base of the cylindrical germanium crystal. The effect of the different geometry on charge collection can be evaluated by calculating the weighting potential within the crystal bulk. The weighting potential describes the amount of charge collected at the electrode for a carrier cloud carrying unit charge at a given position. The weighting potential of a PPC detector is sharply peaked around the point contact, but negligible in most of the active volume. As a charge cloud drifts from the interaction site toward the contact, the charge signal observed at the preamplifier at first rises slowly, corresponding to the low weighting potential at the bulk. The arrival of the cloud at the electrode causes a fast-rising charge pulse, which plateaus as the cloud is fully collected. This behavior is shown in Fig. 2.11. For a multi-site

interaction, the total resulting pulse shape will essentially be a linear superposition of time-offset single-site collection events. This is also shown in the figure.

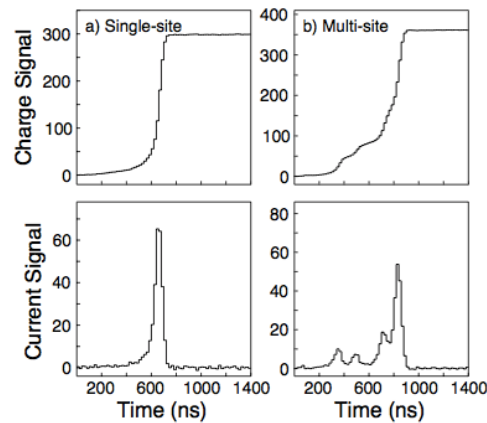


**Figure 2.11: Charge and current pulse signals in a PPC detector for typical single-site (left-hand panels) and multi-site (right-hand panels) interactions. The lower panels show the instantaneous charge, and the upper panels show the time integrated charge collected.**

The visible difference in the waveforms suggests that PSA can effectively be used to reduce background in PPC detectors. The MAJORANA collaboration is currently considering several candidate algorithms. A standard approach discriminates based on the ratio  $A/E$  of the current pulse, where  $A$  is the amplitude, and  $E$  is the energy of the event. As the lower panels of Fig. 2.11 show, multi-site events have a lower charge-amplitude for a given energy. A second algorithm has been proposed in which characteristic single-site events for a given detector are averaged into a basis of “superpulses” [Coo11]. This PSA algorithm uses a  $\chi^2$  test to determine

if a candidate event matches any superpulse. If no  $\chi^2$  surpasses a given threshold, the event is flagged as multi-site. To compare the performance of these PSA algorithms, a standardized procedure for validating and evaluating prospective PSA techniques is required.

Preliminary evaluation of PSA performance can be done using experimental data with known interaction profiles. The single escape (SE) peaks, in particular, contain nearly all multi-site events, while the double escape (DE) peak is essentially a single-site interaction. The ability of the PSA algorithm to reject the SE peaks while retaining the DE peaks can therefore be used as an efficiency test. However, this isn't sufficient for a systematic study of PSA-based cuts. Because escape events occur preferentially near the surface of the detector, their peaks can be contaminated with events of unknown origin, and they only provide data in narrow energy bands. For these reasons, it is desirable to create a framework which can compute pulse-shape data from Monte Carlo simulations of interactions in the crystal bulk. MAJORANA has standardized around a custom simulation package, MaGe, which is based on the GEANT4 toolkit and has been described in detail elsewhere [Bos11]. The present work aims to implement software to generate waveforms for the physics events generated by MaGe. These simulated waveforms will be processed by the PSA algorithm, providing validation of the efficiency and systematic effects of PSA-based cuts.

Simulation of the interaction of the charge cloud in the crystal bulk is performed by software developed at Oak Ridge National Lab. The M3DCR package uses relaxation techniques to

generate electric field and weighting potentials for a given crystal geometry. Given these data and an interaction location, SIGGEN simulates the drift of a charge cloud through the bulk material and generates a pulse shape corresponding to an event at a given interaction site. These packages have been extensively verified to replicate the behavior of real germanium detectors at ORNL and are used in other germanium experiments, including GRETINA [Lee04].

The ORNL packages have been wrapped into the MAJORANA collaboration's standard analysis software, the Germanium Analysis Toolkit (GAT). Within GAT, the event energy is adjusted for transition-layer effects and nuclear quenching. Multi-site events occur when multiple events strike the same detector within the time required for signal digitization. A GAT routine performs time-windowing to group together these events. Pulses are generated by SIGGEN for each event, and events within the same time window are summed to form a multi-site waveform. Finally, GAT provides transforms to simulate the preamplifier response and noise characteristics. The result is a simulated waveform that the PSA algorithm can process interchangeably with experimental data. This framework has now been implemented, and the first study, which will focus on evaluation of the A/E algorithm, is underway.

---

[Bos11] M. Boswell *et al.*, IEEE Trans. Nucl. Sci., **58**, 1212 (2011).

[Coo11] R. Cooper *et al.*, Nucl. Instrum. Methods A, **629**, 303 (2011).

[Lee04] I. Lee *et al.*, Nucl. Phys. A, **746**, 255c (2004).

---

### 2.1.5 The MALBEK Detector: Low-Energy Analysis Update

---

G.K. GIOVANETTI, P. FINNERTY, R. HENNING, M.A. HOWE, J.F. WILKERSON, *TUNL*; A.G. SCHUBERT, *University of Washington, Seattle, WA*

**We have deployed a customized low-background Canberra broad-energy germanium detector at the Kimballton Underground Research Facility in Ripplemead, Virginia. An analysis of 221.49 live days (89.53 kg-d exposure) of data shows no evidence of a signal from light weakly-interacting massive particles.**

As a part of the research and development efforts for the MAJORANA DEMONSTRATOR (see Sect. 2.1.1), a customized 465 g p-type point-contact (PPC) detector manufactured by Canberra Industries was deployed in January 2010 at the Kimballton Underground Research Facility (KURF) in Ripplemead, Virginia. The goals for this detector—the MAJORANA Low-Background BEGe at Kimballton or MALBEK detector—were to study the performance and backgrounds of a PPC detector and to perform a search for light weakly-interacting-massive-particle (WIMP) dark matter with masses below  $10 \text{ GeV}/c^2$ . A description of the MALBEK detector and shielding can be found in Ref. [Fin11], and the DAQ is described in Ref. [Gio12]. Initial results from an analysis of 221.49 live days of data are presented.

The data used for the light-WIMP search were acquired over 287.87 days between November 15, 2011 and August 8, 2012. Due to a period of intermittent power outages at KURF, the dataset is divided into two distinct run periods, 15 November 2011 to March 12, 2012 and April 9, 2012 to August 29, 2012. The two data periods are calibrated separately using a set of low-energy x-ray lines from  $^{68,71}\text{Ge}$ ,  $^{55}\text{Fe}$ ,  $^{65}\text{Zn}$ , and  $^{68}\text{Ga}$ . During data-taking, a pulser was used to inject 100 mV, or roughly 35 keV, signals at a frequency of 0.1 Hz into the test input of the preamplifier. The location and width of the pulser peak in the energy spectrum were measured for every hour-long run, enabling the electronic noise and gain drift to be tracked as a function of time. It was found that the electronic noise remained stable throughout operation at a level of  $69.86 \pm 0.02 \text{ eV}$ , and gain drifts at the detector threshold were smaller than 10 eV. In addition, the reset rate of the preamplifier remained constant within 1 Hz

during the run period, indicating no periods of increased detector leakage current. An event-by-event timing analysis was done to look for periods of increased electronic noise and it was found that non-Poisson processes make up less than 0.5% of the rate below 1.0 keV.

Data analysis was done using the Germanium Analysis Toolkit (GAT), a modular data analysis framework developed by the MAJORANA collaboration. Timing cuts were implemented to remove events coincident with preamplifier inhibit pulses, pulser events, and events occurring within 15 minutes of a liquid nitrogen Dewar fill. An additional series of cuts was performed to remove non-physics events caused by microphonics and high-voltage micro-discharges. These cuts were trained to accept 99% of physics events using a dataset generated by injecting pulses into the test input of the preamplifier with amplitudes ranging from the trigger threshold up to 7 keV.

In PPC detectors, a significant background for dark matter searches comes from interactions occurring near the lithium diffused  $n^+$  contact [Fin12]. Diffusion and recombination processes are hypothesized to dominate charge transport in this region of the detector, resulting in energy degraded signals that take longer to reach their maximum amplitude than events originating in the depleted bulk. The distribution of these events is roughly exponential with energy, closely mimicking the expected signal from a WIMP interaction in a Ge detector. It is therefore extremely important to characterize the residual slow-pulse contamination after any cut designed to remove these slow events.

In order to identify slow signals in the MALBEK detector, a novel pulse shape discrimination technique was developed, based on the wavelet power spectrum of ionization signals.

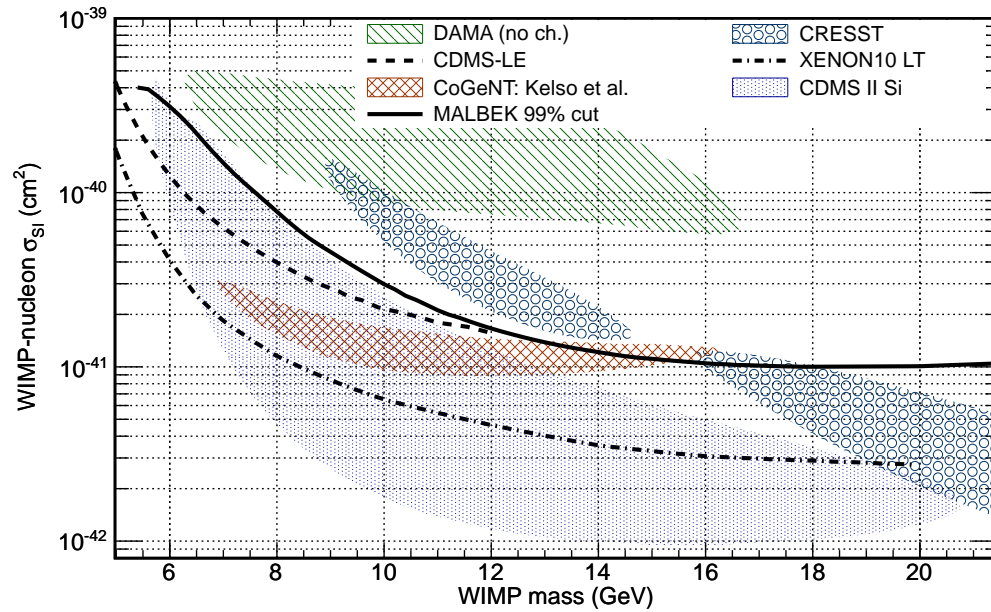


**Figure 2.12:** (Color online). The spin-independent (SI) exclusion limits calculated using the 221 day MALBEK dataset described here. Other experimental results displayed are: CoGeNT results as interpreted by Ref. [Kel12] taking into account slow-signal leakage, XENON10 low threshold analysis [Ang11], CDMS-II low energy analysis [Ahm11], CDMS-II Si [Agn13], CRESST-II [Ang12], and the DAMA/LIBRA result [Ber08]. All results are at 90% CL with the exception of CRESST-II, which are at 95% CL.

The rise-time of an ionization signal is correlated with the amplitude of the level-zero detail coefficient wavelet power spectrum normalized by the square of the energy of the event. This slow event cut was trained to accept 99% of the fast pulser dataset. In this analysis, the acceptance of fast-signal events is well known, but the number of slow events remaining after the cut is not well determined.

An unbinned extended maximum-likelihood fit was performed. It incorporated a flat  $\gamma$ -ray background component, the  $^{65}\text{Zn}$  and  $^{68,71}\text{Ge}$  L-capture lines, an exponential representing the shape of the unknown residual slow event contamination, and a signal from WIMP-induced nuclear recoils. The Rolke method [Rol05] was used to extract 90% confidence limits for WIMP masses ranging from 5.5 GeV to 100 GeV. The 90% exclusion limit is shown in Fig. 2.12 along with recent results from other WIMP searches. Analysis of these data is continuing, with an emphasis on characterizing the remaining slow-event contribution in the dark-matter nuclear-recoil-signal region of interest after the slow-event cut.

[Agn13] R. Agnese *et al.*, arXivV, **1304.4279**

(2013).

[Ahm11] Z. Ahmed *et al.*, Phys. Rev. Lett., **106** (2011).

[Ang11] J. Angle *et al.*, Phys. Rev. Lett., **107** (2011).

[Ang12] G. Angloher *et al.*, Eur. Phys. J. C, **72**, 1 (2012).

[Ber08] R. Bernabei *et al.*, Eur. Phys. J. C, **56**, 333 (2008).

[Fin10] P. Finnerty *et al.*, TUNL Progress Report, **XLIX**, 24 (2010).

[Fin12] P. Finnerty *et al.*, TUNL Progress Report, **LI**, 31 (2012).

[Gio12] G. K. Giovanetti *et al.*, TUNL Progress Report, **LI**, 33 (2012).

[Kel12] C. Kelso, D. Hooper, and M. R. Buckley, Phys. Rev. D, **85** (2012).

[Rol05] W. A. Rolke, A. M. López, and J. Conrad, Nucl. Instrum. Methods A, **551**, 493 (2005).

### 2.1.6 Characterization of $^{76}\text{Ge}$ Detectors for the Majorana Demonstrator using an Azimuthal Scanning Table

A. ZITIN, C. O'SHAUGHNESSY, J. TRIMBLE, M. BUSCH, R. HENNING, J.F. WILKERSON, *TUNL*

**An automated scanning table has been fabricated and assembled at UNC to characterize germanium detectors. A second stand will be built and used to characterize detectors in the Majorana Demonstrator string-test cryostats at the Sanford Underground Research Facility. The design of the scanning table allows a radioactive source to be moved azimuthally and vertically around the string test cryostats.**

Germanium detectors used in the MAJORANA DEMONSTRATOR must be characterized in-situ in their assembled strings. In particular, it is important to understand how radiation interacts with the surface of the detectors, because the behavior at the detector surface may vary from detector to detector. We have designed and assembled a test stand that will provide automated control over the azimuthal and vertical positions of a collimated source of radiation directed at the germanium detector located in the center of the test stand (see Fig. 2.13).

One application of this test stand will be an attempt to characterize the 'dead layer' present on the surface of the germanium detectors due to the implantation of lithium ions. This dead layer will impact the performance of the detector by preventing complete charge collection when radiation interacts with the crystal near its surface. Since this dead layer is present on both the top and side of the disk-shaped detector, an azimuthal scan is needed in addition to a vertical scan so that the performance of the detector when radiation interacts near the dead layer can be fully explored. The dead layer is due to the diffusion of the  $\text{Li}^+$  ions on the crystal surface in order to produce an ohmic contact for the high-voltage detector bias.

It is important to characterize detector performance near the dead layer because, unlike the germanium crystal volume, the lithium layer can trap or slow charges produced by ionizing radiation, leading to the collection of electronic signals that may not accurately represent the event occurring near the dead layer. Understanding the signals emanating from this region of the detector will allow us to discriminate better between actual events of interest occurring in the detec-

tor volume and contaminating signals produced from the dead layer.

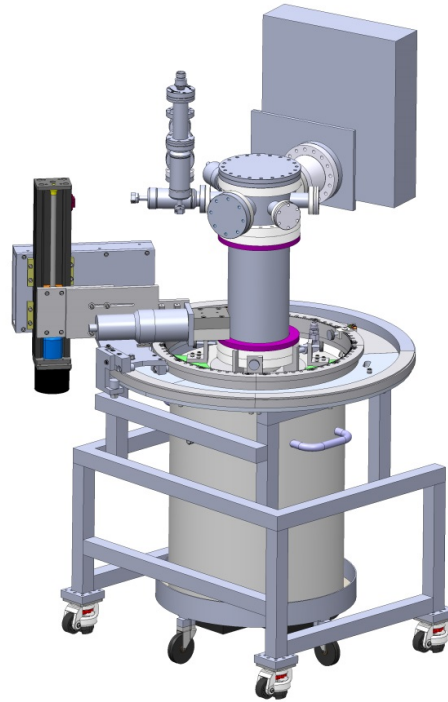


**Figure 2.13:** (Color online) A Solidworks model of the test stand with a string-test cryostat in the center. Included in the model is a scintillation detector that will be used to make  $\gamma$ - $\gamma$  coincidence measurements.

A second application will be the use of coincidence measurements to determine the orientation of the crystal axes of each of the detectors to be used in the MAJORANA DEMONSTRATOR. A NaI

detector with a photomultiplier tube will be attached to the scanning table and will move with the radioactive source as scanning occurs.



**Figure 2.14:** (Color online) Photograph of the test stand at UNC.

We plan to use  $^{133}\text{Ba}$  to produce coincident photons at 356 and 81 keV. Measurements of these coincident photons from the two detectors will provide timing information that can be used to determine whether the collimated beam of radiation lies along one of the crystal axes of the germanium detector. The angular resolution of the test-stand system is important because it places limits on how well we can determine the angular location of the crystal axes. Thus we have designed the test stand with a motor that can drive the collimated source of radiation around the table with a minimum resolution of  $0.074^\circ$ . This resolution allows us to use the stand to accurately determine the crystal axes to within about  $0.1^\circ$ , ignoring the uncertainty associated with the coincidence measurement.

We are currently in the process of testing the functionality of the first test stand at UNC and are preparing to assemble and test the second stand in a cleanroom environment. Once testing has been completed, the clean stand will be sent to the Sanford Underground Research Facility in Homestake, SD to characterize the string-test cryostats located there as a part of the MAJORANA DEMONSTRATOR. The original prototype stand will be sent to the Kimbalton Underground Research Facility in Blacksburg, VA to be used with a germanium detector housed underground as part of an ongoing dark matter search.

### 2.1.7 Simulations of an Azimuthal Scanning Table

A. WASSERMAN, *Rutgers University, Piscataway, NJ*; C. O'SHAUGHNESSY, J. MACMULLIN, J.F. WILKERSON, *TUNL*

**A stand is being developed to characterize strings of germanium detectors for a range of properties including energy resolution, active volume, dead layer, pulse-shape discrimination, and crystal-axis effects. Most of these measurements rely on a collimated point-like source on the detector surface. The work presented here includes the modeling of a source and collimator geometry that can be easily positioned around a cryostat using macro commands.**

An azimuthal scanning table (see Sect. 2.1.6) is being constructed to characterize detectors in cryostats holding either single detectors or a single string of detectors. The table can be used for any characterization that requires a localized source impinging the detector surface at a small spot. Examples are surface-dead-layer or crystal-axis measurements. A computerized control will be used to automate the repetitive data-taking tasks associated with the scanning table. We present here a geometry implementation in the MAGE [Bos11] framework for simulating germanium detectors. The implementation will allow us also to automate the model-generation tasks.

The MAJORANA and Gerda experiments are both using germanium detectors to search for  $0\nu\beta\beta$  decay and have jointly developed a framework, named MAGE, for simulating the response of germanium detectors to radiation sources. MAGE is built around the GEANT4 simulation toolkit [Ago03] and has been designed to simulate the response of low-background detectors to ionizing radiation. MAGE allows the user to specify the experiment's geometry, relevant physical processes, and event generators, all from a macro system that permits the end-user to perform simulations with diverse configurations without re-compiling the source code.

MAGE provides output of simulation data in the form of a Majorana-Gerda Data Object, which allows simulation data from MAGE to be processed similarly to data taken from the DAQ software. These data can then be processed with the germanium-analysis toolkit GAT, which contains processes that add noise, dead-layer, and other performance-related transforms to further model detector properties.

Creating individual parts in a given geometry is accomplished by constructing solids from Boolean operations on primitives such as boxes and cylinders, then specifying a material, and finally placing the part within a larger space that contains the entire geometry. For convenience, sub-components are organized in assembly classes, which contain the placements and materials of any number of parts as well as other assemblies. A geometry class allows for interaction via GEANT4 messenger commands in order to customize aspects of the geometry before initializing it.

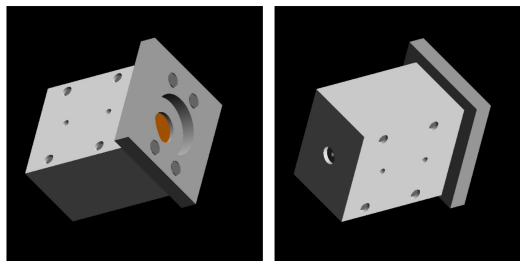


**Figure 2.15:** (Color online) Ray Tracer visualization of the collimator assembly that is placed by the characterization-stand geometry, showing back and front views on the left and right, respectively.

The characterization stand is a stage for placing a pencil beam from a test source at a defined place on the surface of a detector. This is accomplished by collimating the source using a lead brick with a channel that is 3.0 mm in diameter and 86.4 mm in length. A standard disk source fits in the collimator, which can be driven in the azimuthal and vertical axes of a detector.

A rendering of the collimator assembly is shown in Fig. 2.15. It is designed to accept detectors in both conventional cryostats from a detector vendor and in custom cryostats designed by the collaboration to test strings of detectors.

To initialize the geometry, one must run the `/MG/geometry/detector` command with an argument `MJCharacterization`. For the purposes of simulation, only the collimator, source, and surrounding mechanical structure were constructed. The source geometry has a disc of polyethylene surrounding a millimeter-sized radioactive isotope. Either  $^{133}\text{Ba}$ ,  $^{60}\text{Co}$ , or  $^{241}\text{Am}$  can be specified as the source material through the `/MG/characterization/sourceMaterial` command by giving the respective arguments `Barium-133`, `Cobalt-60`, or `Americium-241`. This does not however, change the actual decays generated, which must happen with the standard MAGE generator commands. The user can specify the position of the source using `/MG/characterization/sourceRadius`, `sourceAngle`, and `sourceZ` commands.

The source is always placed with the collimator facing inward toward the central axis-of-rotation, to match the physical stand orientation. The origin of the assembly is at the outer face of the disc source. It is therefore necessary to set

the radius of the assembly at least 9 cm away, plus an additional distance for the radius of the test cryostat. Various assemblies can be included in the geometry using Boolean commands. These include `/MG/characterization/cavernOn`, `standOn`, `cryostatOn`, and `stringOn`. The choice of cryostat is currently limited to the Ortec PopTop cryostat or a string-test cryostat and is set using the command `/MG/characterization/cryostat` with an argument of `PopTop` or `STC` respectively.

In summary, a flexible geometry class of a newly designed characterization stand has been implemented in the MAGE simulation framework. This will provide simple scripting support for source scans of germanium detectors in the test cryostats used by the MAJORANA Collaboration. Soon the class will be fully debugged and an example script for stepping through scans representative of the data-taking configurations will be generated.

- 
- [Ago03] S. Agostinelli *et al.*, Nucl. Instrum. Methods A, **506**, 250 (2003).
- [Bos11] M. Boswell *et al.*, IEEE Trans. Nucl. Sci., **58**, 1212 (2011).

---

### 2.1.8 Investigation of Pulse-Tube Refrigerators for Germanium-Detector-Array Cooling

---

M.P. GREEN, C. O'SHAUGHNESSY, M. BUSCH, J.F. WILKERSON, *TUNL*

**While the baseline design for the MAJORANA DEMONSTRATOR cryogenic system relies on a liquid-nitrogen-cooled closed-loop thermosyphon system, it is prudent to investigate alternative technologies, particularly as design work begins for a tonne-scale array. A pulse-tube refrigerator is being investigated as a potential cooling technology for germanium detector arrays.**

In the MAJORANA DEMONSTRATOR a cryostat is housed in a layered copper, lead, and polyethylene passive shield. Detectors are assembled in vertical strings of four to five detectors each and mounted to the underside of a copper cold plate, thermally isolated from the vacuum vessel. A thin copper infrared-radiation shield encloses the array. Penetrating the shield, a 4-inch diameter copper tube provides a path for vacuum and cryogenic systems plus electrical cabling.

The baseline cryogenic design specifies a closed-loop liquid-nitrogen thermo-siphon [Agu12] to cool the cold plate of the cryostat. Engineering calculations have estimated the total heat load for a MAJORANA-DEMONSTRATOR cryostat to be about 16.2 W at 80 K, depending on the number of detectors deployed and the emissivity of the copper components following fabrication and surface treatment for the removal of radioactive contaminants.

This work uses the MAJORANA DEMONSTRATOR prototype cryostat to investigate a pulse-tube cryocooler (PTC) as a potential cooling technology for germanium-detector arrays. To cool the prototype cryostat, a Cryomech, Inc. model PT-60 commercial PTC is connected to the cold plate via an evacuated copper thermosiphon tube that is left in place and is used as a cold finger. The cold head is coupled to the tube by way of a pair of custom-fabricated thermal straps composed of many strands of copper wire. These flexible elements allow for efficient heat conduction while minimizing vibration coupled to the detectors from the cold head. Each of these thermal straps was designed with a thermal conductance of 0.5 W/K at 65 K, and was evaluated at the manufacturer to conform to this standard. Assuming the thermal straps to be the

dominant impedance of the thermal conduction path implies a temperature difference between the cold head and the cold finger of about 16 K at steady-state, while the cold head is generating 16 W of cooling capacity. The power rating of the PTC [PT607] suggests a theoretical achievable temperature of 53 K for a fully-loaded cryostat.

While it is possible that the HPGe detectors may be able to function at temperatures as low as 53 K, the front-end electronics used to read out the detectors are tuned for higher operating points. The PT60 pulse-tube cooler system does not offer any temperature control; it can either be run at full power or disabled. In order to tune temperatures in the prototype cryostat, silicon diode temperature sensors have been installed on the cryostat cold plate and along a string of detectors. These temperature sensors are read out by a Lakeshore 336 temperature controller. The Lakeshore 336 contains a built-in proportional-integral-derivative (PID) controller, which uses feedback from one temperature sensor on the cryostat cold-plate to supply current to one of a pair of 50-ohm heater resistors installed in the thermal path between the cold finger and the thermal straps. By adjusting the heater current, it is possible to tune the cryostat cold-plate temperature to a desired value, and ensure long-term stability of the temperature in a laboratory with variable environmental conditions.

A cool-down of the prototype cryostat with a single string of detectors (out of a possible seven strings) is shown in Fig. 2.16. The plot of the temperature measured at the cryostat cold plate shows that the PTC is capable of bringing the cryostat to operating temperature in approximately 24 hrs. The detectors themselves,

however, have considerable thermal mass, characterized by a mass of 0.6 to 1.0 kg each and a heat capacity of  $310 \text{ J kg}^{-1} \text{ K}^{-1}$ . They thus require additional time to reach operating temperatures. The dashed curve indicates the power dissipated in one of the 50-ohm heater resistors (only one resistor is operated at a time). After 25.5 hrs of cooling, the PID control loop was enabled with a setpoint-temperature of 80 K. Due to the large thermal mass of the system, and the hours-long time constants associated with temperature change driven by the heater and PTC respective powers, the temperature-control loop typically requires four to five hours to reach stability. Once achieved, however, the temperature measurement remains stable to within 0.01 K indefinitely under typical laboratory conditions.

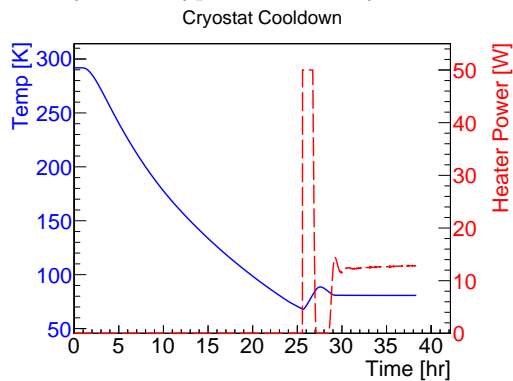


Figure 2.16: (Color online) Temperature as a function of time (solid blue curve) and heater power (dashed red curve) during initial cool-down and PID-stabilized temperature control.

To understand the capability of the pulse-tube refrigerator to cool the prototype cryostat loaded with detectors, the temperature at the cold plate of the cryostat was measured while a constant current was supplied to one of the heater resistors. Figure 2.17 shows the cold-plate temperature as a function of heater power after the temperature was given sufficient time to equilibrate. These measurements were taken prior to the installation of any detector strings in the prototype cryostat. The addition of seven strings of detectors to the cryostat should introduce about an additional 6 W of thermal load. Examination of Fig. 2.17 indicates that in this configuration, we can expect a base operating temperature of about 67 K for a fully-outfitted cryostat.

Furthermore, a calculation of the total heat-load of the cryostat can be made using the data in Fig. 2.17. To set the temperature of the cold-

plate to 80 K requires 11.1 W of heating. If the dominant thermal impedance is again assumed to be the thermal straps, then it is possible to calculate the cryostat’s heat load based on the cooling-capacity curve supplied by the manufacturer [PT607]. The thermal power absorbed by the cold head is the sum of the power generated in the heater and the thermal load of the cryostat. With a 1 W/K thermal conductance through the cold finger, additional power is required due to the temperature difference between the refrigerator cold finger, where the manufacturer specifications are valid, and the cold plate. Combining this information with the manufacturer specifications, it is estimated using this simplistic approach that the total heat load of the cryostat is about 21 W when maintained at 80 K.

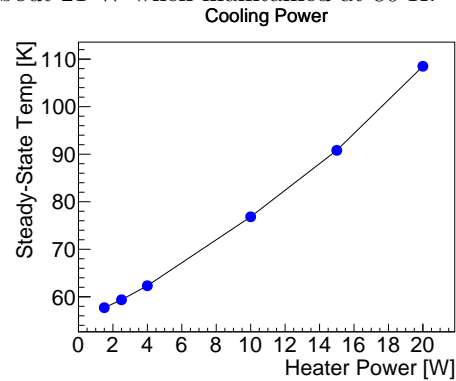


Figure 2.17: (Color online) Steady-state cryostat cold-plate temperature as a function of power supplied to a resistive heater.

It has been demonstrated in our testing that the pulse-tube cooler is sufficient for supplying the cooling power required to lower a fully-outfitted cryostat of the design implemented for the MAJORANA DEMONSTRATOR to the operating temperatures required for high-purity germanium detectors. Additionally, temperature feedback through a PID-control system provides a convenient and stable method for tuning detector temperatures between 60 and 100 K. Ongoing work will evaluate the microphonically-coupled electrical noise in detectors cooled using this apparatus.

[Agu12] E. Aguayo, J. Fast, and D. J. Reid, AIP Conf. Proc., **1434**, 425 (2012).

[PT607] *PT60-UL Cryorefrigerator Capacity Curve*, [http://www.cryomech.com/capacitycurve/PT60\\_cc.pdf](http://www.cryomech.com/capacitycurve/PT60_cc.pdf), 2007.

## 2.1.9 Underground Low-Background Assay at KURF

K. VORREN, R. HENNING, J.F. WILKERSON, *TUNL*

Two HPGe detectors are in operation at the Kimballton Underground Research Facility, located within a mine near Ripplemead, VA. These detectors are used for materials assay in a low-background environment. A status update of the low-background-counting facility is provided.

### Facility Overview

The Kimballton Underground Research Facility (KURF) is located about 25 miles from Virginia Polytechnic and State University in the Kimballton mine owned by Lhoist North America. The facility is located in a building on the 14th level of the mine at a depth of 520 meters, providing 1450 meters of water-equivalent shielding. The low-background-counting (LBC) facility is operated by UNC/TUNL and housed within a Naval Research Laboratory (NRL) modified shipping container.

The LBC facility has two HPGe detectors used exclusively for low-background assay work. The first detector, “MELISSA,” is a 1.1kg, 50% RE (relative efficiency compared to NaI) Canberra LB (low-background) detector. MELISSA is oriented vertically and is cooled using a dipstick cryostat. MELISSA’s shield consists of 15 cm of Doe-run lead and 2.54 cm OFHC (oxygen-free high conductivity) copper. The FWHM at 1.33 MeV is 1.70 keV, and the threshold is 20 keV. The other detector, “VT-1,” is a 0.956 kg, 35% RE ORTEC LLB Series detector in a J-type configuration. VT-1’s shield consists of a 10.1 cm ORTEC commercial lead shield and 0.3 cm of OFHC copper. VT-1 has a FWHM of 1.80 keV at 1.33 MeV, and the threshold is 20 keV. For more technical details regarding the facility and detector setup, see Ref. [Fin11].

Monitoring and data acquisition are controlled by ORCA which is run on a small Mac Mini in the NRL trailer [How13]. With ORCA, it is possible to stop and start runs, control the liquid nitrogen (LN) levels in the detector Dewars, and monitor the data in real time. TUNL personnel are only present at KURF about once every two weeks, so the slow controls and DAQ are regularly accessed remotely.

### Pumping of the Melissa Detector

Late last year it was discovered that LN in the MELISSA detector was evaporating at a higher than normal rate. Eventually the preamplifier would no longer output a cold signal even if the coldfinger had been submerged in LN for multiple days. It was determined that the vacuum required for thermal insulation was no longer sufficient and that the detector would need to be brought to the surface for repair. This was unfortunate, as the detector had likely been underground for over 20 years, enough time for cosmogenically activated isotopes to decay away.



**Figure 2.18:** (Color online) Setup for pumping of the Melissa detector.

The shield for MELISSA was unstacked in mid-October 2012, and it was confirmed that loss of vacuum was the cause of the cooling issues. The detector was brought back to UNC for pumping; the setup is shown in Fig. 2.18. Due to some issues with the scroll pump, pumping did not occur until mid-November. The detector was pumped on for one week, with the vacuum reaching about  $5 \times 10^{-5}$  torr. The coldfinger was baked at about

**Table 2.1: Sample Activities (mBq/kg)**

Sample	Source	U	Th
Mandrel Shavings	MAJORANA	< 300	< 90
Steel Rods	MAJORANA	$8 \pm 3$	< 4
Lanthanated Rods	MAJORANA		$3400 \pm 400$
OFHC Copper	MAJORANA	< 15	< 12
E-formed Copper*	MAJORANA	$1 \times 10^{-4}$	$0.6 \times 10^{-4}$

\*ICPMS from ORNL. Results are below KURF detection limits

75° C for an hour about half way through the pumping.

Once pumping had finished, the detector was tested at UNC, and it was found that the cooling problem had been resolved. A simple count at UNC using  $^{60}\text{Co}$  was set up to check the efficiency and FWHM of the 1333-keV line. No significant change from the values listed above was found. MELISSA was returned to KURF and has been operating since.

### Sample Analysis

The MAJORANA collaboration has an ongoing assay campaign as part of an effort to understand backgrounds in the  $^{76}\text{Ge}$   $0\nu\beta\beta$ -decay region-of-interest, a 4-keV wide region centered at 2039 keV. The LBC facility at KURF has assayed samples from parts machined underground at the Sanford Underground Research Facility in Lead, SD. These include samples of electroformed copper, samples from the stainless-steel mandrel on which the electroformed copper is grown, and welding rods used for welding the mandrels. Various other samples have been assayed as well, as indicated in Table 2.1.

For analysis, a sample spectrum is compared to the background. Background and sample spectra are normalized by dividing out the counting time. A library of common  $\gamma$ -ray lines is used to search for peaks and determine the activity of the sample. A Gaussian plus a linear-background function is fit to each peak used for analysis. The peak area is then extracted by subtracting the fit-determined linear background from the inte-

gral of the peak. The net peak area is found by subtracting the peak area of a background peak from the corresponding sample peak. If there is no peak on the background spectrum, the background peak area is set to zero.

The activity is determined using the equation,

$$A_{\gamma} = \frac{N}{\epsilon_{\gamma}m}, \quad (2.1)$$

where  $N$  is the net peak area,  $\epsilon_{\gamma}$  is the peak efficiency, and  $m$  is the mass of the sample. Peak efficiency is determined using a MAGE [Bau06] Monte Carlo simulation. The simulation has been validated by checking peak efficiencies against calibrated samples [Fin11].

### Conclusion

The LBC at KURF has been in operation for over four years. With sufficient notice, samples can be assayed fairly quickly. While most of the assayed samples come from the MAJORANA collaboration, samples from other institutions have also been assayed. At present both detectors are in operation and assaying samples.

[Bau06] M. Bauer *et al.*, J. Phys. Conf. Ser., **39** (2006).

[Fin11] P. Finnerty *et al.*, Nucl. Instrum. Methods A, **642**, 65 (2011).

[How13] M. Howe, <http://orca.physics.unc.edu/~markhowe/>, 2013.

## 2.1.10 Neutron-Capture Cross-Section Measurements of $^{136}\text{Xe}$ in the Energy Region 0.4-14.8 MeV

M. BHIKE, W. TORNOW, *TUNL*

**Activation measurements of the fast neutron-capture cross section on  $^{136}\text{Xe}$  were carried out between 0.4 and 14.8 MeV. This result is important for interpreting potential neutron-induced backgrounds in the EXO and KamLAND-Zen neutrinoless double-beta decay searches that use xenon highly enriched in  $^{136}\text{Xe}$  as both source and detector. A high-pressure gas cell of  $^{136}\text{Xe}$  was irradiated with monoenergetic neutrons, and the activities of the reaction products were measured by  $\gamma$ -ray spectroscopy. The results are compared to values from ENDF/B-VII.1 and TENDL-2012.**

The isotope  $^{136}\text{Xe}$  has been considered as one of the most promising candidates for neutrinoless double-beta decay ( $0\nu\beta\beta$ ) due to its large  $Q$  value of 2458 keV and its ideal characteristics for use in large-scale experiments. The experiments named EXO (Enriched Xenon Observatory) [Aug12] located at the Waste Isolation Pilot Plant (WIPP) in Carlsbad, NM, and KamLAND-Zen (Kamioka Liquid Scintillator Anti-Neutrino Detector-Zero Electron Neutrino) [Gan13a] at the Kamioka mine in Japan are currently taking data. Combining the available results from these two experiments provides the lowest upper limit for the electron-antineutrino mass:  $< (120 - 150)$  meV [Gan13a]. However, pushing this limit to considerably lower values or even to the discovery of  $0\nu\beta\beta$  decay, is a very challenging task.

Although these experiments operate underground, neutron-induced background reactions will become a major concern, because they could potentially produce  $\gamma$ -ray radiation at the energy of interest for  $0\nu\beta\beta$  decay, (2458 keV for  $^{136}\text{Xe}$ ). Here the neutrons are produced either by muon-induced spallation reactions or by  $(\alpha, n)$  reactions in the detector material itself or its associated shielding. In order to reliably predict the neutron-induced background in these experiments, both the relevant cross sections and the neutron flux at the location of the experiment must be known.

Neutron capture on  $^{136}\text{Xe}$  produces the radioactive isotope  $^{137}\text{Xe}$  with  $T_{1/2} = 3.82$  min. The beta decay of  $^{137}\text{Xe}$  to  $^{137}\text{Cs}$  results in a number of de-excitation  $\gamma$  rays with energies in the vicinity of the  $^{136}\text{Xe}$   $0\nu\beta\beta$   $Q$  value. The  $\gamma$  rays at 2463.3 and 2474.8 keV are of con-

cern for EXO, while for KamLAND-Zen, with its poorer energy and spatial resolution, the  $\gamma$  rays at 2422.7, 2444.0, 2452.4, and 2490.4 keV have to be considered as well.

The neutron activation of  $^{136}\text{Xe}$  was carried out using the 10 MV FN Tandem Accelerator at TUNL. Monoenergetic neutron beams were produced at six energies in the range from 0.4 to 3.5 MeV via the  $^3\text{H}(p, n)^3\text{He}$  reaction, at four energies between 4.2 and 7.45 MeV using the  $^2\text{H}(d, n)^3\text{He}$  reaction, and at 14.8 MeV using the  $^3\text{H}(d, n)^4\text{He}$  reaction. The  $^{136}\text{Xe}$  gas target has a purity of 99.9%, a mass of 725 mg, and was pressurized to 250 atm. It was contained in a titanium sphere with inner diameter of 0.96 cm and wall thickness of 0.2 mm. Two high-purity indium or gold foils were attached to the front and back side of the sphere for incident neutron fluence determination. To eliminate the effect of thermal neutrons, the  $^{136}\text{Xe}$  cell and the monitor foils were enclosed in a 0.5 mm thick cylindrical cage made out of cadmium. The distance between the center of the  $^{136}\text{Xe}$  sphere and the end of the neutron production cell was 1.0 cm.

The neutron flux was monitored by a liquid-scintillator-based neutron detector positioned about 3 m from the neutron-production target and at  $0^\circ$  relative to the direction of the proton or deuteron beam. This neutron monitor was also essential in determining the mean neutron energy. For this purpose the incident charged-particle beam was pulsed at a repetition rate of 2.5 MHz, with an overall time resolution of 2.5 ns. The neutron energy was inferred from the measured neutron time-of-flight. Because the half-life of  $^{137}\text{Xe}$  is 3.82 minutes, the neutron irradiation

time was limited to 15 minutes. The neutron flux at the location of the  $^{136}\text{Xe}$  sphere varied between  $1 \times 10^7$  and  $9 \times 10^7$   $\text{n}/(\text{cm}^2\text{s})$ .

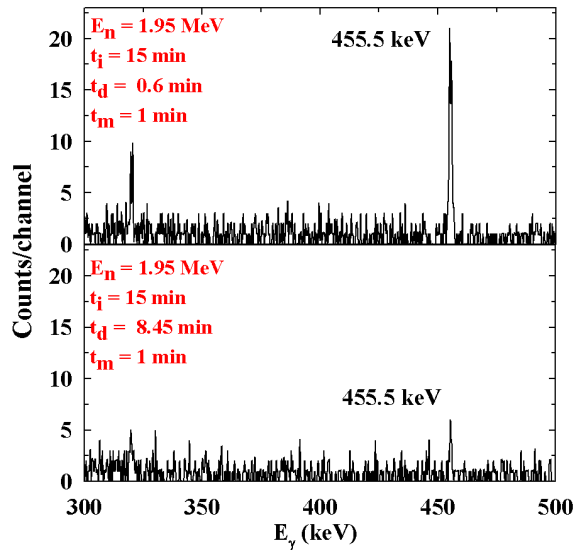


Figure 2.19: (Color online) Portion of  $\gamma$ -ray spectra collected for a  $^{136}\text{Xe}$  target after activation with 1.95 MeV neutrons. The  $\gamma$ -ray line at 455.49 keV associated with the decay of  $^{137}\text{Xe}$  is indicated.

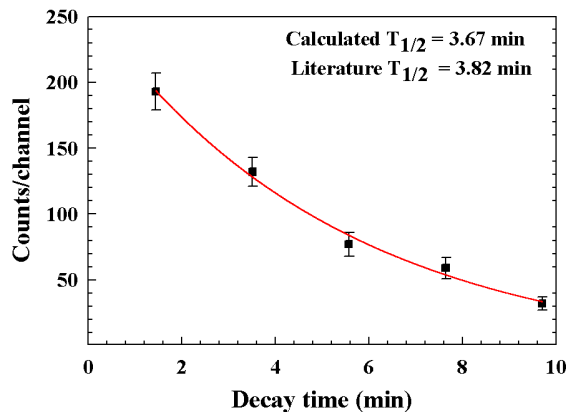


Figure 2.20: (Color online) Decay curve for the 455.49 keV  $\gamma$ -ray line of  $^{137}\text{Xe}$  measured at  $E_n = 3.6$  MeV

Following irradiation, the activity induced in the  $^{136}\text{Xe}$  sphere and the monitor foils was measured with well-shielded HPGe detectors of 60% relative efficiency. To reduce the transfer time from the irradiation site to the counting site to around 30 s, the  $^{136}\text{Xe}$  HPGe station was mounted just outside of the NTOF target room,

while the monitor foils were counted in TUNL's low-background counting facility. The characteristic  $\gamma$ -ray radiation of 455.49 keV (31%) from the de-excitation of  $^{137}\text{Xe}$  was used for determining the cross section of the  $^{136}\text{Xe}(n,\gamma)^{137}\text{Xe}$  reaction. The intensity of this  $\gamma$ -ray line was measured in about 2 minute intervals over a period of more than three half lives. Fig. 2.19 shows a typical  $\gamma$ -ray spectrum of the activated  $^{136}\text{Xe}$  sphere acquired just after irradiation and after 8.5 minutes. Fig. 2.20 shows the decay curve for the 455.49 keV  $\gamma$  ray obtained after irradiation with 1.95 MeV neutrons.

Figure 2.21 shows our data and the previously existing datum at  $E_n = 1$  MeV from Ref. [Hug53]. In the energy range between 0.4 and 14.8 MeV, the cross section is of the order of 1 mb or somewhat lower.

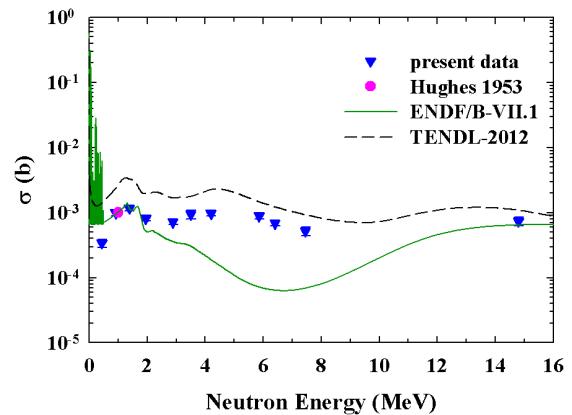


Figure 2.21: (Color online) Excitation function of the  $^{136}\text{Xe}(n,\gamma)^{137}\text{Xe}$  reaction.

The comparison of our data to the Evaluated Nuclear Data Libraries ENDF/B-VII.1 and TENDL-2012 [Kon05] shows that TENDL consistently predicts a larger cross section than obtained in the present work. ENDF/B-VII.1 is in excellent agreement with our data below 2 MeV and at 14.8 MeV, but predicts much lower values between 3 and 7.5 MeV.

[Aug12] M. Auger, Phys. Rev. Lett., **109**, 032505 (2012).

[Gan13] A. Gando, Phys. Rev. Lett., **110**, 062502 (2013).

[Hug53] D. Hughes, Phys. Rev., **91**, 1423 (1953).

[Kon05] A. J. Koning, S. Hilaire, and M. C. Duijvestijn, In *AIP Conf. Proc.*, volume 769, p. 1154, 2005.

### 2.1.11 The $^{40}\text{Ar}(n,\gamma)^{41}\text{Ar}$ Cross Section between 0.4 and 14.8 MeV

M. BHIKE, W. TORNOW, *TUNL*

**Activation measurements of the cross section for the reaction  $^{40}\text{Ar}(n,\gamma)^{41}\text{Ar}$  were carried out in the energy range from 0.43 to 14.8 MeV. These results are important for identifying backgrounds in liquid-argon-based neutrino detectors and in the neutrinoless double-beta-decay experiment GERDA, which uses argon as the cooling and shielding medium. Our results are compared to values from ENDF/B-VII.1 and TENDL-2012.**

Argon in its liquid form is a favorable detection medium for neutrinoless double-beta ( $0\nu\beta\beta$ ) decay and dark matter searches. It not only features a high stopping power for ionizing radiation and good light yield, but it also allows for any desired detector shape. In addition, its low cost makes a large detector mass affordable, and a very low background can be reached due to ease of purification (except for removing  $^{39}\text{Ar}$ ). The Germanium Detector Array (GERDA) searches for the neutrinoless double-beta decay of  $^{76}\text{Ge}$ . It is located at the Laboratori Nazionali del Gran Sasso, Italy and employs argon as the coolant and shielding material [Ago13]. Although the decay radiation of  $^{41}\text{Ar}$  does not directly produce  $\gamma$ -rays at the  $Q$  value for the  $0\nu\beta\beta$  decay of  $^{76}\text{Ge}$  at 2039 keV, Compton scattered  $\gamma$ -rays originating from the decay of  $^{41}\text{Ar}$  levels with energies above 2300 keV can produce  $\gamma$ -rays in the energy region of interest.

Liquid argon also provides very sensitive pulse-shape discrimination based on scintillation timing, and hence it is useful in direct searches for weakly interacting massive particles (WIMPs). One such search is DEAP-1, where the separation of  $\beta$ - $\gamma$  interactions from nuclear recoils is critical [Bou09]. The recently proposed Long-Baseline Neutrino Experiment facility (LBNE) at Fermilab plans to construct a liquid-argon time-projection chamber at the SURF site. Liquified argon will be employed as the target material to detect accelerator neutrinos as well as neutrinos and antineutrinos from supernova explosions. Again, decay radiation of  $^{41}\text{Ar}$  is a concern for these studies.

The neutron capture cross section of  $^{40}\text{Ar}$  was measured at ten different energies between 0.4 and 14.8 MeV using the 10 MV tandem accelerator at TUNL. Monoenergetic neutrons were

produced at energies between 0.4 and 3.5 MeV using the  $^3\text{H}(p,n)^3\text{He}$  reaction, between 4.2 and 7.45 MeV using the  $^2\text{H}(d,n)^3\text{He}$  reaction, and at 14.8 MeV using the  $^3\text{H}(d,n)^4\text{He}$  reaction.

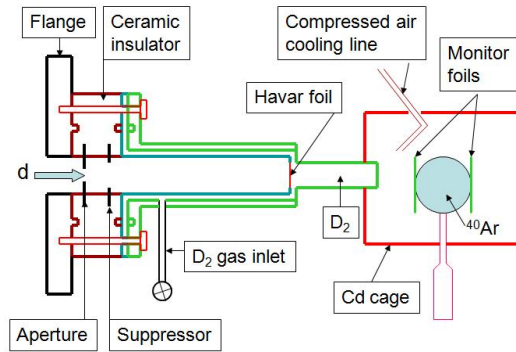


**Figure 2.22:** (Color online) Schematic view of the experimental arrangement for the  $^{40}\text{Ar}(n,\gamma)^{41}\text{Ar}$  cross-section measurements using the  $^2\text{H}(d,n)^3\text{He}$  reaction

As shown in Fig. 2.22, the experimental setup for the measurements with the  $^2\text{H}(d,n)^3\text{He}$  reaction consists of a 3-cm-long gas cell pressurized to 3 atm with high-purity deuterium gas. A 6.5 mm Havar foil separates the gas from the accelerator vacuum. Typical incident deuteron currents were  $2\ \mu\text{A}$ . For deuteron energies above 2.225 MeV, the deuterons can break up on the entrance collimator, the Havar foil, or the tantalum beam stop, resulting in lower energy neutrons than the primary neutrons of interest from the  $^2\text{H}(d,n)^3\text{He}$  reaction. Auxiliary measurements were performed with the deuterium gas pumped out, leaving all the parameters unchanged. The incident deuteron beam charge deposited on the deuterium gas cell was used for normalization

purposes for these two types of experiments.

The tritiated titanium target cell used in connection with the  ${}^3\text{H}(p,n){}^3\text{He}$  reaction consists of 2.1 Ci of  ${}^3\text{H}$  loaded into a  $2.2\text{ mg/cm}^2$  thick layer of titanium with a diameter of 16 mm. This, in turn, is evaporated onto a 0.4 mm thick copper backing. Typical proton beam currents were  $3.5\text{ }\mu\text{A}$ . Once the proton energy exceeds about 3 MeV, corresponding to a primary neutron energy greater than 2.2 MeV, the primary neutrons are accompanied by low-energy neutrons originating from  $(p,n)$  reactions on the titanium and copper backing. Therefore, at  $E_n = 2.88$  and 3.5 MeV, auxiliary measurements were performed with an untritiated, but otherwise identical target. The two individual measurements were normalized to the accumulated proton charge on target. The tritiated target described above was also used for the  ${}^3\text{H}(d,n){}^4\text{He}$  reaction to produce 14.8 MeV neutrons. In this case, lower energy neutrons are not produced due to the low incident deuteron energy.

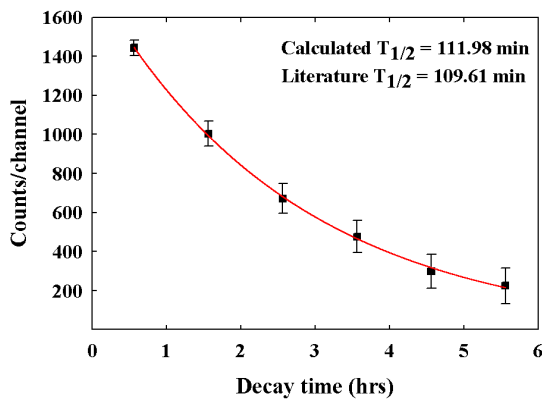


Figure 2.23: (Color online) Decay curve for the 1293.64 keV  $\gamma$ -ray line of  ${}^{40}\text{Ar}$  measured at  $E_n = 4.2$  MeV.

The natural argon gas (99.6%  ${}^{40}\text{Ar}$ ) was contained in a stainless steel sphere with an inner diameter 20 mm and a wall thickness of 0.5 mm. The mass of argon was 1.585 g, resulting in a pressure of 210 atm inside the sphere. The sphere was placed at a distance of 2 cm from the neutron production site and was sandwiched between two monitor foils (either gold or indium). It was enclosed by a cadmium cage.

Irradiation at each energy was carried out for 2 hours, and the neutron-induced  $\gamma$ -ray activity

was counted with lead-shielded HPGe detectors at TUNL's low-background facility.

The  $\gamma$ -ray line at 1293.64 keV (99.16% abundant) was used for cross-section calculation. Its half-life of  $T_{1/2} = 109.61$  min was confirmed by following the decay of this line for up to 7 hours. It was found to be in agreement with the literature value, as illustrated in Fig. 2.23. Figure 2.24 shows the measured cross sections and the previously existing data at  $E_n = 0.136, 0.2, 0.3, 0.4$  and 1 MeV [Bos59], along with the ENDF/B-VII.1 and TENDL-2012 evaluations. In the energy range between 0.4 and 14.8 MeV, the cross section is of the order of 1 mb or somewhat lower. The TALYS evaluation (TENDL-2012) is in perfect agreement with the present data at all energies except at 14.8 MeV, where it slightly over-predicts our measurement. ENDF/B-VII.1 is in good agreement with our data at 4.2 MeV, but over-predicts our data at 1.95, 2.88, 3.6 and 14.8 MeV and under-predicts our values at 5.85, 6.4 and 7.45 MeV.

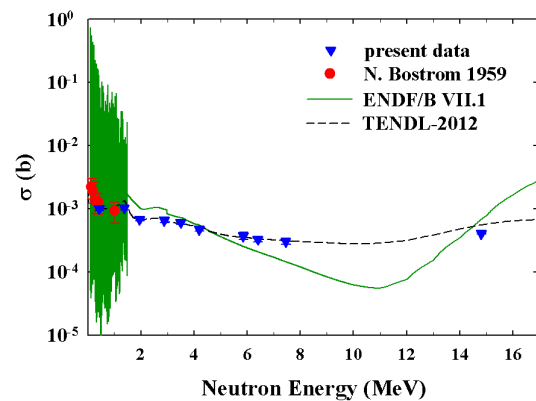


Figure 2.24: (Color online) Excitation function of the  ${}^{40}\text{Ar}(n,\gamma){}^{41}\text{Ar}$  capture cross section.

[Ago13] M. Agostini, Phys. Rev. Lett., **111**, 122503 (2013).

[Bos59] N. A. Bostrom, Technical Report WADC-TC-59-107, Wright Air Development Center Reports No. 59, 1959.

[Bou09] M. G. Boulay *et al.*, arXiv:astro-ph.IM, page 0904.2930v1 (2009).

### 2.1.12 Measurements of the Neutron-Capture Cross-Sections of $^{74}\text{Ge}$ and $^{76}\text{Ge}$ from 0.4 to 14.8 MeV for $0\nu\beta\beta$ -Decay Applications

M. BHIKE, W. TORNOW, *TUNL*

Excitation functions for the reactions  $^{74}\text{Ge}(n,\gamma)^{75}\text{Ge}$  and  $^{76}\text{Ge}(n,\gamma)^{77}\text{Ge}$  were measured at energies of 0.4 to 14.8 MeV. The data are important to test theoretical models and improve the evaluations needed to estimate neutron-induced backgrounds in experiments searching for the  $0\nu\beta\beta$  decay of  $^{76}\text{Ge}$ . Targets enriched in  $^{76}\text{Ge}$  were irradiated with mono-energetic neutrons, and the  $\gamma$ -ray decay spectra after the  $\beta$  decay of  $^{75}\text{Ge}$  and  $^{77}\text{Ge}$  were measured. The present results are compared with values from TALYS.

The Germanium Detector Array (GERDA) collaboration [Ago13] and the MAJORANA collaboration [Abg13] use germanium-diode detectors in their searches for the neutrinoless double-beta ( $0\nu\beta\beta$ ) decay of  $^{76}\text{Ge}$ . These highly enriched detectors, which consist of 86%  $^{76}\text{Ge}$  and 14%  $^{74}\text{Ge}$ , serve as both source and detector. The recent experimental result reported by the GERDA collaboration gives a half-life of greater than  $3.0 \times 10^{25}$  yr. In order to increase the sensitivity of such experiments, the neutron-induced background must be well understood. Unfortunately, neutron-capture cross-section data in the MeV energy range do not exist for  $^{76}\text{Ge}$ , except for a single datum at 14 MeV [Beg07].

Although there are no levels in  $^{77}\text{Ge}$  or its daughter nuclei which directly produce  $\gamma$ -rays of 2039 keV (the  $Q$  value for the  $0\nu\beta\beta$  decay of  $^{76}\text{Ge}$ ) the decay of levels with excitation energies above 2300 keV could produce Compton-scattered  $\gamma$  rays in the 2039 keV region. There is a  $\gamma$  ray of 2037.87 keV resulting from the decay of the 2513.47 keV level of  $^{77}\text{As}$ , the daughter of  $^{77}\text{Ge}$ , but it is in coincidence with either a  $\gamma$  ray of 475.48 keV or two  $\gamma$  rays of 264.426 keV and 211.03 keV, making it less likely to be detected as a 2037.87 keV event. For the  $^{74}\text{Ge}$  isotope, neutron capture data are available at neutron energies up to 4 MeV. Again for  $^{74}\text{Ge}$ , Compton scattering of  $\gamma$  rays with energies above 2300 keV resulting from the decay of  $^{75}\text{Ge}$ , could produce  $\gamma$  rays within the 2039 keV window used by GERDA and MAJORANA.

In order to increase the database for both isotopes, neutron-capture cross-section data were obtained at TUNL in the MeV energy range. Square shaped targets of germanium with 86%

$^{76}\text{Ge}$  and 14%  $^{74}\text{Ge}$  were used. The targets were 2 mm thick. They had an area of 1 cm $\times$ 1 cm and a mass of around 1.5 g. To monitor the neutron flux, gold or indium foils of the same area were attached to the front and back sides of the targets. The target assembly was surrounded by a cadmium cage and was placed at a distance of about 1 cm from the neutron source. The cadmium cage removes the influence of thermal neutrons from the measurement. Monoenergetic neutrons were produced by three different reactions. The  $^3\text{H}(p,n)^3\text{He}$  reaction was used for neutron energies up to 3 MeV. For higher energies the  $^2\text{H}(d,n)^3\text{He}$  was employed, except at 14.8 MeV, where the  $^3\text{H}(d,n)^4\text{He}$  reaction was used. After irradiation,  $\gamma$  rays from the activated samples were counted with well-shielded and calibrated HPGe detectors of known efficiency. Both  $^{75}\text{Ge}$  and  $^{77}\text{Ge}$  emit  $\gamma$  rays with an energy of 264 keV, but with different half-lives, as indicated in Table 1.

**Table 2.2:** Relevant decay data for the reactions of interest

Nucleus	$T_{1/2}$	$E_\gamma$ (keV)	$I_\gamma$ (%)
$^{75}\text{Ge}$	82.78(4)min	264.6	11.4
		198.6	1.19(12)
$^{75m}\text{Ge}$	47.7(5)s	139.68	39.36
$^{77}\text{Ge}$	11.211(3)h	264.45	53.3
		215.51	27.9(7)
$^{77m}\text{Ge}$	53.7(6)s	215.53	21

A systematic approach was used to separate the two components. The decay radiation was recorded for 3 days. Because the relatively short-lived component  $^{75}\text{Ge}$  decayed away quickly, the data obtained after more than one day of count-

ing were used to fit the  $^{77}\text{Ge}$  decay curve. This fit was then extrapolated back in time, and the  $^{77}\text{Ge}$  yield was subtracted from the total, providing the decay yield for  $^{75}\text{Ge}$ .

Our results for  $^{76}\text{Ge}(n,\gamma)^{77}\text{Ge}$  are plotted in Fig. 2.25, along with the previous datum at a neutron energy of 14.7 MeV [Beg07]. TENDL-2012 under-predicts both the present data and the datum from the literature at 14.7 MeV. However, it roughly agrees with our measurement at 0.4 MeV. In the future, additional data will be taken at 3.5 and 5.5 MeV.

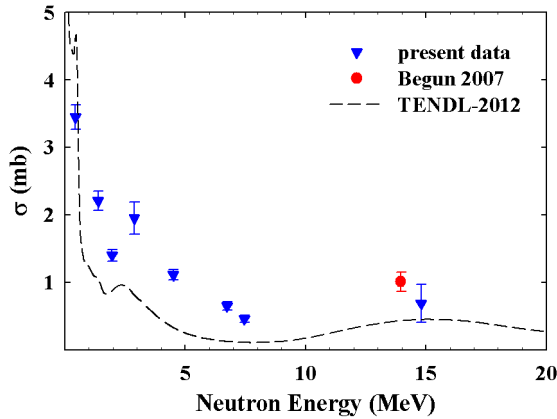


Figure 2.25: (Color online) Excitation function of the  $^{76}\text{Ge}(n,\gamma)^{77g}\text{Ge}$  reaction.

For the  $^{74}\text{Ge}(n,\gamma)^{75g}\text{Ge}$  reaction (Fig. 2.26), literature data exist up to 4 MeV [Pas58, Tol68]. The TALYS results are closer to the present data between 1.9 and 7.45 MeV than they are to the values found in the literature, but they under-predict the measurements at 1.04 and 1.38 MeV, and they over-predict the datum at 0.4 MeV by as much as a factor of 2. However, in the lower energy region up to 1.7 MeV, the evaluation matches the earlier data of Ref. [Tol68]. In the future, additional data will be taken between 2 and 4 MeV.

Comparing the  $^{76}\text{Ge}(n,\gamma)^{77}\text{Ge}$  and  $^{74}\text{Ge}(n,\gamma)^{75}\text{Ge}$  cross-section results found in the

present work below a neutron energy of 5 MeV, it is obvious that the  $^{74}\text{Ge}(n,\gamma)^{75}\text{Ge}$  neutron-capture reaction potentially produces as much background in the GERDA and MAJORANA detectors as the  $^{76}\text{Ge}(n,\gamma)^{77}\text{Ge}$  reaction, although the  $^{74}\text{Ge}$  abundance in these detectors is about a factor of six less than that of  $^{76}\text{Ge}$ . This finding is of special interest for the MAJORANA DEMONSTRATOR [Abg13], in which cryostat 1 will contain both enriched and natural germanium detectors. In the latter, the abundance of  $^{74}\text{Ge}$  is 36.5%.

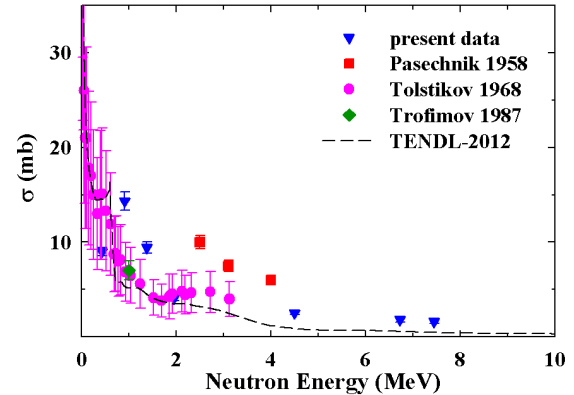


Figure 2.26: (Color online) Excitation function of the  $^{74}\text{Ge}(n,\gamma)^{75g}\text{Ge}$  reaction.

[Abg13] N. Abgrall, arXiv, **1308.1633v1** (2013).

[Ago13] M. Agostini, Phys. Rev. Lett., **111**, 122503 (2013).

[Beg07] S. V. Begun *et al.*, arXiv:nucl-ex, **0701039v1** (2007).

[Pas58] M. V. Pasechnik, In *Second International Atomic Energy Conference*, volume 15, p. 18, 1958.

[Tol68] V. A. Tolstikov, Yad. Fiz. [Sov. J. Nucl. Phys], **6**, 5 (1968).

### 2.1.13 $2\nu\beta\beta$ Decay of $^{96}\text{Zr}$ to the First Excited $0^+$ State

S.W. FINCH, W. TORNOW, *TUNL*

**A search for the double-beta decay of  $^{96}\text{Zr}$  to the first excited  $0^+$  state of  $^{96}\text{Mo}$  is currently taking data at KURF. An isotopically enriched  $^{96}\text{Zr}$  sample is placed between two germanium detectors in order to observe coincidence  $\gamma$  rays from the resulting cascade. Our current limit for the half-life of this decay is a factor of 2.35 better than the previous limit.**

Observation of neutrinoless double-beta  $0\nu\beta\beta$  decay would identify the neutrino as a Majorana particle and allow for a measurement of the neutrino mass. The  $0\nu\beta\beta$  decay rate is proportional to the neutrino mass and a nuclear matrix element (NME). Extracting the neutrino mass requires a theoretical evaluation of the NME, which is very difficult at present. Two-neutrino double-beta ( $2\nu\beta\beta$ ) decay rate is used to calibrate these calculations. By measuring  $2\nu\beta\beta$  decay to an excited final state (see Fig. 2.27) we can provide additional information to help fine tune NME calculations.

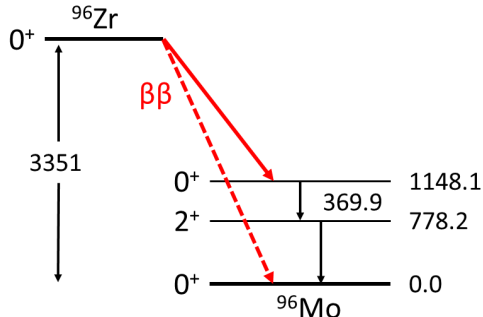


**Figure 2.27:** (Color online) The double-beta decay scheme for  $^{96}\text{Zr}$ .

The experimental apparatus consists of two coaxial high-purity germanium detectors, with the isotope of interest sandwiched between them. The detectors record the two coincident  $\gamma$  rays from the  $0^+ \rightarrow 2^+ \rightarrow 0^+$  decay sequence. Detectors and sample are housed inside a NaI annulus, which is used as an active veto. Passive shielding includes 0.75 in. of copper, 6 in. of lead, and the 1450-meter-water-equivalent overburden at KURF. This apparatus has previously measured the double-beta-decay half-life of  $^{100}\text{Mo}$  and  $^{150}\text{Nd}$  to their excited  $0_1^+$  states

[Kid09, Kid13].

The goal of this experiment is to extend these successful measurements to include  $^{96}\text{Zr}$ . The NEMO-3 collaboration [Arg10] measured the ground state  $2\nu\beta\beta$  decay of  $^{96}\text{Zr}$  and found a half-life of  $T_{1/2}^{2\nu} = [2.35 \pm 0.14(\text{stat}) \pm 0.16(\text{syst})] \times 10^{19}$  y. A search for the decay to the first excited  $0_1^+$  was conducted [Bar96] using a single-well HPGe detector and produced a lower limit of  $6.8 \times 10^{19}$  years.

$^{96}\text{Zr}$  differs from other double-beta-decay isotopes in that single-beta decay is energetically allowed, but only via a long-lived fourth-forbidden decay. The half-life has been theoretically estimated [Hei07] as  $2.4 \times 10^{20}$  y. The daughter nucleus,  $^{96}\text{Nb}$ , decays to  $^{96}\text{Mo}$  and emits a cascade of  $\gamma$  rays as it de-excites to the ground state. This cascade proceeds through the  $2^+$  level of interest for double-beta decay to excited final states, but not through the  $0_1^+$  state. Previous attempts to measure  $^{96}\text{Zr}$ 's  $\beta\beta$  decay to an excited final state looked at the single 778.2 keV  $\gamma$  ray from the  $2^+ \rightarrow 0^+$  part of the decay. Because this  $\gamma$  ray also appears in the  $\gamma$ -ray cascade resulting from single-beta decay, single-detection experiments are only sensitive to  $T_{1/2}^{\beta+\beta\beta}$ . With our coincidence technique, we can independently measure both the  $\beta$  and  $\beta\beta$  decay modes.

A rough estimate of the background present in the setup may be found by analyzing the data collected during the  $^{150}\text{Nd}$  and background runs. After 2.25 years of data collection, there are five events corresponding to coincidences like the 778.2 + 369.9 keV coincidence for  $^{96}\text{Zr}$ . These are shown in Fig. 2.28, panels (c) and (d). The energy cuts utilized are  $\pm 3\sigma$ , where  $\sigma$  is the standard deviation of the detector resolution. Typically,  $3\sigma$  is 2 to 3 keV, depending on the run and the  $\gamma$ -ray energy. This analysis does not include any radioactive contamination that may be

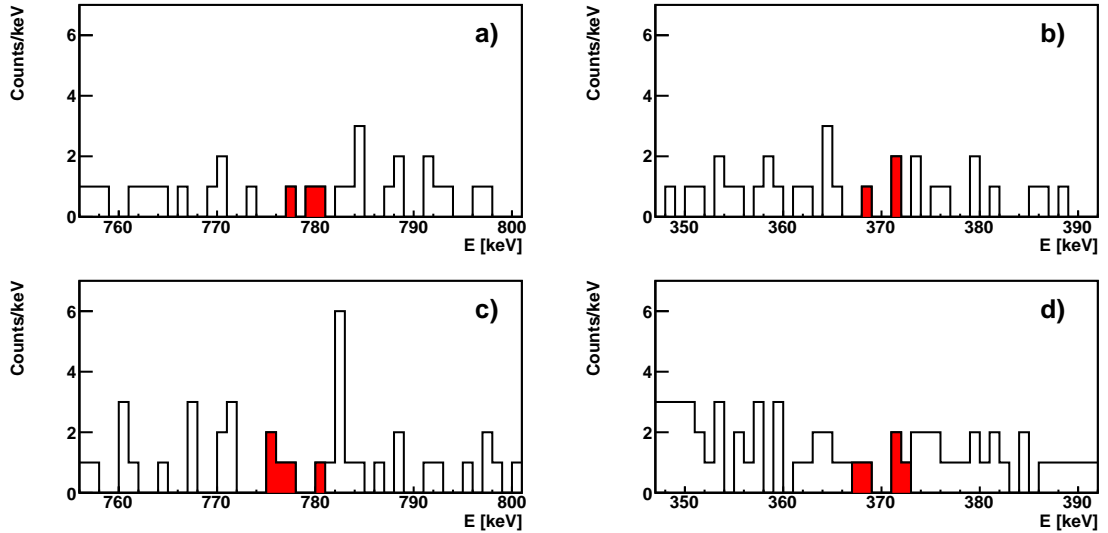


Figure 2.28: (Color online) Plots (a) and (b) show the  $^{96}\text{Zr}$  region of interest after 1.31 years of data acquisition with the enriched sample; the three events passing all cuts are highlighted. (c) and (d) show the same region after 2.25 years with no  $^{96}\text{Zr}$  present; there are five events passing all cuts. (a) and (c) are events in coincidence with 369.9 keV  $\gamma$  rays while (b) and (d) are in coincidence with 778.2 keV  $\gamma$  rays.

present in the zirconium sample.

Our  $^{96}\text{Zr}$  source consists of two  $\text{ZrO}_2$  samples: one with 7.284 g enriched to 91.39%  $^{96}\text{Zr}$  and the other with 26.969 g enriched to 64.15%, giving a total of 17.914 g  $^{96}\text{Zr}$ . After 1.31 years with the sample in place, there are three candidate events matching the selection criteria, as shown in Fig. 2.28 (a) and (b). This result is consistent with the background discussed above. Furthermore, there is no peak above background visible in the spectra. The limit on the half-life is given by

$$T_{1/2} > \frac{\ln 2 t N_0 \epsilon_{\gamma\gamma}^{\text{tot}}}{N_d}, \quad (2.2)$$

where  $t$  is the counting time,  $N_0$  is the number of nuclei present,  $\epsilon_{\gamma\gamma}^{\text{tot}}$  is the coincidence efficiency, and  $N_d$  is a statistical factor indicating the upper limit of counts indistinguishable from background.

The coincidence efficiency was measured as a function of position using a  $^{102}\text{Rh}$  source, which follows the same  $0^+ \rightarrow 2^+ \rightarrow 0^+$  decay scheme as  $^{96}\text{Zr}$ . There are three corrections that must be applied to this efficiency measurement. First, an adjustment must be made to account for the different  $\gamma$ -ray energies of the two sources. The energy dependence of both detectors was measured using the point sources  $^{125}\text{Eu}$ ,  $^{60}\text{Co}$ ,  $^{137}\text{Cs}$ , and  $^{22}\text{Na}$ . This correction is calculated to be  $0.827 \pm 0.024$ . The second correction involves the attenuation of the signal  $\gamma$  rays through the tar-

get. The original source measurements had 5 mm of molybdenum metal on each side of the target to mimic attenuation for the measurement of  $^{100}\text{Mo}$ 's  $2\nu\beta\beta$  decay to excited states. The molybdenum metal and the  $^{96}\text{ZrO}_2$  target were modeled in GEANT4 to calculate the attenuation effects. This correction is a factor of  $2.763 \pm 0.004$ . This large correction is due to the  $\text{ZrO}_2$  sample being much less dense than molybdenum metal. A third correction factor of 1.023 accounts for the detectors being closer together and therefore covering a larger solid angle.

Combining all of these effects, we achieve a limit on the half-life of  $T_{1/2} > 1.6 \times 10^{20}$  years at the 90% confidence level. This includes a 5% systematic uncertainty arising from the efficiency measurements. Our result represents a factor of 2.35 improvement over the previous limit [Bar96].

[Arg10] J. Argyriades *et al.*, Nucl. Phys., **A847**, 168 (2010).

[Bar96] A. S. Barabash *et al.*, J. Phys. G, **22**, 487 (1996).

[Hei07] H. Heiskanen *et al.*, J. Phys. G, **34**, 837 (2007).

[Kid09] M. F. Kidd, J. H. Esterline, and W. Tornow, Nucl. Phys., **A821**, 251 (2009).

[Kid13] M. F. Kidd *et al.*, Submitted to Phys. Rev. C, (2013).

### 2.1.14 Search for Resonant Double-Electron Capture of $^{156}\text{Dy}$

S.W. FINCH, W. TORNOW, *TUNL*

**Resonant double-electron capture is a possible experimental alternative to neutrinoless double-beta decay. The decay may be detected by observing the  $\gamma$  rays emitted as the excited-state daughter nucleus decays to the ground state. In this experiment, two clover HPGe detectors surround an enriched  $^{156}\text{Dy}_2\text{O}_3$  target and search for the de-excitation  $\gamma$  rays.**

In electron capture, the nucleus captures an atomic electron, decreases its atomic number, and emits a neutrino. As the only directly emitted particles are neutrinos, this process would be very hard to observe if not for atomic x-ray or nuclear  $\gamma$ -ray transitions in the daughter state. Double-electron capture is also possible and can proceed through a zero-neutrino mode ( $0\nu\text{ECEC}$ ), if the neutrino is a Majorana particle. If the  $Q$  value of the transition is degenerate with an excited state of the daughter nucleus, the decay rate may be resonantly enhanced. In this case, the phase space available for neutrinos is so restricted that the neutrinoless mode dominates over the  $2\nu$  mode. This process is detectable by the  $\gamma$ -ray cascade from the excited state to the ground state in the daughter nucleus. Thus detection of this cascade would be evidence for Majorana neutrinos. A possible resonant  $0\nu\text{ECEC}$  decay in  $^{156}\text{Dy}$  is shown in Fig. 2.29. The two coincidence  $\gamma$  rays establish the experimental signature.

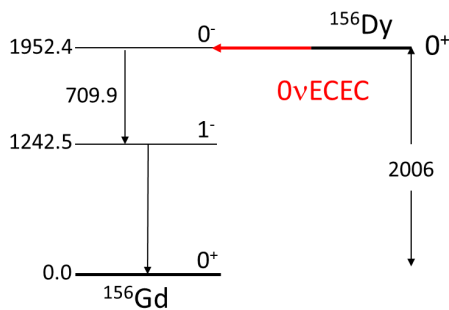


**Figure 2.29:** (Color online) A possible resonant double-electron capture scheme for  $^{156}\text{Dy}$ .

New  $Q$ -value measurements [Eli11] show that  $^{156}\text{Dy}$  is a promising candidate for  $0\nu\text{ECEC}$ , al-

though it suffers from an extremely low natural abundance: 0.056%. Four possible transitions are summarized in Table 1. For each of these transitions, there is an estimate of the rate enhancement factor and the electron wave-function overlap. An estimate of the decay rate involves the product of these two terms:

$$\lambda_{0\nu} \propto |M|^2 |\langle m_\nu \rangle|^2 |\Psi_X|^2 |\Psi_Y|^2 (EF), \quad (2.3)$$

where  $M$  is the nuclear matrix element,  $m_\nu$  is the neutrino mass,  $\Psi$  is the wave-function overlap, and  $EF$  is the enhancement factor as given in Table 2.3.

In order search for  $0\nu\text{ECEC}$ , an apparatus was setup at TUNL using two HPGe clover detectors, as shown in Fig. 2.30. This device was initially tested at TUNL with a plastic veto, which worked well to veto cosmic rays, but was insufficient as a Compton suppression system. After moving the apparatus to KURF, the plastic veto was replaced by a NaI annulus to further reduce background  $\gamma$  rays. Passive shielding includes six inches of lead surrounding the clover detectors and NaI annulus.

Clover detectors are utilized because they have a higher efficiency than conventional coaxial HPGe detectors, especially at higher energies. The easiest way to increase the efficiency of a HPGe detector is to increase the size of the active volume; however, germanium crystals larger than those currently in use are expensive to grow and often have poor timing resolution. An alternative is to use segmented detectors comprised of multiple crystals, such as the clover detector comprised of four crystals. Summing together the different crystals (known as add-back mode) allows for a 40% increase in efficiency at 1 MeV, compared to using each crystal as an individual detector.

Another advantage of clover detectors is the

**Table 2.3:** The possible excited states in the daughter,  $^{156}\text{Gd}$ , after  $0\nu\text{ECEC}$  of  $^{156}\text{Dy}$ . The physical state in the daughter has energy  $E$ . Electrons are captured from the  $XY$  orbitals with a total binding energy  $B_{XY}$ . The degree of degeneracy for the decay is given by  $\Delta = Q - E - B_{XY}$ , where  $Q$  is the ECEC  $Q$  value of 2006 keV. For each transition there is an enhancement factor, **EF**, in the rate and a wave-function overlap for the atomic electrons and the nucleus in atomic units,  $|\Psi_X|^2|\Psi_Y|^2$  [Eli11].

$E$ (keV)	$I^\pi$	$e^-$ orbitals (XY)	$B_{XY}$ (keV)	$\Delta$ (keV)	EF	$ \Psi_X ^2 \Psi_Y ^2$
1946.375	$1^-$	$\text{KL}_1$	58.822 (8)	0.75 (10)	26	$1.23 \times 10^{10}$
1952.385	$0^-$	$\text{KM}_1$	52.192 (8)	1.37 (10)	35	$2.68 \times 10^9$
1988.5	$0^+$	$\text{L}_1\text{L}_1$	16.914 (8)	0.54 (24)	8	$1.65 \times 10^9$
2003.749	$2^+$	$\text{M}_1\text{N}_3$	2.160 (24)	0.04 (24)	15	$1.52 \times 10^1$

higher coincidence efficiency. One possible decay involving two coincident  $\gamma$ -rays that will be investigated in this experiment is shown in Fig. 2.29. A large reduction in background is made by imposing a  $\gamma$ - $\gamma$  coincidence and detecting the two separate  $\gamma$  rays in this cascade. In the two-clover apparatus we can search for coincidences between the two clovers as well as within the four-fold segmentation of a single clover detector. Extensive efficiency measurements were performed on this apparatus while at TUNL, including measurements of the coincidence efficiency for cascades with two  $\gamma$  rays.

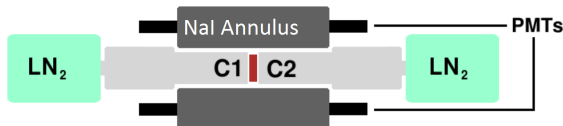


**Figure 2.30:** (Color online) Schematic of the two clover detectors and NaI annulus as installed at KURF. The sample is shown in red, between the two detectors.

The detectors, shielding, and electronics were moved to KURF during the summer of 2012 and the first underground data were collected during December of 2012. In March of 2013 we received the NaI annulus from Saint-Gobain. After testing at TUNL, the annulus was installed at KURF.

For this experiment we have acquired two enriched  $\text{Dy}_2\text{O}_3$  samples: 803 mg enriched to

21.59% and 344 mg enriched to 20.9%. This totals only 213 mg of  $^{156}\text{Dy}$ , which greatly limits the sensitivity of such an experiment. An important side goal, however, is to investigate radioactive impurities contained in the enriched  $^{156}\text{Dy}$  sample obtained from ORNL. These could interfere with a large scale ECEC experiment using  $^{156}\text{Dy}$  produced by the same enrichment processes.

Another experiment recently reported lower limits on  $T_{1/2}$  ranging from  $3.0 \times 10^{14}$  to  $1.1 \times 10^{16}$  for the different possible transitions [Bel12]. This experiment used a 322 g sample of natural  $\text{Dy}_2\text{O}_3$ , containing to only 157 mg of  $^{156}\text{Dy}$ . The sample was counted for 105 days using a single HPGe detector located at Gran Sasso National Lab. Our experiment will improve upon these limits by: 1) using an enriched sample to reduce signal attenuation in the sample, 2) covering a larger solid angle of the sample, 3) employing a  $\gamma$ - $\gamma$  coincidence to lower the background. Currently, we have collected 100 days worth of data with only the 803 mg sample in place and 15 days of data with both enriched samples in place. Analyses are currently ongoing to search for  $0\nu\text{ECEC}$  and to quantify radioactive backgrounds present in the sample.

[Bel12] P. Belli *et al.*, arXiv:nucl-ex, **1201.4581** (2012).

[Eli11] S. Eliseev *et al.*, Phys. Rev. C, **84**, 012501 (2011).

### 2.1.15 TUNL’s KamLAND Effort

H.J. KARWOWSKI, W. TORNOW, *TUNL*; D.M. MARKOFF, *North Carolina Central University, Durham, NC*

Our group has continued to provide KamLAND and KamLAND-Zen shift service, both remotely and on site. Reduced anti-neutrino flux at the KamLAND reactor allowed us to confirm and constrain the backgrounds for the reactor-neutrino oscillation results and to increase the sensitivity to neutrinos from uranium and thorium in the earth. The search for the  $^{136}\text{Xe}$  neutrinoless double-beta ( $0\nu\beta\beta$ ) decay continued with the KamLAND-Zen detector. The first phase of the experiment yielded a lower limit for the  $0\nu\beta\beta$ -decay half-life of  $1.9 \times 10^{25}$  y.

The KamLAND-Zen detector (see Fig. 2.31) is a modification of the existing KamLAND detector. The  $\beta\beta$  source/detector is thirteen tons of  $^{136}\text{Xe}$ -loaded liquid scintillator (Xe-LS) contained in a 3.08-m-diameter spherical inner balloon (IB). The IB is constructed from 25- $\mu\text{m}$ -thick transparent nylon film and is suspended at the center of the KamLAND detector by twelve thin strips of the same material. The IB is surrounded by 1 kton of liquid scintillator (LS) contained in a 13-m-diameter spherical outer balloon (OB) made of 135- $\mu\text{m}$ -thick nylon/EVOH composite film. The outer LS is 0.1% less dense than the Xe-LS and acts as an active shield for external  $\gamma$  rays and as a detector for internal radiation from the Xe-LS in the IB. The Xe-LS consists of 82% decane and 18% pseudocumene by volume, containing 2.7 g/l of 2,5 diphenyloxazole and 2.5% by weight of enriched xenon gas. The isotopic abundances in the enriched xenon are 90.9%  $^{136}\text{Xe}$  and 8.9%  $^{134}\text{Xe}$ , resulting in about 300 kg of  $^{136}\text{Xe}$  in the IB. The light yield of the Xe-LS is 3% lower than that of the LS. Buffer oil between the OB and the 18 m diameter spherical stainless-steel containment tank shields the liquid scintillator from external radiation. Scintillation light is recorded by 1325 17-inch and 554 20-inch photo-multiplier tubes mounted on the tank to provide 34% solid-angle coverage. The stainless-steel tank is surrounded by a 3.2 kton water-Cherenkov outer detector (OD), which was built by TUNL more than a decade ago.

The visible energy spectrum obtained with KamLAND-Zen contains an unexpected peak at around 2600 keV, most likely coming from metastable  $^{110m}\text{Ag}$ . We recently embarked on

a purification campaign to remove this isotope. This required extracting the xenon from the detector, thus marking the end of the first phase of KamLAND-Zen.

The data collected in this phase [Gan13a] yield the most stringent test to date on the claimed observation of  $0\nu\beta\beta$  decay in  $^{76}\text{Ge}$  [Kla06]. Combining the limits on  $^{136}\text{Xe}$   $0\nu\beta\beta$  decay by KamLAND-Zen and EXO-200 [Aug12], we find that the Majorana mass range expected from the claimed  $^{76}\text{Ge}$   $0\nu\beta\beta$  half-life is excluded at the  $> 97.5\%$  confidence level for a representative range of nuclear-matrix-element estimations. KamLAND-Zen and EXO-200 demonstrate that we have arrived at an exciting new era in the field and that the technology needed to judge the claimed  $^{76}\text{Ge}$   $0\nu\beta\beta$  with other nuclei has been achieved.

The main KamLAND detector is continuing its operation to measure the anti-neutrino flux from reactors and radioactive sources in the earth. The Fukushima accident caused the gradual shut-down of all Japanese nuclear reactors. The resulting lack of reactor anti-neutrinos is providing KamLAND with the opportunity to enhance its sensitivity to detecting terrestrial anti-neutrinos and other rare events, for which the reactor anti-neutrinos are a source of background. A combined three-flavor analysis of solar and KamLAND data gives fit values for the oscillation parameters of  $\Delta m_{21}^2 = (7.53 \pm 0.81) \times 10^{-5}$  eV<sup>2</sup> and  $\sin^2\theta_{13} = 0.023 \pm 0.002$  [Gan13b].

During the reporting period, we also organized a successful three-day KamLAND collaboration meeting in Chapel Hill, attended by about forty collaboration members.

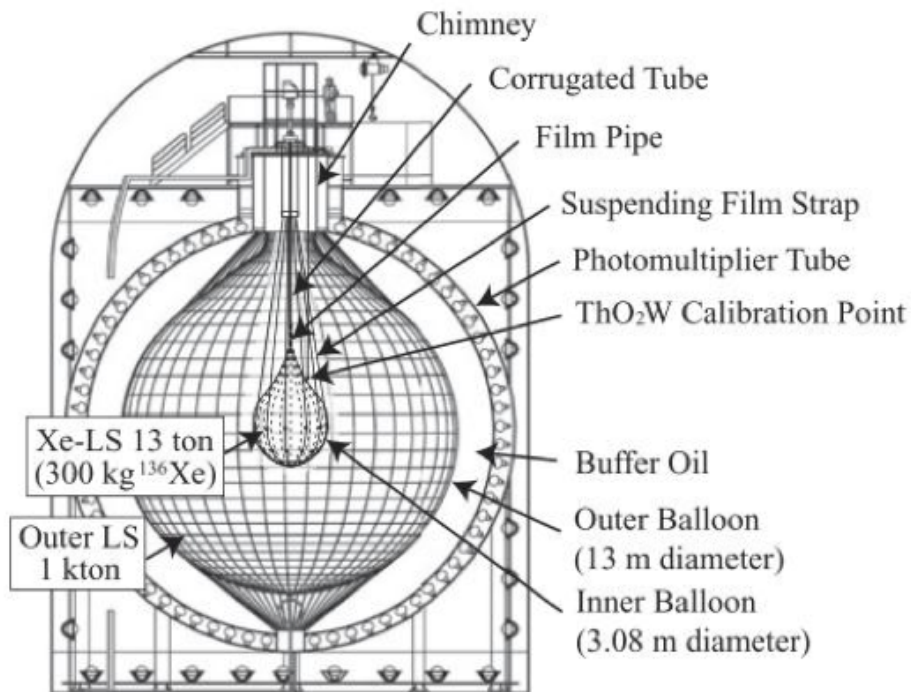


Figure 2.31: Schematic diagram of the KamLAND-Zen detector.

- [Aug12] M. Auger and others (EXO Collaboration), *Phys. Rev. Lett.*, **109**, 032505 (2012).
- [Gan13a] A. Gando and others (KamLAND-Zen Collaboration), *Phys. Rev. Lett.*, **110**, 062502 (2013).
- [Gan13b] A. Gando and others (KamLAND Collaboration), *Phys. Rev. D*, **88**, 033001 (2013).
- [Kla06] H. V. Klapdor-Kleingrothaus and I. V. Krivosheina, *Mod. Phys. Lett. A*, **21**, 1547 (2006).

## 2.2 Tritium $\beta$ Decay

### 2.2.1 Commissioning of the KATRIN Main Spectrometer

F.M. FRÄNKLE, T.J. CORONA, K. WIERMAN, J.F. WILKERSON, *TUNL*;

The KATRIN main spectrometer is a major component of the KATRIN experiment. Its purpose is the precise energy analysis of tritium  $\beta$ -decay electrons. This report provides a short introduction of the working principle of the spectrometer and presents the first results of the commissioning measurements.

#### The KATRIN Main Spectrometer

A major component of the KATRIN experiment [The05] is the main spectrometer (see Fig. 2.32), which is 24 m long and 10 m in diameter. Its purpose is the high-precision energy analysis of tritium  $\beta$ -decay electrons. It features an energy resolution  $\Delta E$  of about 1 eV at 18.6 keV obtained by using the magnetic-adiabatic-collimation-plus-electrostatic-filter (or MAC-E filter) technique.



Figure 2.32: (Color online) The KATRIN main spectrometer and the air coil system.

In general, a MAC-E filter consists of two solenoids which create a strong guiding magnetic field for electrons (see Fig. 2.33). In this configuration the guidance of the electrons from the source to the detector is adiabatic, and the magnetic moment  $\mu$  is constant. Hence, the transverse energy component of the electrons is transformed into longitudinal energy as they move towards the minimum magnetic field  $B_{min}$ . The energy analysis is done with an electrostatic retarding potential at  $B_{min}$  which is created by an electrode system operated on a (variable) scan-

ning potential  $U_0$ . Thus a MAC-E filter acts as an integrating high-pass filter with an energy resolution  $\Delta E$ .

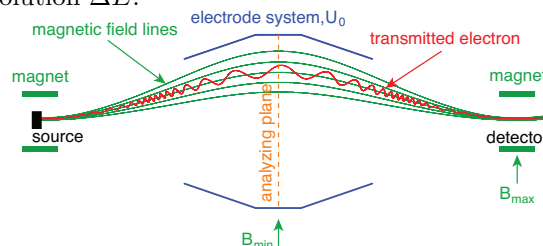


Figure 2.33: (Color online) Schematic of a MAC-E filter with guiding magnetic field lines, source, electrostatic spectrometer and detector.

The background rate of the main spectrometer needs to be less than 0.01 cps to reach the planned KATRIN sensitivity. In order to reach this goal, a MAC-E filter has intrinsic background suppression via magnetic shielding. The KATRIN main spectrometer is additionally equipped with a two-layer inner wire-electrode system that can be operated on a variable electric potential more negative than that of the spectrometer vessel, in order to shield secondary emission electrons.

#### Commissioning Measurements

The KATRIN main spectrometer commissioning measurements started in May 2013. An important aspect of the measurements is the detailed investigation of the spectrometer backgrounds. From previous experiments it is known that there are several processes that can generate background in a MAC-E filter:

- Penning discharge:

Due to the presence of strong magnetic and electric fields in a MAC-E filter, Penning traps can be created. In the event of a Penning discharge, this can lead to high background rates of over 100 cps.

- **Radioactive decays:**  
Radioactive decays, especially radon decays, occurring inside the spectrometer volume can produce a large number of secondary electrons, in particular if a high-energy electron originating from the decay is magnetically trapped inside the spectrometer [Fra11].
- **Magnetic field inhomogeneities:**  
Inhomogeneities of the magnetic field allow the drift of electrons into the volume of the spectrometer.
- **Field Emission:**  
Localized increases of electric fields due to the geometry of the spectrometer or due to surface properties (microscopic tips) can cause field emission.

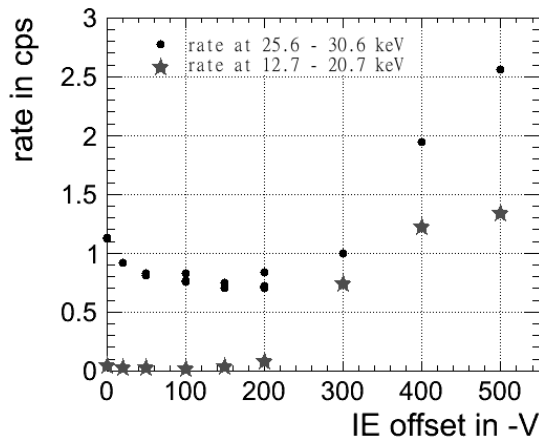


**Figure 2.34:** Background rate as a function of inner electrode voltage for electrons (circle) and  $H^-$  ions (star)

Figure 2.34 shows the rate at the detector as a function of the inner wire electrode (IE) offset voltage while the main spectrometer was kept at about -18.4 kV. A post acceleration electrode

mounted in front of the detector was operated at +10 kV, therefore electrons (black circles) from the main spectrometer arrive in the energy window 25.6 to 30.6 keV (detector energy resolution about 1.9 keV FWHM). The events in the energy window 12.7 to 20.7 keV (stars) are attributed to negative hydrogen ions ( $H^-$ ), which loose about 11 KeV in the 100-nm dead layer of the detector. These ions do not influence the energy window used for the neutrino mass measurements and therefore are of less concern.

The behavior of the electron rate can be explained with three different background components. The increase of rate towards lower IE offset voltages is due to secondary emission electrons which typically have starting energies of less than 50 eV. With increasing IE, the electron rate increases, most likely due to field emission from the wire electrode system. In addition, there is a background component due to magnetically stored electrons that were created in radon decays. This background rate is independent of the IE voltage, since the electrons are generated inside the volume of the spectrometer. Many additional measurements with different settings for the magnetic fields and electric potentials are in good agreement with this picture of the background composition. No evidence of backgrounds related to Penning discharge were found during the measurements.

So far, the commissioning measurements show that the KATRIN main spectrometer background can be explained with the expected background processes. Further measurements are under way to investigate the reduction of radon induced-background via passive (liquid-nitrogen-cooled baffles) and active (magnetic pulses, electric-dipole pulses) counter measures.

[Fra11] F. Fraenkle *et al.*, *Astropart. Phys.*, **35**, 128 (2011).

[KAT05] KATRIN Collaboration, *KATRIN Design Report*, Technical Report FZKA 7090, Forschungszentrum Karlsruhe, 2005.

## 2.2.2 Comparison of Field Calculations to Commissioning Measurements for the KATRIN Experiment

T.J. CORONA, J.F. WILKERSON, *TUNL*

The Karlsruhe Tritium Neutrino, or KATRIN, collaboration commissioned a solenoidal retarding electrostatic spectrometer known as the *main spectrometer*. The spectrometer is the largest of its type in existence and consists of complicated and precisely-defined electrodes that shape the electric potential used to filter electrons. Software has been developed to simulate the electromagnetic fields within the main spectrometer using hybrid parallel computational techniques on GPU-equipped computer clusters.

The Karlsruhe Tritium Neutrino (KATRIN) experiment is a large, international tritium  $\beta$ -decay experiment designed to make a direct, model-independent measurement of the neutrino mass with a sensitivity of  $m_\beta = 0.2$  eV at the 90% confidence level. This is an order of magnitude lower than the current established limit. This sensitivity is predominantly due to the predicted efficacy of KATRIN's main spectrometer (see Fig. 2.35), an integrating, solenoidal, retarding electrostatic spectrometer with a theoretical filter resolution of  $< 1$  eV. The main spectrometer can be described as a magnetic-adiabatic collimation combined with an electrostatic (MAC-E) filter [Pic92].

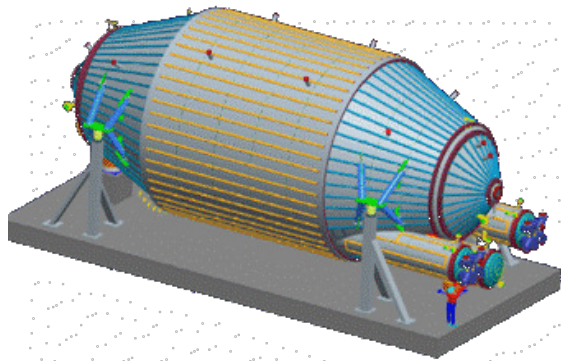


**Figure 2.35:** (Color online) A rendering of the KATRIN main spectrometer. Image taken from [KAT13]

With a maximum diameter of about 10 m and a length of 23.3 m, the KATRIN main spectrometer is the world's largest MAC-E filter [KAT96]. Along the entire inner surface of the spectrometer, there are about two hundred comb-shaped

wire modules, each housing about 100 wires, providing an inner surface area of about 650 m<sup>2</sup>. Additionally, there are superconducting magnets at the entrance and exit of the spectrometer, and many shaping coils and additional current loops to compensate for the earth's magnetic field, in order to precisely shape the magnetic field throughout the spectrometer.

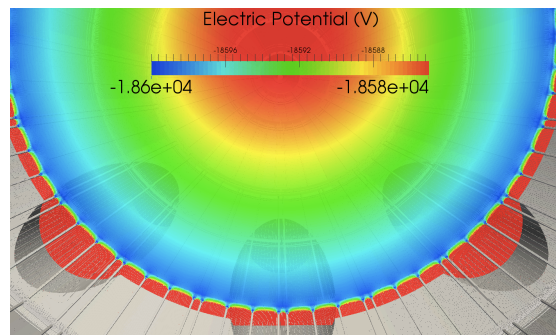


**Figure 2.36:** (Color online) A cross-section of a fully three-dimensional simulation of the electrostatic potential within KATRIN's main spectrometer for a given electrode setting.

Software tools that can precisely calculate electrostatic fields within three-dimensional models of the main spectrometer have been constructed using hybrid parallel computational techniques. These tools employ the boundary element method with Dirichlet and Neumann surface primitives to represent electrodes and dielectric media, respectively. A unique feature of our field computation software is the analytic computation of the Green's functions for rectangles, triangles, and line segments, over which a constant charge density is assumed. This fea-

ture allows us to maximize the utility of a hybrid MPI (message-passing interface) + OpenCL framework by performing these Green's functions on single graphics-processing-unit (GPU) streams [MPI, Ope08]. Additionally, the software can compute magnetostatic fields from axially symmetric superconducting magnets using both direct numerical integration of elliptic integrals [Gar63] and via the zonal-harmonic-expansion technique [Gar51, Glü11]. This software has recently been revised to allow for future development, including the computation of magnetostatic fields, as well as frequency-dependent electromagnetic fields using RWG (Rao-Wilton-Glisson) basis functions [Rao82].

Using this software on the GPU sub-cluster within UNC's Killdevil computing system, models that discretize the surfaces of the main spectrometer into over five million elements can be processed for field solving in just two days, facilitating the computation of multiple electromagnetic configurations with high precision. As a result, it is now possible to simulate particle trajectories through fully three-dimensional models of the main spectrometer. Two examples of simulated electrostatic potentials in different regions of the main spectrometer are shown in Figs. 2.36 and 2.37. The simulation shown in Fig. 2.37 was performed to examine the effect of the vessel wall potential on the electric potential at the analyzing plane. The potential from the vessel can be seen penetrating the wire comb structure in between the wire comb support structure in the main spectrometer.

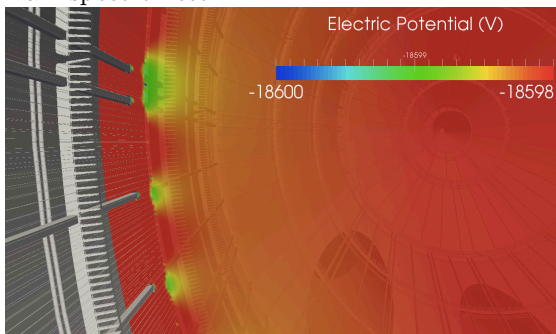


**Figure 2.37:** A close-up of the simulated electrostatic potential near the wire comb support structure, or *C-profiles*, in the main spectrometer.

This summer, the KATRIN collaboration performed several measurements designed to commission the main spectrometer (see Sect. 2.2.1). Results from measurements designed to determine the azimuthal dependence cannot be verified using axially symmetric simulation techniques. One example of a study requiring a fully three-dimensional field calculation is the asymmetric effects of the support structure of the wire modules (colloquially referred to as *C-profiles*). This asymmetry is seen in Fig. 2.37. Ongoing work is designed to verify our simulations against measurement and to further adapt our models to better describe the spectrometer.

- 
- [Gar51] M. Garrett, *J. Appl. Phys.*, **22**, 1091 (1951).
  - [Gar63] M. Garrett, *J. Appl. Phys.*, **34**, 2567 (1963).
  - [Glü11] F. Glück, *Prog. Electromag. Res. B*, **32**, 319 (2011).
  - [KAT96] J. Angrik *et al.*, *KATRIN Design Report 2004*, <http://www-ik.fzk.de/~katrin>, 1996.
  - [KAT13] The KATRIN collaboration, *The KATRIN Homepage*, <http://www.katrin.kit.edu/>, 2013.
  - [MPI] *The Message Passing Interface (MPI) standard Homepage*, <http://www-unix.mcs.anl.gov/mpi/index.htm>.
  - [Ope08] Khronos OpenCL Working Group, *The OpenCL Specification, version 1.0.29*, <http://www.khronos.org/registry/cl/specs/opencl-1.0.29.pdf>, 2008.
  - [Pic92] A. Picard *et al.*, *Nucl. Instrum. Methods*, **B63**, 345 (1992).
  - [Rao82] S. Rao, D. Wilton, and A. Glisson, *IEEE Trans. Antennas Propag.*, **30**, 409 (1982).

### 2.2.3 Characterization of the Muon Veto for the KATRIN Experiment

K.J. WIERMAN, T.J. CORONA, F.M. FRAENKLE, M. HOWE, J.F. WILKERSON, *TUNL*; F. HARMS, A. KOPPMANN, M. STEIDL, S. WUESTLING, *Karlsruhe Institute of Technology, Karlsruhe, Germany*; J. BARRETT, J.A. FORMAGGIO, D.L. FURSE, N.S. OBLATH, *Massachusetts Institute of Technology, Boston, MA*; T.H. BURRITT, P.J. DOE, S. ENOMOTO, G.C. HARPER, E.L. MARTIN, D.S. PARNO, R.G.H. ROBERTSON, T.D. VAN WECHEL, *University of Washington, Seattle, WA*

**In order to achieve the required low background rates, the Karlsruhe Tritium Neutrino Experiment uses a veto system to reject events due to cosmic-ray muons. The veto system was used this year in the characterization of the KATRIN main spectrometer, and studies of its long-term stability and efficiency were carried out.**

The Karlsruhe Tritium Neutrino (KATRIN) Experiment is a model-independent measurement to determine the mass of the neutrino. This is accomplished through the analysis of the spectral shape of the endpoint region of tritium  $\beta$  decay. The measurement uses a next-generation spectrometer that is coupled to a 148-pixel pin-diode array, denoted as the focal-plane detector (FPD) [The05].

Simulations of the detector region show that in order to produce the desired experimental sensitivity, background events must be suppressed to the level of 0.001 counts/sec. Cosmic-ray-induced events contribute a majority of the background events [Leb10], and a veto system is required to reject them.

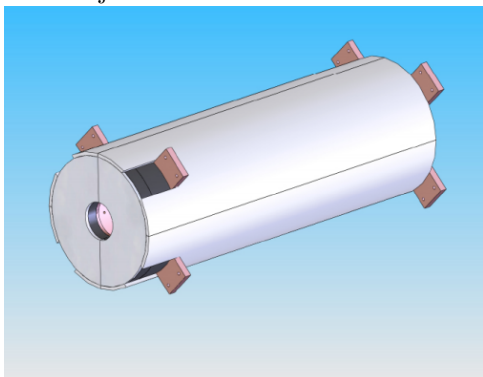


**Figure 2.38:** (Color online) Design drawing of the veto system [Ste07]. The shield is 105 cm long and 14.5 cm in diameter.

The adopted veto system, designed at the Massachusetts Institute for Technology (MIT), consists of a passive 3-cm-thick lead and copper

shield and an active layer of Bicron-408 plastic scintillator panels. Copper was chosen to line the interior of the lead shield due to its relative radio-purity and therefore its ability to absorb lead x-rays, reducing the intrinsic background due to the shield itself. The scintillator panels are formed into a cylinder around the FPD. Figure 2.38 shows how they are split into four long panels that form the barrel and two panels that form the end cap. Each of the long panels is read out by six St. Gobain wavelength-shifting fibers, while the end caps are read out by four fibers [For09].

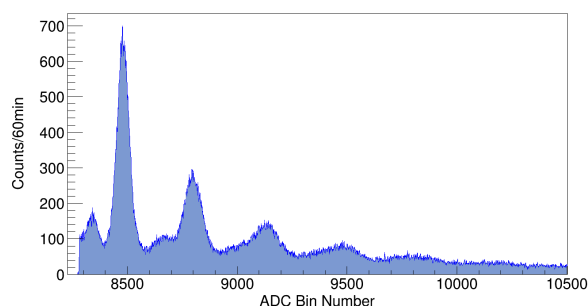


**Figure 2.39:** (Color online) Discretized output of the MPPCs. Each peak represents the number of photons impinging on the face of the detector.

The light-detection mechanism for the veto system is an array of thirty-two Hamamatsu Mult-Pixel Photon Counters (MPPCs). These devices consist of a pixelated array of avalanche photo diodes with reverse bias voltage held in the Geiger regime. Simultaneous discharge of pixels due to photonic excitations allows for integrally

discretized signals that indicate the number of photons incident on the detector. Sample output from the MPPCs is shown in Fig. 2.39. Additionally, the insensitivity of the devices to magnetic fields is required for integration into KATRIN, due to the magneto-static filtering utilized by the spectrometers.

Electronics for amplification and the provision of bias voltages for the MPPC units, as well as digitization of the output pulses, were designed at the Karlsruhe Institute of Technology (KIT). The data acquisition hardware was also designed at KIT. It consists of a DAQ crate containing twenty first-level-trigger cards, each with twenty-four input channels. Each card contains field-programmable gate arrays (FPGAs) that allow for the customization of input filtering and processing as needed for the specifications of detector outputs. Signals are processed by the DAQ crate at 20 Mhz, which pushes the Nyquist limit of the MPPC 50 ns signal width of the MPPC. TUNL personnel identified and implemented an FPGA scheme which optimizes detection efficiency of the signals [Wie13].

The veto system was initially delivered to the University of Washington for detector commissioning. After improvements were made by TUNL personnel in the stability of the electronics, the system was delivered to KIT in August 2011. Further revisions in detection efficiency were made by TUNL personnel at KIT, and the system was characterized. The system was recently used in commissioning the KATRIN main spectrometer.

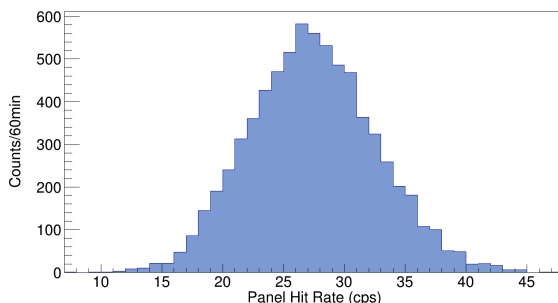


**Figure 2.40:** Sample histogram of muon rates for a single scintillation panel. Rates are binned in 1 sec intervals and histogrammed over a one hour period.

In order to reduce thermally induced excitations, the MPPCs are cooled to  $-18^{\circ}\text{C}$  using parallel Peltier cooling devices and a chilled-water system. TUNL personnel worked with MIT and KIT students to perform a study of the rates and spectral stability as a function of time to deter-

mine the long-term stability of the system (see Fig. 2.40). They have determined that the system is consistent with statistical fluctuations for the commissioning of the detector system.

**Table 2.4:** The measured efficiencies for each panel.

Panel# (Type)	Efficiency (%)	Error (%)
6(Long)	91.80	0.49
1(Long)	84.21	1.09
2(Long)	96.45	3.01
8(Long)	94.57	2.66
8(End)	98.10	0.01
6(End)	98.75	0.0001

System efficiency was measured by stacking panels in a hodoscope-style configuration. Coincident-event comparison between panels provided a first order estimation of the efficiency of the individual panels, as shown in Table 2.4. The efficiencies were studied as a function of the coincidence window between fibers in a given panel and the coincidence window between panels. The DAQ-crate FPGAs require that the coincidence time between MPPCs can be adjusted in 50-ns increments, and they provide a signal indicating that a single panel has been hit by a muon. Additionally, the DAQ logic can require how many fibers are required to fire simultaneously for a panel-wide event. For each of the four long panels and two end-cap panels, the available coincidence conditions were tested in the efficiency setup. Using the FPD as a comparison for the muon veto, a preliminary total system efficiency is projected at  $94.2 \pm 0.51\%$ .

- [For09] J. Formaggio, *Test Plans for the KATRIN active and passive shield*, Technical report, Massachusetts Institute of Technology, 2009.
- [Leb10] M. L. Leber, *Monte Carlo Calculations of the Intrinsic Detector Backgrounds for the Karlsruhe Tritium Neutrino Experiment*, Proquest, Umi Dissertation Publishing, 2010.
- [Ste07] M. Steidl *et al.*, *KATRIN detector design document*, Technical report, University of Washington, 2007.
- [The05] The KATRIN Collaboration, *KATRIN Design Report*, Technical Report 7090, FZKA, 2005.
- [Wie13] K. Wierman, Master's thesis, University of North Carolina, Chapel Hill, Department of Physics and Astronomy, 2013.



# Nuclear Astrophysics

---

Chapter 3

- Nucleosynthesis in Hydrostatic and Explosive Environments
- Thermonuclear Reaction Rates

## 3.1 Nucleosynthesis in Hydrostatic and Explosive Environments

### 3.1.1 The $^{14}\text{N}(p,\gamma)^{15}\text{O}$ Reaction at Low Stellar Energies

S. DAIGLE, M.Q. BUCKNER, K.J. KELLY, C. HOWARD, A.E. CHAMPAGNE, C. ILIADIS, *TUNL*

**We report on a proof-of-principle measurement of the  $^{14}\text{N}(p,\gamma)^{15}\text{O}$  reaction using a position-sensitive NaI array.**

All stars produce energy via the CN cycle, either during or at the end of their main-sequence lifetimes, or while on the red-giant branch. At the burning temperatures characteristic of these evolutionary stages, the  $^{14}\text{N}(p,\gamma)^{15}\text{O}$  reaction is the slowest in the cycle and thus regulates the rate of energy generation. As a result, it impacts several areas of stellar structure and evolution, including ages derived for globular clusters, and nucleosynthesis in red giants and novae. The ground-state transition in  $^{14}\text{N}(p,\gamma)^{15}\text{O}$  comprises 9 to 27% of the S-factor at zero energy but is still rather poorly constrained by experiment, in part because of a complicated reaction mechanism. The low-energy S-factor features a relatively weak resonance at  $E_r^{cm} = 259$  keV and a prominent interference dip arising from a subthreshold resonance at  $E_r^{cm} = -504$  keV, which interferes with higher-lying resonances. In addition, the existing low-energy data were taken with HPGe detectors in close geometry, and hence coincident-summing corrections were significant and represented the limiting factor on precision. A recent, multi-channel R-matrix analysis of  $^{14}\text{N} + p$  that includes new  $^{14}\text{N}(p,p)^{14}\text{N}$  data [Ber10] yields an S-factor for the ground-state that is significantly higher than that obtained from the capture data alone [Ade11].

In an effort to clarify the contribution of the ground-state transition to the total S-factor, we have performed a new measurement of the  $^{14}\text{N}(p,\gamma)^{15}\text{O}$  reaction using an APEX NaI detector. The detector, which is on loan from Argonne National Laboratory, is a cylindrical array of twenty-four 55-cm-long, position-sensitive NaI(Tl) crystals [Kal93]. With the addition of new spectroscopy-grade photomultiplier tubes, the energy resolution is 14%, and the position resolution is 3.5 cm (both FWHM). By requir-

ing that only one detector fires, the full-energy peak for the ground-state transition can be measured with only insignificant summing corrections. Thus, we sacrifice energy resolution for efficiency and insensitivity to summing. The performance of the APEX detector has been thoroughly simulated using GEANT4 [Ago03], and the predicted efficiency agrees very well with measurements. The ability to model the individual components of the measured spectrum is an important part of data reduction, as described below. The position sensitivity was measured using a collimated  $^{60}\text{Co}$  source.

We performed initial measurements using the JN accelerator at  $E_p = 214, 236,$  and  $257$  keV, corresponding to effective center-of-mass energies of  $E_{\text{eff}} = 195, 216,$  and  $235$  keV, respectively. The energy region near the full-energy peak of the ground-state transition is dominated by secondary  $\gamma$ -rays from direct capture into the states of  $^{15}\text{O}$  at 5.183, 6.176, and 6.793 MeV and by cosmic-ray-induced background. Since these lines are members of two-photon cascades, a requirement that precisely two separate detectors fire for an event to be considered valid isolated these transitions.

The comparatively poor resolution of NaI made it difficult to derive decay strengths by integrating the full-energy peaks, so a more sophisticated analysis scheme was employed. Since the GEANT4 simulations of the APEX detector were able to accurately reproduce its performance, the simulations were used to generate spectra for the individual transitions in  $^{15}\text{O}$ . Background measurements with no beam served as a template for the background component of the spectrum. The simulated and measured spectra became probability-density functions for a fitting procedure in which the normalizations of the simulated

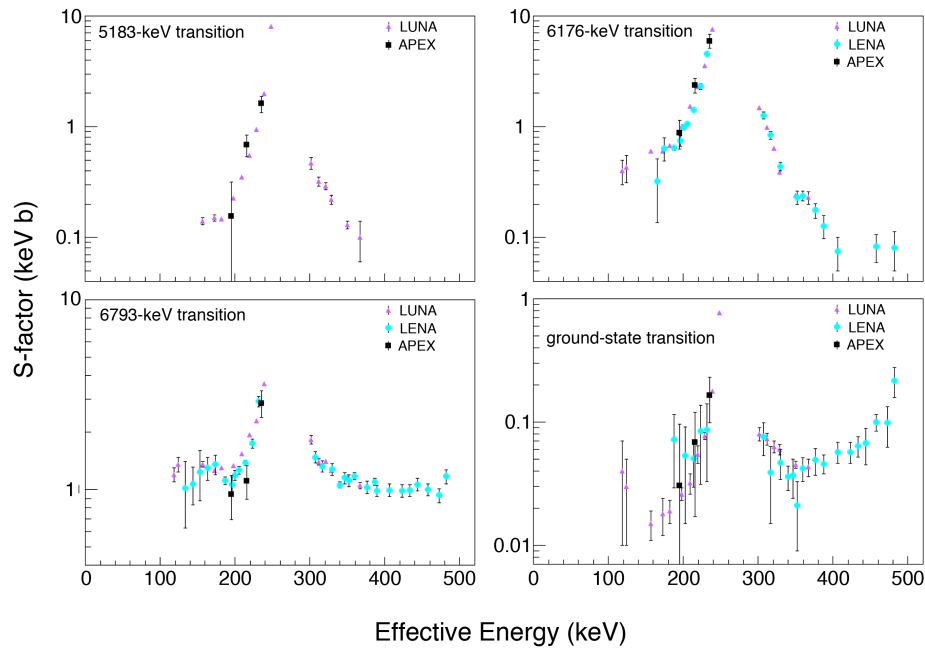


Figure 3.1: (Color online) S-factor data for the major transitions in the  $^{14}\text{N}(p,\gamma)^{15}\text{O}$  reaction. Previous results from LUNA [Imb05] and LENA [Run05] are also shown. Present results, labeled apex, are denoted by the black data points.

spectra (including Compton events) and background were varied in order to best fit the measured spectrum. This procedure was validated using data collected for the 259-keV resonance, where the individual branching ratios are well known. A multiplicity-one condition was used to extract the strength of the ground-state transition, while the multiplicity-two fits were used to constrain the strengths of the lines at 5.183, 6.176, and 6.793 MeV, which also appeared in the multiplicity-one spectra.

The resulting astrophysical S-factors are shown in Fig 3.1. The uncertainties, which include systematic uncertainties associated with the fitting procedure, detector efficiency, target thickness, and beam-current integration, are dominated by counting statistics. The position sensitivity of the APEX detector could also be used to measure the angular correlations of the 2-photon cascades. This information is of interest because summing corrections usually assume no angular correlations. Angular-correlations were measured for the largest decay branches of the 259-keV resonance and agree well with theoretical predictions. Unfortunately, because of poor statistics it was only possible to extract an off-resonance angular correlation for the direct-capture  $\rightarrow 6176\text{keV} \rightarrow 0$  transition at  $E_{\text{eff}} = 235$  keV, and even here the data quality is insufficient to yield an accurate correlation coefficient. Nonetheless, the extracted  $a_2 = -0.2$  implies

that the summing corrections in this energy region are overestimated by 8% if it is assumed that there is no angular correlation.

Because of counting-statistics limitations, these measurements can only demonstrate the utility of the APEX detector for measurements of the  $^{14}\text{N}(p,\gamma)^{15}\text{O}$  reaction. Further progress will require a cleaner target, such as a windowless gas target, and better shielding to reduce cosmic-ray-induced backgrounds. Better shielding coupled with the high beam currents produced by the electron-cyclotron-resonance ion source will permit a measurement of the ground-state transition in the region of the interference minimum.

- 
- [Ade11] E. G. Adelberger *et al.*, Rev. Mod. Phys., **83**, 195 (2011).  
 [Ago03] S. Agostinelli *et al.*, Nucl. Instrum. Methods A, **506**, 250 (2003).  
 [Ber10] P. Bertone, Ph.D. thesis, University of North Carolina at Chapel Hill, 2010.  
 [Imb05] G. Imbriani *et al.*, Eur. Phys. J. A, **25**, 455 (2005).  
 [Kal93] N. Kaloskakis *et al.*, Nucl. Instrum. Methods A, **330**, 447 (1993).  
 [Run05] R. C. Runkle *et al.*, Phys. Rev. Lett., **94**, 082503 (2005).

### 3.1.2 The $^{23}\text{Na}(p,\gamma)^{24}\text{Mg}$ Reaction and Sodium in AGB Stars

A.E. CHAMPAGNE, *TUNL*

**We have performed Monte Carlo network calculations to explore the influence of our new rate for the  $^{23}\text{Na}(p,\gamma)^{24}\text{Mg}$  reaction on the nucleosynthesis of sodium in AGB stars.**

The abundance of sodium in globular clusters is a long-standing puzzle that may reveal information about the history of star formation within the cluster. Every well-studied globular cluster shows star-to-star abundance variations for light elements (C, N, O, Na, Mg, and Al) with correlations between Na and Al and anti-correlations between O and Na and between Mg and Al [Gra04]. One possible source of these anomalous variations is massive asymptotic giant branch (AGB) stars [Ven01, D’A02, Den03].

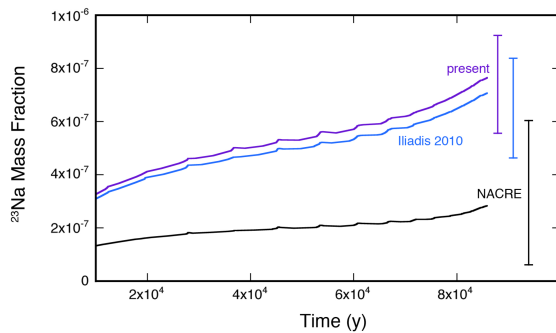


**Figure 3.2:** (Color online) The calculated evolution of  $^{23}\text{Na}$  at the base of the convective envelope during AGB evolution. The error bars show the 16%–84% uncertainty in the final abundance.

We have recently measured a resonance strength  $\omega\gamma_{\text{UL}} \leq 5.17 \times 10^{-9}$  eV (with indications of a signal at the 90% confidence level) for the  $E_{\text{cm}} = 138$  keV resonance in the  $^{23}\text{Na}(p,\gamma)^{24}\text{Mg}$  reaction, and new reaction rates have been calculated for both this and the  $^{23}\text{Na}(p,\alpha)^{20}\text{Ne}$  reaction. To explore the influence of these new rates on sodium production, we have performed one-zone post-processing calculations using a  $5 M_{\odot}$ ,  $Z \sim 10^{-3}$  AGB model from Ventura and D’Antona [Ven05, Ven13]. The calculations used the temperature-density profile at the base of the convective envelope and did not include any mixing between thermal pulses. Con-

sequently, they are not meant to represent observable surface abundances, but merely to show the effect of the present results at the base of the convective envelope. The time evolution of  $^{23}\text{Na}$  is shown in Fig. 3.2, which follows from the beginning of the thermal-pulsing stage (at  $t = 0$ ) through to the end of last pulse. Reaction rates were taken from the STARLIB compilation [Sal13] with the exception of the rates for the  $^{23}\text{Na}(p,\gamma)^{24}\text{Mg}$  and  $^{23}\text{Na}(p,\alpha)^{20}\text{Ne}$  reactions. In addition to the present results for these reactions, we have also taken rates from Refs. [Ili10] and [Ang99]. The uncertainties in the final abundances, assuming a 68% coverage probability, were calculated using a Monte Carlo procedure [Lon12] in which the rates for all 1657 reactions in the network were sampled simultaneously and independently by introducing a variation factor  $p_i$  for each reaction. This factor is a randomly sampled multiplier of the log-normal standard deviation for each reaction [Lon12, Sal13]. Results were obtained from 1,000 samples of each of the three reaction networks.

Figure 3.2 shows that the current, significant reduction in the  $^{23}\text{Na}(p,\gamma)^{24}\text{Mg}$  rate leads to increased  $^{23}\text{Na}$  production, as would be expected, but by a statistically insignificant 13% over what was expected from the rates in Ref. [Ili10]. On the other hand, the final  $^{23}\text{Na}$  abundance is about 2.5 times greater than that calculated using the NACRE rates [Ang99]. The uncertainties shown in Fig. 3.2 arise from all of the reaction-rate uncertainties in the reaction network, and clearly the reduction in the uncertainty of the  $^{23}\text{Na}(p,\gamma)^{24}\text{Mg}$  reaction over the rate in Ref. [Ili10] does not produce a commensurate reduction in the uncertainty of the final abundance. Other reactions are important.

Fig. 3.3 shows the correlation between the final  $^{23}\text{Na}$  abundance and the rates of the key reactions that determine that abundance, expressed in terms of the variation factor  $p_i$  for each reac-

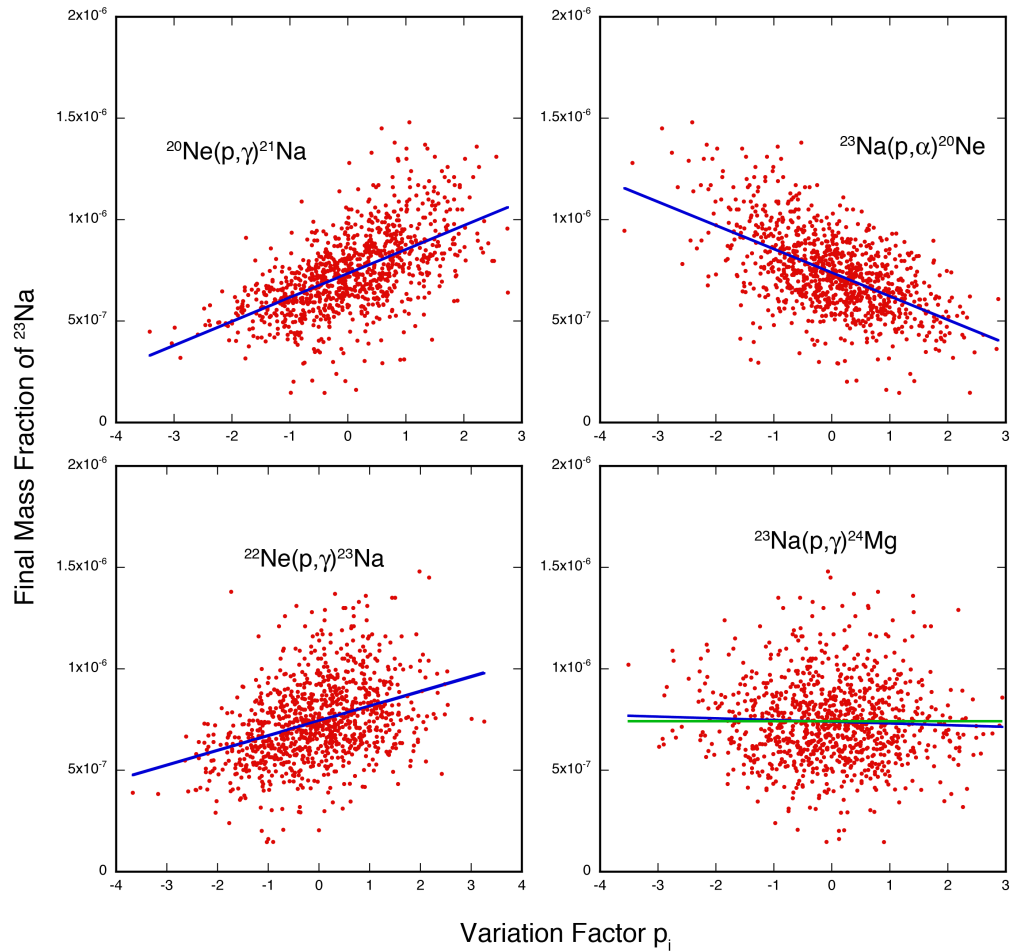


**Figure 3.3:** (Color online) Correlations between the final abundance of  $^{23}\text{Na}$  and the rate-variation factor  $p_i$  for each of the 1,000 samples of the reaction network. The sloped lines are linear fits to the correlations. For  $^{23}\text{Na}(p,\gamma)^{24}\text{Mg}$ , the horizontal line would be consistent with no correlation.

tion. Clearly, the reactions that have the largest impact on the  $^{23}\text{Na}$  abundance are (in order of the slope of the correlation)  $^{20}\text{Ne}(p,\gamma)^{21}\text{Na}$ ,  $^{23}\text{Na}(p,\alpha)^{20}\text{Ne}$  and  $^{22}\text{Ne}(p,\gamma)^{23}\text{Na}$ . In contrast, the  $^{23}\text{Na}(p,\gamma)^{24}\text{Mg}$  reaction has negligible impact on the  $^{23}\text{Na}$  abundance. These results have been submitted for publication.

[Ang99] C. Angulo *et al.*, Nucl. Phys., **A656**, 3 (1999).

[D'A02] F. D'Antona *et al.*, Astron. Astrophys., **395**, 69 (2002).

[Den03] P. Denissenkov and F. Herwig, Astrophys. J. Lett., **590**, L99 (2003).

[Gra04] R. Gratton, C. Sneden, and E. Carretta, Ann. Rev. Astron. Astr., **42**, 385 (2004).

[Ili10] C. Iliadis *et al.*, Nucl. Phys., **A841**, 31 (2010).

[Lon12] R. Longland, Astron. Astrophys., **548**, A30 (2012).

[Sal13] A. L. Salaska *et al.*, Astrophys. J. Suppl., **207**, 18 (2013).

[Ven01] P. Ventura *et al.*, Astrophys. J. Lett., **550**, L65 (2001).

[Ven05] P. Ventura and F. D'Antona, Astron. Astrophys., **431**, 279 (2005).

[Ven13] P. Ventura, private communication, 2013.

### 3.1.3 Nuclear Mixing Meters for Classical Novae

K.J. KELLY, C. ILIADIS, L.N. DOWNEN, A.E. CHAMPAGNE, *TUNL*

**Observations of classical novae indicate the existence of a mixing event between the solar accreted material and the outer layers of the underlying white dwarf. Ratios of ejected elemental abundances from hydrodynamic simulations of ONe novae were investigated for sensitivity to the mixing fraction and peak nova-burning temperature, and a set of five elemental ratios were identified as useful mixing meters. These meters are robust against current nuclear-physics uncertainties and reveal a mixing fraction of 25% or lower in ONe novae.**

Classical novae result from the accretion of solar, hydrogen-rich matter from a main-sequence star onto the surface of a nearby white-dwarf partner, where it burns under degenerate conditions in a thermonuclear runaway [Sta72, Pri78]. Observations of novae imply that white-dwarf matter is mixed into the burning region prior to thermonuclear runaway, but the mechanism by which this occurs is still not understood.

Thus, the purpose of this work is to identify a set of elemental ratios of ejected material from novae that vary strongly with the mixing fraction (i.e. the total amount of mixing that has occurred in a nova) while showing minimal variation with respect to the peak nova-burning temperature. These ratios are referred to as mixing meters. Since the peak nova-burning temperature is closely related to the underlying white dwarf mass, these meters allow for an identification of the mixing fraction achieved in observed novae irrespective of the underlying white dwarf mass.

Mixing meters were identified by analyzing elemental abundances of ejected material from a set of twelve hydrodynamic ONe-nova simulations performed with the code SHIVA [Jos98]. These simulations were created from combinations of four white-dwarf-mass values (1.15, 1.25, 1.30, and 1.35  $M_{\odot}$ ) and three mixing fractions (25%, 50%, and 75%) used as input parameters. The mixing fraction is defined as the percent white-dwarf material, by mass, in the burning region prior to thermonuclear runaway. From this study, five mixing meters were identified in  $\Sigma\text{CNO}/\text{H}$ ,  $\text{Ne}/\text{H}$ ,  $\text{Mg}/\text{H}$ ,  $\text{Al}/\text{H}$ , and  $\text{Si}/\text{H}$ .

Reaction rates used for these simulations were taken from the recommended rates of the STARLIB reaction-rate library [Sal13]. These recom-

mended rates are derived from the 50th percentile of the rate probability-density function (PDF) provided for each reaction [Lon10, Ili10]. The rate PDF's are convenient for a Monte Carlo rate-variation procedure [Lon12] in which all reactions rates are randomly sampled according to their corresponding PDF's for each sequential simulation in a single Monte-Carlo calculation. The end result is a distribution of abundances for each elemental ratio, the spread of which is indicative of the uncertainties in the reaction rates leading to the final abundances of each ratio [Lon12].

Currently, hydrodynamic simulations of novae are very time consuming. Therefore, it is not feasible to carry out the thousands of sequential computations needed for a Monte Carlo calculation within the hydrodynamic models. Instead, the temperature and density evolution profile of each hydrodynamic simulation is extracted and used as input for post-processing calculations of the expected nucleosynthesis resulting from those profiles. Two approximations for convection within the burning region are employed and reproduce the hydrodynamic nucleosynthetic to within a factor of two. These calculations take minutes, as opposed to the weeks required for a single hydrodynamic simulation.

Monte Carlo post-processing calculations with one thousand sequential runs were carried out for both approximations used to match hydrodynamic results for each of the twelve hydrodynamic models considered, yielding twenty-four thousand total post-processing calculations. Monte Carlo calculations with ten thousand sequential runs yielded results identical with these to within 5%. An example of the resulting distribution for the  $\text{Ne}/\text{H}$  ratio from a hydrodynamic simulation with a 1.30  $M_{\odot}$  white dwarf and a

25% mixing fraction is shown in Fig. 3.4. Low, median, and high ratio values of each mixing meter are derived from the 16<sup>th</sup>, 50<sup>th</sup>, and 84<sup>th</sup> percentiles of the corresponding cumulative distribution function. This spread in meter value indicates the impact of current nuclear-physics uncertainties on that particular meter.

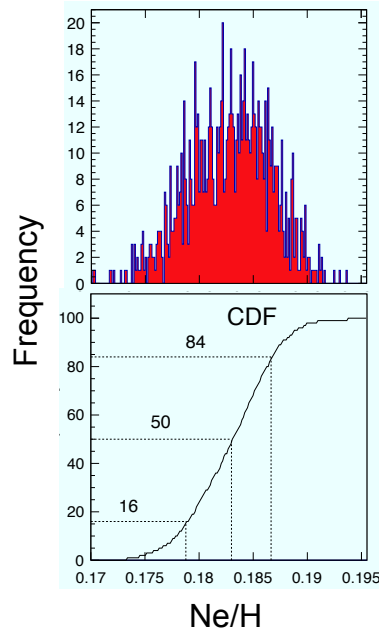


Figure 3.4: An example of a calculated mixing-meter abundance distribution (top) and the corresponding cumulative distribution function (bottom).

Final results for the mixing meters are shown in Fig. 3.5. The error bars represent the spread in mixing-meter elemental-abundance values due to peak-temperature variations and to nuclear-physics uncertainties. Clearly, since no error bars intersect for any mixing meters, these results are robust against current nuclear-physics uncertainties.

Comparisons to observations of ONe novae reveal that a 25% or lower mixing fraction is common. This result contrasts with the 50% mixing fraction that is usually taken as representative of novae [Pol95, Jos98, Smi02]. An article describing this research was recently published in *Astrophysical Journal* [Kel13]. Further research, either confirming this result or providing evidence otherwise, would be very interesting for future

studies of classical novae.

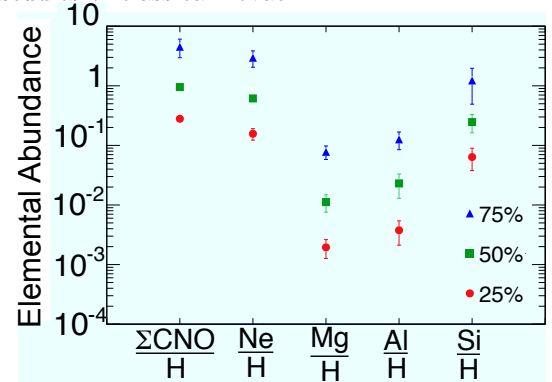


Figure 3.5: (Color Online) Final results for the five mixing meters identified in this work. Different data points represent the different mixing fractions used. Error bars represent variations in elemental abundance with respect to peak temperature with all nuclear-physics uncertainties included.

- 
- [Ili10] C. Iliadis *et al.*, *Nucl. Phys.*, **A841**, 31 (2010).
  - [Jos98] J. José and M. Hernanz, *Astrophys. J.*, **494**, 680 (1998).
  - [Kel13] K. J. Kelly *et al.*, *Astrophys. J.*, **777**, 130 (2013).
  - [Lon10] R. Longland *et al.*, *Nucl. Phys.*, **A841**, 1 (2010).
  - [Lon12] R. Longland, *Astron. Astrophys.*, **548**, A30 (2012).
  - [Pol95] M. Politano *et al.*, *Astrophys. J.*, **448**, 807 (1995).
  - [Pri78] D. Prialnik, M. M. Shara, and G. Shaviv, *Astron. Astrophys.*, **62**, 339 (1978).
  - [Sal13] A. Sallaska *et al.*, *Astrophys. J. Suppl. Ser.*, **207**, 18 (2013).
  - [Smi02] M. S. Smith *et al.*, In *Proceedings of the International Conference on Classical Nova Explosions*, eds. M. Hernanz and J. José, p. 161. American Institute of Physics, 2002.
  - [Sta72] S. Starrfield *et al.*, *Astrophys. J.*, **176**, 169 (1972).

## 3.2 Thermonuclear Reaction Rates

### 3.2.1 Relative Monte Carlo Reaction-Rate Contributions

R. LONGLAND, C. ILIADIS, *TUNL*

**Reaction rates of interacting nuclei in stellar environments can often be calculated by the coherent sum of individual resonant and non-resonant contributions. We report on an effort to extend the `RATESMC` Monte Carlo code to compute the relative contributions of individual resonances to the total reaction rate. An automated script has been developed to produce publication-ready plots to aid in experiment planning.**

Thermonuclear reaction rates describe the rate at which material is burned in stellar environments and are thus an essential ingredient of astrophysical models. These rates are temperature-dependent quantities computed from the convolution of nuclear reaction cross sections with particle energies described by the Maxwell-Boltzmann distribution. At astrophysically interesting temperatures, these rates are frequently uncertain, owing to uncertainties in nuclear reaction properties.

Prior to developing, proposing, and performing experiments to precisely measure reaction cross sections, it is beneficial to characterize the reaction rate uncertainty using present data. A Monte Carlo method for propagating uncertainties in nuclear physics quantities through to reaction rates was developed [Lon10]. It provides temperature-dependent reaction-rate uncertainties, which can be used in stellar models to identify reactions whose cross sections should be further constrained (see Sect. 3.1.2 for an example of this). However, once a reaction has been identified in this way, the nuclear properties that should be constrained (i.e., the resonances that contribute most to the rate in the temperature region of interest) are not easily identifiable. Here, we report on an extension to the `RATESMC` code that provides this information. This is coupled to an automated script to generate publication-ready figures to present this information in a visual form.

#### 3.2.1.1 Reaction Rate Calculations

Full details on calculating reaction rates from cross sections are available in Ref. [Ili07]. Here, for clarity, we summarize the simple case of cal-

culating a reaction rate from a cross section dominated by narrow resonances. The reaction rate per particle-pair is

$$\langle\sigma v\rangle = \left(\frac{2\pi}{\mu kT}\right)^{3/2} \hbar^2 \sum_n \omega\gamma_n e^{-E_{r,n}/kT}, \quad (3.1)$$

where  $\mu$  is the reduced mass,  $k$  is the Boltzmann constant,  $T$  is the temperature in the astrophysical environment, and  $\omega\gamma_n$  is the resonance strength of the  $n$ -th resonance at energy  $E_{r,n}$ .

Note that in this narrow-resonance case, the total reaction rate is given by a coherent sum over individual resonant contributions. In fact, this assumption of coherence is valid for many reaction rates involving wide, Breit-Wigner resonances and is key to calculating the rates presented in Ref. [Ili10]. In that evaluation, a Monte Carlo method was developed to evaluate reaction rates and their uncertainties in the  $A = 14$  to 40 region. The foundation of the method was in finding statistically realistic probability density functions (PDFs) to describe the uncertainties in nuclear physics inputs to the code, thus yielding the most accurate reaction rate uncertainties to date. The Monte Carlo method itself is trivial: (i) sample every input parameter according to its PDF, (ii) calculate a sample reaction rate, being careful to correctly propagate quantities like energy through the entire calculation, (iii) repeat steps (i) and (ii) many times, and (iv) analyze the final distribution of reaction rate samples to find temperature-dependent descriptive statistics. In Ref. [Ili10], median reaction rates and their associated factor uncertainties are presented, and were found to describe the rate PDFs well.

### 3.2.1.2 Monte Carlo Contributions

The Monte Carlo method has opened up a host of opportunities for evaluating the effects of rate uncertainties on nucleosynthesis. Examples of using the statistically realistic rate PDFs discussed above are shown in Ref. [Sal13]. However, there was previously no functionality in the RATESMC code to determine which resonances contribute most to the rate at the temperatures of interest.

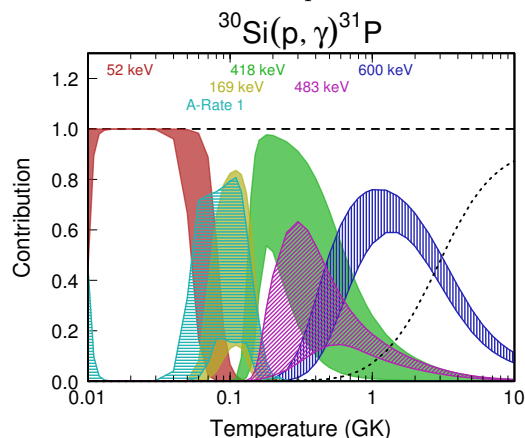


**Figure 3.6:** (Color online) Relative reaction rate contributions for the  $^{30}\text{Si}(p,\gamma)^{31}\text{P}$  reaction. Labels for each contributing resonance are displayed above each curve. ‘A-Rate’ denotes the non-resonant analytical rate.

Functionality has now been added to RATESMC to calculate the relative contribution of every resonance to the total rate for every rate sample in step (ii) above. Performing the calculation in this way yields a PDF of resonance contributions that can be analyzed in step (iv) above. The result of this added functionality is a new output file of low, median, and high contributions for each resonance at each temperature considered in the calculation, where the low and high contributions represent  $1 - \sigma$  uncertainties. A separate analysis code has been developed to read this (sometimes very large) file and automatically produce figures. The automated production script is written to maximize contrast between overlapping contribution bands by automatically picking colors and computing overlap factors to apply hatching if necessary. This automation is necessary owing to the large number of reaction rates analyzed in Ref. [Ili10]. Examples of such graphs can be seen in Figs. 3.6 and 3.7.

Figure 3.6, for example, shows that for the  $^{30}\text{Si}(p,\gamma)^{31}\text{P}$  reaction, the analytical rate (i.e. the

reaction rate arising from non-resonant contributions) and the 169-keV resonance dominate the rate at  $T = 0.1$  GK, but their relative contributions cannot be known to good precision because of large nuclear physics uncertainties. These properties should therefore be the focus of any experimental study to reduce nucleosynthesis uncertainties arising from this reaction. On the other hand, despite the poorly measured 224-keV resonance causing a factor of 10 uncertainty in the rate around 0.06 GK, Fig. 3.7 shows that it always dominates the rate between 0.04 and 0.5 GK regardless of the actual value of its cross section. This case serves to highlight that care must be taken in interpreting relative rate contributions and that these contributions should be used in combination with total reaction rate uncertainties.

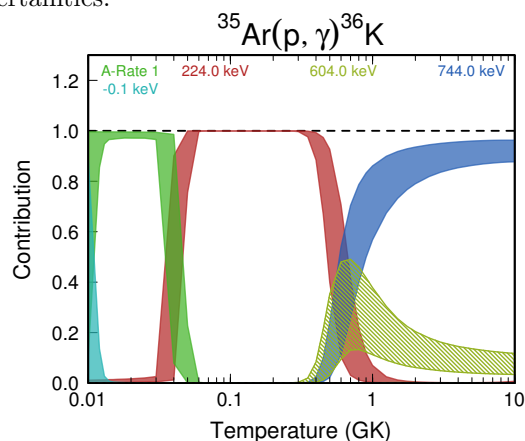


**Figure 3.7:** (Color online) Relative reaction rate contributions for the  $^{35}\text{At}(p,\gamma)^{36}\text{K}$  reaction.

Monte Carlo rate contributions will be computed and plotted for the list of reactions included in Ref. [Ili10]. This information will be useful as an additional tool in planning nuclear astrophysics experiments and will help insure that experiments target astrophysically important quantities.

[Ili07] C. Iliadis, *Nuclear Physics of Stars*, Wiley-VCH, 2007.

[Ili10] C. Iliadis *et al.*, Nucl. Phys., **A841**, 31 (2010).

[Lon10] R. Longland *et al.*, Nucl. Phys., **A841**, 1 (2010).

[Sal13] A. L. Sallaska *et al.*, Astrophys. J. Supl. Ser., **207**, 18 (2013).

### 3.2.2 Mean Proton and $\alpha$ -Particle Reduced Widths of the Porter-Thomas Distribution and Astrophysical Applications

C. ILIADIS, I. POGREBNYAK, C. HOWARD, G.E. MITCHELL, R. LONGLAND, *TUNL*;

**The Porter-Thomas distribution is of crucial importance for estimates of thermonuclear reaction rates, where the contributions of certain unobserved resonances to the total reaction rate need to be taken into account. We derived mean-reduced-width values for protons and  $\alpha$  particles of compound nuclei in the  $A = 28$ – $67$  mass range and estimated improved stellar rates for the  $^{40}\text{Ca}(\alpha,\gamma)^{44}\text{Ti}$  reaction.**

The statistical theory of nuclear reactions assumes that the reduced width amplitude for formation or decay of an excited compound nucleus is a random variable, with many small contributions from different parts of configuration space. If the contributing nuclear matrix elements are random in magnitude and sign, then the reduced width amplitude is represented by a Gaussian probability density centered at zero, according to the central limit theorem of statistics. Consequently, the corresponding reduced width (i.e., the square of the amplitude) is described by a chi-squared probability density with one degree of freedom. The latter distribution was proposed by Porter and Thomas [Por56] in the 1950s and has been shown to be a key prediction of the Gaussian orthogonal ensemble in random matrix theory. The validity of the Porter-Thomas distribution for neutron and charged-particle reduced widths has been well established over many decades of experimental and theoretical research, and claims to the contrary have always been debated extensively.

The Porter-Thomas distribution is also of crucial importance for nuclear applications. It has recently been shown [Lon10] to impact estimates of thermonuclear reaction rates in situations where the contributions of unobserved resonances to the total reaction rate need to be taken into account. In particular, for estimating such reaction-rate contributions by randomly sampling over the Porter-Thomas distribution, the mean value of the reduced width must be known. Unfortunately, mean reduced width values are usually not reported in the literature. A first attempt at extracting this information from existing proton-elastic-scattering and  $(p,\alpha)$  reaction data for application to nuclear astrophysics

was reported in Ref. [Lon10]. However, the data set analyzed in that work was relatively small, and therefore those results should be considered only as preliminary. In the present work, we re-analyzed a more extensive data set for  $A = 28$ – $67$  target nuclei. Our results are summarized below.

For  $\alpha$ -particles, we analyzed eleven level sequences in the  $A = 28$ – $40$  range and find that the extracted mean reduced width values depend only weakly on mass number. If we combine all level sequences, regardless of mass number  $A$  and spin-parity  $J^\pi$ , into one set, a value of  $\langle\theta_\alpha^2\rangle = 0.018 \pm 0.002$  is found. This value is about a factor of 2 higher than the result reported previously [Lon10], which was based on a subset of the  $(p,\alpha)$  data set analyzed here. Mean proton reduced widths were extracted for 33 level sequences in the  $A = 34$ – $67$  range. We find significant scatter in the mean values for different mass numbers and  $J^\pi$  values. For a given spin  $J$ , the  $\langle\theta_p^2\rangle$  values scatter over up to an order of magnitude, depending on mass number. For  $A \leq 40$  the mean reduced proton widths are higher, on average, compared to the  $A > 40$  range. These results are important because they facilitate an improved random sampling of thermonuclear reaction rates: instead of using one global mean reduced proton width value for all mass numbers and spin-parities, our results allow us, for the first time, to employ local values in the random sampling.

In order to demonstrate the implications of our results, we calculated new thermonuclear rates for the  $^{40}\text{Ca}(\alpha,\gamma)^{44}\text{Ti}$  reaction ( $Q_{\alpha\gamma} = 5127$  keV), which is responsible for the production of  $^{44}\text{Ti}$  during the  $\alpha$ -rich freeze-out in core-collapse supernovae. The radioactive decay of  $^{44}\text{Ti}$  is of paramount importance for core-collapse super-

nova light curves,  $\gamma$ -ray astronomy, and isotopic anomalies measured in presolar grains. For the observed resonances, we adopted resonance energies and strengths from Refs. [Coo77, End90, Voc07, Rob12]. In addition, eleven natural parity states between the  $\alpha$ -particle threshold and the lowest-lying observed resonance can contribute to the total rate. The compound nucleus  $^{44}\text{Ti}$  exhibits a strong  $\alpha$ -cluster structure, which was investigated in several works using  $\alpha$ -particle transfer experiments. We chose this example because, interestingly, there is a resonance at  $E_r^{c.m.} = 2373$  keV ( $E_x = 7500$  keV,  $J^\pi = 1^-$ ), that has not been observed in any of the  $\alpha$ -particle transfer studies. Since this level does not exhibit an  $\alpha$ -cluster structure and no experimental information is known about the  $\alpha$ -particle spectroscopic factor, it can be assumed that the probability density function of its reduced width is given by a Porter-Thomas distribution.

The new Monte-Carlo-based reaction rates are displayed in Fig. 3.8. The colored shading indicates the coverage probability in percent. For example, the area enclosed by the thick black lines (i.e., the high and low Monte Carlo rates) corresponds to a coverage probability of 68%, while the area enclosed by the thin black lines contains a coverage probability of 95%. The dotted line is obtained when assuming a maximum possible contribution of the unobserved  $E_r^{c.m.} = 2373$  keV resonance and represents the upper limit of the previous (“classical”) reaction rate. As can be seen, the probability density distribution of the  $^{40}\text{Ca}(\alpha,\gamma)^{44}\text{Ti}$  reaction rate in the temperature range of  $T = 1\text{--}3$  GK is concentrated around much smaller values compared to the classical upper limit, and therefore the latter rates represent an unlikely estimate. In fact, the Monte Carlo rates (thick black lines for a 68% coverage probability) that are obtained by randomly sampling using a Porter-Thomas distribution for this single unobserved resonance are smaller by up to a factor of about three compared to the classical upper limit (dotted line). As a comparison, the dashed lines show the (classical) “upper limit,” “complete rate,” and “lower limit” from the recent study of Robertson *et al.* [Rob12]. The large deviation of almost one order of magnitude near  $T = 1$  GK is caused by the fact that none of the unobserved resonances were taken into account by Ref. [Rob12]. Our new rates could have a significant impact on the final  $^{44}\text{Ti}$  yields in core-collapse supernovae. This work has now been published [Pog13].

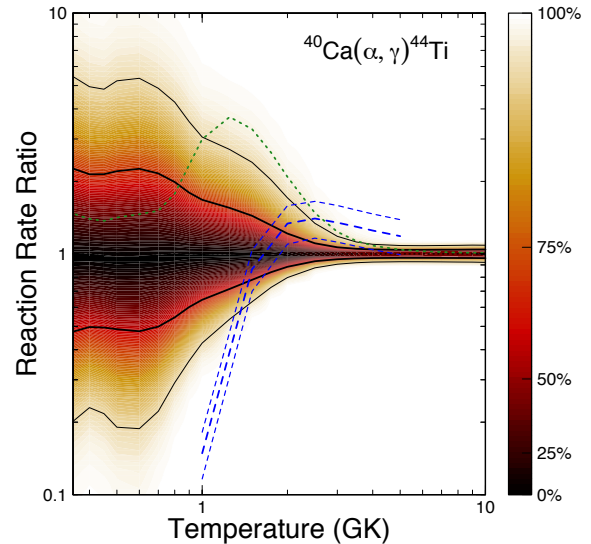


**Figure 3.8:** (Color online) Reaction rates for  $^{40}\text{Ca}(\alpha,\gamma)^{44}\text{Ti}$ . For a better comparison, all rates are normalized to the present recommended (median) Monte Carlo rate. Red (shading): contour plot of Monte Carlo based rates; the shading indicates the coverage probability in percent (legend on right-hand side). Blue (dashed): previously reported “upper limit,” “complete rate,” and “lower limit” from Ref. [Rob12]. Green (dotted): classical “upper limit” rate obtained if the maximum contribution of the  $E_\alpha^{c.m.} = 2373$  keV is adopted.

- 
- [Coo77] E. L. Cooperman, M. H. Shapiro, and H. Winkler, Nucl. Phys., **A284**, 163 (1977).
- [End90] P. M. Endt, Nucl. Phys., **A521**, 1 (1990).
- [Lon10] R. Longland *et al.*, Nucl. Phys., **A841**, 1 (2010).
- [Pog13] I. Pogrebnyak *et al.*, Phys. Rev. C, **88**, 015808 (2013).
- [Por56] C. E. Porter and R. G. Thomas, Phys. Rev., **104**, 483 (1956).
- [Rob12] D. Robertson *et al.*, Phys. Rev. C, **85**, 045810 (2012).
- [Voc07] C. Vockenhuber *et al.*, Phys. Rev. C, **76**, 035801 (2007).



# Nuclear Structure and Reactions

---

Chapter 4

- Reaction Dynamics of Light Nuclei
- Preequilibrium Nuclear Reactions
- Neutron-Induced Reactions

## 4.1 Reaction Dynamics of Light Nuclei

### 4.1.1 Measurement of the $^{10}\text{B}(p,\alpha)^7\text{Be}$ Reaction Cross Section between 2.1 and 6.0 MeV

A. KAFKARKOU, M.W. AHMED, P.H. CHU, H.J. KARWOWSKI, D.P. KENDELLEN, G. LASKARIS, I. MAZUMDAR, J.M. MUELLER, L.S. MYERS, M.H. SIKORA, H.R. WELLER, W.R. ZIMMERMAN, TUNL; R.H. FRANCE III, *Georgia College and State University, Milledgeville, GA*; R.M. PRIOR, M.C. SPRAKER, *University of North Georgia, Dahlonega, GA*

**The differential cross section of the  $^{10}\text{B}(p,\alpha)^7\text{Be}$  reaction has been measured at proton energies between 2.1 and 6.0 MeV and at laboratory angles from  $30^\circ$  to  $150^\circ$ . This reaction is important for proposed boron-fueled colliding-beam reactors. The total cross section was extracted at each proton energy. On average, the results of this experiment are about 16% higher than previously reported results.**

The  $^{11}\text{B}(p,\alpha)$  reaction has been proposed for aneutronic energy production in boron-fueled colliding-beam reactors [Ros03] and has been previously studied at TUNL [Sta11, Spr12]. Natural boron consists of 19.9%  $^{10}\text{B}$ , so the reactions  $^{10}\text{B}(p,\alpha_0)^7\text{Be}$  and  $^{10}\text{B}(p,\alpha_1)^7\text{Be}^*$  can also take place in the nuclear fuel. These two reactions produce  $^7\text{Be}$  which decays with a half-life of about 53 days. This is long enough that significant quantities can pose serious radiation-safety problems. The use of enriched  $^{11}\text{B}$  can suppress these problems. An accurate measurement of the cross sections of the  $^{10}\text{B}(p,\alpha_0)^7\text{Be}$  and  $^{10}\text{B}(p,\alpha_1)^7\text{Be}^*$  reactions will play a key role in determining the necessary enrichment level. The total cross section of the  $^{10}\text{B}(p,\alpha_0+\alpha_1)^7\text{Be}$  reactions (summed over both  $\alpha$ -particle channels) were extracted by fitting the angular distributions of the differential cross sections for proton bombarding energies between 2.1 and 6.0 MeV. This summed cross section is also the total  $^7\text{Be}$  production cross section.

The experiment was conducted at TUNL using the 10 MV FN tandem accelerator. The protons were accelerated to energies of 2.1 to 6.0 MeV and were directed into the scattering chamber. The beam-energy uncertainty was determined to be  $\pm 10$  keV. The target consisted of a thin layer of boron, enriched to about 98% in  $^{10}\text{B}$  and with a nominal thickness of  $100 \mu\text{g}/\text{cm}^2$  deposited on a carbon foil with a thickness of about  $40 \mu\text{g}/\text{cm}^2$ . The energy loss in the target was less than 0.5%. The beam current was measured by

a Faraday cup biased at  $-300$  V to eliminate the effects of secondary electrons. A systematic uncertainty of 3.5% is estimated for the integrated charge. The chamber was kept under a vacuum of about  $10^{-6}$  torr, and a liquid nitrogen trap was used to avoid carbon build-up on the target.

The outgoing particles were detected using  $\Delta E$ - $E$  silicon surface-barrier (SSB) telescopes. The detectors were placed at scattering angles between  $30^\circ$  and  $150^\circ$ , at a distance of about 16 cm from the target. The  $\Delta E$  detectors could stop all the  $\alpha$ -particles, but they would not stop the elastically and inelastically scattered protons. This was done to separate  $\alpha$ -particles from protons in cases where their energies were equal. Behind each  $\Delta E$  detector, a  $300 \mu\text{m}$  thick SSB detector was placed to detect the protons scattered off the boron target, in order to monitor target thickness. A gold foil target was used for solid-angle calibrations. More details about the setup can be found in Ref. [Kaf13].

Figure 4.1 shows a spectrum taken at  $30^\circ$  with a 4.0 MeV proton beam. The collected spectra were fit with Gaussian functions at each angle and energy, and the yields of the  $^{10}\text{B}(p,\alpha_0+\alpha_1)^7\text{Be}$  reactions were determined. Using these yields and information from elastic-scattering spectra from the  $^{10}\text{B}$  and the gold targets, the differential cross sections were extracted at each angle and energy. Figure 4.2 shows an angular distribution determined for 4.0 MeV incident protons. The statistical uncertainties were less than 2.0% in all cases. An overall 7% system-

atic uncertainty from charge measurements and target thickness was used for each energy.

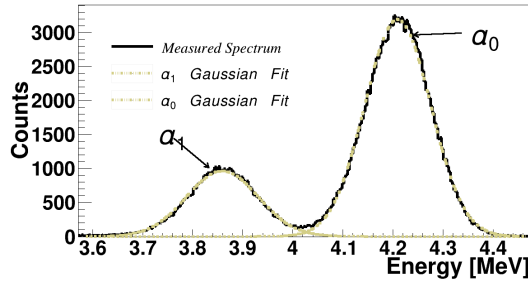


Figure 4.1: (Color online) A sample spectrum taken at  $30^\circ$  for a 4.0 MeV proton beam. The  $\alpha_0$  and  $\alpha_1$  peaks are labeled, and the Gaussian fits to both of them are shown.

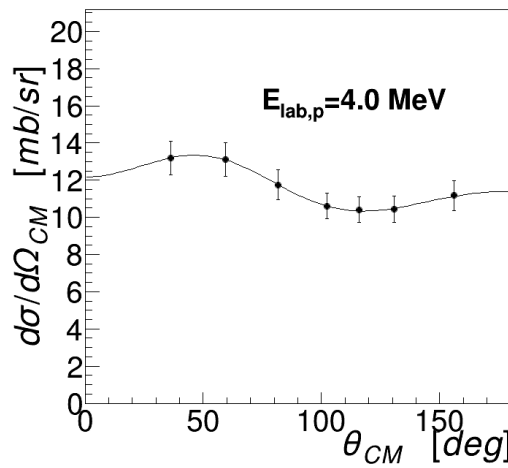


Figure 4.2: Center-of-mass angular distribution for a 4.0 MeV proton beam. The statistical uncertainties are not visible with the chosen scale. The visible error bars are the overall 7% systematic uncertainties. The solid line shows a fit with Legendre polynomials.

The angular distributions were fit with Leg-

endre polynomials, and the total cross sections were extracted at each energy. Figure 4.3 shows the results compared to data from previous measurements [Jen64]. On average, the present results are about 16% higher than the results in Ref. [Jen64]. The published results of this work [Kaf13] give the parameters from the Legendre polynomial fits, the differential cross sections, and the total cross sections. The astrophysical S-factors were determined from the total cross sections and are also presented in Ref. [Kaf13].

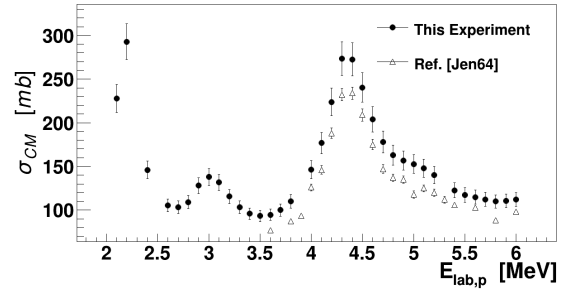


Figure 4.3: Excitation function for the  $^{10}\text{B}(p, \alpha_0 + \alpha_1)$  reaction compared to the data from Ref. [Jen64]. Our error bars denote the overall systematic uncertainties (7%). The statistical uncertainties are negligible.

[Jen64] J. G. Jenkin, L. G. Earwaker, and E. W. Titterton, Nucl. Phys., **50**, 516 (1964).

[Kaf13] A. Kafkarkou *et al.*, Nucl. Instrum. Methods B, **316**, 48 (2013).

[Ros03] N. Rostoker, A. Qerushi, and M. Binderbauer, J. Fus. Energy, **22**, 83 (2003).

[Spr12] M. C. Spraker *et al.*, J. Fus. Energy, **31**, 357 (2012).

[Sta11] S. Stave *et al.*, Phys. Lett., **B696**, 26 (2011).

### 4.1.2 Cross-Section Measurements of the $^{10}\text{B}(p,\gamma)^{11}\text{C}$ Reaction between 2.0 and 6.0 MeV

A. KAFKARKOU, M.W. AHMED, D.P. KENDELLEN, I. MAZUMDAR, J.M. MUELLER, L.S. MYERS, M.H. SIKORA, H.R. WELLER, W.R. ZIMMERMAN, *TUNL*

The total cross section of the  $^{10}\text{B}(p,\gamma)^{11}\text{C}$  reaction has been measured at proton energies between 2.0 and 6.0 MeV. This reaction is relevant to potential next-generation boron-fueled colliding-beam reactors. The total cross section was measured by activating a  $^{10}\text{B}$  target with protons and detecting the 511 keV  $\gamma$  rays emitted from the  $\beta^+$  decay of  $^{11}\text{C}$ . Our results indicate that this reaction will not be a significant concern for radiation safety.

The  $^{11}\text{B}(p,\alpha)\alpha$  reaction, which was recently studied at TUNL [Sta11, Spr12], is a candidate for aneutronic energy production in next-generation boron-fueled colliding-beam reactors [Ros03]. However natural boron contains 19.9%  $^{10}\text{B}$ , and the  $^{10}\text{B}(p,\gamma)^{11}\text{C}$  reaction, which leads to the production of the radioactive nucleus  $^{11}\text{C}$  can also occur in the fuel. It has a half-life of about 20.4 min, leading to potential radiation-safety concerns. Thus, an accurate measurement of the  $^{11}\text{C}$  production cross section is important for the design of these reactors.

The experiment was conducted at TUNL using the 10 MV FN tandem accelerator. The protons were accelerated to energies of 2.0 to 6.0 MeV in 500 keV steps and were directed to the center of a small vacuum chamber kept at  $10^{-6}$  torr. The beam-energy uncertainty from the accelerator was  $\pm 10$  keV, and the energy spread in the target was about 13 keV for the lower incident energies. A 98% enriched  $^{10}\text{B}$  target with a nominal thickness of  $1.7\ \mu\text{m}$  was placed in the center of the chamber. The target was deposited on a piece of tantalum that was thick enough to stop all of the protons. The integrated beam current was measured from the target using a beam-current integrator. The target was biased to +300 V to eliminate the effects of secondary electrons.

At each proton energy, the target was irradiated for an activation time of one hour. The  $^{11}\text{C}$  nuclei produced decay to  $^{11}\text{B}$  by emitting a positron, which annihilates with atomic electrons giving two 511 keV  $\gamma$  rays in coincidence. After the end of the activation period, the beam was stopped, and the 511-keV  $\gamma$ -ray-coincidence events were counted for another hour using two LaBr<sub>3</sub>:Ce detectors. These detectors were placed

outside the chamber at a scattering angle of  $90^\circ$ , ob the left and right sides of the beam. Only events that arrived within 10 ns of each other were recorded, in order to ensure coincidence. Also, the energies of the coincident events were used to select only the 511-keV events and reject accidental coincidences (see Fig. 4.4). The number of coincident events as a function of time gave the decay curve shown in Fig. 4.5. The integrated charge on the target was also recorded as a function of time.

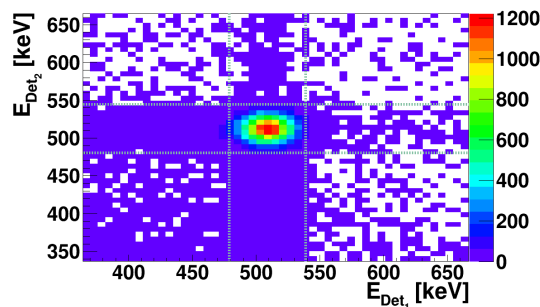


Figure 4.4: (Color online) Two-dimensional plot of the energy signals from the two detectors for 4.0 MeV incident protons. To eliminate accidental coincidences, only the events included between the two horizontal and the two vertical dashed lines were used (511 keV events).

The number of observed decays was extracted by fitting the decay curves (see Fig. 4.5) with the sum of two exponential functions plus a constant, using the extended-unbinned-maximum-likelihood method. One of the two exponentials accounted for the  $^{11}\text{C}$  decays, while the second accounted for  $^{13}\text{N}$   $\beta^+$  decays.  $^{13}\text{N}$  could be produced during the irradiation from  $(p,\gamma)$  reactions

on  $^{12}\text{C}$  nuclei in the target (for example from carbon build-up). The constant accounted for any flat background. From the number of observed decays and the integrated charge, the yield  $Y$  (number of observed decays per incident proton) of the reaction was determined. This procedure was repeated several times at each energy, and several yields were determined. To minimize the uncertainty, the weighted average from all the yields at each energy was used. The uncertainties of the average yields (coming from charge measurements and the fit) ranged from 1.8 to 4.5%. Finally, to convert the yields to total cross sections, our data were normalized to the data from Ref. [Wie83] for 1.8 and 2.0 MeV incident protons. This procedure introduced an overall 5.5% systematic uncertainty for all the energies.

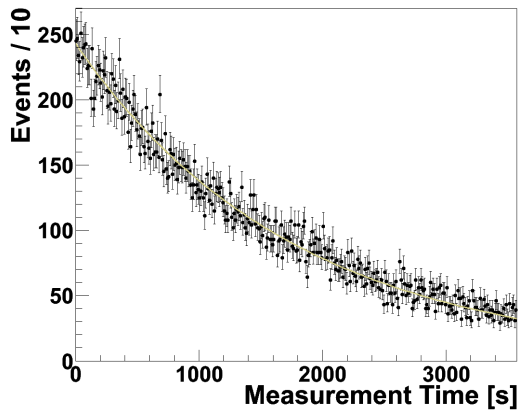


Figure 4.5: (Color online) The  $^{11}\text{C}$  decay curve for 4.0 MeV incident protons. The data points represent the number of 511 keV coincidence counts per 10-second bin as a function of time. The solid line is the result of fitting these data.

The results are shown in Fig. 4.6 and are compared with results from Refs. [Kua70, Wie83]. The cross sections determined in this experiment are larger than those determined in Ref. [Kua70]. This was expected since in Ref. [Kua70] only the

$^{10}\text{B}(p,\gamma_0)^{11}\text{C}$  reaction was measured. Comparing the results of this experiment with the cross sections for the  $^{10}\text{B}(p,\alpha)^7\text{Be}$  reaction [Kaf13], we see that the cross section for the  $^{10}\text{B}(p,\gamma)^{11}\text{C}$  reaction is three orders of magnitude smaller. Thus the production of  $^{11}\text{C}$  in boron-fueled colliding-beam reactors will be a minor issue for radiation safety, compared with the production of  $^7\text{Be}$ .

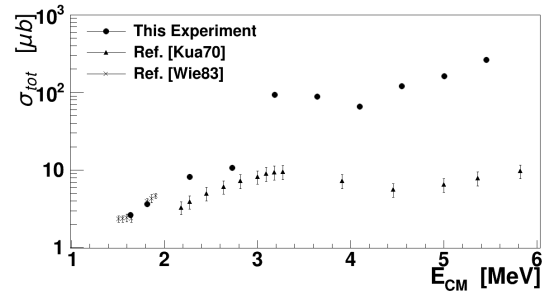


Figure 4.6: Excitation function for the  $^{10}\text{B}(p,\gamma)^{11}\text{C}$  reaction. The uncertainties from the weighted averaged yields cannot be shown with the chosen scale. An additional 5.5% overall systematic uncertainty also exists for all the points.

[Kaf13] A. Kafkarkou *et al.*, Nucl. Instrum. Methods B, **316**, 48 (2013).

[Kua70] H. M. Kuan *et al.*, Nucl. Phys., **A151**, 129 (1970).

[Ros03] N. Rostoker, A. Qerushi, and M. Binderbauer, J. Fus. Energy, **22**, 83 (2003).

[Spr12] M. C. Spraker *et al.*, J. Fus. Energy, **31**, 357 (2012).

[Sta11] S. Stave *et al.*, Phys. Lett., **B696**, 26 (2011).

[Wie83] M. Wiescher *et al.*, Phys. Rev. C, **28**, 1431 (1983).

## 4.2 Preequilibrium Nuclear Reactions

### 4.2.1 Preequilibrium Reaction Phenomenology

C. KALBACH WALKER, *TUNL*

The validity of a new phenomenological model for projectile breakup reactions has been tested for incident  $\alpha$ -particles at energies of 80 to 160 MeV, complementing earlier work on  $d$ - and  ${}^3\text{He}$ -induced reactions. The breakup cross section for all projectiles increases with increasing energy and can account for more than 60% of the total reaction cross section.

For reactions induced by projectiles with  $A \leq 4$  at incident energies of 14 to 200 MeV, the semi-classical exciton model of preequilibrium nuclear reactions provides a simple way to describe the continuum energy and angular distributions of the light particles emitted during energy equilibration. The TUNL code system PRECO is based on the exciton model and has been used, either alone or in Hauser-Feshbach codes, in applied projects, in support of rare-isotope-accelerator studies, and in other basic research. Model development uses simple physical concepts and is guided by available data from the literature.

The exciton model, its associated direct-reaction models, the code, and the global input set are being continually refined and benchmarked against data. Work in recent years has centered on projectile-breakup reactions. One of PRECO's strengths is its ability to treat reactions with complex particles in the entrance channel and/or exit channel, but for loosely bound projectiles— $d$ ,  $t$  and  ${}^3\text{He}$ —at all energies and for  $\alpha$  particles at incident energies above about 50 MeV, the lack of a projectile-breakup model has made the description incomplete.

A phenomenological breakup model has now been developed for inclusion in PRECO. Projectile breakup is here defined as the emission of a projectile fragment with a fairly narrow energy distribution peaked at an emission energy corresponding to the projectile velocity. When the undetected fragment interacts with the target nucleus, the fused system will undergo energy equilibration. Particle emission occurring during that equilibration will need to be included in the exciton model calculations.

Meanwhile, interest in deuteron-induced reactions has increased. The International Atomic

Energy Agency recently completed a Coordinated Research Project to upgrade the Fusion Energy Nuclear Data Library to version FENDL-3. One of the important additions was “data” (mostly model-generated) for deuteron-induced reactions. For this work the code TALYS [Kon04] was modified by its author to use an early version of the TUNL breakup model.

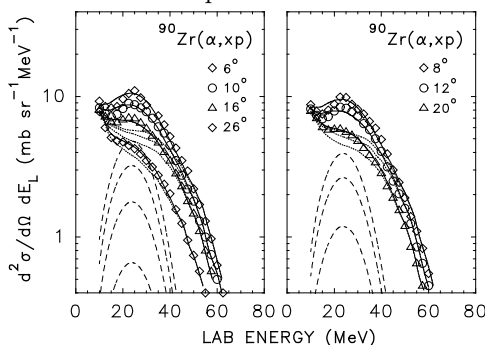
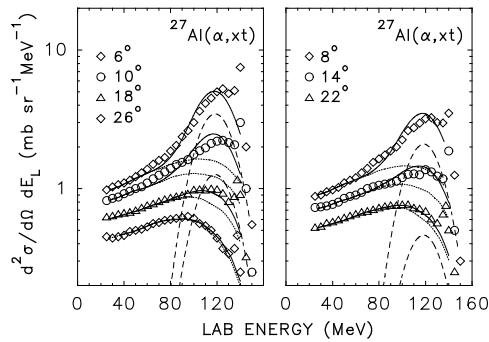


Figure 4.7: Comparison between model results and experiment for the reaction  ${}^{90}\text{Zr}(\alpha,p)$  at an incident energy of 80 MeV. The points show the data from [Wu79], the dashed, dotted, and solid curves show, respectively, the calculated breakup peaks, estimates of the underlying continuum, and the resulting total spectra.

Comparisons of the results of model calculations with data were previously carried out for  $d$ - and  ${}^3\text{He}$ -induced reactions [Kal10], and additional work was carried out to describe a second breakup peak in measured  $(\alpha,d)$  spectra [Kal11]. Further work on comparisons for the breakup of incident  $\alpha$  particles was suspended pending insights from new work on the systematics of continuum angular distributions, which was reported last year [Kal12]. This year, the comparisons

were completed, and typical results for  $p$ ,  $t$ , and  ${}^3\text{He}$  emission are shown in Figs. 4.7 to 4.9. There is a great deal of uncertainty about the underlying continuum, but overall the results give a good account of the major features of the measured spectra.



**Figure 4.8:** Comparison between model results and experiment for the reaction  ${}^{27}\text{Al}(\alpha,t)$  at an incident energy of 160 MeV. The points and curves have the same significance as in Fig. 4.7.

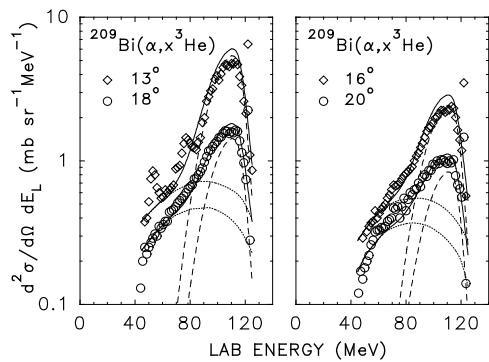


**Figure 4.9:** Comparison between model results and experiment for the reaction  ${}^{209}\text{Bi}(\alpha,{}^3\text{He})$  at an incident energy of 140 MeV. The points and curves have the same significance as in Fig. 4.7 except that the data are from Ref. [Wu78].

Having verified the general validity of the breakup model, the breakup cross section from all breakup channels for a given reaction were summed, assuming that neutron fragments follow the systematics of proton fragments. The breakup cross section was then compared with the total reaction cross sections used in PRECO. The results are shown in Fig. 4.10. The breakup fraction for different targets bombarded by the same projectile at the same incident energy typically increases with the target mass-number. The

general trends in the figure have been fit with the equation

$$f_{\text{bu}} = 0.7 \left[ 1 - \frac{1}{\exp[0.059 (E_{\text{inc}} - B_a) / B_a]} \right]. \quad (4.1)$$

Here  $E_{\text{inc}}$  is the projectile energy in the laboratory system and  $B_a$  is the minimum energy required to break the projectile into two fragments.

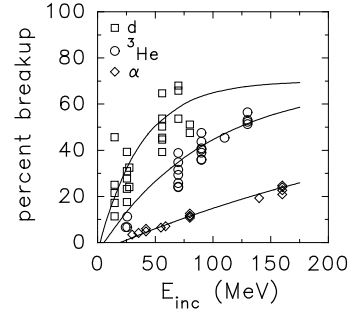


**Figure 4.10:** Percent of the total reaction cross section due to projectile breakup. The points show the results for the individual reactions studied, and the curves display the overall trend given by Eq. 4.1.

The results show that projectile breakup can account for as much as two-thirds of the reaction cross section (as much as 20% for incident  $\alpha$  particles), underscoring the importance of including this mechanism in preequilibrium model reaction calculations. A journal article describing the model is being prepared.

[Kal10] C. Kalbach Walker, TUNL Progress Report, **XLIX**, 96 (2010).

[Kal11] C. Kalbach Walker, TUNL Progress Report, **L**, 80 (2011).

[Kal12] C. Kalbach Walker, TUNL Progress Report, **LI**, 79 (2012).

[Kon04] A. J. Koning, S. Hilaire, and M. C. Duijvestijn, *TALYS: A Nuclear Reaction Program*, Technical Report 21297/04.62741/P FAI/AK/AK, NRG Petten, 2004.

[Wu78] J. R. Wu, C. C. Chang, and H. D. Holmgren, *Phys. Rev. Lett.*, **40**, 1013 (1978).

[Wu79] J. R. Wu *et al.*, *Phys. Phys. C*, **20**, 1284 (1979).

## 4.3 Neutron-Induced Reactions

### 4.3.1 Neutron-Capture Experiments

G.E. MITCHELL, B. BARAMSAI, E. BATCHULUUN, A. CHYZH, C.L. WALKER, *TUNL*; OTHERS, *Charles University, Prague and Rez Institute of Nuclear Physics, Rez, Czech Republic; Los Alamos National Laboratory, Los Alamos, NM; Lawrence Livermore National Laboratory, Livermore, CA*

**Our measurements of neutron-capture reactions utilize the DANCE detector array—a highly efficient calorimeter consisting of 160 BaF<sub>2</sub> detectors. The high degree of segmentation is used to perform neutron resonance spectroscopy. Several new methods have been developed to determine resonance spins from the multiplicity distributions. The study of the statistical  $\gamma$ -ray cascade from different resonances and for different multiplicities provides unique opportunities to test models of the photon strength function.**

Our research efforts emphasize neutron-capture reactions measured with the Detector for Advanced Neutron Capture Experiments (DANCE) located at the Los Alamos Neutron Science Center (LANSCE) at LANL. We focus on nuclei that are important for applied science and for nuclear structure interests. Much of the support for this work comes from an NNSA Academic Alliances grant.

DANCE is an array of 160 barium fluoride crystals. This calorimeter identifies capture by the total  $\gamma$ -ray energy. The high efficiency of the calorimeter means that measurements can be made with very small targets. The capture cross sections for specific nuclei are extremely valuable for stewardship science, for advanced-fuel-cycle calculations, and for nuclear astrophysics. The primary nuclear structure interest is in the photon low-energy collective excitations, namely the scissors mode and pygmy resonances. Specifically, we use the properties of the  $\gamma$ -ray cascade from isolated neutron resonances to determine resonance properties and properties of the photon strength function.

We utilize the computer program DICEBOX, developed by our Prague collaborators, to model the  $\gamma$ -ray spectrum for all multiplicities. We vary the photon strength functions in order to obtain the best agreement with experiment.

Thus far we have measured  $^{89}\text{Y}$ ,  $^{94,95,97}\text{Mo}$ ,  $^{117,119}\text{Sn}$ ,  $^{151,153}\text{Eu}$ ,  $^{152,154,155,156,157,158}\text{Gd}$ , and  $^{163}\text{Dy}$ . Our immediate project for late 2013 is the measurement of  $^{161}\text{Dy}$ . We also have collaborated on measurements of  $^{87}\text{Sr}$  both with

the DANCE array and with the neutron time-of-flight (nTOF) system at CERN. We have finished the analysis of  $^{89}\text{Y}$ ,  $^{94,95}\text{Mo}$ , and the europium and gadolinium isotopes. Preliminary analysis of the  $^{97}\text{Mo}$  and  $^{117,119}\text{Sn}$  data has been completed, and final analysis is in progress. Recent publications include a study of the resonances in the  $^{155}\text{Gd}(n,\gamma)$  reaction [Bar12] and of the strength of the scissors mode in the odd-mass gadolinium isotopes [Kro13] produced through neutron capture on the four even-mass isotopes that we have measured.

Detailed agreement with the pure statistical model was obtained for neutron capture on  $^{95}\text{Mo}$ . This was verified by a separate measurement of the two-step cascade at the Institute of Nuclear Physics, Rez, Czech Republic. Of particular interest is the behavior of the scissors-mode resonance as a function of mass and deformation in the gadolinium isotopes. Analysis of the  $\gamma$ -cascade data in the gadolinium isotopes leads to the clear conclusion that scissors-mode resonances are built not only on the ground state, but also on excited levels in all product nuclei studied, thus confirming the Brink hypothesis.

We have also collaborated with the nTOF group at CERN. They have used their nTOF calorimeter to study the same strontium target that was used for the DANCE measurement. In addition to providing detailed spectroscopic information, this measurement will enable a direct comparison of the relative merits of the two most advanced calorimeters for neutron-capture measurements.

Finally, we have collaborated with an astrophysics group to use proton- and  $\alpha$ -particle-resonance data to determine reaction rates for proton- and  $\alpha$ -particle-induced reactions [Pog13].

In favorable cases, the average multiplicity of the  $\gamma$ -ray decay is sufficient to determine the spin of an  $s$ -wave resonance. In general, however, it is necessary to perform a detailed analysis of the multiplicity distribution. One method that we have developed [Bar12] involves pattern recognition theory. This method works for well-isolated resonances but is inconclusive for doublets. In collaboration with our colleagues from Prague, we have developed an alternate method that adopts prototype multiplicity distributions for resonances with known spin, and decomposes the experimental cross section into cross sections

for the separate spins. This method [Bec11] works well even for doublets, but provides no quantitative measure of the assignment's correctness. In practice we utilize a combination of the two methods.

---

[Bar12] B. Baramsai, Phys. Rev. C, **85**, 024622 (2012).

[Bec11] F. Becvar, Nucl. Instrum. Methods, **647**, 73 (2011).

[Kro13] J. Kroll, Phys. Rev. C, **88**, 034317 (2013).

[Pog13] I. Pogrebnyak, Phys. Rev. C, **85**, 015808 (2013).



# Photonuclear Reactions at $\text{HI}\gamma\text{S}$

---

Chapter 5

- Nuclear Astrophysics
- Few-Body Interactions
- Study of Many-Body Systems

## 5.1 Nuclear Astrophysics

### 5.1.1 Further Measurement of the $2_2^+$ State in $^{12}\text{C}$ with the HI $\gamma$ S OTPC

W.R. ZIMMERMAN, M.W. AHMED, A. KAFKARKOU, I. MAZUMDAR, J.M. MUELLER, L.S. MYERS, M.H. SIKORA, S. STAVE, A.G. SWINDELL, H.R. WELLER, *TUNL*; M. GAI, *University of Connecticut at Avery Point, Groton, CT*

The predicted second  $J^\pi = 2^+$  state in  $^{12}\text{C}$  has been directly observed at HI $\gamma$ S in the photodisintegration of  $^{12}\text{C}$  into three  $\alpha$  particles. Recent measurements using beam energies up to 11.2 MeV show this state to have an excitation energy of  $10.13^{+0.06}_{-0.05}$  MeV, a total width of  $2080^{+330}_{-260}$  keV, and an electromagnetic-decay width to the ground state of  $135^{+16}_{-12}$  meV. These results will help to constrain models describing the structure of the  $0^+$  ‘Hoyle’ state.

An experiment to search for a possible  $2_2^+$  state in  $^{12}\text{C}$  was performed at HI $\gamma$ S, using a  $\text{CO}_2$  target and nearly mono-energetic  $\gamma$ -ray beams. Recoiling  $\alpha$  particles from the  $^{12}\text{C}(\gamma, \alpha)^8\text{Be}$  reaction were detected with an optical time-projection chamber (O-TPC) [Gai10]. By using a  $\gamma$ -ray beam, the  $2_2^+$  state in  $^{12}\text{C}$  can be measured without contributions from the  $3_1^-$  state at 9.6 MeV or the  $0_3^+$  state at 10.3 MeV [AS90] which have plagued previous experiments. Furthermore, this technique allows for a precise measurement of the electromagnetic-decay width of the  $2_2^+$  state to the ground state. Results from a subset of these data have been previously reported [Zim13].

Yields and angular distributions were measured at a total of fourteen different  $\gamma$ -ray beam energies between 9.1 and 11.2 MeV. The separated E1 and E2 components of the cross section were fit to Breit-Wigner resonances with energy-dependent widths [Lan58], convolved with the measured  $\gamma$ -ray beam energy distribution. The channel radius was fixed to be  $1.4 \text{ fm} \times (4^{1/3} + 8^{1/3})$ . Figure 5.1 shows the fits to the measured E1 and E2 cross-section data.

The previously-measured  $1_1^-$  state in  $^{12}\text{C}$  [AS90] was identified in the E1 cross-section data at an energy of  $E_{\text{RES}} = 10.913^{+0.020}_{-0.018}$  MeV, and the previously assigned spin, parity and isospin assignments of  $J^\pi; T = 1^-; 0$  were confirmed. The complete  $1_1^-$  parameters from the fit to the E1 cross section data are listed in Table 5.1. The reduced  $\alpha$ -decay width was measured to be  $0.088^{+0.012}_{-0.011}$  times the Wigner limit, which excludes an  $\alpha$ -cluster description of the state. The

isospin-forbidden E1 transition-strength to the ground state is seen to have a very small  $B(\text{E1})$ .

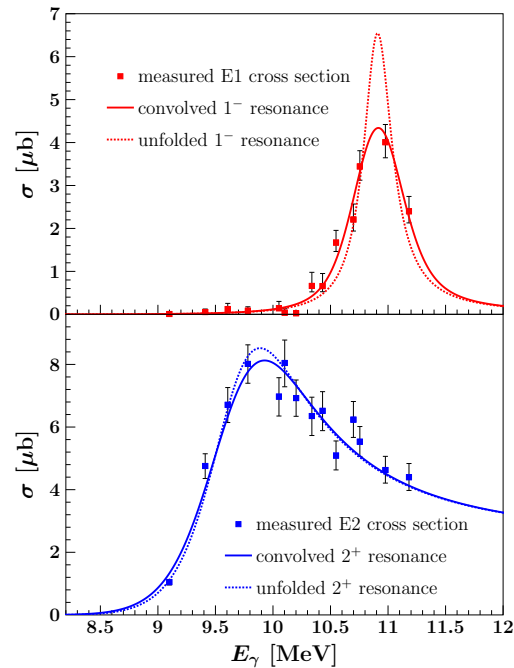


Figure 5.1: (Color online) The E1 (top) and E2 (bottom) cross-section data as a function of beam energy are shown along with the fit used to extract the  $1_1^-$  and  $2_2^+$  resonance parameters. Both the convolved and unfolded cross-section line shapes are shown.

The E2 cross section data allow us to unambiguously identify the  $2_2^+$  state in  $^{12}\text{C}$ . This state was predicted over fifty years ago [Mor56]

Table 5.1: Measured resonance parameters for the  $1_1^-$  and  $2_2^+$  states in  $^{12}\text{C}$ 

	$E_{\text{RES}}$ (MeV)	$\Gamma_\alpha$ (keV)	$\Gamma_\gamma$ (meV)	(keV)	$\gamma_\alpha^2$ ( $\gamma_\alpha^2/\gamma_w^2$ )	$\text{B}(E\lambda \rightarrow 0_1^+)$ ( $\text{e}^2 \text{fm}^{2\lambda}$ )	(W.u.)
$1_1^-$	$10.913^{+0.020}_{-0.019}$	$305^{+40}_{-36}$	$32.4^{+2.1}_{-2.0}$	$82.4^{+10.5}_{-9.5}$	$0.088^{+0.012}_{-0.011}$	$4.84(30) \times 10^{-5}$	$1.43(9) \times 10^{-4}$
$2_2^+$	$10.13^{+0.06}_{-0.05}$	$2080^{+330}_{-260}$	$135^{+16}_{-12}$	$1470^{+160}_{-120}$	$1.57^{+0.17}_{-0.13}$	$1.57^{+0.14}_{-0.11}$	$0.963^{+0.083}_{-0.069}$

to exist as an excitation of the Hoyle state, and this experiment definitively confirms the existence of the state as well as the spin, parity and isospin assignments  $J^\pi; T = 2^+; 0$ . The  $2_2^+$  state was directly observed at an energy of  $E_{\text{RES}} = 10.13^{+0.06}_{-0.05}$  MeV with a total width of  $\Gamma = 2080^{+330}_{-260}$  keV. The complete  $2_2^+$  parameters from the fit to the E2 cross section data are listed in Table 5.1. The reduced  $\alpha$ -decay width of the  $2_2^+$  state is  $1.57^{+0.17}_{-0.13}$  times the Wigner limit, which strongly supports an  $\alpha$ -cluster description of the state.

In addition to the E1 and E2 relative cross sections, the angular distributions also provide measurements of the phase difference  $\phi_{12}$ . Fig. 5.2 shows measured phase differences, along with a curve representing a calculation of  $\phi_{12}$  using a two-resonance model [Lan58]. Agreement between the measured phase differences and those predicted by this two-resonance model firmly establishes the resonance nature of the  $2^+$  strength reported here and indicates that there is little or no contribution from other amplitudes.

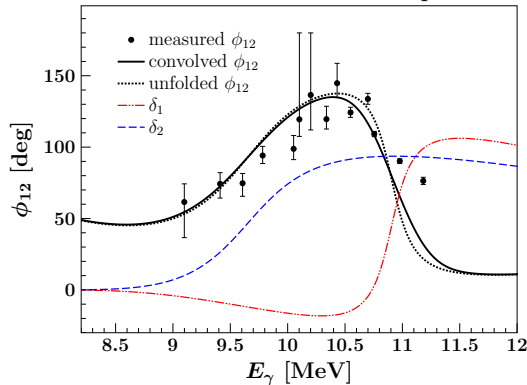


Figure 5.2: (Color online) Measured values of the E1–E2 relative phase angle  $\phi_{12}$  along with a calculation of  $\phi_{12}$ .

Following an argument put forth by Freer *et al.* [Fre12], constraints can be placed on the  $\alpha$ -

cluster structure of the Hoyle state using a simple semi-classical model by assuming that the  $2_2^+$  state is the first member of its rotational band. The excitation energy of the first member of its rotational band can be calculated for various arrangements of the three  $\alpha$  particles. If, for example, the  $\alpha$  particles are arranged in a linear chain [Mor56], then the  $2_2^+$  state would be 1.0 MeV above the Hoyle state at an excitation energy of 8.65 MeV. The results of the present experiment exclude this configuration.

If, however, the  $\alpha$  particles are arranged in an equilateral triangle and rotated about an axis which passes through one of the  $\alpha$  particles and halfway between the other two, then the  $2_2^+$  state would be 2.75 MeV above the Hoyle state, at an excitation energy of 10.4 MeV. While the results of this experiment cannot exclude this equilateral triangle configuration, the measured excitation energy of the  $2_2^+$  state ( $10.13^{+0.06}_{-0.05}$  MeV) can be exactly reproduced with an isosceles triangle formed by lengthening one side of the equilateral triangle to 2.58(3) times the  $\alpha$ -particle charge radius.

- [AS90] F. Ajzenberg-Selove, Nucl. Phys. **A506**, 1 (1990).
- [Fre12] M. Freer *et al.*, Phys. Rev. C, **86**, 034320 (2012).
- [Gai10] M. Gai *et al.*, J. Instrum., **5**, P12004 (2010).
- [Lan58] A. M. Lane and R. G. Thomas, Rev. Mod. Phys., **30**, 257 (1958).
- [Mor56] H. Morinaga, Phys. Rev., **101**, 254 (1956).
- [Zim13] W. R. Zimmerman *et al.*, Phys. Rev. Lett., **110**, 152502 (2013).

### 5.1.2 New Triple- $\alpha$ Reaction Rates from the $2_2^+$ State in $^{12}\text{C}$

W.R. ZIMMERMAN, H.R. WELLER, *TUNL*; C. FRÖHLICH, *North Carolina State University, Raleigh, NC*

**The second  $J^\pi = 2^+$  state in  $^{12}\text{C}$  was recently observed in the  $^{12}\text{C}(\gamma, \alpha)^8\text{Be}$  at HI $\gamma$ S. The new  $2^+$  state affects the thermonuclear reaction rate for the production of  $^{12}\text{C}$  through the triple- $\alpha$  process at the high temperatures that are thought to occur during core-collapse supernovae. New triple- $\alpha$  thermonuclear reaction rates have been calculated, and simulations based on the  $\nu p$  process have been performed, illustrating the effect of the second  $2^+$  state in  $^{12}\text{C}$  on the outcome of explosive nucleosynthesis.**

The  $2_2^+$  state in  $^{12}\text{C}$ , predicted to exist over fifty years ago as an excitation of the Hoyle state, was recently observed in the  $^{12}\text{C}(\gamma, \alpha)^8\text{Be}$  at HI $\gamma$ S using an optical time projection chamber (see Sect. 5.1.1). This state serves as a resonance in the  $^8\text{Be}(\alpha, \gamma)^{12}\text{C}$  reaction, increasing the thermonuclear reaction rate of the triple- $\alpha$  process at high temperatures [Buc06]. The exact parameters of the  $2_2^+$  state will affect the outcome of heavy-element production during the explosive nucleosynthesis that is thought to occur during core-collapse supernovae and other astrophysical phenomena.

Ambiguity in the existence of the  $2_2^+$  state in  $^{12}\text{C}$  has led to large disagreements in the triple- $\alpha$  reaction rates published in several recent compilations. The Nuclear Astrophysics Compilation of Reaction Rates (NACRE) [Ang99] includes in its calculations a purely theoretical  $2_2^+$  state in  $^{12}\text{C}$ , while the Joint Institute for Nuclear Astrophysics (JINA) ‘REACLIB’ database [Cyb10] lists the rates calculated using the results from the  $\beta$ -delayed  $\alpha$ -decay experiment of Fynbo *et al.* [Fyn05]. Unlike the NACRE reaction rates, the JINA rates do not include a contribution from a  $2_2^+$  state in  $^{12}\text{C}$ , and the reaction rates listed by the two compilations disagree at high temperatures by more than an order of magnitude. The recent direct observation of the  $2_2^+$  state in  $^{12}\text{C}$  in the  $^{12}\text{C}(\gamma, \alpha)^8\text{Be}$  reaction allows us to calculate the reaction rates and resolve this long-standing disagreement.

Triple- $\alpha$  reaction rates were calculated according to the formalism presented in NACRE [Ang99]. The reaction is assumed to proceed through two distinct steps: (i) two  $\alpha$  particles form a  $^8\text{Be}$  nucleus which (ii) fuses with a third

$\alpha$  particle before it decays. The calculations were done numerically for temperatures between 0 and 10 GK using the experimentally measured  $2_2^+$  and  $1_1^-$  states in  $^{12}\text{C}$  (see Table 5.1 in Sect. 5.1.1). In addition to the  $1_1^-$  and  $2_2^+$  states measured in this experiment, the calculated reaction rates also included contributions from the  $0_2^+$  Hoyle state at 7.6542 MeV and the  $3_1^-$  state at 9.641 MeV. Figure 5.3 shows the calculated triple- $\alpha$  reaction rates along with the reaction rates published in several compilations [Ang99, Cyb10, Cau88].

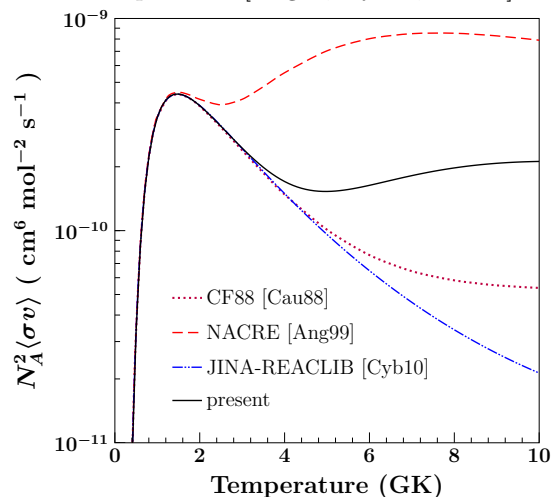


**Figure 5.3: (Color online) Thermonuclear triple- $\alpha$  reaction rates calculated here, compared with the rates listed by several compilations.**

The possible effects of these new reaction rates on the outcome of explosive nucleosynthesis during core-collapse supernovae were studied through simulations using the method described by Fröhlich *et al.* [Fro06a]. These simulations in-

cluded the  $\nu p$ -process, in which neutrino-driven winds contribute to the synthesis of heavy elements by allowing neutron-deficient nuclei to capture the neutrons which are produced when proton-rich matter interacts with a strong anti-neutrino flux [Fro06b]. The simulations used a trajectory [Arc12] which assumes that the neutrino-driven wind terminates at a temperature of 2 GK, and that the duration of the constant temperature phase associated with the wind termination is 0.5 s. The simulation was run using the triple- $\alpha$  reaction rates calculated in this work as well as the rates listed in the JINA-REACLIB compilation [Cyb10].

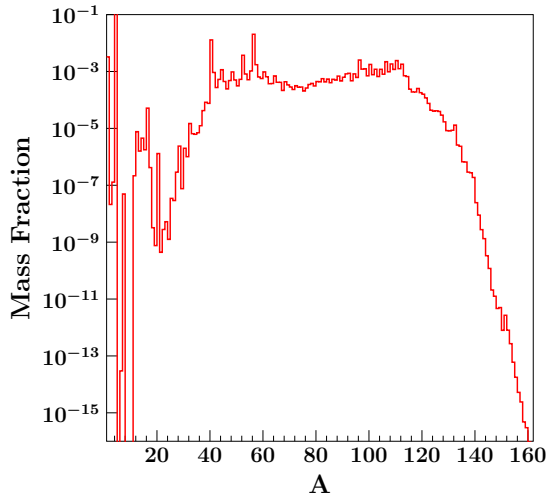


Figure 5.4: (Color online) Mass fractions in supernova ejecta from simulations [Arc12], using the triple- $\alpha$  reaction rates calculated in this work.

Figure 5.4 shows the mass fractions produced in the simulated explosive nucleosynthesis using the new triple- $\alpha$  reaction rates for each mass number  $A$ . Figure 5.5 shows a comparison between these results and those listed in the JINA-REACLIB compilation [Cyb10]. The new triple- $\alpha$  reaction rates enhance the production of certain isotopes of elements between rhodium and cadmium ( $Z$  of 45 to 48 and  $A$  of 100 to 110) while severely suppressing the production of many heavier nuclei.

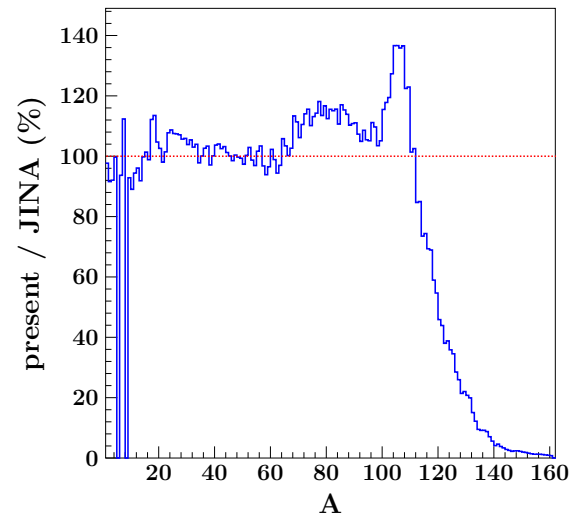


Figure 5.5: (Color online) Ratio of mass fractions simulated using the triple- $\alpha$  reaction rates calculated in this work to the mass fractions simulated using the rates published in the JINA-REACLIB compilation [Cyb10].

- 
- [Ang99] C. Angulo *et al.*, Nucl. Phys., **A656**, 3 (1999).
- [Arc12] A. Arcones, C. Fröhlich, and G. Martínez-Pinedo, Astrophys. J., **750**, 18 (2012).
- [Buc06] L. R. Buchmann and C. A. Barnes, Nucl. Phys., **A777**, 254 (2006).
- [Cau88] G. R. Caughlan and W. A. Fowler, At. Data Nucl. Data Tables, **40**, 283 (1988).
- [Cyb10] R. H. Cyburt *et al.*, Astrophys. J. Suppl. Ser., **189**, 240 (2010).
- [Fro06a] C. Fröhlich *et al.*, Astrophys. J., **637**, 415 (2006).
- [Fro06b] C. Fröhlich *et al.*, Phys. Rev. Lett., **96**, 142502 (2006).
- [Fyn05] H. O. U. Fynbo *et al.*, Nature, **433**, 136 (2005).

## 5.2 Few-Body Interactions

### 5.2.1 Three- and Two-Body Photodisintegration of $^3\text{He}$ with Double Polarizations

H. GAO, M. W. AHMED, P. CHU, A. S. CROWELL, C. R. HOWELL, M. HUANG, A. KAFKARKOU, H. J. KARWOWSKI, D. KENDELLEN, G. LASKARIS, J. M. MUELLER, L. S. MYERS, C. PENG, H. R. WELLER, Y. K. WU, X. YAN, Q. J. YE, Y. ZHANG, W. ZIMMERMAN, *TUNL*; T. AVERETT, *College of William and Mary, Williamsburg, VA*; D. DUTTA, *Mississippi State University, Starkville, MS*; B. TSANG, J. MANFREDI, *Michigan State University, East Lansing, MI*; Q. YE, *University of Maryland, College Park, MD*; A. DELTUVA, A. C. FONSECA, *Universidade de Lisboa, Lisboa, Portugal*; J. GOLAK, R. SKIBIŃSKI, H. WITAŁA, *Jagiellonian University, Kraków, Poland*; P. U. SAUER, *Leibniz Universität Hannover, Hannover, Germany*.

**We present double-differential cross-sections from an experiment on three-body photodisintegration of polarized  $^3\text{He}$  that took place in 2011 using a circularly polarized photon beam at incident energies of 12.8 and 14.7 MeV. We also present the progress on the PAC-approved experiment on the two-body photodisintegration of  $^3\text{He}$  with double polarizations at 25 and 30 MeV.**

The goal of the experiments on the three- and two-body photodisintegration of  $^3\text{He}$  with double polarizations is to test state-of-the-art three-body calculations and carry out the first investigation of the GDH sum rule [Dre66, Ger66] on  $^3\text{He}$  by studying its integrand below the pion-production threshold.

The first measurements of three-body photodisintegration of  $^3\text{He}$  using a longitudinally polarized  $^3\text{He}$  target and a circularly polarized  $\gamma$ -ray beam at 12.8 and 14.7 MeV took place at the HI $\gamma$ S facility at TUNL. The facility provided a nearly monoenergetic, approximately 100% circularly polarized  $\gamma$ -ray beam. The photon beam was collimated using a 12-mm-diameter collimator, resulting in beam energy spreads  $\Delta E_\gamma/E_\gamma$  of 3 to 5%. A high-pressure  $^3\text{He}$  target cell was employed and was polarized using the spin-exchange–optical-pumping technique [Hap72]. The neutrons from the three-body breakup of  $^3\text{He}$  were detected using sixteen liquid-scintillator detectors positioned at scattering angles from  $30^\circ$  to  $165^\circ$ . The photon flux was monitored with a D $_2$ O target and two additional liquid scintillator detectors. The spin of the target was flipped every 15 min, and the cross sections for target-spin parallel or antiparallel to the beam direction were extracted.

Figure 5.6 shows the spin-dependent double-

differential cross sections for parallel and antiparallel spin-helicity states at  $E_\gamma = 14.7$  MeV. They are compared with the calculations of Deltuva *et al.* [Del05, Del07] and Skibiński *et al.* [San03, San05].

Good agreement between the data and the Deltuva *et al.* calculations was found. The contributions from the three-body photodisintegration channel to the  $^3\text{He}$  GDH integrand were also extracted, and the results are published in Ref. [Las13]. Although, the dominant contribution in the GDH integral below the pion-production threshold is predicted to be due to the three-body breakup channel, it is important to test this prediction by carrying out measurements on the two-body break-up channel.

To study the feasibility of such a measurement, a beam test was performed in April 2013 at  $E_\gamma = 30$  MeV with a beam energy spread of about 3%. The protons from the two-body photodisintegration of an unpolarized  $^3\text{He}$  target were detected by sixteen fully depleted silicon surface barrier (SSB) detectors. The detectors were positioned at proton angles of  $45^\circ$ ,  $70^\circ$ ,  $95^\circ$ , and  $120^\circ$  (four detectors at each angle) and were about 11 cm away from the center of the  $^3\text{He}$  target cell. A reference cell was also employed for background subtraction. Figure 5.7 shows the acquired spectra from the beam test.

A clean proton signal from the  ${}^3\text{He}(\gamma,p){}^2\text{H}$  reaction was observed at the three more forward angles, whereas the detector at  $120^\circ$  had a significantly higher proton background.

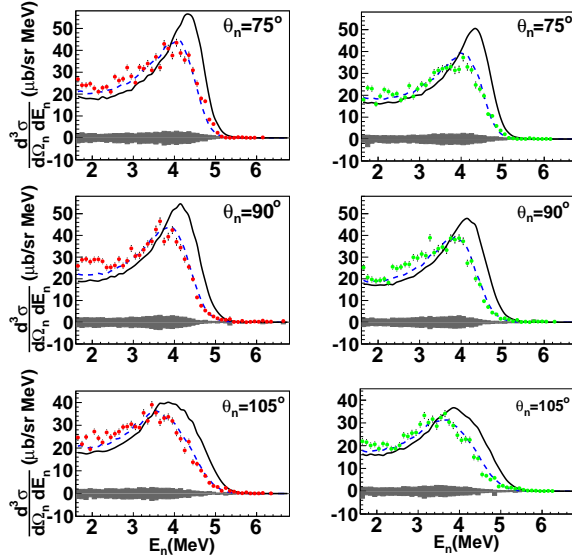


Figure 5.6: (Color online) Experimental spin-dependent double-differential cross sections for parallel (left panel) and antiparallel (right panel) states as a function of the neutron energy at  $E_\gamma=14.7$  MeV compared with the calculations of Deltuva *et al.* (dashed curves) and Skibiński *et al.* (solid curves). The bin width is 0.2 MeV. The band shows the combined systematic uncertainties.

An experiment on the two-body photodisintegration of  ${}^3\text{He}$  using a longitudinally polarized target and circularly polarized  $\gamma$ -ray beams at 25 and 30 MeV was approved for 250 hours of beam time. Two new  ${}^3\text{He}$  targets with 0.7 and 1 mm wall thicknesses and filled with approximately 4.5 and 6.5  $\mu\text{mol}$  of  ${}^3\text{He}$  will be constructed for the measurements at 25 and 30 MeV, respectively.

The protons from  ${}^3\text{He}(\vec{\gamma},p){}^2\text{H}$  will be detected by 72 fully depleted SSB detectors positioned at the aforementioned angles (eighteen detectors at each angle). The newly designed detector support is composed of six aluminum hemispheres, three on each side of the cell facing each other. Twelve SSB detectors will be mounted on each aluminum hemispherical shell. Collimators with rectangular apertures of  $2\text{ cm} \times 0.4\text{ cm}$  and a length of 3 cm will be positioned in front of the detectors. The collimators will define the solid angle and reduce the uncertainty in the angular acceptance. The angular acceptance was simulated using a GEANT4 code, and it is estimated to be  $\Delta\theta = \pm 15^\circ$ . The detector thicknesses range from 300 to 500  $\mu\text{m}$ , and

their efficiency for detecting charged particles is about 100%. The detectors have already been acquired and were tested with the proposed electronics setup at the tandem accelerator facility at TUNL. The new  ${}^3\text{He}$  cells are being constructed and will be tested in our polarized  ${}^3\text{He}$  laboratory at Duke during fall 2013. The collaboration is expected to be ready to take data as early as spring 2014.

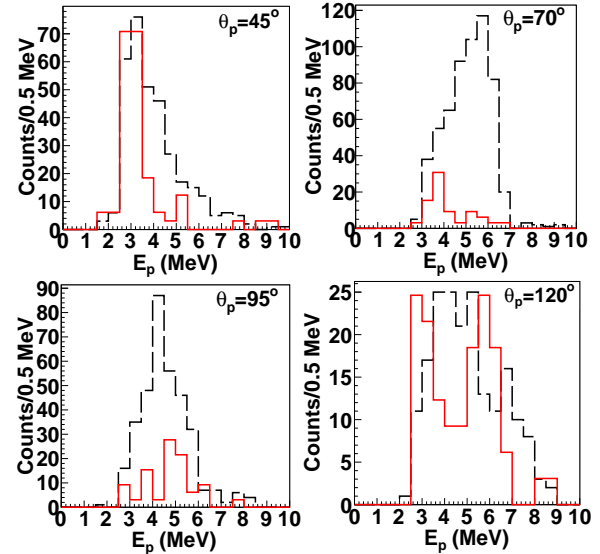


Figure 5.7: (Color online) Proton spectra from two-body  ${}^3\text{He}$  photodisintegration (dashed black line) compared with the reference-cell backgrounds (solid red line) normalized to the same integrated flux.

- 
- [Del05] A. Deltuva, A. C. Fonseca, and P. U. Sauer, *Phys. Rev. C*, **71**, 054005 (2005).
  - [Del07] A. Deltuva, A. Fonseca, and P. Sauer, *Nucl. Phys.*, **A790**, 344c (2007).
  - [Dre66] S. D. Drell and A. C. Hearn, *Phys. Rev. Lett.*, **16**, 908 (1966).
  - [Ger66] S. Gerasimov, *Sov. J. Nucl. Phys.*, **2**, 430 (1966).
  - [Hap72] W. Happer, *Rev. Mod. Phys.*, **44**, 169 (1972).
  - [Las13] G. Laskaris *et al.*, *Phys. Rev. Lett.*, **110**, 202501 (2013).
  - [San03] R. Skibiński *et al.*, *Phys. Rev. C*, **67**, 054001 (2003).
  - [San05] R. Skibiński *et al.*, *Phys. Rev. C*, **72**, 044002 (2005).

## 5.2.2 Differential Cross-Section Measurements of Three-Body Photodisintegration of the Triton

F.Q.L. FRIESEN, M.W. AHMED, A.S. CROWELL, L.C. CUMBERBATCH, B. FALLIN, C. R. HOWELL, D. TICEHURST, W. TORNOW, *TUNL*; B.J. CROWE, *North Carolina Central University, Durham, NC*; I.J. GRAY, *University of Minnesota Twin Cities, Minneapolis, MN*; H. WITALA, *Jagiellonian University, Krakow, Poland*

We describe ongoing work in the design and development of an apparatus for measuring the differential cross section for the  ${}^3\text{H}(\gamma,p)nn$  reaction. The measurement will be conducted at HI $\gamma$ S using a linearly polarized  $\gamma$ -ray beam at 15 and 25 MeV. The system will consist of gas targets constructed from thin foil, wire chambers for tracking outgoing particles, and silicon-strip detectors for calorimetry and position measurements.

The three-nucleon (3N) system provides a theoretically solid platform for examining the nuclear Hamiltonian in an environment where both nucleon-nucleon and 3N interactions are important. The substantial agreement between ab-initio 3N calculations and data gives confidence in the theoretical treatment of the system. However, there are some significant discrepancies between calculations and data that suggest there might be features in the reaction dynamics that are not well understood. For example, the measured cross section for neutron-neutron ( $nn$ ) quasi-free scattering (QFS) and the space-star configuration in neutron-deuteron ( $nd$ ) breakup are about 20% larger than predicted by theory [Cou12, Sie02, Rua07, Set05].

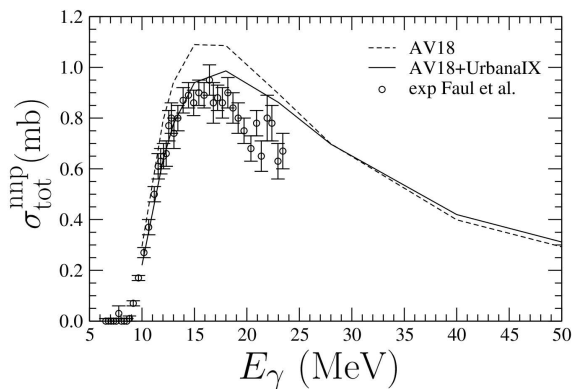


Figure 5.8: Total cross section for three-body  ${}^3\text{H}$  photodisintegration.

The differential cross section measurements will be performed with sufficient accuracy to re-

solve discrepancies in existing data for the total cross section and to obtain a value for the  ${}^1\text{S}_0$   $nn$  scattering length  $a_{nn}$ . This reaction is well suited for investigating features of the  $nn$  interaction because of its high sensitivity to details of the  $nn$  force and its low sensitivity to 3N force effects. The existing total-cross-section data [Fau81] for this reaction in comparison with 3N calculations [Ski02] are shown in Fig. 5.8.

These discrepancies suggest that the  ${}^1\text{S}_0$   $nn$  force might be stronger than would be expected from charge symmetry. We are conducting two complementary measurements at TUNL to gain insight into this dilemma: cross-section measurements of  $nn$  QFS in  $nd$  breakup and the  ${}^3\text{H}(\gamma,p)nn$  reaction. The  $nd$ -breakup experiment will be conducted in the tandem lab, and the latter measurements will be carried out at HI $\gamma$ S.

The experimental setup to be used for our measurements is shown in Fig. 5.9. The performance goals of the system are:

- An energy resolution of  $\leq 300$  keV for protons around 4.5 MeV, including about a 1.5% spread in the beam energy;
- Measurement for each event of  $\theta$ , the polar angle relative to the  $\gamma$ -ray beam axis, to  $0.5^\circ$  and  $\phi$ , the azimuthal angle measured from the horizontal scattering plane, to  $1^\circ$ ;
- Construction from thin and low-density materials, to minimize proton energy loss en route to the detectors;
- Particle identification of  $\alpha$ ,  $d$ , and  $p$ ; and

- Provision for eventual placement of liquid-scintillator neutron detectors 1.5 m from the targets at  $\theta = 90^\circ$  and distributed in  $\phi$ .

The detector system will consist of symmetric sets of wire chambers on both sides of the targets, with silicon strip detectors (SSDs) behind the wire chambers. The wire chambers will provide three position measurements for each event, and the SSDs will provide one dimension of position plus measurement of particle energy. With this information, it will be possible to reconstruct particle tracks through the detectors. Most background processes will produce particles with higher energies than events in the region of interest. The events remaining after an energy cut will be discriminated using  $\Delta E$ - $E$  particle identification, a requirement for coincidence with beam pulses, and target fiducial cuts. Neutron detectors will be added to allow for kinematically complete measurements of configurations of particular interest. The system will be commissioned in the fall of 2014 using  $^3\text{He}$  and  $^2\text{H}$  targets.

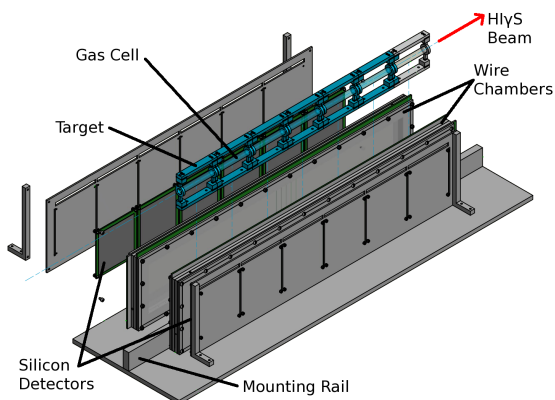


**Figure 5.9:** (Color online) Exploded schematic view of the experimental setup. The targets will be mounted to a rail located between the wire chambers. On both sides of the targets are a set of wire chambers followed by SSDs. The apparatus is about 80 cm long by 30 cm high. By using a linearly polarized beam with the polarization plane perpendicular to the face of the detectors, about 90% of the protons are within the detector acceptance in the  $\phi$  direction. The neutron detectors are not shown.

We are investigating the feasibility of using SSDs that are available at Fermilab. Detector samples from previous experiments were obtained from Fermilab to evaluate their efficacy in this experiment. There are two models available:

500- $\mu\text{m}$ -thick units produced for the CMS detector by ST Microelectronics, and 300- $\mu\text{m}$ -thick Hamamatsu detectors originally intended for the D0 upgrade. The former were obtained with multiplexed APV25 readout chips on kapton hybrids. The position resolution of both detectors exceeds the requirements of this experiment, but testing is necessary to determine if it will be possible to achieve an energy resolution of  $\leq 100$  keV FWHM for low-energy protons. This testing will be carried out in the tandem laboratory.

A GEANT4 simulation was written during the summer of 2013. The geometry of the experimental setup was entered into the simulation by reading CAD files of the detector systems. This simplifies the process of updating changes to the geometry and reduces the risk of inconsistencies. The simulated data will be used to develop and test the data analysis software, the methods for making fiducial cuts, and improved calculations of systematic uncertainties. It will also be employed for optimizing the setup geometry and performance specifications. Refinements are ongoing.

Each side of the detector system will have a set of three wire chambers sandwiched together such that they share two of the four total cathode planes. The cathodes will consist of thin aluminized Mylar, with an anode-cathode spacing of approximately 7 mm and anode wire spacing of 2 mm or greater. The working gas will be helium with a quenching admixture. The system will be surrounded by helium, which will help reduce proton energy loss, help exclude contaminant gases, and minimize silicon-detector exposure to moisture and oxygen. Protons in the region of interest will deposit roughly 1 MeV or more in the wire chambers, providing a strong  $\Delta E$  signal for use in particle identification and tracking.

- 
- [Cou12] A. Couture, Phys. Rev. C, **85**, 054004 (2012).
- [Fau81] D. Faul, Phys. Rev. C, **24**, 849 (1981).
- [Rua07] X. Ruan, Phys. Rev. C, **75**, 057001 (2007).
- [Set05] H. Setze, Phys. Rev. C, **71**, 034006 (2005).
- [Sie02] A. Siepe, Phys. Rev. C, **65**, 034010 (2002).
- [Ski02] R. Skibinski, Ph.D. thesis, Jagiellonian University, 2002.

## 5.3 Study of Many-Body Systems

### 5.3.1 Measurement of the Isovector Giant Quadrupole Resonance in $^{124}\text{Sn}$ via Polarized Compton Scattering at HI $\gamma$ S

M.H. SIKORA, G. FELDMAN, *George Washington University, Washington DC*; M.W. AHMED, A. KAFKARKOU, D.P. KENDELLEN, J.M. MUELLER, L.S. MYERS, W.R. ZIMMERMAN, H.R. WELLER, *TUNL*

**We have measured the isovector giant quadrupole resonance in  $^{124}\text{Sn}$  using linearly polarized nuclear Compton scattering for incident photon energies of 20 to 34 MeV. Scattered photons were detected in the HI $\gamma$ S NaI detector array. The ratio of out-of-plane to in-plane yields is sensitive to the resonance parameters. Preliminary values for  $^{124}\text{Sn}$  are presented.**

As part of the Compton@HI $\gamma$ S program, we conducted a polarized nuclear Compton scattering measurement on  $^{124}\text{Sn}$  to measure its isovector giant quadrupole resonance (IVGQR). Nuclear-Compton-scattered photons were measured at  $\theta = 55^\circ$  and  $125^\circ$  in planes parallel and perpendicular to the plane of photon polarization using the eight-element NaI calorimeter at HI $\gamma$ S known as HINDA (see Fig. 5.10). Based on a phenomenological model of the Compton-scattering amplitude developed in Ref. [Wri85], the polarization ratio  $R(\theta) = \sigma_\perp / \sigma_\parallel$  is parameterized by

$$\frac{\sigma_\perp}{\sigma_\parallel} = [\cos^2 \theta + f_{\text{E1E2}}]^{-1}. \quad (5.1)$$

The  $(\cos^2 \theta)^{-1}$  term is the value of  $R(\theta)$  in the absence of E2 strength, while the second term,  $f_{\text{E1E2}}$ , arises due to the interference of the E1 and E2 amplitudes, with

$$f_{\text{E1E2}} = \frac{2|f_{\text{E2}}| \cos(\phi_{\text{E2}} - \phi_{\text{E1}}) [\cos^3 \theta - \cos \theta]}{|f_{\text{E1}} + D(E_\gamma, \theta)|}, \quad (5.2)$$

where  $\phi_{\text{E1}}$  and  $\phi_{\text{E2}}$  are the amplitude phases, and  $D(E_\gamma, \theta)$  is the modified Thomson amplitude. The quantity  $f_{\text{E1E2}}$  changes sign for  $\theta$  symmetric about  $90^\circ$  and is maximal at  $55^\circ$  and  $125^\circ$ . The sign change between forward and backward angles can be used to identify the pure E1 contribution to  $R(\theta)$ , and any deviation from this line is an unambiguous observation of E2 strength. The accurate extraction of E2 strength by measuring  $R(\theta)$  at both forward and backward angles significantly reduces the uncertainty in the extracted IVGQR parameters, as was first demonstrated at

HI $\gamma$ S in  $^{209}\text{Bi}$  [Hen11]. These measurements are a convenient way to study the symmetry energy term in the nuclear equation of state [RM13], which can provide insight into the properties of neutron stars [Pie11].

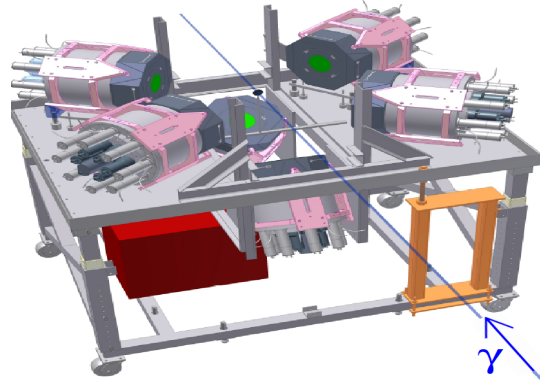


**Figure 5.10: (Color online) Drawing of HINDA and the target. The upper vertical detectors are not shown for visual clarity.**

The beam time consisted of approximately ninety hours of production running at fifteen incident photon energies from  $E_\gamma = 20$  to 34 MeV. This includes scattering with a circularly polarized beam at  $E_\gamma = 20$  and 27.5 MeV, to correct for instrumental asymmetries. Typical spectra at forward and backward angles are shown in Fig. 5.11. The backward-angle spectra are background-free, while at forward angles, a non-negligible background from atomic interactions extends into the elastic peak.

Yields were extracted using a GEANT4 simula-

tion of the Compton scattering process to obtain the response function of each HINDA core. These simulated spectra were then convolved with a Gaussian to fit the scattering data, with the addition of an exponential at forward angles. This exponential was then subtracted from the scattering spectrum. At each photon-beam energy, the convolved response functions were used to determine consistent summing windows with a constant fraction of the GEANT4 spectrum within the integration region for each core.

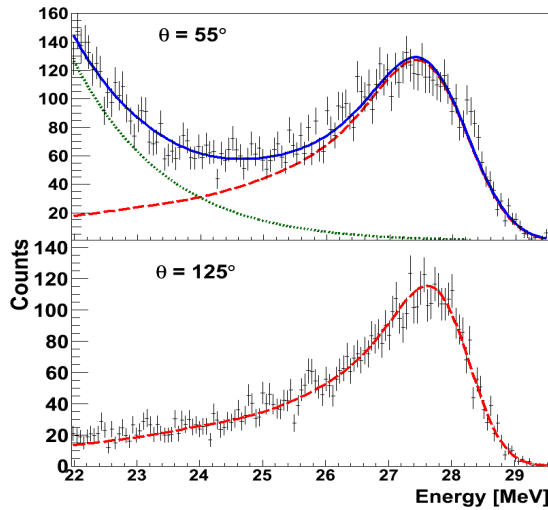


Figure 5.11: (Color online) Sample spectra at forward and backward angles. The simulated detector response convolved with a Gaussian is shown as dashed lines. An exponential (dotted line) is added at forward angles to model the background, and the total fit (solid line) is the sum of these two contributions.

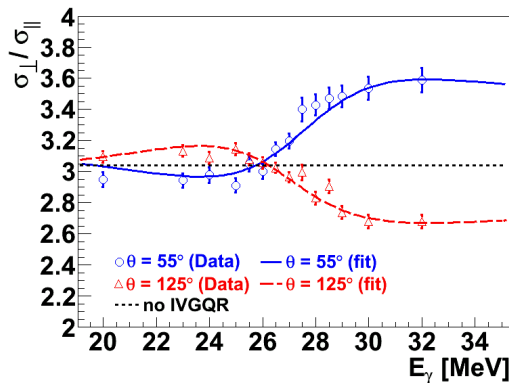


Figure 5.12: (Color online) Preliminary fit of the measured polarization ratios to the model prediction. The pure E1 contribution is given by the straight, short-dashed line. The 34 MeV data are still under analysis and are not shown.

After applying small corrections obtained from the circularly polarized scattering data, the ratio of perpendicular to parallel yields was formed at both forward and backward angles (Fig. 5.12). The IVGQR excitation energy, width  $\Gamma$ , and strength in units of the isovector energy weighted sum rule appear as free parameters in the  $f_{E2}$  term in Eq. (5.1). Preliminary results for the resonance parameters are shown in Fig. 5.13 alongside previous IVGQR measurements [Hen11, Pit80, Zor87].

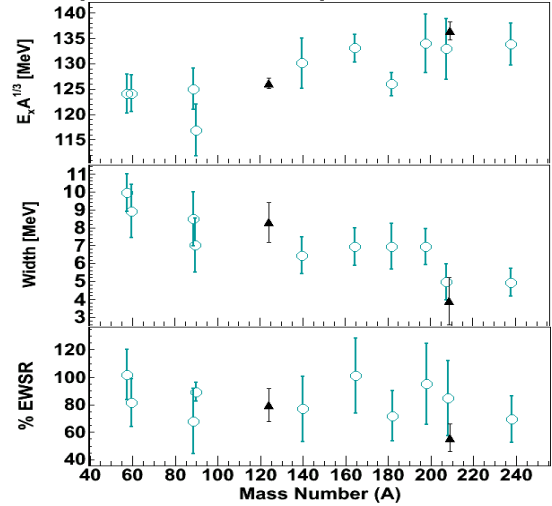


Figure 5.13: (Color online) Extracted IVGQR parameters of previous experiments (open circles) and the HI $\gamma$ S results (triangles).

Future work will include the characterization of systematic uncertainties and testing the stability of the procedure used to extract the resonance parameters.

[Hen11] S. Henshaw *et al.*, Phys. Rev. Lett., **107**, 22501 (2011).

[Pie11] J. Piekarewicz, Phys. Rev. C, **83**, 034319 (2011).

[Pit80] R. Pitthan, In F. Bertrand, editor, *Giant Multipole Resonances: Proceedings of the Giant Multipole Resonance Topical Conference*, Oak Ridge, TN, 1980. Harwood Academic Publishers.

[RM13] X. Roca-Maza *et al.*, Phys. Rev. C, **87**, 034301 (2013).

[Wri85] D. Wright *et al.*, Phys. Rev. C, **32**, 1174 (1985).

[Zor87] R. Zorro *et al.*, Nucl. Phys., **A472**, 125 (1987).

### 5.3.2 Beam Test of Compton Scattering from Unpolarized $^3\text{He}$

H. GAO, M.W. AHMED, P. CHU, C.R. HOWELL, T. CLEGG, M. HUANG, S.S. JAWALKAR, A. KAFKARKOU, H. KARWOWSKI, D. KENDELLEN, G. LASKARIS, M. MEZIANE, L.S. MYERS, J.M. MUELLER, C. PENG, M. SIKORA, H.R. WELLER, Y. WU, X. YAN, Q.J. YE, A. YOUNG, Y. ZHANG, *TUNL*; T. AVERETT, *College of William and Mary, Williamsburg, VA*; J.P. CHEN, *Thomas Jefferson National Accelerator Facility, Newport News, VA*; D. DUTTA, *Mississippi State University, Starkville, MS*; X. QIAN, *Brookhaven National Lab, Upton, NY*; Q. YE, *Oak Ridge Associated Universities, Oak Ridge, TN*

The first measurement of neutron spin polarizabilities using a circularly polarized photon beam and a polarized  $^3\text{He}$  target as an effective polarized neutron target was proposed in 2010. It was approved for 60 hours of beam time for the performance of a test at 100 MeV. The beam test was performed in March 2013, and the results are presented.

Neutrons and protons (nucleons) are basic building blocks of the visible matter in the universe. To understand the internal structure of nucleons, probes such as electrons and photons have been used in various experiments. When a nucleon is probed by photons, the nucleon structure manifests itself in the response of the nucleon to the photon field (external electromagnetic field). The spin-independent response of the nucleon to an external electromagnetic field through Compton scattering can be parameterized by the electromagnetic polarizabilities  $\alpha$  and  $\beta$ , while the spin-dependent ones are parameterized by the spin polarizabilities  $\gamma_1$ ,  $\gamma_2$ ,  $\gamma_3$  and  $\gamma_4$  [Rag93]. Compared with the nucleon's electromagnetic polarizabilities, very little is known about the nucleon's spin polarizabilities. The only quantities that have been determined experimentally are the forward and backward spin polarizabilities.

Recent theoretical investigations of double-polarized elastic Compton scattering from polarized  $^3\text{He}$  have demonstrated sensitivity to the neutron's spin polarizabilities [Shu09]. The spin-dependent differential-cross-section difference (DCS difference)  $\Delta_z$  corresponds to the difference of the DCSs with the target spin being parallel and anti-parallel to the circularly polarized photon beam. The sensitivity of  $\Delta_z$  to  $\gamma_1$  from Ref. [Shu09] is shown with simulated data points in Fig. 5.14. Experimentally measured  $\Delta_z$  values will provide constraints on  $\gamma_1$ ,  $\gamma_2$ , and  $\gamma_4$ .

The measurement of elastic Compton scattering using a polarized  $^3\text{He}$  target and a circularly

polarized photon beam was proposed to the HI $\gamma$ S PAC in 2010, requesting a beam flux of at least  $5 \times 10^7 \gamma/s$  at 120 MeV. A 60-hour beam test was approved by the PAC for studying the signal-to-background ratio.

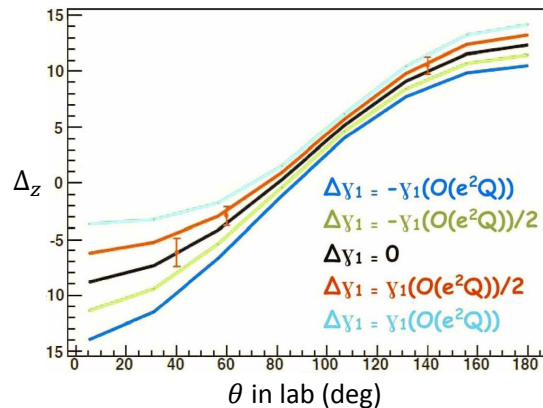


Figure 5.14: (Color online) Calculated asymmetry  $\Delta_z$  (in units of nb/sr) at an incident photon energy of 120 MeV. Different curves correspond to varying  $\gamma_1$  by different amounts ( $\Delta\gamma_1$ ), with positive variations raising the value of  $\Delta_z$  and negative variations lowering it.

The beam test with an unpolarized  $^3\text{He}$  target took place in March 2013. The average photon flux on target was  $6.7 \times 10^6 \gamma/s$  at 87 MeV. The beam was incident on the  $^3\text{He}$  target cell named ELVIS, which had a filling density of 7.77 amg. Apart from  $^3\text{He}$ , the cell contained 0.11 amg of  $\text{N}_2$ . A total of 10 hrs were used to acquire data

on the N<sub>2</sub> reference cell and 50 hrs on the <sup>3</sup>He cell.

The scattered photons were detected by the HI $\gamma$ S NaI Detector Array (HINDA). Two HINDA detectors were positioned at each of three scattering angles. The count rate of Compton scattering at scattering angles of 40°, 87°, and 130° were estimated to be 0.17, 0.15, and 0.09 counts per hour, respectively. Each HINDA detector consists of a core NaI detector, surrounded by a ring of 8 NaI detector shields. This core-and-shield structure was used for cosmic-ray-background rejection.

To reject the beam-induced photon background, we used tungsten collimators to cover the windows of the <sup>3</sup>He cell; lead walls positioned upstream of the target to suppress the beam-induced background; and vacuum pipes upstream and downstream of the target to suppress scattering from the air. In addition to the anti-coincidence-shield-cut algorithm developed based on a GEANT4 simulation, cosmic background is also suppressed by the beam's time-structure.

Figure 5.15 shows a comparison between the energy-deposition distributions in the core of the detector with and without cuts. The cuts used are: the anti-coincidence-shield cut, the beam-time-structure cut, and their combination. A comparison between <sup>3</sup>He and N<sub>2</sub> target runs, and a cosmic-ray background run (no beam, no target) can be seen in Fig. 5.16. All curves are normalized to one hour and have the anti-coincidence-shield cut.

The beam test is considered successful, since no beam-induced background was observed between 80 and 90 MeV, where the signal from the Compton scattering on the <sup>3</sup>He nucleus is expected. But the low count rate of Compton signal prohibits the acquisition of statistically meaningful data in a reasonable amount of beam time. We conclude that an increase in the beam flux by at least one order of magnitude is necessary for a successful measurement of double-polarized elastic Compton scattering from polarized <sup>3</sup>He.

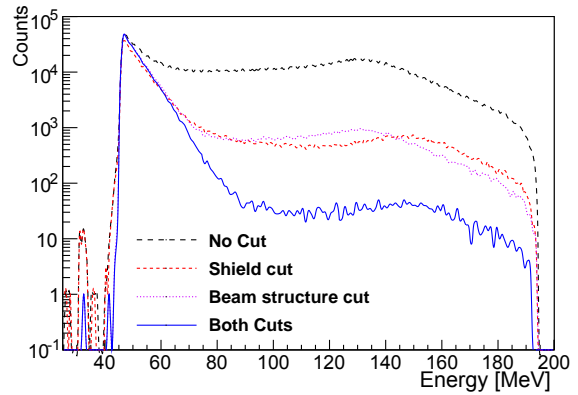


Figure 5.15: (Color online) <sup>3</sup>He run with cosmic rejection methods

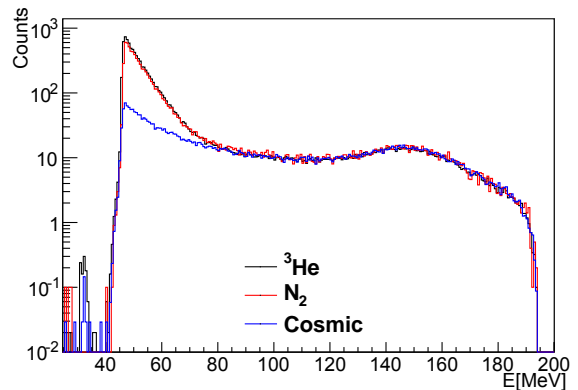


Figure 5.16: (Color online) <sup>3</sup>He, N<sub>2</sub>, and cosmic (no beam, no target) runs with the anti-coincidence-shield-cut. The <sup>3</sup>He and N<sub>2</sub> results are indistinguishable, while the N<sub>2</sub> curve is lower near the maximum.

[Rag93] S. Ragusa, Phys. Rev. D, **47**, 3757 (1993).

[Shu09] D. Shukla, A. Nogga, and D. Phillips, Nucl. Phys., **A819**, 98 (2009).



# Applications of Nuclear Physics and Nuclear Data Evaluation

---

Chapter 6

- **Homeland and National Nuclear Security**
- **National Ignition Facility Activities**
- **Public Health Research**
- **Plant Physiology Research**
- **Nuclear Data Evaluation**

## 6.1 Homeland and National Nuclear Security

### 6.1.1 Dipole Transitions in $^{240}\text{Pu}$

B. FALLIN, M. BHIKE, M.E. GOODEN, C.R. HOWELL, D. TICEHURST, W. TORNOW, *TUNL*; R.S. PEDRONI, *North Carolina A&T State University, Greensboro, NC*

**During this reporting period we measured the distribution of dipole transitions in  $^{240}\text{Pu}$  over the excitation energy range between 1.9 and 3.0 MeV using nuclear resonance fluorescence. The energy, spin, parity, and branching ratios of observed de-excitations in  $^{240}\text{Pu}$  have been determined. Observed dipole transitions are in agreement with those previously reported.**

The characterization of dipole states is important for studying the collective-motion and single-particle degrees of freedom in deformed nuclei such as the actinides. In addition, the identification of strong dipole excitations in the actinides at  $\gamma$ -ray energies above 2 MeV is important for developing technologies for remote interrogation of cargo and for the analysis of spent nuclear fuel using  $\gamma$ -ray beams. Nuclear resonance fluorescence (NRF) is a powerful technique for studying the properties of low-lying dipole states in nuclei. This technique is non-destructive and can be used to identify isotope-specific signatures in the measured energy spectrum of the detected  $\gamma$  rays. Recent NRF studies at TUNL have focused on even-even actinides due to the decreased fragmentation of their dipole states (and hence greater expected dipole strength) compared to even-odd nuclei. Significant E1 and M1 strength has previously been observed in other even-even actinides, such as  $^{232}\text{Th}$  [Ade11] and  $^{238}\text{U}$  [Ham12]. In the present study, dipole transitions in  $^{240}\text{Pu}$  between 1.9 and 3.0 MeV were determined.

Dipole transitions were excited using linearly-polarized, quasi-monoenergetic  $\gamma$  rays produced at HI $\gamma$ S. The  $\gamma$ -ray beam was delivered to the target at energies from 1.95 to 2.95 MeV in 100 keV steps. The beam was collimated through a 0.75 in. circular aperture in lead, resulting in a FWHM energy spread of 3 to 4.5%. The experimental setup is shown in Fig. 6.1. The incident  $\gamma$  rays were polarized in the horizontal plane and four HPGe detectors were placed at  $90^\circ$  around the  $^{240}\text{Pu}$  target, two in and two out of the plane of beam polarization. The detectors were positioned such that their front faces were

an average of approximately 8 cm from the center of the  $^{240}\text{Pu}$  target. In this configuration, E1 transitions emit  $\gamma$  rays only in the direction of the detectors in the vertical plane. In contrast, states that decay via M1 and E2 transitions emit  $\gamma$  rays only in the direction of the detectors in the horizontal plane. The target was irradiated for between 3.5 and 5.5 hours at each incident  $\gamma$ -ray beam energy where dipole transitions were observed. At incident  $\gamma$ -ray energies where transitions to the ground state were observed in the horizontal plane detectors, additional measurements were made with detectors at  $90^\circ$  and  $135^\circ$  in the plane of beam polarization for a enough time to allow M1 transitions to be distinguished from E2 transitions. All detectors were passively shielded with 2.5 to 5 mm of lead and with 2.5 mm of copper disks in front of the detector face to reduce the counting rate from scattering of the primary  $\gamma$ -ray beam and from the intrinsic activity of the  $^{240}\text{Pu}$  target.

The target was obtained on loan from Lawrence Berkley National Laboratory. It consisted of 4.65 g of  $^{240}\text{Pu}$  in the form of  $\text{PuO}_2$  powder. The target contained milligram quantities of  $^{239}\text{Pu}$ ,  $^{241}\text{Pu}$ , and  $^{241}\text{Am}$ . The  $\text{PuO}_2$  powder was wrapped in 30- $\mu\text{m}$ -thick aluminum foil and placed inside a 2.8 cm diameter aluminum canister. The walls of the canister were approximately 1 mm thick. To reduce the effects of  $\gamma$ -ray scattering off of air in the vicinity of the detectors, the target canister was placed inside an evacuated plastic tube.

The energy distribution of the  $\gamma$ -ray beam was measured at low flux using a high efficiency HPGe detector positioned at  $0^\circ$ . This measurement was also used to determine the primary  $\gamma$ -

ray flux on the  $^{240}\text{Pu}$  target by cross calibrating the  $0^\circ$  detector with an upstream plastic scintillator paddle. Since the  $\gamma$  rays at HI $\gamma$ S are produced by Compton-backscattering, the  $\gamma$ -ray beam distribution possesses strong spatial-energy correlation. Simulations of the  $0^\circ$  detector were performed with GEANT4 to determine the absolute efficiency of the detector for each  $\gamma$ -ray energy in the distribution. The  $\gamma$ -ray distribution measured by the  $0^\circ$  detector was then corrected by these efficiency values. Paddle counts were also corrected to subtract counts from natural background and beam contaminants. Using the cross calibration, the  $\gamma$ -ray flux on target was found to be approximately  $2.5 \times 10^6$   $\gamma/s$  for a typical production run with a 2.45 MeV incident  $\gamma$ -ray beam.



Figure 6.1: (Color online) Experimental setup with two detectors at  $90^\circ$  in the plane of beam polarization and two detectors in the plane perpendicular to the plane of beam polarization.

The distribution of dipole transitions in  $^{240}\text{Pu}$  has been determined for excitation energies between 1.9 and 3.0 MeV. The energy, spin, and parity have been determined for each observed de-excitation. In addition to ground state transitions, accompanying transitions from the same parent level to the first excited state of  $^{240}\text{Pu}$  at 42.8 keV were observed for most dipole excitations. Nine confirmed M1 ( $J^\pi = 1^+$ ) ground state transitions, each with an accompanying transi-

tion to the first excited state, and an additional two likely M1 transitions have been observed. New  $\gamma$ -ray transitions to the ground state with energies of 2444.3 and 2834.3 keV were observed for the first time. The latter transition is shown in Fig. 6.2. The other dipole transition energies are in agreement with those previously observed by Quiter *et al.* [Qui12]. Branching ratios have also been calculated for transitions observed at incident  $\gamma$ -ray energies of 2.45, 2.65, and 2.85 MeV. Analysis is ongoing, and branching ratios and integrated cross sections for all observed transitions will be determined in the coming year.

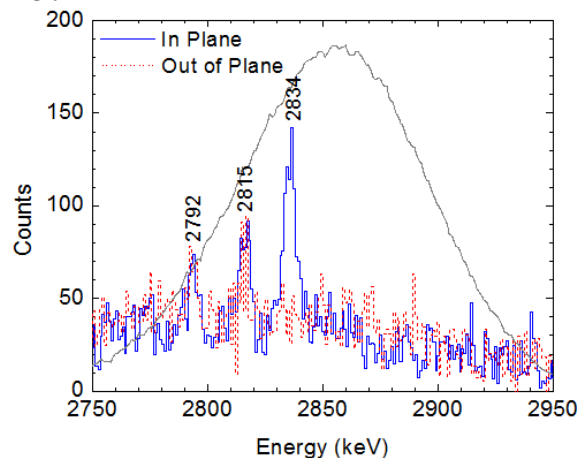


Figure 6.2: (Color online) Energy spectra (with background subtracted) showing dipole transitions in  $^{240}\text{Pu}$  with an incident  $\gamma$ -ray beam energy of 2.85 MeV. The spectra are representative of approximately four hours of irradiation. The beam envelope is overlaid for reference.

- 
- [Ade11] A. S. Adekola *et al.*, Phys. Rev. C, **83**, 034615 (2011).
- [Ham12] S. L. Hammond *et al.*, Phys. Rev. C, **85**, 044302 (2012).
- [Qui12] B. J. Quiter *et al.*, Phys. Rev. C, **86**, 034307 (2012).

### 6.1.2 Fission-Product Yields of $^{235}\text{U}$ , $^{238}\text{U}$ , and $^{239}\text{Pu}$ at Incident Neutron Energies of 1.4, 2.4 and 14.8 MeV

M.E. GOODEN, M. BHIKE, B. FALLIN, S. FINCH, C.R. HOWELL, J.H. KELLEY, W. TORNOW, TUNL; C.W. ARNOLD, M.M. FOWLER, D.J. VIERA, J.B. WILHELMY, *Los Alamos National Laboratory, Los Alamos, NM*; J.A. BECKER, M.A. STOYER, A.P. TONCHEV, *Lawrence Livermore National Laboratory, Livermore, CA*

The possible energy dependence for fission product isotope yields is being studied using three dual-fission ionization chambers dedicated to  $^{235}\text{U}$ ,  $^{238}\text{U}$ , and  $^{239}\text{Pu}$  target foils. The targets were irradiated at the tandem accelerator using nearly mono-energetic neutron beams at energies of 1.37, 2.4 and 14.8 MeV. The activated target foils were counted for about two months in the low-background counting area. Relative and absolute fission-product yields have been determined for numerous isotopes.

Based on examinations of the existing fission-product-yield data [Cha10, Tho12], it was determined that there is compelling evidence that the yield for certain fission-product isotopes depends on the incident neutron energy. Focusing on the  $^{239}\text{Pu}$  fission product  $^{147}\text{Nd}$ , an energy dependence in the range of 0.2 to 1.9 MeV was found, as seen in Fig. 6.3. A joint TUNL-LANL-LLNL collaboration has been formed to verify this energy dependence and fill in needed data points for neutron energies above 2 MeV (see Fig. 6.4) using the nearly mono-energetic neutron beams at TUNL.

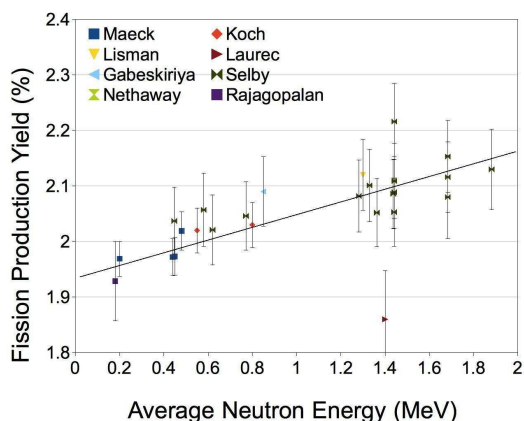


Figure 6.3: (Color online) Low energy fission-product-yield data for  $^{147}\text{Nd}$ . Least-squares fitting of the data was done by Chadwick et al. [Cha10].

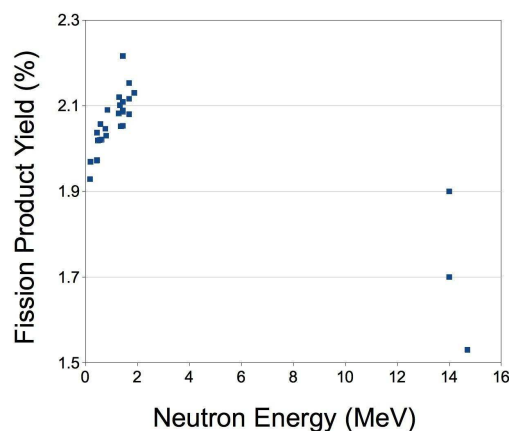


Figure 6.4: (Color online) Available  $^{147}\text{Nd}$  fission-product-yield data from  $^{239}\text{Pu}$  over the entire energy range of interest.

#### 14.8 MeV Data

The first measurement during the current reporting period was done at 14.8 MeV. Neutrons at this energy are produced via the  $^3\text{H}(d,n)^4\text{He}$  reaction, whose large  $Q$  value of 17.589 MeV allows neutron production using incident deuteron energies below the deuteron breakup threshold. Therefore, this reaction at this energy produces mono-energetic neutrons and no corrections for off-energy neutrons are needed. The discrepant data around 14 MeV, shown in Fig. 6.4, show the need for a reliable measurement in this energy region to confirm or reject the existing data

sets. Preliminary analysis of our data suggests that the lower two data points in the figure are incorrect.

### 1.37 and 2.4 MeV Data

Neutrons at 1.37 MeV are produced using the  ${}^3\text{H}(p,n){}^3\text{He}$  reaction. Here, there is a negligible contribution from off-energy neutrons which, at higher proton energies, are produced by  $(p,n)$  reactions on the copper backing of the tritiated target. Therefore, the neutron spectrum is very clean, and no corrections to the determined fission-product yields are needed. This energy gives a convenient data point near the center of the energy region in Fig. 6.3.

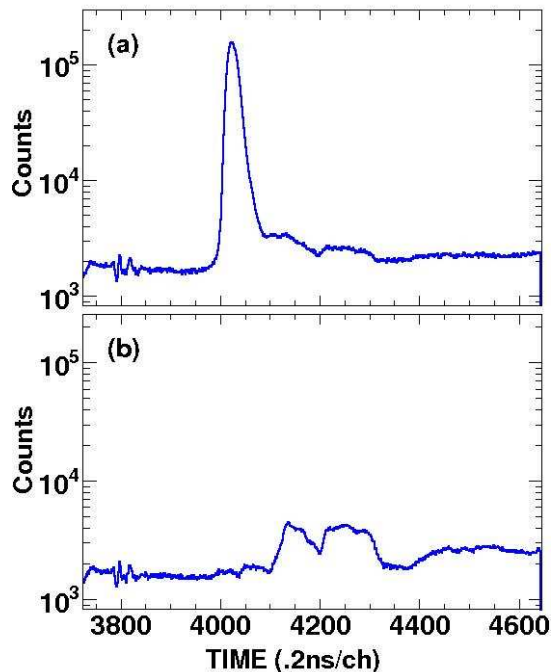


Figure 6.5: (Color online) Neutron time-of-flight using a BC-501A scintillator neutron detector placed 295 cm downstream from the neutron-production source. (a) with a tritiated target. (b) with an identical untritiated target.

At 2.4 MeV, neutrons are produced by the same reaction as at 1.37. However, at this energy  $(p,n)$  neutrons from the backing make a non-negligible contribution to the total fission rate. By using time-of-flight techniques and running

with both our tritiated neutron-production target and an identical but untritiated target, we are able to estimate the off-energy neutron contribution. This test can be seen in Fig. 6.5. We find that the off-energy neutron contribution is about 4%, and therefore the deduced fission product yields (FPYs) require correction. The data at 1.37 and 2.4 MeV are currently being analyzed.

### Future Work

A measurement at 0.5 MeV using the  ${}^7\text{Li}(p,n){}^7\text{Be}$  reaction is planned for late 2013 or early 2014. This reaction has a  $Q$  value of -1.644 MeV and therefore allows the production of low-energy neutrons using modest proton energies. However, at these proton energies, reaction channels in various target backing materials are open, so care must be taken in constructing the lithium targets. Also, there exists an off-energy channel due to an excited state of  ${}^7\text{Be}$  at 429 keV, thus limiting the range of energies for mono-energetic neutrons from this reaction to below 650 keV. With this data point, we will have 3 measurements in the 0 - 2 MeV energy range and will be able to make a very strong case in confirming or refuting the energy dependence of fission products like  ${}^{147}\text{Nd}$ .

### Summary

As part of a TUNL-LANL-LLNL collaboration, FPY studies of  ${}^{235}\text{U}$ ,  ${}^{238}\text{U}$  and  ${}^{239}\text{Pu}$  at TUNL were continued. Using dual-fission chambers as a means to measure the neutron fluence on our samples, FPYs as a function of incident neutron energy are being determined. Both relative measurements of FPYs and absolute determinations of the FPYs have been made. Analysis is underway on all data sets. Future measurements are planned to verify the observed energy dependence in the  ${}^{147}\text{Nd}$  yield, and to fill in the obvious gap in data between 2 and 14 MeV as seen in Fig. 6.4.

[Cha10] M. Chadwick *et al.*, Nucl. Data Sheets, **111**, 2964 (2010).

[Tho12] I. Thompson *et al.*, Nucl. Sci. Eng., **171**, 85 (2012).

## 6.2 National Ignition Facility Activities

### 6.2.1 Study of the $^{169}\text{Tm}(n,2n)^{168}\text{Tm}$ and $^{169}\text{Tm}(n,3n)^{167}\text{Tm}$ Reactions and the National Ignition Facility

M. BHIKE, M.E. GOODEN, W. TORNOW, *TUNL*; M. BOSWELL, *LANL*; A.P. TONCHEV, *LLNL*

The reactions  $^{169}\text{Tm}(n,2n)^{168}\text{Tm}$  and  $^{169}\text{Tm}(n,3n)^{167}\text{Tm}$  have been studied at TUNL using the activation technique at incident neutron energies of 15.8 and 17.8 MeV in preparation for inertial confinement fusion experiments at the National Ignition Facility. The yield ratio  $^{167}\text{Tm}/^{168}\text{Tm}$  can be used to obtain information on the deuterium-tritium plasma density achieved in inertial-confinement-fusion capsules. The TUNL measurements played an important role in determining the sensitivity of the measured yield ratio and inferring the deuterium-tritium plasma density obtained in two inertial-confinement-fusion shots.

Researchers at the National Ignition Facility (NIF) at LLNL are trying to find out why energy “break-even” has not yet been achieved when their 192 laser beams are directed onto a tiny pellet filled with a mixture of deuterium and tritium. Unknown plasma-physics phenomena are currently blamed for the failure of NIF (a facility costing more than five billion dollars) to produce the predicted neutron yield needed to gain as much energy as is put into the deuterium-tritium (DT) cell by the facility’s powerful lasers.

Nuclear physics reactions are an important diagnostic tool for obtaining information on the density of the plasma created in inertial-confinement-fusion (ICF) experiments. Of special interest is the ratio of neutrons with energies above and below 14.7 MeV, because it provides a measure of the density of the DT plasma.

The reaction  $^3\text{H}(d,n)^3\text{He}$ , with its  $Q$  value of 17.589 MeV, is known to produce 14.1 MeV neutrons at collision energies around 10 keV, the typical energies present in DT-ICF plasmas. However, higher and lower neutron energies are also produced in a DT-ICF plasma. Here, we concentrate on the higher energy neutrons, which are called neutrons-in-flight or tertiary neutrons. In the DT plasma, the density is expected to be as large as  $10^3$  g/cm<sup>3</sup>. At such high densities, neutrons produced initially via the  $^3\text{H}(d,n)^3\text{He}$  reaction can scatter elastically off deuterons and tritons, producing recoil deuterons and tritons in the MeV energy range. These, in turn, can initiate the  $^3\text{H}(d,n)^3\text{He}$  or  $^2\text{H}(t,n)^3\text{He}$  reactions, producing neutrons with energies as high as 30

MeV. Therefore, the ratio of neutrons with energies above and below 15 MeV is a direct measure of the density in the ICF plasma. Unfortunately, due to the high yield of about  $10^{15}$  neutrons per shot (where a shot lasts less than a nanosecond), direct measurements of the neutron energy distribution produced in ICF plasmas is not trivial with existing direct-detection techniques such as neutron-time-of-flight.

However, the neutron activation technique using the mono-isotopic element thulium ( $^{169}\text{Tm}$ ) is a potentially powerful tool for such a task. A number of factors make it stand out as a candidate technique. These include its threshold energies of 8.1 MeV for the  $^{169}\text{Tm}(n,2n)^{168}\text{Tm}$  reaction and 15.0 MeV for the  $^{169}\text{Tm}(n,3n)^{167}\text{Tm}$  reaction, the well-known cross sections for these two reactions, the convenient half lives ( $T_{1/2} = 93$  d for  $^{168}\text{Tm}$  and  $T_{1/2} = 9.2$  d for  $^{167}\text{Tm}$ ), and the strong  $\gamma$ -ray lines for  $^{168}\text{Tm}$  (198 keV occurring in 51% of decays) and  $^{167}\text{Tm}$  (208 keV and 41%). The isotope  $^{167}\text{Tm}$  is produced only by neutrons with energies greater than 15.0 MeV, while the isotope  $^{168}\text{Tm}$  is produced by neutrons with energies above 8.1 MeV. Therefore, the intensity ratio of the two  $\gamma$ -ray lines at 208 keV and 198 keV provides a direct determination of the percentage contribution of neutrons with energies greater than 15.0 MeV to those with energies above 8.1 MeV. This information is then compared to the predictions of plasma-model calculations, in which the stopping power and density of the ICF plasma is an adjustable parameter.

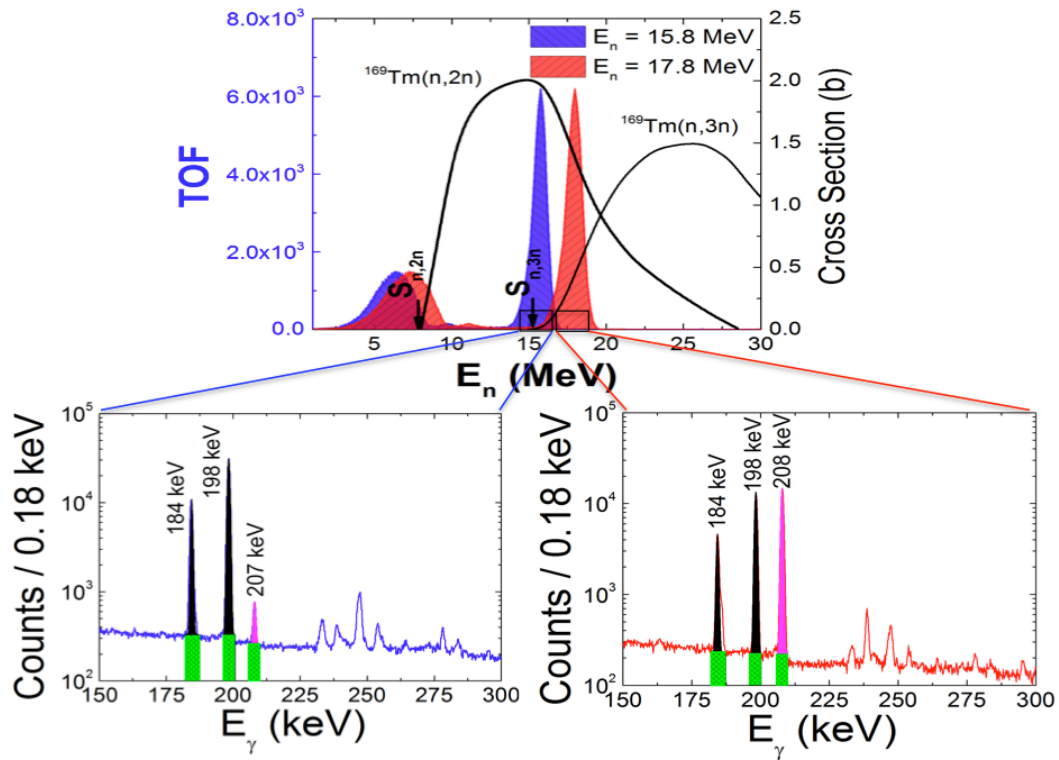


Figure 6.6: (Color online) Neutron energy spectra obtained with the  ${}^2\text{H}(d,n){}^3\text{He}$  reaction at  $E_n = 15.8$  and  $17.8$  MeV and the associated  $\gamma$ -ray spectra from the  $(n,2n)$  and  $(n,3n)$  reactions on  ${}^{169}\text{Tm}$ . The events between 0 and 10 MeV in the neutron energy spectra are due to deuteron breakup reactions associated with the primary neutron reaction  ${}^2\text{H}(d,n){}^3\text{He}$ . The solid curves in the upper panel show the excitation functions for the reactions of interest.

At TUNL, the  ${}^2\text{H}(d,n){}^3\text{He}$  reaction was used to produce  $15.8$  MeV and  $17.8$  MeV neutrons. A square thulium foil,  $12.7$  mm on a side and with a thickness of  $0.1$  mm, was positioned  $17$  mm from the end of the deuterium gas cell. Two layers of aluminized Mylar were wrapped around the thulium foil to avoid oxidation. Gold and aluminum foils with the same area as that of the thulium target were placed behind the thulium foil for neutron fluence determination. This foil assembly was irradiated for twenty-five hours at  $E_n = 15.8$  MeV, and a similar foil assembly was irradiated for three hours at  $E_n = 17.8$  MeV. Figure 6.6 shows the associated neutron energy spectra for  $15.8$  MeV and  $17.8$  MeV incident neutrons, along with the cross sections for the two reactions of interest. The bottom left and right spectra are  $\gamma$ -ray spectra measured with HPGe

detectors at the two energies of interest. The two  $\gamma$ -ray lines at  $198$  and  $208$  keV are clearly visible, with the  $208$  keV line much weaker at  $15.8$  MeV than at  $17.8$  MeV. Preliminary analysis of the  ${}^{169}\text{Tm}(n,2n){}^{168}\text{Tm}$  and  ${}^{169}\text{Tm}(n,3n){}^{167}\text{Tm}$  reaction-cross-section measurements shows that the TUNL values are in good agreement with literature data.

In shots at NIF on September 31, 2013, thulium foils were placed at a distance of about  $0.5$  m from the ICF-DT cell. The activated foils were measured at LANL, and it was found that the tertiary neutron contribution was about  $10^{-4}$  of the total neutrons produced in that shot. This was the first observation of tertiary neutrons in ICF plasmas, and it provided valuable information on the stopping power of charged particles in ICF plasmas.

### 6.2.2 The $^{124}\text{Xe}(n,\gamma)^{125}\text{Xe}$ and $^{124}\text{Xe}(n,2n)^{123}\text{Xe}$ Reactions and NIF

M. BHIKE, W. TORNOW, *TUNL*; N. LUDIN, *University of Denver, Denver, CO*

Measurements of the neutron capture reaction  $^{124}\text{Xe}(n,\gamma)^{125}\text{Xe}$  are underway at energies from 0.4 to 14.8 MeV. In addition, the  $^{124}\text{Xe}(n,2n)^{123}\text{Xe}$  reaction is being studied between threshold and 14.8 MeV. The results of these measurements provide sensitive diagnostic tools for investigating properties of the inertial confinement fusion plasmas at the National Ignition Facility. Since  $^{124}\text{Xe}$  is a p-process nucleus, the neutron capture cross section is also of interest for nuclear astrophysics. Preliminary results are given.

Nuclear reactions play an important role in understanding the complicated physics governing the inertial confinement fusion (ICF) plasma. Currently, a consistent theory of stopping powers for charged particles in ICF plasmas does not exist. However, the neutron energy distribution created in deuterium-tritium ICF plasmas strongly depends on the stopping power of deuterons and tritons in the plasma. Therefore, efforts are underway at the National Ignition Facility (NIF) to accurately measure the neutron energy distribution obtained in deuterium-tritium (DT) shots employing 192 powerful lasers, which deposit up to 500 TW of peak power—1000 times more than the US uses at any one moment—and up to 1.85 MJ of UV light on the DT pellet.

A diagram of the DT pellet is shown in Fig. 6.7. The radius of the pellet is about  $400\ \mu\text{m}$ , and the DT gas pressure is around 20 atm. Radiochemical (radchem) tracer nuclei are bonded to the inside of the ablator (Be or CH), which completely burns away when hit by the 192 laser beams. The goal is to use a mixture of  $^{124}\text{Xe}$  and  $^{136}\text{Xe}$  as radchems, because the two isotopes are expected to have very different neutron capture cross sections in the entire energy range of interest, but equal  $(n,2n)$  cross sections at 14 MeV, if the existing evaluations are correct. The  $^{136}\text{Xe}(n,\gamma)^{137}\text{Xe}$  cross section is predicted to be around 1 mb at 1 MeV, while evaluations predict the capture cross section of  $^{124}\text{Xe}$  to be a factor of five hundred greater. Even at 10 MeV the  $^{124}\text{Xe}$  capture cross section is predicted to be a factor of ten larger than that of  $^{136}\text{Xe}$ . Data for the reactions  $^{136}\text{Xe}(n,\gamma)^{137}\text{Xe}$  (see Sect. 2.1.10) and  $^{136}\text{Xe}(n,2n)^{135}\text{Xe}$  [Bha13] have recently been obtained at TUNL, but data for  $^{124}\text{Xe}$  do not exist,

except for three conflicting measurements for the  $^{124}\text{Xe}(n,2n)^{123}\text{Xe}$  reaction at 14.5 MeV.

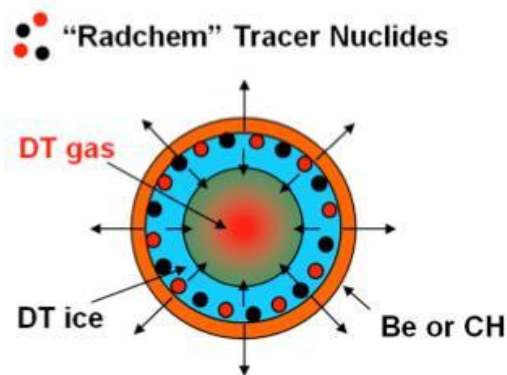


Figure 6.7: (Color online) Schematic view of a deuterium-tritium pellet used at NIF.

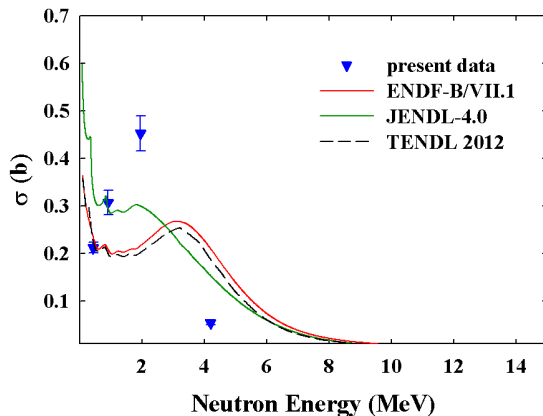
The parameters relevant to the  $^{124}\text{Xe}(n,\gamma)^{125}\text{Xe}$  reaction rates at TUNL and NIF are summarized in Table 6.1. Although the values for the individual parameters are very different at the two facilities, the quantity of interest, neutron fluence times sample mass, is basically the same.

The  $^{124}\text{Xe}$  target gas consists of 2.6968 g enriched to 99.99% and is contained in a stainless steel sphere with an inner diameter of 20.0 mm and wall thickness of 0.6 mm, corresponding to a pressure of about 115 atm. For the  $(n,\gamma)$  measurements, the  $^3\text{H}(p,n)^3\text{He}$  reaction was used to produce neutron beams at 0.4, 1.04, and 1.95 MeV, while the  $^2\text{H}(d,n)^3\text{He}$  was employed at 4.6 MeV. The center of the target sphere was typically positioned 16 mm from the end of the neutron production target. Indium monitor foils were attached to the upstream and downstream

**Table 6.1: Parameters determining the reaction rate of  $^{124}\text{Xe}(n,\gamma)^{125}\text{Xe}$  at TUNL and NIF.**

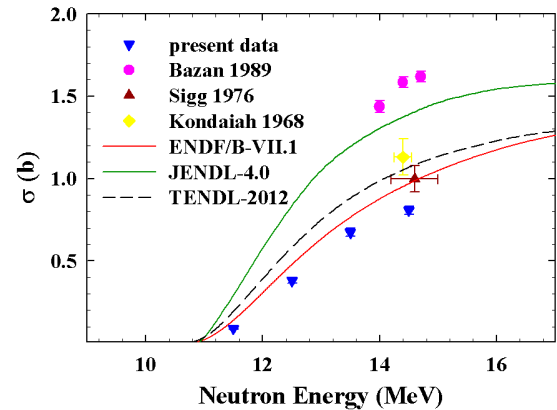
Parameter	TUNL	NIF
Activation time	$1.8 \times 10^4$ s ( $3 \times T_{1/2}$ )	$\sim 10^{-9}$ s
Sample mass	2.7 g ( $1.3 \times 10^{22}$ atoms)	$\sim 1$ $\mu\text{g}$ ( $10^{15}$ atoms)
Neutron flux	$7 \times 10^6$ n/( $\text{cm}^2\text{s}$ )	$\sim 10^{14}$ n/ns
Neutron fluence	$1.3 \times 10^{11}$ n/ $\text{cm}^2$	$\sim 1 \times 10^{18}$ n/ $\text{cm}^2$
Fluence $\times$ sample mass	$1.7 \times 10^{33}$ n/cm $\times$ g	$\sim 1 \times 10^{33}$ n/ $\text{cm}^2 \times$ g

side of the sphere for neutron fluence determination. The sphere assembly was surrounded by a cover made of cadmium to efficiently absorb thermal neutrons. Neutron irradiation times varied between 1.5 and 4 hours. After irradiation,  $\gamma$  rays from the  $^{124}\text{Xe}$ -filled sphere were counted using a well-shielded HPGe detector of known efficiency. The yield of the  $\gamma$ -ray line at 188.418 keV from the decay of  $^{125}\text{Xe}$  with  $I_\gamma = 53.8\%$  and  $T_{1/2} = 16.9$  h was recorded as a function of time. An identical but empty stainless steel sphere was irradiated to prove that there were no  $\gamma$ -ray lines in the region of interest. Preliminary results for the  $^{124}\text{Xe}(n,\gamma)^{125}\text{Xe}$  cross section are shown in Fig. 6.8 along with values from various evaluations. None of the evaluations are in agreement with the experimental data, although the order of magnitude is reasonably well predicted.

**Figure 6.8: (Color online) Preliminary results for the  $^{124}\text{Xe}(n,\gamma)^{125}\text{Xe}$  cross section compared to various evaluations.**

For the measurements of the  $^{124}\text{Xe}(n,2n)^{123}\text{Xe}$  cross section (threshold  $E_n = 10.569$  MeV) the  $^2\text{H}(d,n)^3\text{He}$  reaction was used. Data were obtained for neutrons between 11.5 and 14.5 MeV in 1 MeV steps. Gold foils were used for neutron fluence determination. The cadmium cover was not used. The irradiation time was 1.5 hours at 11.5 MeV and 1 hour at 14.5 MeV. The yield of the 148.9 keV ( $I_\gamma = 48.9\%$ )  $\gamma$ -ray line from

the decay of  $^{123}\text{Xe}$  ( $T_{1/2} = 2.08$  h) was used for the cross section determination. The preliminary cross section results are shown in Fig. 6.9 and compared with existing data around 14.5 MeV and with evaluations. Our datum at 14.5 MeV is in fair agreement with the datum of Sigg *et al.* [Sig76], while the results of Kondaiah *et al.* [Kon68] and, especially, of Bazan *et al.* [Baz89] give larger cross-section values. Focusing on the evaluations, we observe that our data are in better agreement with ENDF/B-VII.1 than with TENDL-2012, and they deviate considerably from the JENDL-4.0 evaluation.

**Figure 6.9: (Color online) Present results for the  $^{124}\text{Xe}(n,2n)^{123}\text{Xe}$  cross section compared to earlier data near  $E_n=14.5$  MeV and various evaluations.**

[Baz89] F. Bazan, In *Progress Report U.C. Lawrence Radiation Laboratory No. 53929*, p. 162, 1989.

[Bha13] C. Bhatia, *Phys. Rev. C*, **87**, 011601 (R) (2013).

[Kon68] E. Kondaiah, *Nucl. Phys.*, **A120**, 337 (1968).

[Sig76] R. A. Sigg, *Nucl. Sci. Eng.*, **60**, 235 (1976).

---

### 6.2.3 Neutron Capture Cross Section of $^{181}\text{Ta}$ and $^{197}\text{Au}$ in Relation to NIF

---

M. BHIKE, S.W. FINCH, M.E. GOODEN, W. TORNOW, *TUNL*

**A program has been initiated at TUNL to measure the neutron capture cross section of  $^{181}\text{Ta}$  and  $^{197}\text{Au}$  in the neutron energy range between 3 and 14.8 MeV. The data are needed to better understand details of the abundance pattern of heavy nuclei and are important for diagnostic purposes at the National Ignition Facility, where nuclear reactions are being used to study the physics governing the plasma.**

In 2009 the National Ignition Facility (NIF) was commissioned as the world's premier inertial-confinement-fusion facility. NIF uses an array of 192 laser beams to implode a capsule containing small quantities of deuterium and tritium to temperatures and densities in excess of those in the interior of the sun, with the goal of producing a high-energy-density plasma. In addition to studying the ignition problem, the conditions in the plasma ( $T > 10^8$  K and density  $\rho > 10^3$  g/cm<sup>3</sup>) are ideal for understanding the nuclear processes that power stars and form the majority of the elements above iron in the periodic table through neutron capture. This is because the neutron fluence in a NIF capsule is 10 to 15 orders of magnitude larger than that found in a star, resulting in a neutron capture rate equal to what would be expected in thousands to millions of years in a stellar interior.

A prerequisite for the full understanding of the neutron-flux distribution at NIF and the development of a long-term nuclear-science program is a knowledge of the characteristics of the NIF neutron spectrum. For this reason fast-neutron-capture reactions are envisioned as an important component for the NIF science program. The predicted NIF neutron-energy spectrum is characterized by a pronounced 14.1 MeV peak and a strong multi-keV component. The interpretation of neutron-induced-reaction measurements requires a detailed analysis of the reaction contributions from the different neutron energy components. Neutron-induced reactions are sensitive to the areal density  $\rho R$  (where  $R$  is the radius of the plasma), burn asymmetry, and deuterium-tritium mixture in the NIF capsule. For example, the simultaneous measurement of the  $(n,\gamma)$  and  $(n,2n)$  reactions can sense

two different regions in the NIF neutron-energy spectrum. In general, the  $(n,\gamma)$  cross section is mostly sensitive to neutrons below 8 MeV, and the cross section increases as the neutron energy decreases. On the other hand, the  $(n,2n)$  reaction has a large cross section at 14 MeV.

One caveat of this method is that the  $(n,\gamma)$  reactions are sparsely known in the MeV region. In the case of  $^{197}\text{Au}$ , the experimental data scatter by a factor 2.5 at 14.5 MeV, and important information is missing between 7.5 and 14.0 MeV. The situation for  $^{181}\text{Ta}$  is even worse. The experimental data scatter by a factor of 10 at 14.5 MeV, and data are missing between 5.0 and 14.0 MeV. The  $^{181}\text{Ta}(n,2n)^{180}\text{Ta}$  cross section has recently been measured at TUNL (see Sect. 6.2.1). The  $^{197}\text{Au}(n,2n)^{196}\text{Au}$  cross section is fairly well known, although researchers at NIF have recently requested more accurate data.

In order to address the lack of  $(n,\gamma)$  data we started a program to obtain accurate data for this observable on  $^{181}\text{Ta}$  and  $^{197}\text{Au}$  in the energy range from 3 to 14.8 MeV. Careful tests were performed below 7 MeV to ensure that the well-known  $(n,\gamma)$  cross section of  $^{115}\text{In}$  was reproduced by our measurements. Indium foils attached to both sides of the tantalum and gold foils were used for neutron fluence determination. At the same time the indium foils removed the influence of thermal neutrons on our observable of interest, due to the large  $^{113}\text{In}$  thermal-neutron capture cross section. The tantalum and gold foils were typically activated for thirty-six hours. After irradiation, the  $\gamma$ -ray activities of  $^{182}\text{Ta}$  and  $^{198}\text{Au}$  were measured with well-shielded HPGe detectors of known efficiency. Table 6.2 summarizes the relevant information.

Table 6.2: Decay characteristics of the radio isotopes produced after  $(n,\gamma)$  reactions on  $^{181}\text{Ta}$ , and  $^{197}\text{Au}$

Isotope	$T_{1/2}$	Decay Mode	$J^\pi$ ( $\hbar$ )	$E_\gamma$ (keV)	$I_\gamma$ (%)
$^{182}\text{Ta}$	114.74 d	$\beta^-$ (100%)	$3^-$	1121.290	35.24
$^{198}\text{Au}$	2.6948 d	$\beta^-$ (100%)	$2^-$	411.80	95.62

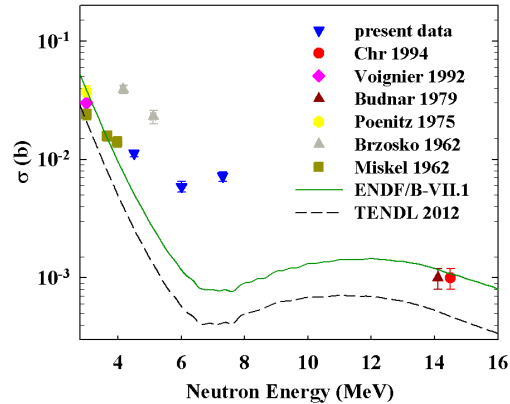


Figure 6.10: (Color online) Neutron-capture cross-section data on  $^{181}\text{Ta}$ . Not all existing data at 14.5 MeV are shown.

Preliminary data for  $^{181}\text{Ta}$  are shown in Fig. 6.10 and for  $^{198}\text{Au}$  in Fig. 6.11, both in comparison to values from the literature.

In the future, we will try to obtain data at higher energies. In this case, the  $^{27}\text{Al}(n,\gamma)^{24}\text{Na}$ ,  $^{58}\text{Ni}(n,2n)^{57}\text{Ni}$ , and  $^{197}\text{Au}(n,2n)^{196}\text{Au}$  reactions will be used for neutron fluence determination. In this energy range the neutron-capture cross section is generally less than a few percent of the total cross section and therefore is difficult to measure in the presence of such dominant competing reactions as elastic and inelastic scattering. In addition, neutron multiple scatter-

ing and attenuation corrections in the sample, corrections for room-return neutrons, and, especially, breakup neutrons from the source reactions can cause large corrections. We plan to pulse the neutron beam in order to measure the breakup-neutron contribution during the  $(n,\gamma)$  measurements. Furthermore, the neutron source anisotropy will be an issue if the targets are mounted very close to the neutron production target. Finally, during the  $\gamma$ -ray counting, the  $\gamma$ -ray attenuation in the sample has to be taken into account. We also plan to use a calibrated fission chamber for absolute neutron flux determination, in addition to the monitor foils referred to above.

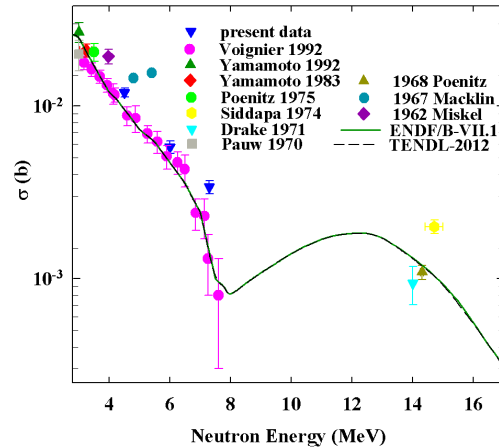


Figure 6.11: (Color online) Neutron capture cross-section data on  $^{197}\text{Au}$ . Not all existing data at 14.5 MeV are shown.

## 6.3 Public Health Research

### 6.3.1 Degradation Studies of Water Purification Membranes Using Rutherford Backscattering Spectrometry

J. POWELL, L. LIN, O. CORONELL, *University of North Carolina, Chapel Hill, NC* T.B. CLEGG, *TUNL*

We characterized the degradation by free chlorine of the polyamide active layer of SWC4+ reverse-osmosis membranes using Rutherford backscattering spectrometry (RBS). We found that RBS can be used to quantify the uptake of chlorine atoms and the degree of chain scission in the polyamide active layer. Results showed that chlorine uptake and chain scission increased with decreasing and increasing pH, respectively, and that they depend on the product of exposure time and free chlorine concentration in solution.

Polyamide-based thin-film composite reverse-osmosis (RO) membranes are a widely used technology for water reuse and seawater desalination because they are capable of removing a broad range of contaminants from water. The structure of most commercial reverse-osmosis membranes consists of three layers: a thin active layer usually made of polyamide (20 to 200 nm in thickness), a porous support made of polysulfone (20 to 50  $\mu\text{m}$ ), and a backing layer of polyester fibers (about 300  $\mu\text{m}$ ).

Polyamide-based membranes suffer from bio-fouling which causes a decrease of water flux and an increase of required operating pressure, thus leading to costly cleaning procedures [Bak98]. Free chlorine (i.e., bleach) is used as an effective pre-treatment for the feed-water to minimize bio-fouling; however, the polyamide active layers of RO membranes are degraded by free chlorine [Kan07]. Even though the physico-chemical changes in the top 7 nm or so of the active layer resulting from exposure to free chlorine have been studied by X-ray photoelectron spectroscopy [Do12], the volume-averaged changes in the bulk polyamide active layers have not. Two physico-chemical changes that polyamide experiences as a result of exposure to free chlorine are uptake of chlorine atoms and polyamide chain scission, both of which lead to loss of polymer integrity and, therefore, to increased salt passage [Do12].

Accordingly, in this study we use Rutherford backscattering spectrometry (RBS) to characterize the volume-averaged chlorine atom (Cl) up-

take and chain scission by the bulk region of polyamide active layers. A reverse osmosis membrane (SWC4+, Hydranautics, Oceanside, CA) was exposed to free Cl at various concentrations, exposure times, and pH conditions. Both Cl uptake and chain scission were then quantified by RBS, and conclusions regarding the degradation mechanisms were drawn. Chain scission was quantified by silver ion ( $\text{Ag}^+$ ) tagging of the carboxylic groups produced, followed by quantifying the silver concentration in the active layer by RBS [Cor08].

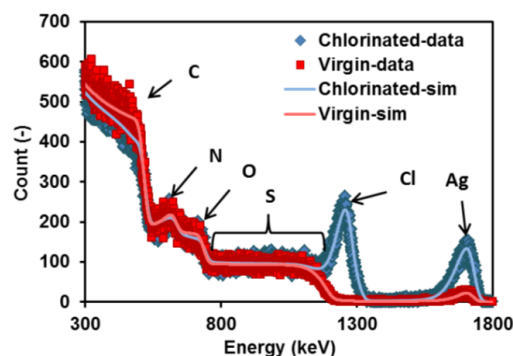


Figure 6.12: (Color online) RBS spectra for virgin and chlorinated SWC4+ reverse-osmosis membranes, showing chlorine (Cl) and silver (Ag) peaks in the active layers.

Figure 6.12 presents RBS spectra of membrane samples before and after exposure to free chlorine. The exposed RBS spectrum corresponds to a sample chlorinated at free Cl con-

concentrations of 750 ppm for 10 hours at pH = 4. The carbon, oxygen, nitrogen and sulfur signals correspond to the C, O, and N in the polyamide active layer and the C, O, and S in the polysulfone support layer; hydrogen cannot be seen in RBS spectra. The chlorine and silver peaks in the RBS spectra of chlorinated samples indicate Cl uptake and chain scission, respectively. The RBS spectra were analyzed with the simulation software SIMNRA to quantify the concentration of Cl and  $\text{Ag}^+$  in the active layers. These analyses show that the concentrations of Cl and Ag in the active layer were 0.05% and 0.073%, respectively, before chlorination, and 6.9% and 0.5%, respectively, after chlorination.

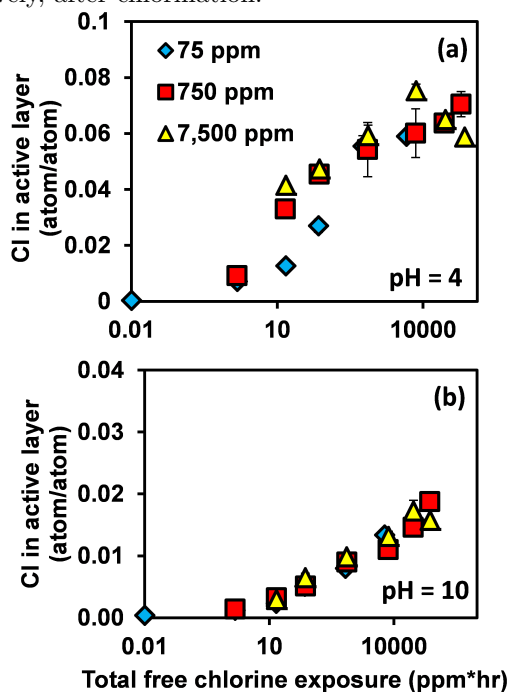


Figure 6.13: Elemental fraction of atomic chlorine in the polyamide active layers of reverse osmosis SWC4+ membranes as a function of exposure to free Cl (ppm·hr) at (a) pH=4 and (b) pH=10. Free Cl solutions had concentrations of 75, 750, and 7500 ppm.

Figure 6.13 presents Cl uptake at a range of free Cl concentrations and exposure times at pH

values of 4 and 10. The results show that, under both acidic and alkaline conditions, Cl uptake increases with free Cl concentration and exposure time and that Cl uptake is a function of the product of free Cl concentration and exposure time (i.e., to the total free Cl exposure in ppm·hr). Thus, the results indicate that Cl uptake is first order with respect to free Cl concentration. The results in Fig. 6.13 also show that Cl uptake was higher at pH=4 than at pH=10. Additional data (not shown) obtained for membrane samples chlorinated at pH=5 and 7.5 confirm that, in general, the rate of Cl uptake increased with decreasing pH.

The Ag concentrations in samples chlorinated at pH values of 4, 7.5 and 10 with solutions having free Cl concentrations of 750 ppm (results not shown) indicate that under alkaline conditions (pH=10) chain scission was a function of free Cl exposure. A maximum of about 10% of the amide links were observed to break at the maximum free-Cl exposure tested of 75,000 ppm·hr. Under acidic conditions, chain scission was found to be negligible.

In summary, the results of this study showed that Cl uptake in the bulk region of polyamide active layers increased with increasing free chlorine concentration and exposure time and with decreasing pH. The results also showed that at a given pH, Cl uptake is a function of free Cl exposure (ppm·hr) which is defined as the product of free Cl concentration in solution and exposure time. Chain scission was also found to be a function of free Cl exposure and to increase with increasing pH.

- [Bak98] J. S. Baker and L. Y. Dudley, *Desalination*, **118**, 81 (1998).
- [Cor08] O. Coronell *et al.*, *Environ. Sci. Technol.*, **42**, 5260 (2008).
- [Do12] V. T. Do *et al.*, *Environ. Sci. Technol.*, **46**, 852 (2012).
- [Kan07] G. D. Kang *et al.*, *J. Membr. Sci.*, **300**, 165 (2007).

## 6.4 Plant Physiology Research

---

### 6.4.1 Production of $^{52}\text{Fe}$ for Plant Physiology Studies

---

A.S. CROWELL, B.A. FALLIN, C.R. HOWELL, C.R. WESTERFELDT, *TUNL*; G. BIDA, *Duke University Medical Center, Durham, NC*; A.G. WEISENBERGER, J.E. MCKISSON, *Thomas Jefferson National Accelerator Facility, Newport News, VA*

**We are developing techniques based on positron emission tomography using  $^{52}\text{Fe}$  for tracking the absorption and allocation of iron in potato plants. This year we produced and assayed a sample of  $^{52}\text{Fe}$ . The production procedures and assay measurements are described.**

It is estimated that almost a quarter of the world's population suffers from iron deficiency. This problem is growing because of the increase in world-wide competition for iron-rich foods, such as meats and fish. A solution being considered is to find ways of increasing the iron concentration in staple foods such as potatoes, rice, and wheat, which normally have low levels of iron. Researchers have found that potato roots have a high efficiency for absorbing iron-oxide in such a way that the iron is retained in the tissue of the tuber without significantly altering the concentrations of other minerals and nutrients. The mechanisms for absorbing and breaking the oxide down into elemental iron are not well understood.

A plant physiology research group at Virginia Technological University is interested in using the short-lived positron-emitting radioisotope,  $^{52}\text{Fe}$ , to track the distribution of iron in potato plants. The eventual goal of such a study would be to develop techniques to maximize the concentration of iron in the most promising species of potatoes, thus increasing their nutritional value as food sources in third world countries. Once the  $^{52}\text{Fe}$  isotope is available, the Virginia Tech group would use the Duke-Jefferson Lab PET imaging system to study the uptake of iron into the potato tubers at the Duke Phytotron.

$^{52}\text{Fe}$  is the only isotope of iron to decay by positron emission with a half-life of over 10 minutes ( $\tau_{1/2} = 8.28$  hr). Despite the fact that  $^{52}\text{Fe}$  has previously been used in medical imaging studies [Pri77], its availability is not widespread. Our attempts to acquire  $^{52}\text{Fe}$  from commercial vendors or national laboratories were unsuccessful. Journal searches indicated that the  $^{50}\text{Cr}(\alpha, 2n)^{52}\text{Fe}$  reaction was a promising method

of radioisotope production, with a cross section that peaks at around 30 MeV. In an effort to quickly assess the issues related to producing  $^{52}\text{Fe}$ , discussions were held with researchers at the Duke University Medical Center (DUMC) Cyclotron facility and a plan for a set of preliminary experiments using their accelerator was developed. The DUMC Cyclotron is primarily used for production of  $^{211}\text{At}$  for radiotherapy, so any  $^{52}\text{Fe}$  production was constrained to have the same particle energy and target configuration.

The first measurement was on a blank aluminum target holder to see what  $\gamma$ -ray background lines would be present. An aluminum target holder, 4-in long by 13/16-in wide by 1/4-in thick, was placed at a grazing angle in the cyclotron and bombarded with 28-MeV  $\alpha$ -particles for approximately 1 hour at a beam current of 20  $\mu\text{A}$ . The aluminum bar was removed from the cyclotron and allowed to sit for 24 hours before being transported to TUNL in a lead-shielded container for assay. An HPGe detector in the low-background counting facility adjacent to LENA was used to record the  $\gamma$ -ray decays from the aluminum bar over a period of many days. Seventy-nine distinct  $\gamma$ -ray transitions were observed from eighteen different isotopes, but no transitions were seen in the region around 169 keV, which is where the dominant  $\gamma$ -ray line from  $^{52}\text{Fe}$  decay would be.

The second measurement used an Al target holder that had been commercially electroplated with a layer of natural chromium, approximately 0.3 to 0.5 mil in thickness. Natural chromium contains about 4%  $^{50}\text{Cr}$ . The irradiation time was 63 minutes with the same beam energy and current as before. The target was again allowed

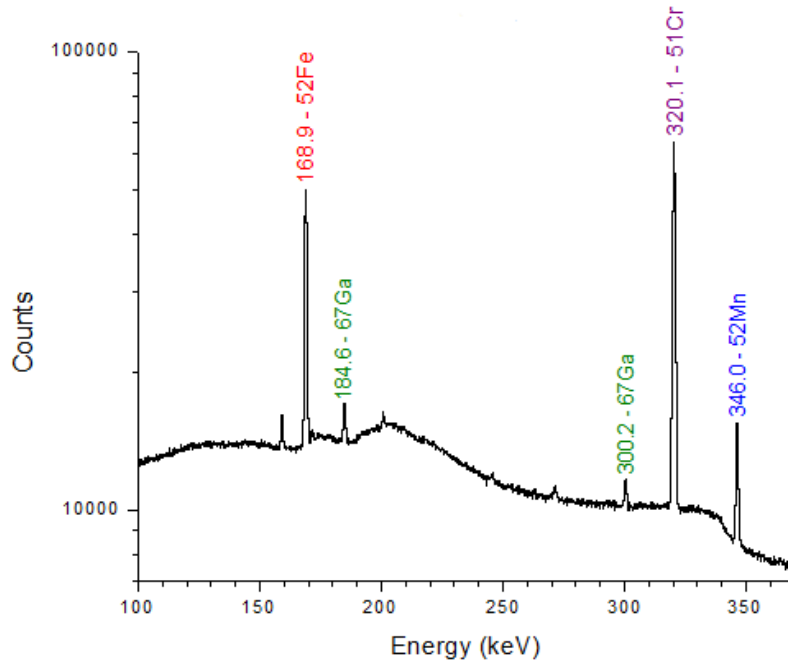


Figure 6.14: (Color online) A  $\gamma$ -ray spectrum of a natural chromium sample that has been irradiated with 28 MeV  $\alpha$ -particles. The low-energy region is featured and clearly shows a prominent peak at around 169 keV that is a signature of  $^{52}\text{Fe}$  decay.

to sit for 24 hours before being transferred to TUNL. Even after 24 hours, the activity in the chromium-plated target was enough to swamp the HPGe detector electronics, so a razor blade was used to scratch off some of the chromium plating, and this small powder sample was assayed. The result was a very clean  $\gamma$ -ray spectrum, a portion of which is shown in Fig. 6.14. The 169-keV peak from  $^{52}\text{Fe}$  decay is clearly visible. The experimental half-life for this peak was determined to be 8.20 hr, which is within 1% of the accepted value for  $^{52}\text{Fe}$ . Decay lines from seven other isotopes were also observed and attributed either to products of other  $\alpha$ -particle reactions on chromium or to reactions on what appears to be a small zinc contaminant.

In summary, we have successfully produced  $^{52}\text{Fe}$  using the DUMC cyclotron. Our next step

will be to explore production of the radioisotope in the tandem laboratory by running  $^4\text{He}$  beams near the accelerator's maximum potential of 10 MV or possibly by using the  $^{50}\text{Cr}(^3\text{He},n)^{52}\text{Fe}$  reaction when  $^3\text{He}$  beams are available early next year. Another significant goal will be to assess the issues involved in tracking the  $^{52}\text{Fe}$  in a potato plant by conducting trial measurements using the JLAB plant PET-imaging system. An early step toward this goal is to put the radioactive iron in a chemical compound that can be efficiently absorbed by the roots of potato plants, e.g., iron oxide.

---

[Pri77] D. Price, *Handbook of Clinical Nuclear Medicine*, Medical Examination Publishing Co., 1977.

## 6.4.2 Simulation of Sugar Allocation and Translocation in Grasses

M. BAI, C.R. HOWELL, A.S. CROWELL, L.C. CUMBERBATCH, B.A. FALLIN, *TUNL*; C.D. REID, *Duke University, Durham, NC*; A.G. WEISENBERGER, B. KROSS, S. LEE, J. MCKISSON, J.E. MCKISSON, *Thomas Jefferson National Accelerator Facility, Newport News, VA*

**We are measuring sugar allocation and translocation in real time using radio-tracer techniques to obtain information about the dynamics of the responses of plants to changes in the external environment. Our data are currently interpreted using an input-output statistical approach that makes no attempt to model the physical processes involved in the substance transport. This year we developed software to analyze our data based on fluid flow dynamics.**

Plants function as modular organisms consisting of morphological subunits, e.g., leaves, shoots and roots, that provide both structure and physiological function [Wat84]. The subunits are functionally integrated to form a complete living organism and are connected via a network of tubular bundles (xylem and phloem) that provides pathways for resource and status information exchange between the subunits. There is evidence that substance allocation is controlled by a regulatory network involving chemical signaling and passive mechanisms driven by changes in macroscopic quantities, e.g., pressure, endogenous and exogenous substance concentrations, water availability, and temperature. However, the feedback mechanisms in the network are not well understood [McI01].

We are performing real time measurements of substance allocation and translocation in small plants using short-lived radioisotopes to obtain insight about the dynamical responses of plants to changes in their external environment. Much of the work has been devoted to studying grasses such as barley. Grasses are chosen for the initial studies because of their importance in the food chain and for practical reasons. This year we developed software based on fluid-flow dynamics to model the movement of sugar in small plants. The model is described and calculations are compared to measured time distributions of  $^{11}\text{C}$ -tagged sugars in barley.

The model simulates the movement of carbon in the plant by sequencing the process into discrete time-steps such that the calculated time dependence of the carbon distribution in each plant section can be compared directly to measurements. The absorption of  $\text{CO}_2$  gas is mod-

eled as diffusion into the leaf. The flow rate is given by

$$J = P(\rho_2 - \rho_1), \quad (6.1)$$

where  $\rho_1$  and  $\rho_2$  are the  $\text{CO}_2$  gas densities inside and outside the leaf, respectively, and  $P$  is the effective permeability of the leaf. For the condition when the exogenous concentration of  $\text{CO}_2$  is a limiting factor in the photosynthesis rate, it may be assumed that  $\rho_2 \gg \rho_1$ , i.e.,  $J \approx P\rho_2$ . The density  $\rho_2$  is proportional to the  $^{11}\text{C}$  decay activity in the gas loop containing the load leaf cuvette. The flow  $J$  (in arbitrary units) is determined from the measured  $^{11}\text{C}$  accumulated in the plant by

$$J(t) = \frac{d}{dt}T(t)e^{\lambda t}, \quad (6.2)$$

where the time distribution  $T(t)$  gives the total number of  $^{11}\text{C}$  nuclei in the plant at time  $t$  and  $\lambda$  is the radioactive decay constant of  $^{11}\text{C}$ . The effective  $P$  (in arbitrary units) is given by  $P = J(t)/\rho_2(t)$ . Though the current measurements do not allow a determination of  $P$  in proper units, they do enable comparisons between measurements performed on the same plant under different conditions.

The plant is modeled as a one-dimensional (1D) structure with four sections, leaf, upper stem, stem, and root as shown in Fig. 6.15. The  $^{11}\text{C}$  tagged  $\text{CO}_2$  is absorbed in the portion of the loop enclosed in the cuvette. The  $^{11}\text{C}$  is incorporated into sugars via photosynthesis. The allocation and movement of the tagged sugars in each section of the plant are recorded by virtual detectors in each time-step. The plant tissue is divided into bins of equal length from the tip of

the load leaf ( $x = 0$ ) to the end of the root, and the phloem runs parallel to the 1D plant tissue. A bin length of 2 mm and time-step of one minute were fine enough to analyze our  $^{11}\text{C}$  labeled data for barley.

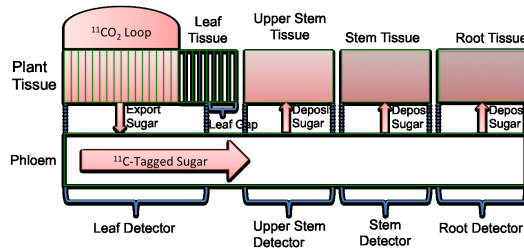


Figure 6.15: Schematic of the 1D structure used to model small plants.

The first step in simulating sugar translocation is the absorption of  $^{11}\text{C}$  into each bin of the leaf inside the cuvette for a time duration of one time-step. The amount of  $^{11}\text{C}$  absorbed is proportional to  $J(t)$ . The  $^{11}\text{C}$  is incorporated in sugar molecules formed during that time-step. A portion of the newly fixed sugars are used or stored locally and the rest are loaded into the phloem as sugar packets (sugar dissolved in water) for transport to other parts of the plant. The mobile sugars that are put in the packet are taken to be those that were formed no earlier  $T_m$  time-steps before the current one. The initial length of each sugar packet is equal to the bin length of the tissue where it was synthesized, and its initial position in the phloem is the same as the location where it was formed in the tissue.

Once in the phloem the sugar packets flow in the direction from source to sink driven by an osmotically maintained pressure gradient [Mun30]. The solute flow rate is given by the condensed version of the Poiseuille-Hagen law

$$J_s(t) = k\left(\frac{\Delta P}{L}\right), \quad (6.3)$$

where  $k$  is the effective conductance of the phloem,  $\Delta P$  is the pressure difference across the section of the phloem of length  $L$ . In addition, diffusion of the sugar in the water solvent is included in the model.

Once a sugar packet has moved beyond the leaf, a portion of the sugar in the packet is deposited into the surrounding tissue in each time-step. The virtual detector in each section counts the total number of  $^{11}\text{C}$  nuclei within its field of view in each time-step. The average speed and allocation of the  $^{11}\text{C}$  tagged sugars in each section, except for the root, which is the sink, are obtained by simultaneously fitting the measured

$^{11}\text{C}$  time distributions for the leaf, upper stem, stem, and root. The shape of the  $^{11}\text{C}$  time distribution in each section is sensitive to the duration that sugars remain mobile in the leaf. The measured time distribution for  $^{11}\text{C}$  tagged sugars in the lower stem of a barley plant is shown Fig. 6.16 in comparison with model calculations for different values of the sugar mobility time  $T_m$ . The best fit to the data is obtained with  $T_m = 30$  time-steps (30 minutes).

In the coming year this simulation will be used to analyze our  $^{11}\text{C}$  labeled data for barley and another grass species known as scirpus that were measured under different nutrient availability conditions and with different concentrations of atmospheric  $\text{CO}_2$ . The results will be compared to those obtained using an input-output transfer function analysis [Min03] of the same data. Also, we are planning experiments in which the absolute value of  $P$  will be determined. A longer term project is to develop systems for making real time measurements of the hydraulic pressure inside the phloem at different locations in the stem. These measurements will enable the determination of the effective phloem conductance in each time-step.

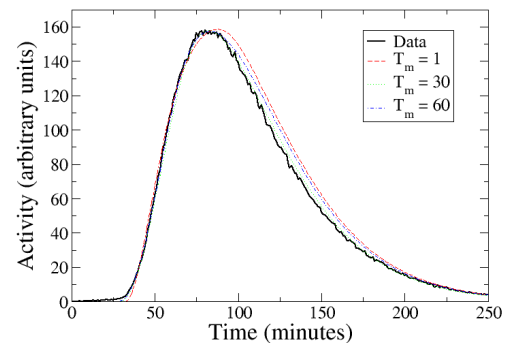


Figure 6.16: Plot of the measured  $^{11}\text{C}$  time distribution of the lower stem in a barley plant compared to model calculations for different values of  $T_m$ .

- [McI01] G. McIntyre, *Physiol. Plant.* **113**, 165 (2001).
- [Min03] P. Minchin and M. Thorpe, *Funct. Plant Biol.* **30**, 831 (2003).
- [Mun30] E. Münch, *Die Stoffbewegungen in der Pflanze*, Gustav Fischer, 1930.
- [Wat84] M. Watson and B. Casper, *Annu. Rev. Ecol. Syst.* **10**, 109 (1984).

## 6.5 Nuclear Data Evaluation

### 6.5.1 Nuclear Data Evaluation Activities

J.H. KELLEY, K. LEUNG, C.G. SHEU, H.R. WELLER, *TUNL*; J.E. PURCELL, *Georgia State University, Atlanta, GA*

The Nuclear Data Evaluation Group at TUNL is part of the United States Nuclear Data Program and the International Nuclear Structure and Decay Data network. After the retirement of Fay Ajzenberg-Selove in 1990, TUNL assumed responsibility for evaluation of nuclides in the mass range  $A = 3$  to 20. The status of the published evaluations and preliminary reviews is presented.

Along with producing evaluations of the  $A = 3$  to 20 nuclei in the “Energy Levels of Light Nuclei” series that is published in Nuclear Physics A, the Nuclear Data Evaluation Group has been charged with providing the corresponding updates to the Evaluated Nuclear Structure Data Files (ENSDF) database that is maintained at the National Nuclear Data Center (NNDC) at Brookhaven National Laboratory. We also provide a web-based service for the nuclear science and applications communities at <http://www.tunl.duke.edu/nucldata/>.

#### Publications

Table 6.5.1 displays the status of our most recent published evaluations and preliminary reviews.

**Table 6.3: Current publication status.**

Nuclear Mass	Publication	Institution
Published:		
$A = 3$	Nucl. Phys. A848 (2010) 1	TUNL
$A = 4$	Nucl. Phys. A541 (1992) 1	TUNL <sup>a</sup>
$A = 5$ to 7	Nucl. Phys. A708 (2002) 3	TUNL <sup>a,b</sup>
$A = 8$ to 10	Nucl. Phys. A745 (2004) 155	TUNL <sup>c</sup>
$A = 11$	Nucl. Phys. A880 (2012) 88	TUNL
$A = 11, 12$	Nucl. Phys. A506 (1990) 1	Penn <sup>d</sup>
$A = 13$ to 15	Nucl. Phys. A523 (1991) 1	Penn <sup>d</sup>
$A = 16, 17$	Nucl. Phys. A564 (1993) 1	TUNL
$A = 18, 19$	Nucl. Phys. A595 (1995) 1	TUNL
$A = 20$	Nucl. Phys. A636 (1998) 247	TUNL <sup>e</sup>
Reviews in Progress:		
$A = 12$	Expected 2014	TUNL

<sup>a</sup> Co-authored with G.M. Hale, LANL.

<sup>b</sup> Co-authored with H.M. Hofmann, Universität Erlangen-Nürnberg, Germany.

<sup>c</sup> Co-authored with D.J. Millener, BNL.

<sup>d</sup> F. Ajzenberg-Selove, University of Pennsylvania.

<sup>e</sup> Co-authored with S. Raman, ORNL.

#### Evaluated Nuclear Structure Data Files

The ENSDF files contain concise nuclear structure information such as tables of adopted level energies and tables of properties for levels that have been observed in various nuclear reactions and decays. The ENSDF files are updated concurrently with the last published reviews in the “Energy Levels of Light Nuclei” series.

Work on the  $A = 2, 3$  and 12 ENSDF files is presently underway.

#### Experimental Unevaluated Nuclear Data List

TUNL has taken responsibility for creating the  $A = 2$  to 20 data sets for the Experimental Unevaluated Nuclear Data List (XUNDL) beginning in April 2009. This activity was developed at McMaster University by Dr. Balraj Singh, who aimed to quickly provide the most current data to users in the high-spin community. The nuclear structure data in recent references is compiled in XUNDL with minimal evaluation effort. Since becoming involved, TUNL has prepared roughly 300 data sets, a rate of 5 per month on average. The data sets are reviewed by Dr. Singh and then added to the database at NNDC.

#### World Wide Web Services

Our group continues to develop web-based services for the nuclear science and applications communities. The website layout and contents are constantly revised and kept up to date, to ensure high-quality service and accurate information. Figure 6.17 displays the usage of our web-

site from the nuclear science communities since April 2002.

The following items are currently available:

- Ground-State Decay Data. This provides evaluated data from recent work on ground-state  $\beta$  decays and charged-particle decays, as well as compiled data from earlier measurements. It has been completed for nuclides with  $A = 3$  to 20.
- Thermal Neutron Capture Data on  $A = 2$  to 20 nuclei, based on compiled data.
- Excitation Function Data. This page provides compiled data related to the level parameters for  $A = 3$  to 20 nuclei populated in proton- and  $\alpha$ -particle-induced reactions.
- PDF and HTML documents for TUNL's and Fay Ajzenberg-Selove's reviews from 1959 to the present. The PDF versions include hyperlinks for references, Tables of Recommended Level Energies, Electromagnetic Transitions Tables, General Tables, Energy Level Diagrams, and Erratum to the Publications. The HTML documents are more comprehensive than the PDF documents, as they include hyperlinks to tables in the PDF and PS formats, reactions and reaction discussions, TUNL and NNDC references, Energy Level Diagrams, and General Tables.

We have essentially completed the re-creation of PDF files for our publications, in order to

provide the most current NNDC reference keys and to correct all errors found since the articles went to press. We will continue to work on the corresponding HTML and table/PS/PDF files for publications prior to 1984.

- Energy Level Diagrams for publication years from 1959 to the present. These are provided in GIF, PDF and EPS/PS formats.
- Tables of Energy Levels. A brief listing of the tables of recommended energy levels (in PDF and PS formats) from the most recent publications for nuclides with  $A = 4$  to 20.
- General Tables. References to theoretical work related to TUNL's most recent reviews for the masses  $A = 5$  to 10. The tables include dynamic links to the Nuclear Science References (NSR) database.
- ENSDF information for  $A = 3$  to 20 nuclides available through the NNDC site.
- A link to NuDat (Nuclear Structure and Decay Data). The link allows users to search and plot nuclear-structure and nuclear-decay data interactively through the NNDC site.
- Links to the NNDC and other useful sites, as well as to the online journals that the nuclear science communities use most often. There is also a sitemap with a complete listing and links to everything on the website.
- A new link with access to TUNL Ph.D. Dissertations from 1949 to the present. About 200 theses have been scanned by our group. This activity is 85% completed.

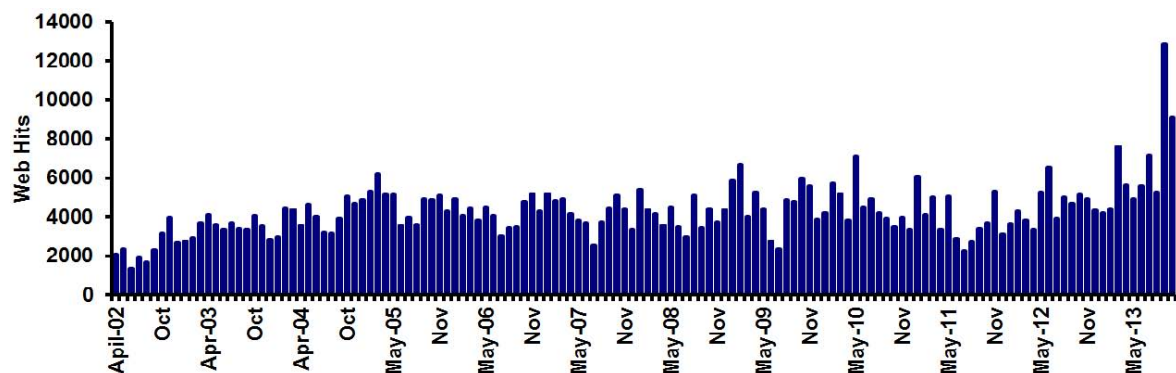


Figure 6.17: (Color online) Overview of web usage deduced from the Analog Web Analysis Package



# Accelerator Physics

---

Chapter 7

- **The High Intensity  $\gamma$ -Ray Source (HI $\gamma$ S)**
- **The FN Tandem Accelerator and Ion Sources**
- **The LENA Accelerator and Ion Sources**

## 7.1 The High-Intensity $\gamma$ -Ray Source (HI $\gamma$ S)

---

### 7.1.1 Operation of the HI $\gamma$ S Facility – Beamtime Summary

---

Y.K. WU, P. WALLACE, S.F. MIKHAILOV, *TUNL*

**From July 1, 2012 through June 30, 2013, the HI $\gamma$ S accelerator facility was operated for a variety of research programs and accelerator-related activities for 2812 hours out of a scheduled 2870 hours, giving a reliability of about 98%. A total of 1748 hours of on-target  $\gamma$ -ray beamtime was delivered to the HI $\gamma$ S user research program.**

Since 2012, the HI $\gamma$ S facility has been operated as a cost center at Duke University, with its budgetary year coinciding with the university's academic year, July 1 through June 30. To eliminate unnecessary confusion in producing performance reports for two slightly different reporting periods, starting with this report, we will compile the annual report on HI $\gamma$ S operation using the cost-center fiscal year. This year, the period is July 1, 2012 to June 30, 2013.

#### HI $\gamma$ S Operation: July 2012 – June 2013

This is the first fiscal year after the installation of the FEL wiggler switchyard, a device to retain all existing  $\gamma$ -ray-beam capabilities while allowing us to develop new or enhanced capabilities at energies above 70 MeV. The wiggler-switchyard installation was completed in early June 2012, and the storage ring was commissioned on June 14, 2012. During this reporting period, the HI $\gamma$ S accelerators were used for  $\gamma$ -ray beam production for nuclear physics research and for several other types of activities, including substantial vacuum scrubbing/conditioning necessitated by the installation of the wiggler switchyard with sections of new vacuum chambers; a number of sessions to condition and characterize new FEL mirrors; and three changeovers of wigglers using the switchyard. Because of these activities, there were several months with either no production beamtime (July 2012) or less than a typical number of beamtime-hours produced for experiments (August 2012, and January and February 2013).

From July 1, 2012 to June 30, 2013, the HI $\gamma$ S accelerator facility operated for 225 days (out of 251 university workdays), providing 2812 hours of beamtime for a variety of research programs

and accelerator-related activities. The operation of the accelerators and HI $\gamma$ S was carried out mostly with a two-shift, five-day operation schedule. However, we did increase the number of overnight shifts—36 overnight shifts in 8 different months (16% of days operated). These were scheduled to satisfy the needs of experiments requiring continuous data taking. This was made possible without sacrificing overall operation reliability because we were able to retain two experienced Ph.D. students from the accelerator physics group as new postdoctoral fellows, saving substantial training time.

In this period, the overall reliability of the operation of the HI $\gamma$ S accelerators and light sources was about 98%, exceeding the typical 95% performance goal set for national synchrotron light sources. This very high level of reliability was realized in spite of the complex and challenging operation of the free-electron lasers and Compton  $\gamma$ -ray source, plus new challenges associated with the first  $\gamma$ -ray production runs above 80 MeV. A detailed break-down of accelerator operation hours is summarized in Table 7.1 and Fig. 7.1.

From July 1, 2012 to June 30, 2013, we delivered 1748 hours of HI $\gamma$ S  $\gamma$ -ray beamtime to basic and applied nuclear physics research programs. Accelerator research and development used 243 hours of beamtime, much of which was spent on tuning up the performance of the accelerators after the wiggler switchyard installation, developing a variety of compensation schemes for the operation of the six FEL wigglers (two of which were new) and the four buncher magnets, and the development of a soft-orbit bump to protect the downstream FEL mirror. Some beamtime was also devoted to studying beam instabilities with a 32-bunch beam at high current.

To deal with vacuum-chamber outgassing, about 258 hours of beamtime were used for vacuum scrubbing and conditioning, using a high current multi-bunch beam at 1 GeV. These vacuum-scrubbing runs were performed after the installation of the new chambers and after the changeover of wigglers.

**Table 7.1: Summary of the accelerator beamtime from July 1, 2012 to June 30, 2012.**

Activities	Beamtime (hrs)	%
HI $\gamma$ S user research	1748	60.9%
Acc. R&D	243	8.5%
Acc./FEL/HI $\gamma$ S setup and tune	563	19.6%
Acc. commissioning/ Vac. scrubbing	258	9.0%
Unscheduled downtime	58	2.0%
All scheduled beamtime	2827	100%

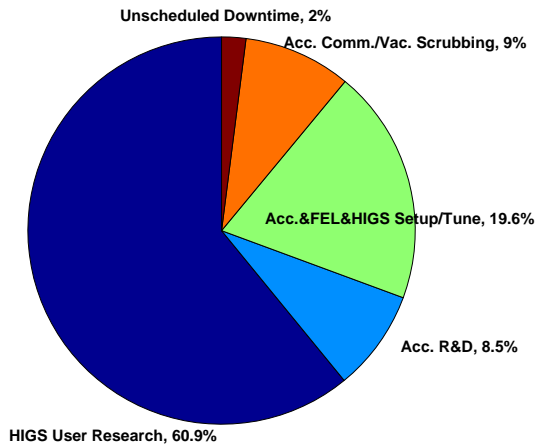


**Figure 7.1: (Color online). Beamtime distribution for a variety of programs from July 1, 2012 to June 30, 2013.**

In addition, 563 hours were used to perform the setup and tuning of the accelerators, FELs, and Compton  $\gamma$  source, plus other related activities. The HI $\gamma$ S user programs in this period demanded frequent changes of  $\gamma$ -ray-beam parameters, including energy, flux, and polarization. This led to frequent changes of the FEL mirrors. With each mirror change, time must be spent on conditioning and aligning the mirrors and on setting up the accelerators, FELs, and Compton  $\gamma$ -ray source. Overall, the time spent on accelerator/FEL/HI $\gamma$ S setup and on accelerator commissioning and vacuum scrubbing

accounted for 19.6% and 9.0% of the total time, respectively (see Table 7.1).

The monthly HI $\gamma$ S user beamtime is shown in Fig. 7.2. The delivered monthly  $\gamma$ -ray beamtime averages about 159 hours per month (for 11 months with accelerator operation). In October, 2012, a total of 301 hours of  $\gamma$ -ray beamtime were delivered to the nuclear physics program with 10 overnight shifts scheduled. A summary of accelerator reliability issues for the HI $\gamma$ S cost-center fiscal year 2013 (July 2012 to June 2013) are presented in Sect. 7.1.2.

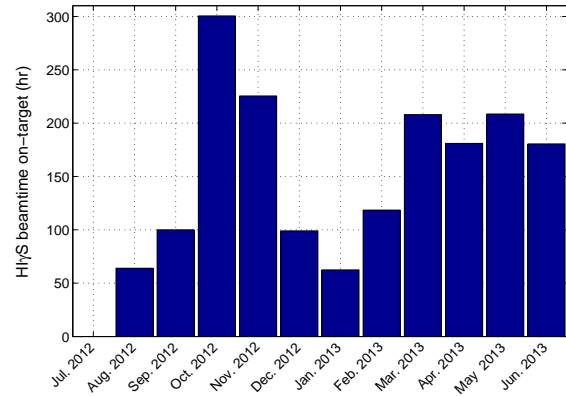


**Figure 7.2: Monthly distribution of  $\gamma$ -ray beamtime delivered to the HI $\gamma$ S experimental program (July 1, 2012 – June 30, 2013).**

### HI $\gamma$ S Operation: July – September 2013

The reporting period for this TUNL Progress Report has been extended to November 30, 2013. This presents us with an opportunity to provide a brief report on HI $\gamma$ S operation from July 1 to September 30, 2013, three more months beyond the fiscal year of the HI $\gamma$ S cost center. In these months, we delivered 741 hours of  $\gamma$ -ray beam on-target for the HI $\gamma$ S experimental program, with an overall operation reliability of 97.7%. See Table 7.2 for the beamtime summary.

**Table 7.2: Summary of the accelerator beamtime for July through September 2013.**

Activities	Beamtime (hrs)	%
HI $\gamma$ S user research	740.5	73.6%
Acc. R&D	169.5	16.9%
Acc./FEL/HI $\gamma$ S setup and tune	72.5	7.2%
Unscheduled downtime	23.5	2.3%
All scheduled beamtime	1006	100%

---

### 7.1.2 Operation of the HI $\gamma$ S Facility – Accelerator Reliability

---

Y.K. WU, P. WALLACE, S.F. MIKHAILOV, *TUNL*

**From July 1, 2012 through June 30, 2013, the HI $\gamma$ S accelerator facility was operated for 2812 hours for a variety of research programs and accelerator related activities with a reliability of about 98%. The largest sources of downtime were failures of the booster and ring RF systems, problems with one of the linac modulators, and the failures of two important components.**

Within the total scheduled 2870 hours of accelerator operation, the unscheduled downtime (UD) was 58 hours or about 2.0%, significantly lower than the 4% to 7% that was typical in many previous years. Figure 7.3 shows that in the last twelve months, two-thirds of the UD hours were from three causes. Failures of the booster and ring RF systems (separate entries in the figure) accounted for 16.5 hours or 28% of the total; problems with one of the linac modulators were responsible for 9.0 hours or 16% of the total; and failures of the CAMAC crate and the FEL mirror piezoactuator each required 7.0 hours or 12% of the total.

The RF problems were generally trips of the RF generator or cavity controls, which could be reset after a short time. However, these caused complete beam loss, and time had to be taken to refill the electrons in the storage ring. In the storage ring RF amplifiers, some unaccountable startup problems occurred in spring 2013. These were finally found to be caused by a set of contact fingers that had burned from arcing; they were replaced.

Modulator #4 had several components that burned up from arcing. It required several hours to locate and install replacements.

The CAMAC crates took hours to replace, because we needed to remove all the cards, take the crate from the rack, identify a working spare, install the crate and the cards, and then get the whole input/output control (IOC) system operating again.

The piezoactuator on the Y axis of the east FEL mirror suddenly required considerably higher current than the high voltage bipolar power supply could supply. At the time, we had no spare piezoactuators, so a backup power sup-

ply was jury-rigged from parts of another project and was adjusted to operate with the usual control signals that the IOC provides.

UD hours from faults of the kicker systems accounted for only one hour—a marked reduction from past years. Steady and careful maintenance and diagnostic testing of these systems was proving its worth. The storage ring PA3 RF tube has had a short between the grid and filament, but monitoring plus periodic “zapping” kept the tube in operation with no UD hours.

While the reliability of the DFELL accelerators has been high, we recognize that we will move into operations at high energies with hundreds of user-operation hours for each run. The high energies will require almost continuous top-off injection, which will put all linac, booster, and kicker systems under greater stress, leading to more frequent—and likely more catastrophic—failures. In 2013, we made several purchases of critical components for spares. More purchases of critical spare parts, subject to the availability of funds, are necessary in the near future. A timely procurement of expensive but critical hardware will remain a challenge in the coming years.

We also plan to make a detailed study of the past performance and failure history of critical components. We do not expect to be able to use this for prediction of future failure rates, since we expect the future higher-stress operations increase failure rates in a non-linear manner. Our goal is to identify other components for which we need to have in-house spares and to be prepared for rapid replacement. Such a study can also highlight components which need ongoing diagnostic testing during scheduled maintenance times, and it can help to identify the symptoms of impending failures.

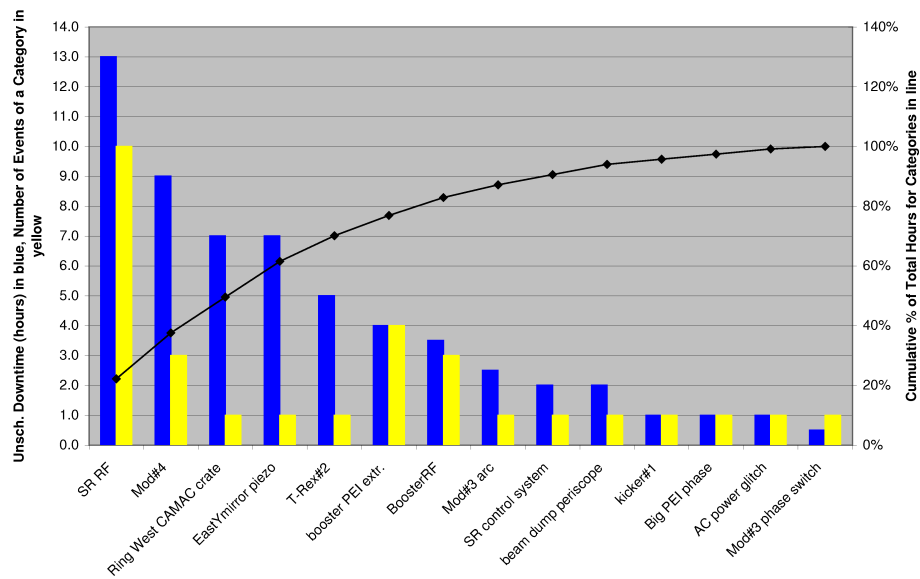


Figure 7.3: (Color online). Chart of the various categories of events (horizontal axis) showing the unscheduled downtime hours (blue or darker bars), the number of events of a category (yellow or lighter bars), and the cumulative percent of the total hours lost by a category of hardware failure (black curve).

### 7.1.3 Commissioning and Operation of the FEL Wiggler Switchyard

Y.K. WU, M. EMAMIAN, M. BUSCH, J. FAIRCLOTH, H. HAO, J.Y. LI, S.F. MIKHAILOV, V.G. POPOV, G. SWIFT, P. WALLACE, P. WANG, W.Z. WU, J. YAN, *TUNL*

**The new FEL wiggler switchyard, a system developed to enable high-gain operation of the UV-VUV FEL and extend HI $\gamma$ S operation to higher energies, was successfully commissioned and, in early 2013, was used to produce a high-intensity, high-energy  $\gamma$ -ray beam for the first nuclear Compton-scattering experiments at HI $\gamma$ S.**

The FEL wiggler switchyard (see Fig. 7.4) is designed to extend HI $\gamma$ S operation above 100 MeV and toward 158 MeV (beyond the pion-threshold energy) by using an FEL with multiple wigglers to overcome the large cavity losses resulting from operating the FEL below 200 nm. The switchyard system makes the high FEL gain possible by allowing simultaneous operation of up to four helical OK-5 wigglers for a total wiggler length of 16 meters. In addition to the two previously installed OK-5 wigglers near the two ends of the straight section, the switchyard system brings two additional OK-5 wigglers to the middle of the section to form a long FEL. In an alternative wiggler configuration, the switchyard allows the FEL system to use either two planar OK-4 wigglers, brought to the middle section with the switchyard, or the two helical OK-5 wigglers on the ends. Using these wigglers with different helicities, the wiggler switchyard preserves all earlier  $\gamma$ -ray beam capabilities: the production of high intensity  $\gamma$ -ray beams between 1 and 65 MeV, with either linear or circular polarization.

The FEL wiggler switchyard was first proposed around 2004 as an incremental upgrade of the HI $\gamma$ S facility to produce higher energy  $\gamma$ -ray beams. This concept was the most cost-effective solution for extending the energy range of HI $\gamma$ S operation with OK-5 wigglers, by employing the existing FEL straight section and FEL cavity system, and using the existing  $\gamma$ -ray beamline and downstream target rooms for nuclear physics experiments. While a preliminary design of the system was developed from 2006 to 2007, a change of funding sources, and the consequent need to operate the HI $\gamma$ S facility extensively for nuclear physics research put the project on hold for several years. The project was restarted in 2010 in

order to meet the demand of nuclear physics experiments to have  $\gamma$ -ray beams at higher energies. From 2010 to early 2012, the wiggler switchyard project went through several stages of development, which are summarized in Table 7.3.

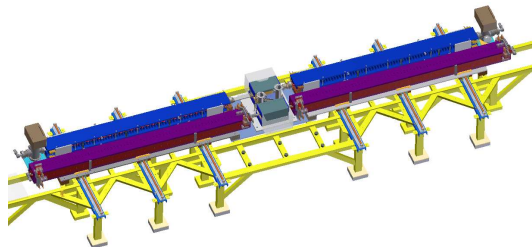


**Figure 7.4: (Color online) The wiggler switchyard system in the middle of the FEL straight section. Electrons travel from left to right.**

From the end of February to early June, the installation of the switchyard went smoothly and was finished ahead of schedule, completing the following tasks: (1) dismantling the old 15-m-long OK-4 beamline and modifying the cooling-water and electrical infrastructure; (2) installing new strongback supports with a series of linear sliding tracks topped by a wiggler platform; (3) installing and aligning two OK-4 wigglers, two OK-5 wigglers, and two buncher magnets on the sliding platform; (4) installing the adjacent quadrupole magnets and restoring cooling water to all magnets; (5) installing new vacuum chambers and connecting these with the existing storage ring; and (6) connecting power bus bars to the OK-5 and OK-4 wigglers and cables to various magnets. The main equipment of the storage ring was first powered up on June 8, 2012. The startup and commissioning of the storage ring with the two new OK-5 wigglers in the middle

**Table 7.3: Milestones and timelines for the wiggler switchyard project.**

Timelines	Milestones
2004–2005	Physics concept
2006–2007	Preliminary mechanical design
Aug. 2010–Feb. 2012	Magnetic lattice design Design of mechanical, vacuum and electrical systems Fabrication, assembly, testing
Feb. 27–Jun. 7, 2012	Wiggler switchyard installation
Jun. 8, 2012	Acc. equipment power-up and injector system recommissioning
Jun. 14, 2012	Storage ring commissioned with stored electron beam
Jun. 18–Aug. 24, 2012	Vacuum scrubbing, FEL mirror tests, and shutdowns for facility upgrades
Aug. 16, 2012	HI $\gamma$ S user test run
Aug. 27, 2012	HI $\gamma$ S user operation resumed

section went extremely smoothly, and the first electron beam was stored in the storage ring (see Fig. 7.5) in just a few hours after the first injection.

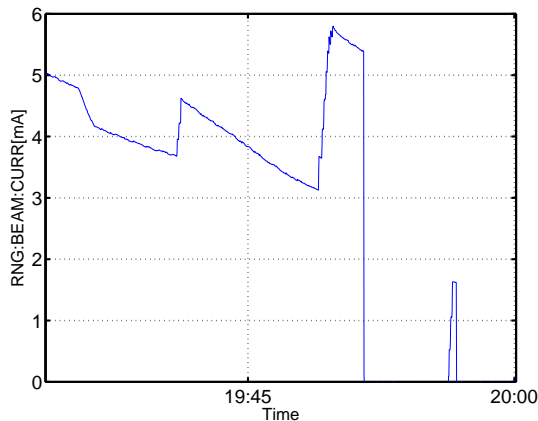


**Figure 7.5: (Color online) The electron beam current in the Duke storage ring during the first day of commissioning the wiggler switchyard on June 14, 2012.**

The vacuum in the center of the FEL straight section (including two new OK-5 chambers and a new chamber for the buncher magnet) was poor initially due to chamber outgassing, especially under the illumination of intense off-axis wiggler radiation. From mid-June to mid-September 2012, substantial time was devoted to vacuum scrubbing/conditioning by operating a multiple-bunch beam at 1 GeV with the beam current raised gradually to 200 mA. The magnetic field in the OK-5 wigglers was varied systematically to allow wiggler radiation to illuminate different

parts of the vacuum chambers. In early June, after about two weeks of vacuum scrubbing, the vacuum recovered enough to start a program to test and condition a number of new FEL mirrors. The first  $\gamma$ -ray-beam production was a test run to produce an 80 MeV beam using a set of new 193 nm mirrors on July 18. On August 16, a  $\gamma$ -ray beam was produced for a test experiment to calibrate new detectors. Following this, on August 24, routine  $\gamma$ -ray-beam production was established to allow the resumption of the HI $\gamma$ S user program.

**Table 7.4: Summary of wiggler switch events using the switchyard.**

Dates	Wiggler Change	Vacuum Recovery
Jul 20–27, 2012	OK-5 to OK-4	4 weeks
Jan 8–10, 2013	OK-4 to OK-5	3 weeks
Apr 8–9, 2013	OK-5 to OK-4	4 days

Since June 2012, the wiggler switchyard has been used three times, and a summary of the switch events is provided in Table 7.4. Following the first two wiggler switches, substantial vacuum scrubbing was needed in order to condition the new vacuum chambers. In April 2013, the wiggler switch was carried out for the third time, but without a need for extensive vacuum conditioning afterward. With this experience, it is projected that wiggler configurations can be switched in about 5 to 6 working days in the future.

In February and March 2013, the switchyard enabled the production of a high intensity, circularly polarized  $\gamma$ -ray beam at about 87 MeV for the first experiments in the nuclear-Compton-scattering program at HI $\gamma$ S.

### 7.1.4 Design of a Soft Orbit Bump for FEL Mirror Protection at the Duke FEL/HI $\gamma$ S Facility

H. HAO, S.F. MIKHAILOV, J. LI, Y.K. WU, *TUNL*

**Edge radiation from the end-of-arc bending magnet at HI $\gamma$ S is a main source of damage to the downstream FEL mirror. To mitigate this effect, a soft orbit bump is designed to change the displacement and angle of the electron beam in this region. Calculations show that the soft orbit bump can significantly reduce high energy photon radiation on the FEL mirror.**

In an oscillator free-electron laser (FEL) with a high energy electron beam, it is critical to protect mirrors from damage caused by high energy photons. These photons could be high-order harmonic radiation from insertion devices, or synchrotron radiation from buncher magnets, correctors, and bending magnets. At HI $\gamma$ S, a set of water-cooled, in-cavity apertures have significantly improved the mirror lifetime by reducing the off-axis high-order harmonic wiggler radiation in high-flux Compton  $\gamma$ -ray production [SLH09]. However, as shown in Fig. 7.6, the first bending magnet of the east arc, E01B, can contribute significantly to mirror damage due to its strong radiation from edge magnetic fields and the short distance to the FEL mirror. To protect the mirror from this radiation, it was proposed to use a local orbit bump around this bending magnet to direct the edge field radiation away from the mirror [SFM12]. The electron beam in the correctors of this orbit bump will produce long wavelength (“soft”) synchrotron radiation, therefore this orbit bump is called “soft.” A soft orbit bump was set up and measured at HI $\gamma$ S using a set of existing correctors near the E01B bending magnet. It showed a significant reduction of edge radiation power on the FEL mirrors [SFM12]. However, this reduction was limited by the distribution and strength of existing correctors. Therefore, it was planned to upgrade the orbit bump by installing additional correctors at appropriate locations to further reduce the amount of edge radiation on the FEL mirror.

Unlike the synchrotron radiation produced by electrons in a uniform magnetic field, the angular power distribution of the edge radiation is not peaked at an angle tangential to the electron trajectory, but has a roughly  $-1/\gamma$  an-

gle deviation, where  $\gamma$  is the relativistic factor of the electron and the minus sign means this angle is in the opposite direction to the bending direction. According to Fig. 7.6, a quantity  $|x_{\text{aper}}| = |x_i + 4.89x'_i|$  is used to characterize the effectiveness of the soft orbit bump, where 4.89 is the distance in meters between the magnet entrance and the in-vacuum aperture, and where  $x_i$  and  $x'_i$  are electron beam horizontal coordinate and angle at the E01 bending magnet entrance, respectively. Here  $|x_{\text{aper}}|$  is the horizontal coordinate of the intersecting point between the tangent line of the electron beam at the E01 bending-magnet entrance and the in-vacuum aperture. A large  $|x_{\text{aper}}|$  could help to reduce the edge radiation on the FEL mirrors. This requirement is usually in conflict with the need to minimize the maximum displacement  $|x_{\text{max}}|$  inside the soft orbit bump. This displacement should be as small as possible to preserve a good injection efficiency and a long beam lifetime. In the design, the multi-objective genetic algorithm (MOGA) [DEB02] is used. This algorithm can efficiently find the optimal solutions for a complicated problem with several independent variables, objectives, and constraints, especially for those with trade-off objectives. For the soft orbit bump design, there are four independent variables, corresponding to four sets of correctors. Two trade-off quantities,  $-|x_{\text{aper}}|$  and  $|x_{\text{max}}|$ , are chosen to be the objectives. The maximum strength of each S10 corrector is constrained to 0.4 mrad, and the S11BC:X:A corrector strength is set to be smaller than 0.8 mrad to ensure the radiation from these correctors is soft.

Figure 7.7 shows the calculated Pareto front of  $10^4$  random seeds evolving for 200 generations. The maximum  $|x_{\text{aper}}|$  could reach 17.2 mm

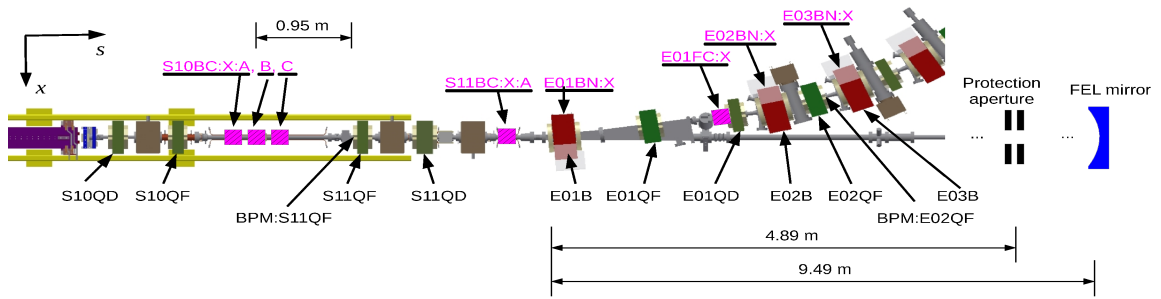


Figure 7.6: (Color online) Layout of magnets at the end of the south straight section and the beginning of the east arc of the Duke storage ring. Correctors used in the upgraded soft orbit bump are labeled with underlines. S10BC:X:B, S11BC:X:A, E01FC:X are newly installed correctors.

within the constraints of correctors, corresponding to an  $|x_{\max}|$  of 8.3 mm. We chose a soft orbit bump configuration at the upper-left end of the Pareto front. The calculated electron beam orbit for this configuration is shown in Fig. 7.8.

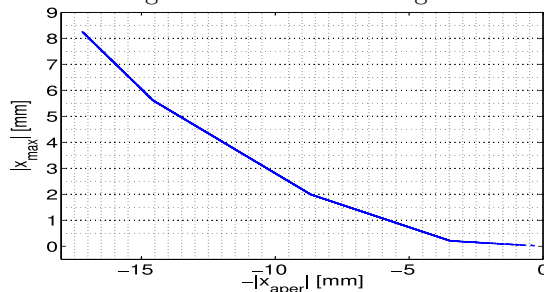


Figure 7.7: (Color online) Pareto front of design objectives at the 200th generation.

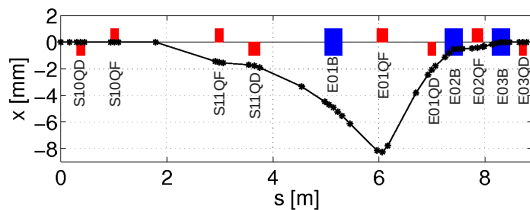


Figure 7.8: (Color online) Electron beam orbit of the upgraded soft orbit bump.

In the experiment, two beam position monitors (BPM:S11QF and BPM:E02QF) inside the orbit bump are taken out of the global orbit feedback to avoid competition between the soft-orbit-bump control and the global orbit feedback. The correctors used in the soft orbit bump are shared by the global orbit feedback using soft control channels. The soft orbit bump was set up and measured with a 1 GeV electron beam. It was found that at this energy the soft orbit bump could be operated at a maximum height  $|x_{\max}| = 21.5$  mm. In this orbit, the S10BC:X correctors were set to 1.5 mrad, slightly higher

than the constraining value in the calculation.

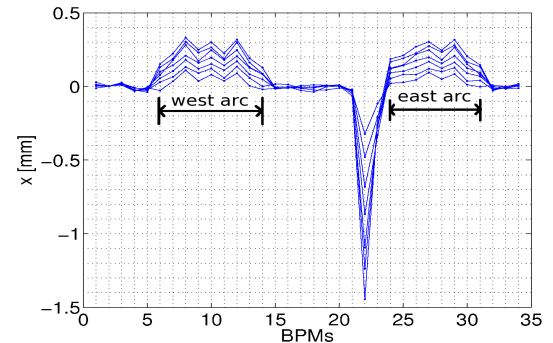


Figure 7.9: (Color online) Measured electron beam orbits for different soft-orbit-bump strengths. The largest orbit corresponds to a corrector setting of 1.28 mrad.

Figure 7.9 shows the measured storing orbits for different soft-orbit-bump heights. There is an orbit leakage of about  $30 \mu\text{m}$  in the straight sections. This can be reduced by fine adjustments to the correctors in the bump. As there was no RF frequency tuning in this experiment, the electron beam energy changed slightly due to the orbit length variation caused by the soft orbit bump. This change induces a non-zero orbit in the dispersive east and west arcs. It is estimated that there was an electron-beam energy increase of about 0.13% for the largest soft orbit bump. This is within the tuning range of the storage ring RF system.

[DEB02] K. Deb *et al.*, IEEE Trans. Evol. Comput., **6** (2002).

[SFM12] S. F. Mikhailov *et al.*, In *International Particle Accelerator Conference*, pp. 1774–1776, 2012.

[SLH09] S. Huang *et al.*, Nucl. Instrum. Methods A, **606** (2009).

### 7.1.5 Protection of VUV FEL Mirrors Using a Soft Orbit Bump at the Duke FEL/HI $\gamma$ S Facility

S.F. MIKHAILOV, H. HAO, J.Y. LI, V.G. POPOV, P. WALLACE, Y.K. WU, *TUNL*

**At the High Intensity  $\gamma$ -ray Source facility, production of high-intensity, high energy  $\gamma$ -ray beams in the energy range of 60 to 158 MeV requires a high-current electron beam at energies of 0.9 to 1.2 GeV. At these energies, the edge radiation from the end-of-arc dipole is the dominant cause of a rapid degradation of the downstream FEL mirror. A soft orbit bump has been further developed to significantly reduce the radiation from this dipole toward the FEL mirror. The first experience of HI $\gamma$ S user runs utilizing the soft bump is presented.**

The Duke storage ring is designed as a dedicated FEL driver and as a host for several FEL wigglers in a thirty-four-meter-long straight section. The main parameters of the Duke accelerators and various FEL configurations are listed in Table 7.5. A planar optical-klystron FEL, the OK-4, consists of two planar wigglers sandwiching a buncher magnet. A pair of OK-5 helical wigglers were located one upstream and one downstream of the OK-4 wigglers. The FEL straight section was recently upgraded to accommodate four OK-5 wigglers instead of two (see Fig. 7.10) [YWu13]. In February and March of 2013, we had the first user runs using 192 nm FEL mirrors at 1 GeV of electron-beam energy to produce 87 MeV  $\gamma$ -ray beams. The number of OK-5 wigglers used in a particular VUV HI $\gamma$ S operation is determined by the available FEL gain compared to the optical cavity loss, while trying to avoid the use of the downstream OK-5 wiggler, in order to reduce the radiation damage to the downstream mirror. Extending FEL operation to 192 nm and further down to 150 nm requires mirrors with increasing losses and thus a higher FEL gain and more wigglers.

#### Soft Orbit Bump Concept

Because of the degradation of UV/VUV mirrors (250, 190, and future 150 nm) caused by the off-axis higher-order VUV wiggler harmonic radiation, high-energy, high-flux HI $\gamma$ S  $\gamma$ -ray beam operation is possible only with the helical OK-5 FEL (Fig. 7.10). The mirrors are protected from off-axis radiation using the in-vacuum mirror protection apertures [SLH09].

In the production of  $\gamma$ -beams with energies above 60 MeV, ( $E_e \geq 900$  MeV), the corner bending magnets and other magnetic elements in the FEL straight section are also significant sources of radiation. For the VUV FEL operation, we try to minimize all other sources of radiation harmful to the downstream FEL mirror. The most intense hard photon source is the corner dipole next to the downstream mirror (E01B in Fig. 7.10). To reduce its radiation directed forward the mirror, we developed an orbit bump using designated orbit correctors.

**Table 7.5: Key beam parameters for OK-5 VUV FEL/HI $\gamma$ S high energy operations.**

$\lambda_{\text{mirror}}$ (nm)	$E_{e \text{ max}}$ (GeV)	$E_{\gamma \text{ max}}$ (MeV)	$\lambda_c$ (nm)	No. of OK5 wigglers
250	0.925	60	1.5	2
192	1.050	97	1.0	2-3
150**	1.200	158	0.7	3-4

\*\* To be developed

In order not to introduce an additional source of radiation, the magnetic field of those correctors is limited to produce very soft radiation with a critical wavelength close to or longer than that of the FEL mirror. The orbit bump deflects the beam orbit inwards at the entrance of E01B, steering the dipole edge radiation (ER) away from the axis of the mirror (see Fig. 7.11). This bump allows us to significantly reduce the ER power on the mirror. Initially, it was a three-kick bump with a maximum horizontal deflection angle of 1.2 mrad at  $E_e = 1$  GeV. Recently it was modified to a six-kick bump, increasing the total angle up to 2 mrad with the same constraints for the magnitude of the orbit change (see Fig. 7.12)

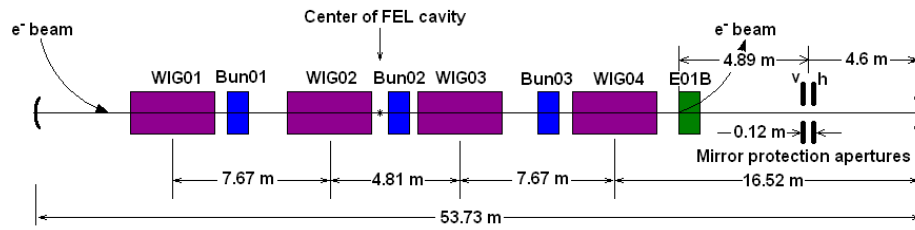


Figure 7.10: (Color online) Configuration of the Duke FEL with helical OK5 wigglers.

[Hao13].

In real high-energy, VUV HI $\gamma$ S operation, with the in-vacuum protection apertures closed normally, the soft orbit bump reduces the radiation power on the FEL mirror from the E01B dipole down to about the same level as, or lower than, that of the wiggler harmonics radiation [SMi13].

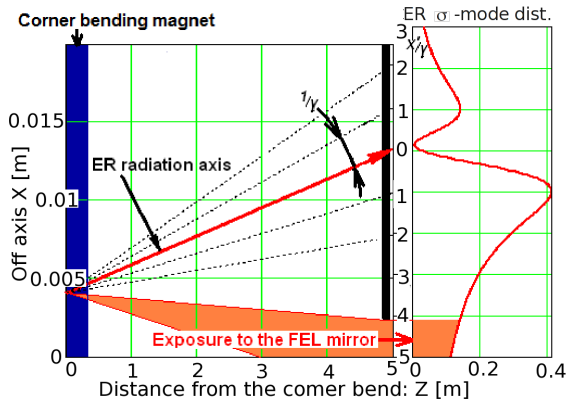


Figure 7.11: (Color online) Concept of an orbit bump to protect the FEL mirror from radiation of the corner dipole.

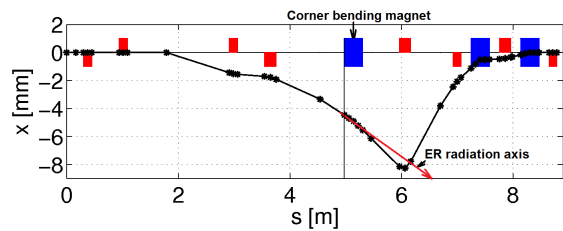


Figure 7.12: (Color online) Six kicks orbit soft bump.

### First User Operation

In the spring of 2013, we completed the first HI $\gamma$ S user runs using 190 nm FEL mirrors. A high-intensity, 87 MeV  $\gamma$ -ray beam was produced with FEL lasing at 192 nm, using an  $e$ -beam current of 90 mA in two bunches, at an  $e$ -beam energy of 1 GeV. The total  $\gamma$ -ray beam time delivered was

165 hours. The three-kick soft orbit bump was successfully tested and used to protect the downstream FEL mirror. These runs demonstrated a significant lifetime for the 190 nm FEL mirrors. Figure 7.13 shows the degradation of the mirrors after about 165 hours of operation, or about 15 ampere-hours of integrated exposure. The downstream mirror was near the end of its life by the end of those user runs. Therefore, the existing mirrors can be used for high-intensity  $\gamma$ -ray production for up to about 200 hours.

Cavity loss [%]

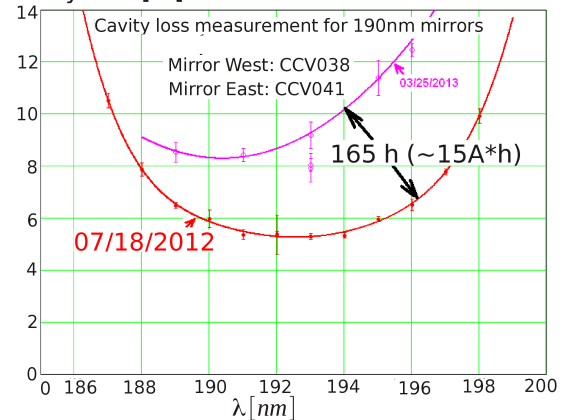


Figure 7.13: (Color online) Degradation of VUV 190 nm mirrors during  $E_\gamma=87$  MeV  $\gamma$ -production runs at  $E_e=1$  GeV.

[Hao13] H. Hao *et al.*, In *International Particle Accelerator Conference*, pp. 2006–2008, 2013.

[SLH09] S. Huang *et al.*, Nucl. Instrum. Methods A, **606** (2009).

[SMi13] S. F. Mikhailov *et al.*, In *International Particle Accelerator Conference*, pp. 1301–1303, 2013.

[YWu13] Y. K. Wu, In *International Particle Accelerator Conference*, pp. 264–266, 2013.

### 7.1.6 Electron-Bunch Cleaning with a Transverse Feedback System

W.Z. WU, J.Y. LI, M.W. AHMED, J.M. MUELLER, W.R. ZIMMERMAN, Y.K. WU, *TUNL*

In 2009, the old analog bunch-by-bunch transverse feedback (TFB) system was upgraded to a digital one using the same field-programmable gate-array technology as the longitudinal feedback system. The upgraded TFB was fully commissioned in 2011. In 2012, a new bunch-cleaning technique was developed to clean spillover bunches using the new TFB system, thus reducing the  $\gamma$ -ray-beam relative background to a level of  $10^{-4}$  per bunch for HI $\gamma$ S operation.

In storage rings, electrons can spill over into adjacent “empty” RF buckets by a variety of mechanisms. These beam spillovers can destabilize the main electron bunches and produce unwanted  $\gamma$ -ray-beam background. Bunch purification can be realized by driving the electrons in the unintended RF buckets into large-amplitude betatron oscillations, causing the loss of these electrons. A new method based on the bunch-by-bunch transverse-feedback (TFB) system has been developed by applying a positive feedback to excite the betatron oscillation of unwanted electrons to remove them from beam-spillover RF buckets.

In the Duke storage ring, the  $\gamma$ -ray beam is produced via the collision (Compton scattering) between an FEL photon beam and the electron beam. The timing structure of the Compton  $\gamma$ -ray beam is determined by the bunch pattern of the electron beam and the FEL pulse structure. For example, in the ideal condition with two equally filled electron bunches separated

by half of the circumference of the storage ring (179 ns), the  $\gamma$ -ray beam would have the same timing structure as the electron beam, with  $\gamma$ -ray pulses separated by 179 ns. In typical HI $\gamma$ S operation, electrons in spillover bunches can produce  $\gamma$ -ray pulses at times other than those of the main ones. Measurement of the timing of the  $\gamma$  rays provides direct information about the spillover bunches. Therefore, the capability and effectiveness of bunch cleaning using the TFB system can be studied by collecting  $\gamma$ -ray events and recording the timing of these events.

At the beginning of such an experiment, two main RF buckets were filled with an equal amount of charge, about 30 mA (10.8 nC) per bunch, with the storage ring operating at 512 MeV and the FEL lasing at 548 nm. In this configuration, an 8.78 MeV  $\gamma$ -ray beam was produced. Eight small bunches were then partially filled to simulate spillover bunches. A schematic of the  $\gamma$ -ray measurement during the bunch cleaning process is shown in Fig. 7.14.

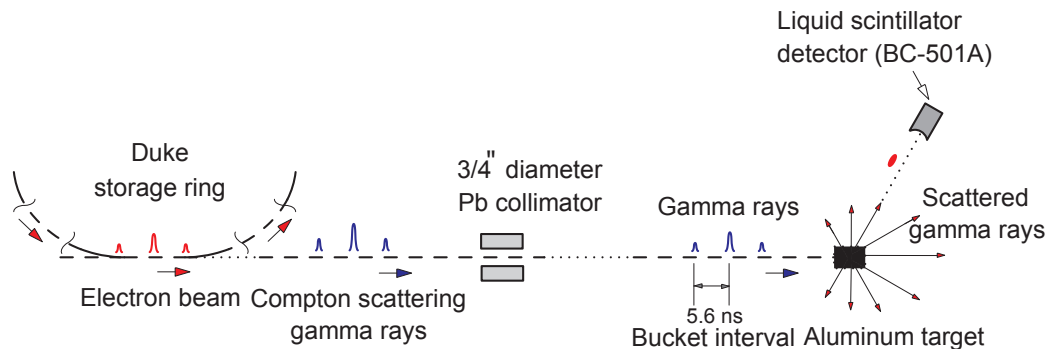
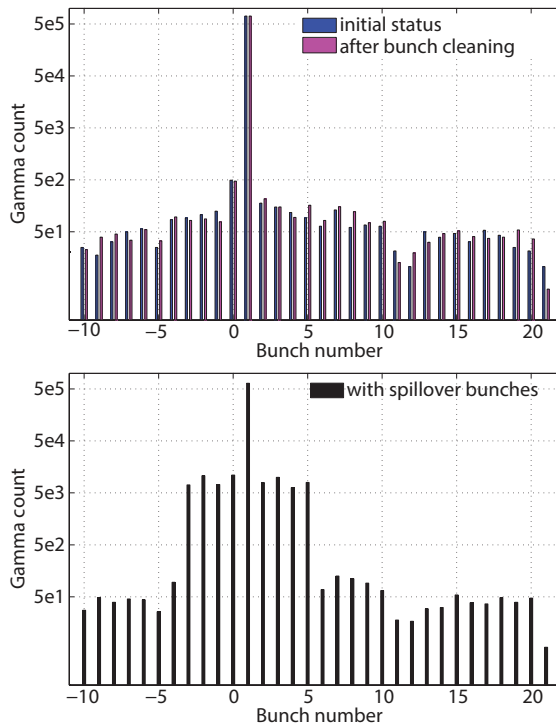


Figure 7.14: Schematic of  $\gamma$ -ray measurements during a bunch-cleaning process. The timing resolution of the detector is less than 200 ps with a counting rate of about 2 kHz.

**Table 7.6:** Relative  $\gamma$ -ray backgrounds produced by 8 electron bunches adjacent to one of the main bunches. The backgrounds are scaled using the main  $\gamma$ -ray beam pulses.

Measurement	Beam configuration	Average background per bunch	Total background in 8 bunches
1	Two main bunches	$2.4 \times 10^{-4}$	$1.9 \times 10^{-3}$
2	Two main bunches + 8 spillover bunches	$1.3 \times 10^{-2}$	$1.1 \times 10^{-1}$
3	Two main bunches after 8 spillover bunches removed	$2.4 \times 10^{-4}$	$1.9 \times 10^{-3}$



**Figure 7.15:** (Color online) Histograms of normalized  $\gamma$ -ray counts for different measurements in the bunch-cleaning process. The upper plot compares the cases before injecting spillover bunches and after cleaning those bunches. The lower plot shows the significant  $\gamma$ -ray background after the eight spillover bunches are filled.

In the target room,  $\gamma$  rays were scattered by an aluminum target and detected by a liquid scintillator detector. This detector was used to measure the timing and energy of individual  $\gamma$  rays. The detector was synchronized to the RF signal of the storage ring with a time detection window width of 171.9 ns. The overall timing resolution of the detector was less than 200 ps, which was much shorter than the 5.6 ns separa-

tion of two adjacent electron bunches. In measurement 1, two main bunches (numbers 1 and 33) were filled for  $\gamma$ -ray production, and the  $\gamma$ -ray counts were accumulated for 1.6 min. Then four small bunches on each side of bunch 1 were filled to simulate spillover bunches with a current of about 1 mA (0.36 nC) per bunch. The second measurement was carried out for 6.4 min using the stored electron beam with two main bunches and the eight small bunches. Finally, the eight spillover bunches were quickly removed using the TFB system, and electrons were filled into two main bunches within a few injection cycles. After bunch cleaning, the third measurement was performed for 5.8 min.

For a better comparison, the results of these measurements are scaled to the time duration of the third measurement as shown in Fig. 7.15. In measurements 1 and 3, the normalized  $\gamma$ -ray counts produced by the main electron bunch are about the same,  $7.1 \times 10^5$ , indicating that the bunch cleaning process does not cause any obvious electron loss in the main bunches. Using the measurement-time window width of 172 ns, the relative  $\gamma$ -ray background of the eight adjacent bunches can be scaled to one half of the whole beam (with a duration of 179 ns), which is about  $10^{-3}$  for the “fresh” injected two-bunch beam, and about  $10^{-1}$  with artificial spillover bunches (see Table 7.6). After bunch cleaning the relative background drops back to  $10^{-3}$ . The  $\gamma$ -ray background due to a particular bunch is at the  $10^{-4}$  level after cleaning. This is the expected level if  $\gamma$ -ray events would be collected in a wider time window to include all  $\gamma$  rays produced by two main bunches and electrons in the other “unfilled 62 RF buckets. For most nuclear physics experiments, this level of background can be tolerated. Therefore, the TFB-based bunch cleaning system is an effective tool to realize the production of a “clean  $\gamma$ -ray beam with a low background.

### 7.1.7 Wiggler Field Compensation at the Duke FEL Storage Ring

H. HAO, J. LI, S.F. MIKHAILOV, Y.K. WU, *TUNL*

**At the Duke storage ring, wiggler field compensation for both planar and helical wigglers is important for reducing the impact of uncompensated magnetic fields on the electron-beam orbit. A set of optimal correctors was used in developing a compensation scheme for all six FEL wigglers (four helical OK-5 wigglers and two planar OK-4 wigglers) using the beam-based technique. The scheme was implemented in the feed-forward controls for the FEL wigglers.**

To produce a high-flux  $\gamma$ -ray beam at the HI $\gamma$ S facility, strong FEL wigglers are used. The range of operational wiggler current is from 0 to 3500 A, but for high flux  $\gamma$ -ray beam production, we typically use currents above 2000 A. At currents above 2400 A, the magnetic poles of the helical OK-5 wigglers start to saturate, causing the wiggler to contribute significantly to the closed-orbit distortion of the electron beam. For FEL/HI $\gamma$ S, a distorted electron beam orbit can degrade the quality of the operation because of a spatial mismatch between electron and FEL beams. Therefore, it is critical to develop a wiggler field compensation scheme to achieve high-performance FEL and  $\gamma$ -ray operations. In 2012, a wiggler switchyard system (see Fig. 7.16) was installed on the Duke storage ring to allow a quick changeover between planar OK-4 and helical OK-5 FEL wigglers [YWu13]. After the switchyard upgrade, the wiggler field compensation schemes for all six FEL wigglers were fully implemented.

Figure 7.17 shows the rms values of the electron beam orbit deviation in the north and south straight sections of the Duke storage ring with the OK-5B wiggler (the second OK-5 wiggler along the electron-beam direction). Its current was varied from zero to the maximum operational value of 3500 A. It can be seen that the horizontal orbit rms values have a linear dependency with the wiggler current settings below 2400 A, with a slope of 0.13 mm/kA. For wiggler current settings between 2400 A and 3500 A, the horizontal orbit distortion increases significantly, with a slope of 1.25 mm/kA. This large change indicates that the first and second order integrals of the uncompensated wiggler field become much larger above 2400 A, an effect attributed to wiggler saturation. For the OK-5 wigglers, the related orbit distortion

is compensated by using four correctors at the ends of the wiggler, two for the horizontal direction, and two for the vertical direction. For the OK-4 wigglers, two adjacent horizontal correctors located upstream and downstream of the OK-4 wiggler provide field compensation.

The wiggler-field-compensation scheme is determined using the beam-based technique. First, the response matrices of the correctors are measured at different wiggler currents. In the measurements, only the readings of straight-section beam-position monitors are included in the matrices. The inverses of these matrices are calculated using the singular-value-decomposition algorithm. The corrector strength can be obtained using this inverse of the response matrices. Figure 7.18 shows the corrector strengths for the OK-5B wiggler field compensation. Here we can also see that the trends of the corrector strengths change at around 2400 A.

The wiggler compensation schemes were implemented in the accelerator control system using the feed-forward scheme [JLi13]. The strengths of the correctors are automatically varied with the wiggler current setting. Figure 7.17 shows the rms values of the measured orbits in the straight sections for different current settings, with and without the feed-forward field compensation. It clearly demonstrates that the orbit distortion caused by the wiggler is effectively reduced by the feed-forward compensation. For wiggler current settings lower than 2400 A, the small orbit distortion is reduced by about 30%. For currents higher than 2400 A, the compensation scheme reduces the orbit distortion by a factor of two to seven.

The closed-orbit distortion around the storage ring is further reduced using the global-orbit-

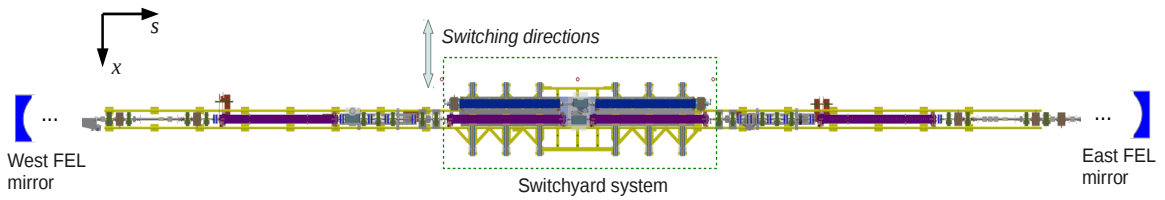


Figure 7.16: (Color online) The wiggler-switchyard system located at south straight section of the Duke storage ring. There are a total of four OK-5 helical wigglers (colored in purple) and two OK4 planar wigglers (colored in blue, shown above the beamline) which can produce circularly and linearly polarized radiation, respectively.

feedback system with up to 56 horizontal and 24 vertical correctors. The electron beam orbits around the ring with and without orbit feedback are shown in Fig. 7.19, where we can see that at some locations the horizontal orbit distortions are reduced from a few hundred microns to a few tens of microns. The impact of the global orbit feedback on the smaller residual vertical orbit distortion is not significant.

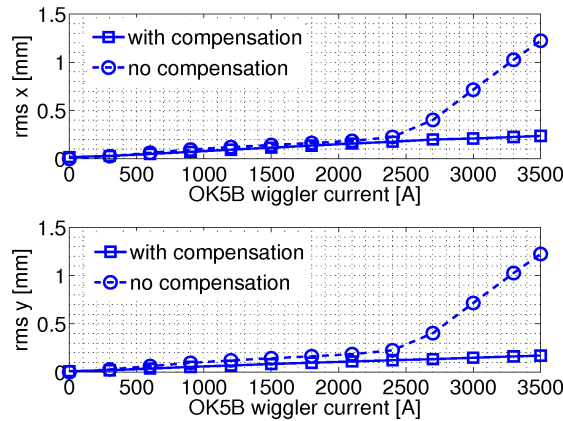


Figure 7.17: (Color online) The rms  $x$  and  $y$  orbits in the straight sections for different OK5-B wiggler current settings with and without wiggler field compensation.

The wiggler field compensations for all six wigglers at Duke storage ring were measured, tested, and implemented in the accelerator control system. In each case, the compensation has effectively reduced the orbit distortion caused by the wiggler fields. A similar technique was applied to the buncher-magnets field compensation, resulting in a significant reduction of the closed-orbit distortion induced by the buncher magnet.

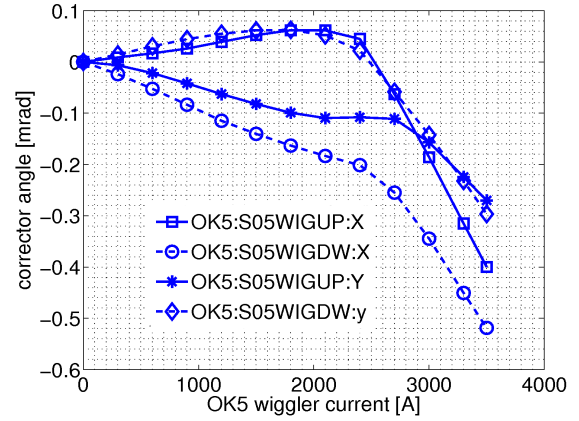


Figure 7.18: (Color online) Correctors strengths for OK-5B wiggler field compensation.

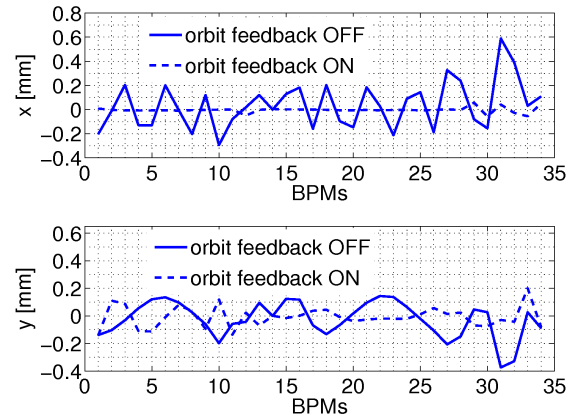


Figure 7.19: (Color online) Electron beam orbits around the storage ring with orbit feedback turned on and off. The OK-5B wiggler is energized and set to 2700 A.

[JLi13] J. Li *et al.*, In *International Particle Accelerator Conference*, pp. 3270–3272, 2013.

[YWu13] Y. K. Wu, In *International Particle Accelerator Conference*, pp. 264–266, 2013.

### 7.1.8 Implementation of Magnetic Lattice and Magnetic Field Compensation Schemes for FEL Wiggler Operation

J.Y. LI, H. HAO, W.Z. WU, S. MIKHAILOV, V. POPOV, Y.K. WU, *TUNL*

The FEL wiggler switchyard, which is used to change between two planar OK-4 and two helical OK-5 wigglers, was installed and commissioned in 2012. With a total of six wigglers, the Duke FEL can be operated in a number of configurations and with a wide range of magnetic fields. Complex compensation schemes have been developed for the operation of the wigglers.

From 2005 until 2012, one of the two 34-meter-long straight sections of the Duke storage ring contained two helical OK-5 wigglers in the two ends, and two planar OK-4 wigglers in the middle section. Using various wiggler configurations, HI $\gamma$ S successfully provided 1 to 60 MeV polarized  $\gamma$ -ray beams for user experiments. It also demonstrated the capability of generating 100 MeV  $\gamma$ -ray beams with considerable flux. To increase the  $\gamma$ -ray flux in the high energy region and extend the capabilities to even higher photon energies, a wiggler switchyard system was developed. It was installed and commissioned in 2012. The wiggler switchyard is used to change between two planar OK-4 wigglers and two helical OK-5 wigglers in the middle of the FEL straight section in a period of a few days.

To minimize the wiggler impact on the electron-beam closed orbit and storage-ring magnetic lattice, complex compensation schemes, including magnetic field and lattice compensation, have been developed and implemented in the storage-ring control system.

Using the switchyard system, the Duke FEL can be operated with various wiggler configurations. Different schemes have been developed to compensate the magnetic lattice for FEL operation with each of these configurations. Nine pairs of quadrupoles in the FEL straight section are used for beta-function matching and tune compensation. These quadrupoles are also used to build a set of tune knobs for operating the storage ring in a transparent manner while preserving optimal performance. Due to the impact of the wigglers, the tune-knob coefficients change with the wiggler configurations and magnetic fields. The total change of the quadrupole strength needed for lattice compensation and tune-knob adjust-

ment is modeled using a polynomial function,

$$\Delta K = \sum_{m=0}^6 a_m \widetilde{K}_w^m + \sum_{n=1}^3 \left[ \sum_{m=0}^6 b_{mn} \widetilde{K}_w^m \Delta\nu_x^n + c_{nm} \widetilde{K}_w^m \Delta\nu_y^n \right] \quad (7.1)$$

where

$$\widetilde{K}_w = \left( \frac{K_w}{10E[\text{GeV}]} \right)^2 = \left( \frac{0.934\lambda_w[\text{cm}]B_0[\text{T}]}{10E[\text{GeV}]} \right)^2 \quad (7.2)$$

is the scaled wiggler strength;  $B_0$  and  $\lambda_w$  are the nominal magnetic field and period of the wiggler, respectively;  $E$  is the electron energy;  $\Delta\nu_{x,y}$  are the tune-knob adjustments,  $a_m$ ,  $b_{nm}$  and  $c_{nm}$  are determined using a large number of designed lattices for each wiggler configuration with varying wiggler strengths and tune-knob settings. The feed-forward tables are calculated using these polynomial coefficients and  $\widetilde{K}_w$ . To accommodate various wiggler configurations, each quadrupole in the FEL straight section is controlled with seven feed-forward tables.

The lattice-compensation and tune-knob schemes are implemented in the EPICS database of the storage-ring control system as illustrated in Fig. 7.20. The wiggler configuration selector (WCS) defines a particular wiggler configuration. The compensation scheme selector is used to select a proper compensation scheme. Different schemes use different sets of feed-forward tables according to the WCS. When the wiggler configuration, wiggler setting, or a tune knob setting is changed, a subroutine record will calculate the quadrupole strength changes  $\Delta K$  according to

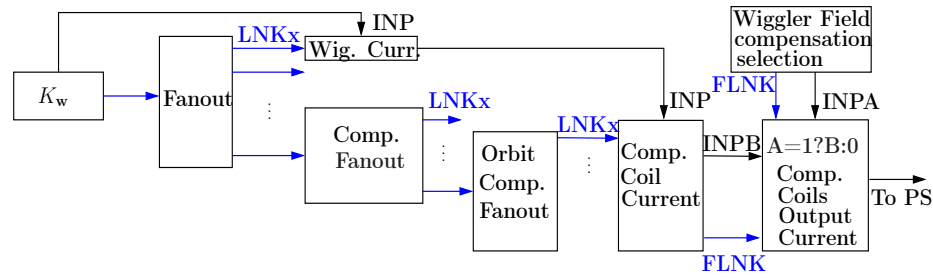


Figure 7.20: (Color online) The block diagram of the lattice-compensation and tune-knob schemes.

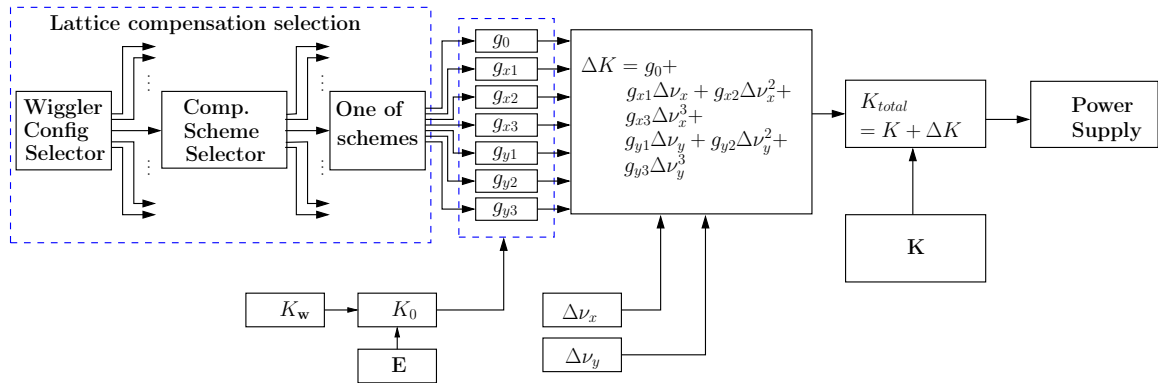


Figure 7.21: (Color online) The block diagram of the wiggler field compensation scheme.

the feed-forward tables. The changes are then added to the corresponding nominal quadrupole values, which leads to resetting the corresponding power supplies.

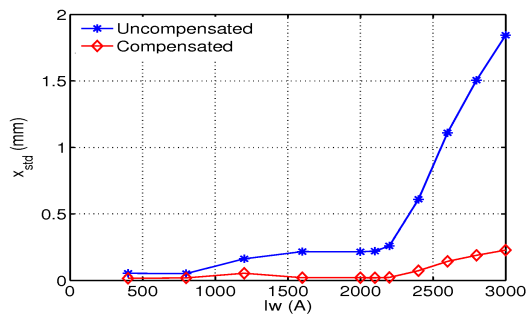


Figure 7.22: (Color online) Horizontal orbit compensation for the downstream OK-4 wiggler.

To minimize the closed-orbit distortion caused by the residual magnetic fields of the wigglers, field compensation schemes have been developed using beam based measurements [Hao13]. The OK-5 wigglers have built-in correctors, while the orbit correctors for the OK-4 wigglers are located just outside the wigglers. The compensation for each wiggler is individually measured. The compensation currents of the correctors are acquired by varying the cor-

rector strength to minimize the orbit distortion around the storage ring. The corrector strengths as a function of wiggler current are used to build feed-forward tables, which are integrated into the storage-ring control system as shown in Fig. 7.21.

The wiggler-field-compensation selector (WFCS), an EPICS record for each wiggler, controls whether the wiggler needs to be compensated. When the setting of a particular wiggler is changed, a record corresponding to each corrector will calculate the current for compensating the resultant orbit distortion. If the WFCS is set for this wiggler, the compensation current is sent to the corresponding corrector power supplies, otherwise no compensation current is applied.

Figure 7.22 shows the effect of field compensation for the downstream OK-4 wiggler. Since the OK-4 wiggler mainly has vertical field, it only affects the horizontal orbit. The compensation can bring the horizontal leakage orbit in the FEL straight section to below 0.2 mm RMS without any significant vertical orbit changes in the full working range of the wiggler (0-3 kA) for a 474 MeV electron beam.

[Hao13] H. Hao *et al.*, In *International Particle Accelerator Conference*, pp. 2006–2008, 2013.

---

### 7.1.9 Developing New Capabilities for the Storage-Ring Injection System

---

V.G. POPOV, S.F. MIKHAILOV, P. WALLACE, P. WANG, Y.K. WU, *TUNL*

**New capabilities have been developed for the injection system for the Duke storage ring. This year, a new beam-monitor system for the linac pre-injector allows continuous and non-invasive measurement of the linac charge. Good progress has been made in developing a new injection scheme to operate the linac in thermionic mode with a longer electron beam pulse to significantly increase the charge injection rate into the storage ring. An electromagnetic chopper is being developed for this purpose.**

The accelerator facility for the Duke FEL and High Intensity  $\gamma$ -Ray Source consists of a linac pre-injector, a booster synchrotron injector, and the storage ring. Since the full-energy booster injector was commissioned in 2006, the storage ring has been operated in top-off mode, and the linac energy was lowered from 270 MeV to 160-180 MeV. The linac, is the oldest of the three accelerators, with many components dating from 1960's to early 1990's. Thus it needs major upgrades in several areas, such as reliability, injection charge improvement, stability enhancement, and improved diagnostics. Without major investments to replace aging hardware for higher reliability, our effort has been devoted to developing beam diagnostics for the linac and new schemes to increase the charge injection rate.

Currently, the  $\gamma$ -ray intensity of HI $\gamma$ S at  $\gamma$ -ray energies above 20 to 25 MeV is limited by the electron injection rate into the storage ring, as Compton-scattered electrons are lost after transferring a large amount of energy to the  $\gamma$ -rays. The electron beam source is an RF photocathode gun, an S-band electron gun with the LaB<sub>6</sub> cathode illuminated using a UV nitrogen laser (337 nm) with a pulse duration of about 1 ns. Beginning in 2009 with the photocathode operation, we have increased the charge injection rate in the storage ring by modifying and improving the operation of the booster and linac. One major development was to modify the booster injection-kicker to allow electrons to be injected into any individual bunch in the booster. This allowed the booster to be operated in multi-bunch mode with multiple RF buckets to be filled and ramped to the extraction energy in the same energy ramp cycle. The other major development was an in-

crease of the repetition rate of the linac from 1 Hz to 4 Hz. With these developments, we have increased the injection rate by about a factor of two.

Here, we report recent progress in developing new capabilities for the injection system, including beam diagnostics and a new scheme to further increase the injection charge rate.

#### Linac Charge Monitor

Reliable and non-destructive monitoring systems for charge along the linac are of critical importance for higher-charge operation. There are three pulse-current transformers located along the linac. The sensitivity of each transformer is 1 V/A. Assuming 0.3 nC charge per pulse with a 1.5  $\mu$ s pulse duration, a transformer output voltage as low as 0.2 mV is expected. A broadband pre-amplifier and a simple analog integrator have been designed and developed to convert a 1.5- $\mu$ s-long pulse into a slowly decaying signal with a time constant of about 50  $\mu$ s and a voltage of a few hundred mV. The fact that the 1.5- $\mu$ s length of the pulse is a few orders of magnitude shorter than the time separation of the electron macropulses (100 ms at 10 Hz) makes it possible to achieve a reasonably accurate integration without the need to reset the integrator and subtract the voltage offset. A "sample-and-hold" circuit triggered by the front edge of the pulse captures the peak value of the pulse, which is proportional to the amount of charge. This signal is held for about 10 ms for further signal processing. For better accuracy, a sample-and-hold device could be triggered from the linac timing system. For radiation protection purposes, we are

interested in charge measurements averaged over a certain period of time—perhaps one minute. Such long-term integration is better done using a digital technique. A voltage proportional to the single-pulse charge is stored in the sample-and-hold unit and converted to a frequency. A multi-stage pulse counter works as a digital integrator, with practically unlimited dynamic range. The digital output of the counter can be used directly or be converted to an analog signal. In our case, an analog signal is the preferred output.

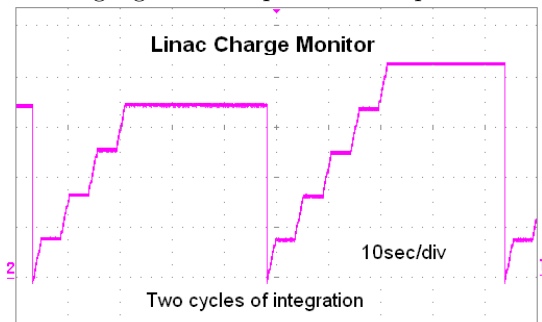


**Figure 7.23:** (Color online) Performance of the linac charge monitor during top-off injection to the storage ring.

Two fully functional charge monitors have been developed and tested successfully. Figure 7.23 shows the performance of the charge monitor used to monitor beam injection. We are planning to use at least two charge monitors, one for beam diagnostics, and the other as part of the personnel protection system to prevent operation beyond the set charge limit.

### Development for Higher Charge Linac Operation

One effective way to increase the injection rate into the storage ring is to operate the electron gun in thermionic mode, thereby increasing the electron beam pulse length and, therefore, the charge. A downside of this solution is an increased level of radiation background in the linac tunnel and in the booster vault. To determine the feasibility of this mode of operation, a test of thermionic injection was made in November 2012. During the test, the gun-cathode current was raised to 6.6 A (normal operation is 5.4 A). The measured charge per pulse was raised to 2.5 nC (normal operation is 0.14 nC). During injection, higher dose rates were found only in the north corridor, peaking at about 0.5 mR/hr at the booster entry (normal operation less than 0.02 mR/hr). We want the peak dose rate to

be about one-tenth of what was measured during the tests. From these tests, we conclude that there are no major radiation issues to solve, and that making additions to local shielding along the linac-to-booster line and around the booster injection devices will maintain our radiation doses in the occupied controlled areas at a safe level.

The beam pulse duration must be about 100 ns to match the booster circumference. To shape the electron pulse, an electromagnetic chopper is needed. The electron gun used on our linac is the same single-cell thermionic RF gun that was previously used on the MKIII FEL at Stanford and later at Duke. A short, multi-nanosecond pulse can be generated by chopping the electron beam with the built-in pulsed electrostatic kicker at an energy of 1 MeV just after the gun. The efficiency of the chopper performance depends on the shape of the high-voltage pulse applied to the kicker plate. We have chosen a single-cable delay line as a pulse forming network (PFN) and a cold-cathode thyatron as a switch. Independently controlling the PFN voltage and bias voltage will allow us to optimize the beam charge transferred during the chopper pulse. A schematic of the high-voltage generator for the beam chopper is shown in Fig. 7.24. The design principles were proved in a detailed computer model and tested in a lower voltage prototype model.

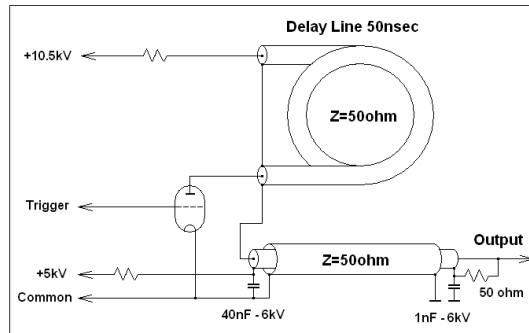


**Figure 7.24:** Schematic diagram of the HV beam chopper generator.

With the good results from the radiation survey, we are moving forward with testing and commissioning the beam chopper system in the near future, followed by a test operation of the electron gun in thermionic mode. Before user operation with a higher injection rate, several critical issues need to be resolved, including the overall radiation background for continuous injection during loss-mode operation of HI $\gamma$ S and the availability of critical hardware spares, such as the gun cathodes and modulator power supplies.

## 7.2 The FN Tandem Accelerator and Ion Sources

---

### 7.2.1 Tandem Accelerator Operation

---

C.R. WESTERFELDT, E.P. CARTER, J.D. DUNHAM, R. O'QUINN, B. WALSH, *TUNL*

The operation, maintenance, and improvements at the TUNL FN tandem accelerator over the last year are summarized.

#### Tandem Operation

During the period September 1, 2012 to August 31, 2013, the TUNL FN tandem accelerator was operated on 225 days for 3063 hours at terminal potentials ranging from 0.4 MV to 8.1 MV. Beams accelerated during this period include unpolarized protons, deuterons, and  $^4\text{He}$ . The terminal operating potential during the reporting period is shown graphically in Fig. 7.25.

The tandem was opened on June 3, 2013 for routine maintenance. One bad column resistor was found at this opening. The foil stripper box was opened and cleaned. A new set of 75 ACF “Classic Carbon” collodian-coated stripper foils was installed. Replacement of these foils is necessary at least once per year due to the number of low-energy  $\alpha$ -particle-beam runs for Rutherford backscattering measurements. The thicknesses of the foils vary from 1 to 3  $\mu\text{g}/\text{cm}^2$ . The Pelletron charging system was inspected and all idlers were replaced as were the charge pickoff wheels. The chain motors were greased, the tension on the low-energy drive belt was adjusted, and the terminal alternator belt was also adjusted. The corona needles were cleaned and the corona shield was replaced. The tandem was closed on June 13. Tandem operations resumed the next day.

#### Laboratory Projects

The off-axis direct-extraction negative-ion source (DENIS) continues to be the most utilized of our three ion sources, with 5100 hours logged (beam

available but not necessarily accelerated) during this reporting period. The most common beam particle was deuterons, which were employed in a variety of nuclear physics reactions as well as Homeland Security and NNSA experiments. Major changes include the replacement of the main diffusion pump and backing pump, and the relocation of some previously remote controls to the main ion source console, so that the operator can now monitor and adjust everything from one location.

The TUNL helium-exchange source was operated for a significant number of hours this past year, delivering 1 to 2  $\mu\text{A}$  of  $^4\text{He}$  beam to the tandem low-energy cup using a sodium charge-exchange canal. A parallel-plate chopper was installed this year at the exit of the ion-source box to permit pulsed beam experiments to occur this fall. A  $^3\text{He}$  gas recirculation system is being constructed for this source to capture the gas pumped by the diffusion pump, purify it, and compress it into a ballast container to be reused (see Sect. 7.2.2). Actual construction and testing of this system will occur this fall.

TUNL has a dedicated beam line for high intensity neutrons. This beam line is located on the 20-degree port of our main switching magnet. This facility was dismantled last winter to permit one of our engineers to design a more accessible beam line, while incorporating better shielding and better collimation of the neutron beam. We anticipate reconstructing this facility this winter with operations resuming in the spring of 2014.

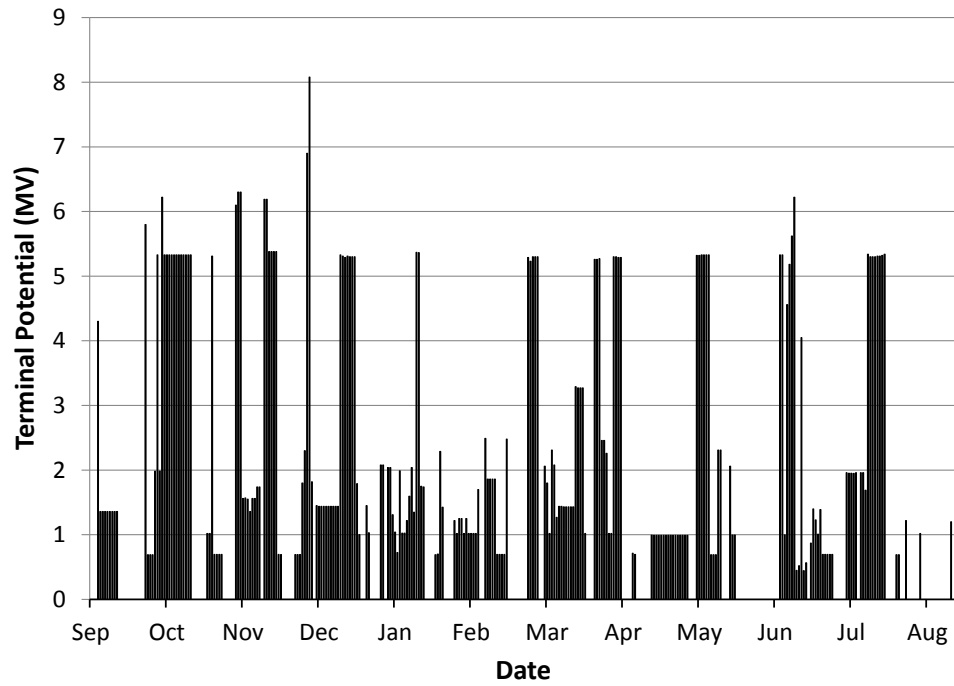


Figure 7.25: The TUNL FN tandem operating potential during the present reporting period.

## 7.2.2 A $^3\text{He}$ Gas-Recirculation System for the Helium Ion Source

D.C. COMBS, J. DUNHAM, C.R. HOWELL, D.R. TICEHURST, C.R. WESTERFELDT, A.R. YOUNG  
*TUNL*;

**A system for recovering and storing  $^3\text{He}$  gas from the helium ion source in the tandem accelerator laboratory is being developed so that  $^3\text{He}$  ion beams can be provided for injection into the tandem. This year the system design was finalized and the main components, including the initial load of  $^3\text{He}$  gas, were procured.**

Neutrinoless double-beta decay ( $0\nu\beta\beta$ ) experiments have the potential to probe the absolute mass scale of the neutrino, but to do so requires accurately knowing the nuclear matrix element associated with the decay. Calculations of the  $0\nu\beta\beta$  matrix element for a given isotope vary considerably depending on the model used [Ell04]. In an effort to constrain the calculated value of the  $^{76}\text{Ge}$   $0\nu\beta\beta$ -decay nuclear matrix element, a series of experiments to study the two-nucleon-transfer reaction ( $^3\text{He},n$ ) on isotopes used in  $0\nu\beta\beta$  experiments will be carried out using the TUNL tandem accelerator. Given the scarcity and high cost of  $^3\text{He}$  [Ade10], a system to recover and recirculate the gas in the helium ion source will be put into service before producing  $^3\text{He}$  beams.

The helium ion source uses a diffusion pump backed by a mechanical pump to evacuate the source chamber. In the existing system the mechanical pump exhausts to atmosphere. Gas flow at the intake of the existing system has been measured to be approximately 10 standard cubic centimeters per second.

The new recirculation system and the existing source are shown in Fig. 7.26. Gas from the reservoir is fed to the source chamber through a flow meter. The reservoir can be refilled from a  $^3\text{He}$  gas cylinder. To keep from introducing pump oil into the recirculating gas, a hermetically sealed rotary vane pump is used to back the diffusion pump. A molecular sieve is in the line between the diffusion pump exhaust and the rotary vane pump input to prevent diffusion pump oil from entering the recirculation system. The gas exhausted by the rotary vane pump passes through a cryogenic sorption pump to further reduce contaminants. The sorption pump can be isolated from the system with a set of valves (V9 and

V11 in Fig. 7.26) and recharged using a mechanical pump cart. A diaphragm compressing pump is used to refill and pressurize the helium reservoir. Similar systems [Ver73, Wik82] have been shown to recover about 90% of the source gas.

Most of the major system components were identified and obtained over the summer. The  $^3\text{He}$  gas arrived in September. A Pfeiffer PentaLine 35M rotary vane pump was selected to serve as the sealed mechanical pump. This pump was received in July. A KNF N143 double-diaphragm pump was selected as the helium compressor and was received in June. Alicat was the selected manufacturer for the mass flow meter, and their M20 mass flow meter was chosen for real-time mass-flow measurements. It was received in August. The valves in the recirculation system (V7-V15 in Fig. 7.26) will be stainless steel bellows-sealed valves with Swagelok connections. The gas lines will be constructed from stainless steel tubing. The remaining components will be procured by the end of October.

Construction will take place in the first half of November. Testing with  $^4\text{He}$  will start in the second half of November and last through the end of the year. Testing with  $^3\text{He}$  will take place in January 2014.

---

[Ade10] S. Adee, *IEEE Spectrum*, **47**, 16 (2010).

[Ell04] S. R. Elliott and J. Engel, *J. Phys. G*, **30**, R183 (2004).

[Ver73] A. Vermeer, N. A. van Zwol, and B. A. Strasters, *Nucl. Instrum. Methods*, **106**, 115 (1973).

[Wik82] J. C. Wikne and E. A. Olsen, *Nucl. Instrum. Methods*, **200**, 179 (1982).

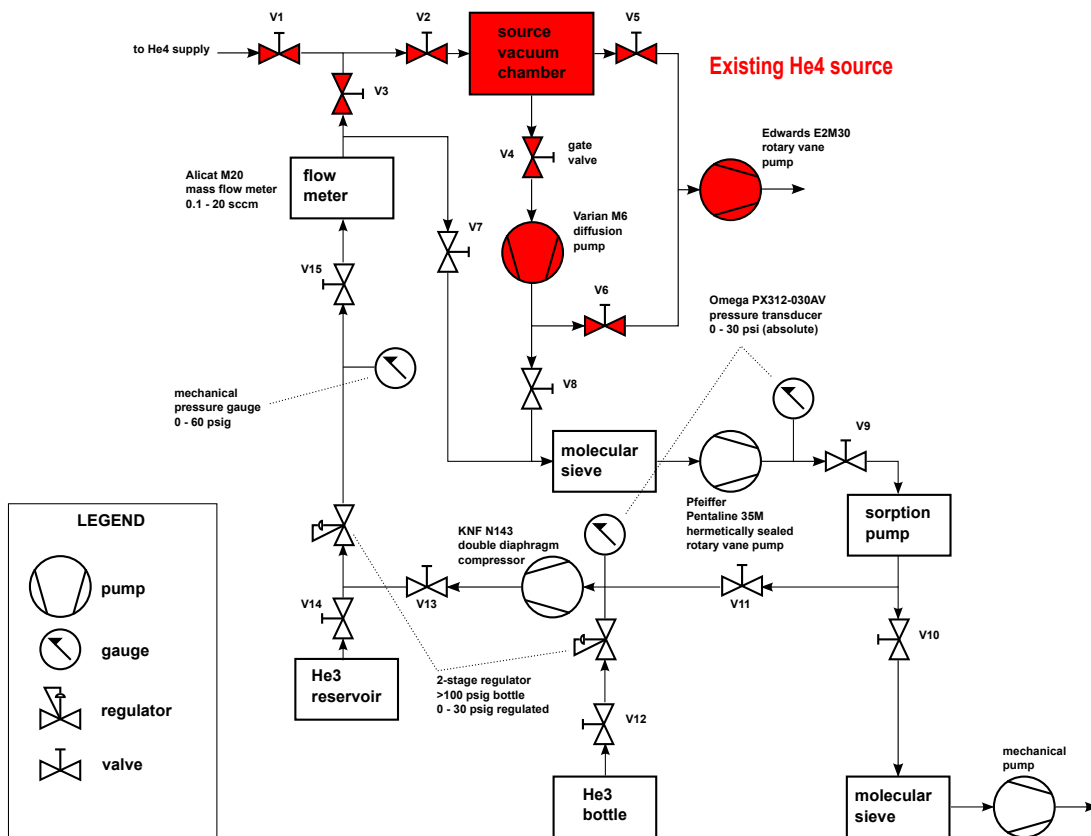


Figure 7.26: (Color online) Schematic diagram of the proposed  $^3\text{He}$  recirculation system. The shaded components are part of the existing source.

## 7.3 The LENA Accelerator and Ion Sources

### 7.3.1 The LENA JN Van de Graaff Accelerator

L.N. DOWNEN, K.J. KELLY, S.M. HUNT, J. SURBROOK, J. DERMIGNY, M.Q. BUCKNER, B.P. CARLIN, R.L. LONGLAND, A.E. CHAMPAGNE, A. COOPER, B. WALSH, T.B. CLEGG, C.R. WESTERFELDT, *TUNL*

**The LENA JN Van de Graaff accelerator has been extensively used both for experiments and for target-characterization studies. Most recently, the JN has been successfully adapted to produce  $\alpha$ -particle beams, despite several performance issues, and a beam rasterizing system has been installed on the beam line to increase target lifetimes.**

The LENA JN Van de Graaff accelerator is a crucial tool not only for exploring nuclear physics in the 200 to 1000 keV energy regime, but also for characterizing targets and monitoring target degradation. Recently the JN has been used for studying the  $^{14}\text{N}(p,\gamma)^{15}\text{O}$  and  $^{17}\text{O}(p,\gamma)^{18}\text{F}$  reactions, as well as for characterizing  $^{29}\text{Si}$  and  $^{22}\text{Ne}$  targets for use in future experiments. In total, LENA has accumulated 1547 hours of JN operation over 90 days in the last year, achieving a maximum current of  $150\ \mu\text{A}$  for a proton beam on target.

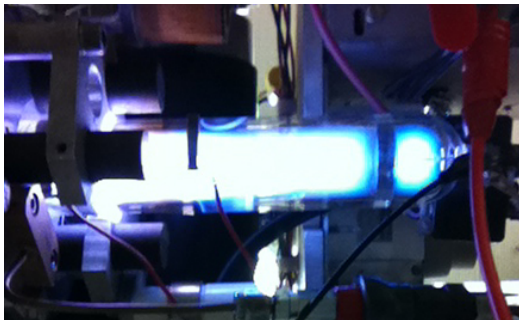


**Figure 7.27:** (Color online) The JN plasma bottle with a helium plasma.

In the last year, major efforts towards adapting the JN for  $\alpha$ -particle-beam production have yielded moderate success. Significant beam-production benchmarks include a measured  $200\ \mu\text{A}$  of  $\alpha$  particles before the analyzing magnet and  $35\ \mu\text{A}$  on target at 250 keV bombarding energy (see Figure 7.27). In order to get to this point in  $\alpha$ -particle-beam production, a number of hurdles had to be overcome, including hydrogen contamination, due to an outgassing ceramic

aperture in the plasma bottle, and the adaptation of the beam-optics settings for the heavier  $\alpha$  particles. Currently, we are faced with optimizing the beam current using beam-transport optics and analyzing-magnet calibrations for a range of beam energies.

While the JN is often used to monitor target degradation, both the JN and the electron-cyclotron-resonance ion source are capable of producing the intense, highly focused beams that are critically important for observing reactions with small cross sections and yet incredibly damaging to nuclear targets. This type of tightly focused, high-current beam causes rapid, non-uniform target wear. Target material inside this “hot spot” is quickly exhausted, leaving the surrounding target material unused. Thus, a magnetic beam-rasterizing system was implemented to move the focused beam continually over the full target area. Autodesk Inventor software was used to design a new mount, roughly 2 m in front of the target chamber. A new magnetic beam-steerer was also installed on the beam line. Control signals for the horizontal- and vertical-motion programmable power supplies, which step coil currents for the electromagnets of the rasterizing system, are provided via spare ports in the currently employed LabVIEW and Fieldpoint remote-control systems. Following its implementation, the rasterizing magnet system was set to move the beam continuously across the target surface either in circles or in multi-loop spirals with a typical angular frequency of  $1^\circ/100\ \text{ms}$ .

The above improvements were achieved despite numerous technical difficulties over the course of the year. Most notably, the JN charging

belt showed signs of age, including belt stretching and cracking. This led to belt alignment issues and loss of terminal voltage stability. Additionally, an acceleration-column resistor failed, resulting in charge buildup on the column and eventual discharge to the JN tank. Finally, it was discovered that damaged insulation on the high-voltage focus wire allowed a connection to be made between neighboring acceleration-tube electrodes.

While the focus wire and failed resistor were easily and successfully replaced, replacement of the charging belt was a long process. Initially, a belt that was later determined to be inferior was installed in the JN. This belt was incapable of holding charge and showed evidence of arcing along its surface. A second replacement belt

was recently installed with some success. Terminal stability has improved greatly at low bombarding energies, but further belt conditioning is necessary to regain stability at higher terminal voltages.

In summary, the LENA JN Van de Graaff is an unparalleled tool for measuring low energy nuclear reactions relevant to astrophysical phenomena. As such, significant time and effort has been invested to keep the JN running at its optimal level and improving and expanding its capabilities, even though further work is needed to reach this goal.

Support was provided for M.Q.B. by the DOE NNSA Stewardship Science Graduate Fellowship under Grant no. DE-FC52-08NA28752.

### 7.3.2 A Proposed Upgrade of the Acceleration Column of LENA's ECR Source

A.L. COOPER, T.B. CLEGG, A.E. CHAMPAGNE, J. SURBROOK, *TUNL*; I. POGREBNIYAK *Michigan State University, East Lansing, MI*

**A design is being developed to upgrade the acceleration tube of the ECR source at TUNL's Laboratory for Experimental Nuclear Astrophysics. The upgrade will enhance both source stability and beam intensity.**

#### Introduction

Given the low energy-regime for nuclear processes in stellar interiors, the Coulomb barrier severely constrains nuclear reaction rates. Hence, a primary experimental objective for the accelerators at TUNL's Laboratory for Experimental Nuclear Astrophysics (LENA) is to maximize their beam intensity to ensure the highest possible nuclear event rate during each experiment [Cea10]. High beam intensity from the electron-cyclotron resonance (ECR) source at LENA is especially important because the beam energies are only 90 to 200 keV.

During the past year the ECR source was upgraded with a microwave power supply that injects 1200 W of power into the plasma discharge chamber, compared with 500 W for our previous supply. The increased power improved both plasma density and beam intensity. This in turn meant that the beam produced greater ionization of background gas in the acceleration column, resulting in a rise in bremsstrahlung x-ray production from accelerated, back-streaming electrons striking electrodes of the acceleration tube. Stray ions and back-streaming electrons striking interior column surfaces heated them enough to weaken the vinyl acetate used to glue the present acceleration column together. [Cha11]. This increased current-load on the column also overheated the inter-electrode resistors, which establish the accelerating voltage gradient. The substantially increased electrical, mechanical, and thermal stresses on the ECR's present acceleration tube motivated our effort to find a new acceleration-tube design to overcome these issues.

The goals for the new beam-acceleration system are that it should: (1) reduce back-streaming

electrons, which cause x-rays when they strike internal column electrodes, (2) establish the required accelerating-voltage gradient by replacing resistors with low-conductivity, deionized water flowing between the column electrodes, and (3) protect the column electrodes with a robust system of spark gaps. To optimize beam transport from the ECR's plasma chamber to the acceleration tube, the extraction electrode's position will be controlled remotely by a stepper motor. Adjusting its axial location will accommodate better beam focusing over a wider range of beam injection and acceleration energies. Ultimately, these planned upgrades should result in a much improved beam-acceleration system that more suitably matches our significantly enhanced microwave system, thus alleviating present difficulties with electrical arcing and thermal stresses on the column.

#### Detailed activities

We set out to upgrade the acceleration column by first conducting charged-particle beam-optics calculations to understand the necessary electrode configuration and voltages to obtain optimum beam transport from the plasma-discharge chamber to the target over the energy range from 90 to 240 keV. This was accomplished via an electromagnetic field-simulation code called KEMFIELD which was supplied by the Karlsruhe Tritium Neutrino (KATRIN) experiment group at UNC. This code establishes the electric and magnetic fields within a region of interest by solving Laplace's equation using the boundary-element method. These fields are then immediately given to KASSIOPEIA, a charged-particle-propagation code that was also provided to us by the KATRIN group. It simulates the ion paths

from the ECR source and down the acceleration column. From these calculations, we have decided that injection energies of 40 keV and voltage differences of 20 kV between each consecutive column electrode will be the optimal solution for our proposed design.

The mechanical basis for our proposed acceleration-tube design is the Hyperion ion source, constructed by Twin Creeks Technologies [Ryd12]. This design succeeded in accelerating about 100 mA of protons to around 1.2 MeV. By contrast, we need only 20 to 30 mA of protons, but with a variable energy between 90 and 240 keV, and our beam must be transported to target through an array of other beamline components—electromagnetic steerers, quadrupoles, and an analyzing magnet. Hence our design is only a rough counterpart of theirs.

Several key physical and mechanical elements of their system will be beneficial for our ECR source. Their basic acceleration tube structure consists of alternating sections of large, 33-cm-diameter aluminum electrodes and ceramic rings, sealed together with O-rings. The large interior diameter enhances vacuum pumping efficiency, while structural integrity is maintained by holding the entire column under compression via insulating G10 fiberglass rods running its entire length. These are threaded into the base of the acceleration tube, which is located at ground, and squeeze the O-rings between the aluminum and ceramic sections, creating the required vacuum seal.

The Hyperion design also affords encouraging solutions to the damaging thermal and x-ray problems mentioned above. The problem of resistor heating should be reduced through the use of deionized water flowing between the electrodes along the column to establish the desired voltage gradient. With this design, leakage current and heat from each electrode can be immediately carried downstream by the water. This

takes the heat away from the ECR source and removes the thermal stress on the column. Conductivity measurements of LENA’s deionized water supply were made to determine the cross sectional area for the water lines necessary to supply enough resistance for such a voltage gradient. Also, spark-gap tests were completed to determine the proper spacing for a 20-kV maximum voltage difference at room temperature and humidity. To limit back-streaming electrons, we will adopt the Twin Creeks solution of transverse magnetic fields along the entire length of the column to divert electrons at their point of creation. These magnetic fields will be established by small permanent magnets, attached around the circumference of every other electrode in the acceleration tube.

Aside from improvements to the 200 kV acceleration column, the ECR source will also receive a new, water-cooled extraction electrode system to extract and focus  $H^+$  ions emerging from the +40 kV plasma chamber. This new acceleration-deceleration system consists of two electrodes that are held at the table voltage and that “sandwich” an electron-suppression electrode at about  $-2$  kV. Downstream, the 40 keV  $H^+$  beam drifts and expands within a hollow conical region before being focused strongly when it reaches the entrance to the acceleration column. For real-time optical-tuning ability, the entire extraction system is designed to rest on Thomson bearings and rods so that it can be freely moved longitudinally in the beamline by a LabView-controlled stepper drive.

- 
- [Cea10] J. Cesaratto, Nucl. Instrum. Methods A, **623**, 888 (2010).
- [Cha11] A. E. Champagne, TUNL Progress Report, **L**, 150 (2011).
- [Ryd12] G. Ryding, Private Communication, (2012).



# Nuclear Instrumentation and Methods

---

Chapter 8

- **Targets**
- **Detector Development and Characterization**
- **Facilities**
- **Data Acquisition Hardware and Software Development**

## 8.1 Targets

---

### 8.1.1 Status Report for the HI $\gamma$ S Frozen-Spin Target

---

P.-N. SEO, D.G. CRABB, R. DUVE, B. NORUM, S. TKACHENKO, *University of Virginia, Charlottesville, VA*; R. MISKIMEN, *University of Massachusetts, Amherst, MA*; M.W. AHMED, C.R. HOWELL, G. SWIFT, H.R. WELLER, *TUNL*

**A number of milestones in the development of the HI $\gamma$ S Frozen-Spin-Target (HIFROST) system have been reached both at TUNL and at UVa. The HIFROST dilution refrigerator was first cooled down with  $^4\text{He}$  and then with a mixture of  $^3\text{He}$  and  $^4\text{He}$  at UVa, and later moved to HI $\gamma$ S. The rest of the subsystems and infrastructure of HIFROST are being developed and tested at HI $\gamma$ S. Here we report on progress in preparing this target system for operation.**

With a motivation of measuring the Gerasimov-Drell-Hearn sum rule integrand for the deuteron below pion production threshold, the UVa group has been developing a frozen spin target system for HI $\gamma$ S in collaboration with TUNL personnel. Work on this project continues both at UVa and at TUNL. While the cryostat/refrigerator has been extensively tested at UVa, the other subsystems and infrastructure of HIFROST are being developed at HI $\gamma$ S. In July 2013 the dilution refrigerator was relocated to HI $\gamma$ S and integrated with the rest of the HIFROST subsystems. Extensive tests were done at room temperature and with liquid helium (LHe).

#### Dilution Refrigerator

After extensive tests at room temperature, the dilution refrigerator (DR) was first cooled down with liquid  $^4\text{He}$  and reached a temperature of 1K in the area where the target cell will be located. Next, a mixture of  $^3\text{He}$  and  $^4\text{He}$  (with a ratio of  $\sim 50/50$ ) was circulated and with  $\sim 15\%$  of the volume introduced, a temperature in the mixing chamber of 270 mK was reached. After the cool down test, the refrigerator was moved to HI $\gamma$ S. A target stand which supports the DR on the beam line, both vertically for target changes and horizontally for operation (see Fig. 8.1), was designed, built, and installed at HI $\gamma$ S. After mechanical tests of swinging the DR between positions, the refrigerator was pumped down at room temperature at HI $\gamma$ S for the first time.

#### Control System

The gas/liquid/vacuum control system consists of the  $^3\text{He}$  and  $^4\text{He}$  pumping system, inner vacuum chamber/outer vacuum chamber, gas manifolds for filling/flushing, and the LHe transfer line. The LHe transfer lines were designed at TUNL and fabricated by Cryofab, Inc. The LHe transfer lines were installed and successfully transferred the liquid during our initial cool down as expected. The HIFROST has three gas storage tanks for  $^3\text{He}$ ,  $^4\text{He}$ , and a mixture of  $^3\text{He}$  and  $^4\text{He}$ . Currently, two tanks are filled with pure  $^4\text{He}$  (99.97%) gas, while one tank has a gas mixture with  $\sim 10\%$  of  $^3\text{He}$  in the mixture. The gas handling control system was successfully tested with the refrigerator.

#### Superconducting magnets

The HIFROST uses two superconducting magnets, a 2.5-T polarizing magnet and a 0.5-T holding magnet. The polarizing magnet and the alignment system are shown in Fig. 8.2. The polarizing magnet is inserted onto the HIFROST using an alignment system as shown in Fig. 8.2. Once polarized, the polarization is maintained with the help of the holding magnet. The superconducting holding coil and the associated leads are kept cold by the  $^4\text{He}$  vapor and LHe as well in the target. Both magnet systems have been successfully tested.



Figure 8.1: (Color online) A target stand supports the dilution refrigerator on the beam line both (a) vertically for target changes and (b) horizontally for operation.

### Microwave System

The HIFROST polarizes the target sample via the dynamic-nuclear-polarization (DNP) technique. The DNP technique uses 70 GHz microwaves at a polarizing field of 2.5-T to achieve the desired polarization. The microwaves are produced using an extensive-interaction oscillator (EIO) and introduced in the target sample via microwave guides. The EIO system is powered by a Cober power supply system. The EIO, waveguides, and the safety interlock system were successfully tested at HI $\gamma$ S.



Figure 8.2: (Color online) Assembled polarizing magnet is being aligned with the target.

### NMR System

The target polarization in the HIFROST is measured using an NMR system. The NMR coils are placed around the target cell. Two NMR coils, one for the case of a proton target and the other for a deuteron target, were constructed using 500  $\mu$ m-diameter cupro-nickle wire. These coils are designed for a 5-cm long target cell. The coils are connected to Q-meters by cables of length  $\lambda/2$  at their resonant frequencies. The Q-meters were tested with an upgraded Labview DAQ. Tests with the 2.5-T polarizing magnet at 1K will be carried out in near future.

### Target material

The target samples can be D-butanol or a CD<sub>2</sub> target. The target samples are irradiated in an electron-beam environment to create paramagnetic centers. The irradiation helps in reaching higher polarizations. During the initial test, we used a non-irradiated CD<sub>2</sub> sample. In this CD<sub>2</sub> target, 15 g of target beads were held in a 1-mm perforated FEP housing in a quartz mixing chamber. In the actual experiment, we plan to use irradiated D-butanol.

### 8.1.2 Beam Test of the Dilution Refrigerator for HIFROST

P.-N. SEO, D.G. CRABB, R. DUVE, B. NORUM, S. TKACHENKO, *University of Virginia, Charlottesville, VA*; R. PYWELL, M. SHARMA, G. PRIDHAM, *University of Saskatchewan, Saskatchewan, Canada*; M.W. AHMED, H.R. WELLER, *TUNL*

In September 2013, we tested the assembled and warm dilution refrigerator of HIFROST with a 6-MeV beam while the neutron detector array was tested. The purpose of the test was to check alignment and background from the HIFROST cryostat. To do this, target beads were made with 15 g deuterated polyethylene powder ( $\text{CD}_2$ ) to measure neutrons and placed in a target holder made with FEP. The dilution refrigerator was assembled and aligned. A neutron detector array was placed around the center of the target. We report this test run and its result.

The first experiment using HIFROST will measure the Gerasimov-Drell-Hearn (GDH) sum rule on the deuteron below pion threshold and test theoretical predictions. The experiment requires a circularly polarized photon beam, a polarized deuteron target, and a neutron detector array. The detectors observe neutrons from photodisintegration of deuteron. In September 2013, at the end of run performed to test the detector system with a 6-MeV circularly polarized beam, we spent about four hours to investigate alignment of the dilution refrigerator and possible backgrounds. Data analysis is in progress.

A frozen target, in general, is surrounded by several layers of cryostat; target holder, a mixing chamber, inner-vacuum-chamber (IVC), radiation shielding, outer-vacuum-chamber (OVC). They are not necessarily concentric along the beam axis. In order to know where is the center of a target with respect to the detector array, we used a beam imaging technique available at FEL. We assembled the dilution refrigerator and mounted it on a target supporting frame. First we aligned it with a laser beam in gamma vault and then with the detector array as seen in Fig. 8.3. For a reference, we placed a screw on the surface of a mechanical center of the OVC nose. The 6-MeV gamma beam was collimated by a 6 long and 0.75 diameter lead collimator. The beam then entered the refrigerator. Before the beam interacts with the  $\text{CD}_2$  target, it passes through, in order, aluminum-coated 0.005 thick Kapton widow, 3 layers of cryogenic superinsulation, stainless-steel dilution refrigerator nose, and 0.6 mm thick copper  $^3\text{He}$  stopper, and then

a 0.25 mm thick FEP target holder. A half of the beam passes through the  $^3\text{He}$  stopper since the stopper is a semi-circle.

The imager detects the transverse beam distribution using a CCD receiving the visible light emitted by a BGO crystal illuminated by the gamma-ray beam. The images were taken using the gamma-ray imager in gamma vault. The pixel size is 0.0768 mm/pixel. The exposure time was about 10 minutes. The image of HIFROST target cryostat with a small screw is shown in Fig. 8.4. The target is aligned well vertically and is off the center by a few mm horizontally.

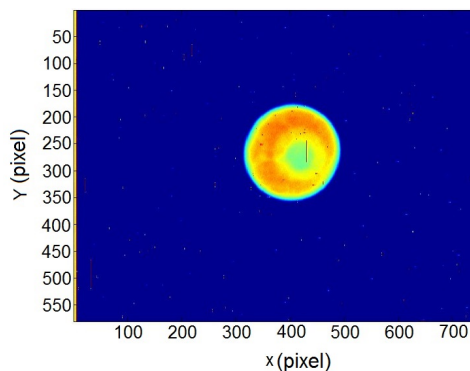


Figure 8.4: (Color online) Image of a target cryostat with a small screw with 6-MeV gamma beam using a BGO crystal.

While the neutron detector system for a measurement of GDH sum rule on deuteron was tested with a gamma beam in September 2013, we placed a target cryostat on a beam to check

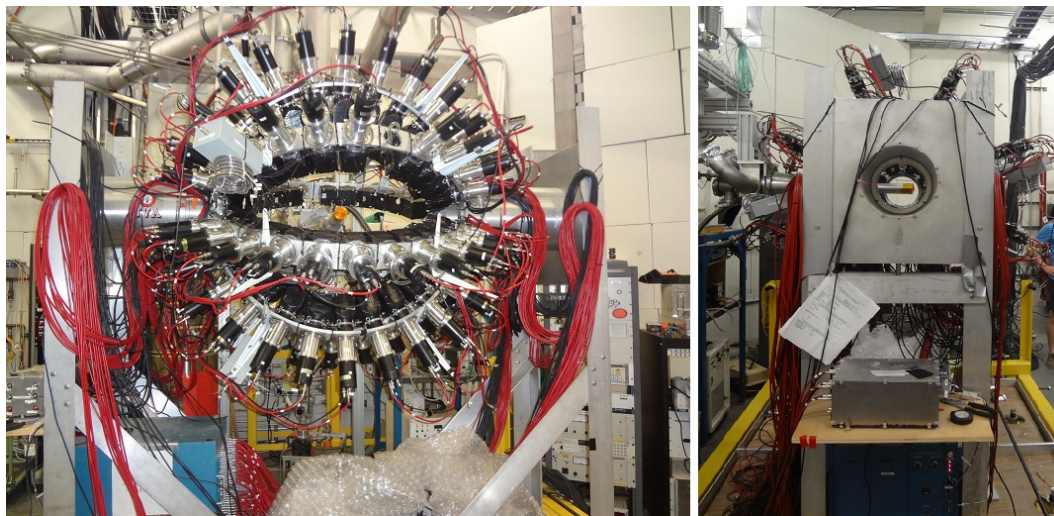


Figure 8.3: (Color online) The dilution refrigerator is aligned with a neutron detector array (Blowfish); front view (left) and side view (right).

background. The assembled target contained non-irradiated CD<sub>2</sub> in a target holder. The 15 gram of the target beads with 5 cm long were made and housed in a perforated FEP holder with 1 mm diameter. In order to prevent <sup>3</sup>He from escaping in dilution process, we made the <sup>3</sup>He stopper with copper. They were located inside a quartz mixing chamber. This is shown in Fig. 8.5.

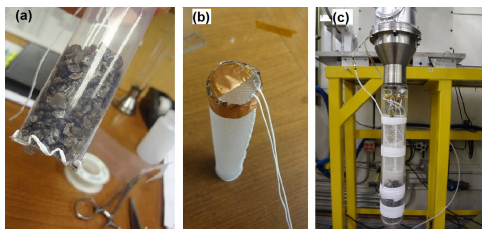


Figure 8.5: (Color online) (a) The non-irradiated CD<sub>2</sub> target beads were made and (b) a perforated FEP target holder with a copper <sup>3</sup>He stopper, and (c) the target in the holder and a <sup>3</sup>He stopper is inside a quartz mixing chamber.

The 6-MeV gamma rays interact with deuterons in the target and neutrons from photodisintegration were detected by the array of neutron detectors. One of the detectors at 90-deg which is closest to the target observed neutrons from the target and its raw time-of-flight spectrum is shown in Fig. 8.6. Gammas scattered off the target are at channel 1100 and neutrons from

photodisintegration are at channel 1300. Because of limited time, we were not able to remove a target from the HIFROST cryostat for a background run. However, the spectrum without the target cryostat shows no neutrons clearly as shown in Fig. 8.7. Despite the very limited time available for us, this spectrum shows that the GDH measurement is not going to have excessive background.

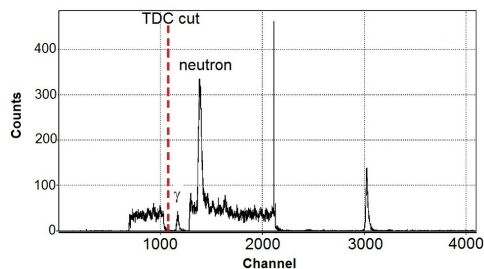


Figure 8.6: (Color online) Raw time-of-flight spectrum of the non-irradiated CD<sub>2</sub> target

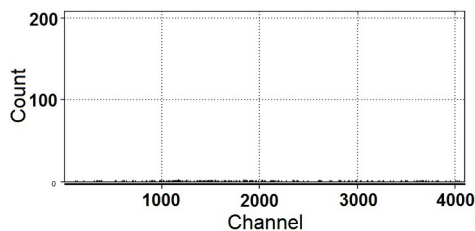


Figure 8.7: (Color online) Raw time-of-flight spectrum with no target cryostat

### 8.1.3 Cool-Down Tests of HIFROST at HI $\gamma$ S

P.-N. SEO, D.G. CRABB, R. DUVE, B. NORUM, *University of Virginia, Charlottesville, VA*; G. SWIFT, H.R. WELLER, *TUNL*

The dilution refrigerator for HIFROST was tested with liquid helium at the University of Virginia, and the target area reached about 270 mK. We then performed cold tests at HI $\gamma$ S. We first checked the liquid helium transfer lines. Then we cooled down the dilution refrigerator with the newly installed  $^3\text{He}$  and  $^4\text{He}$  pumping lines. The third test studied HIFROST with a warm target of  $\text{CD}_2$ .

The dilution capability of the HIFROST refrigerator was tested at the University of Virginia (UVa). A roughly equal mixture of  $^3\text{He}$  and  $^4\text{He}$  was circulated, and with about 15% of the volume introduced, the temperature in the mixing chamber reached 270 mK. The temperature was measured with a calibrated germanium thermal resistor in the target area. The resistance reading and corresponding temperature are shown in Fig. 8.8.

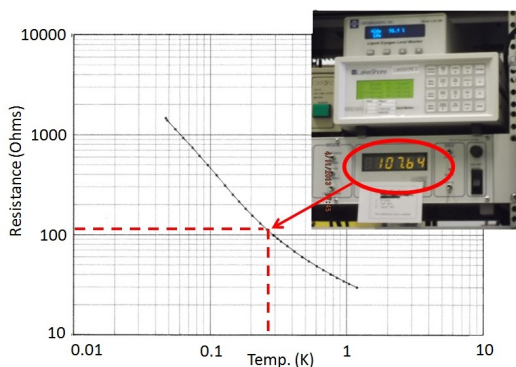


Figure 8.8: (Color online) The temperature in the target area was measured to be 270mK with dilution.

At HI $\gamma$ S, we began to cool HIFROST in stages to test different parts of the system. First, the liquid-helium (LHe) transfer lines were tested. These connect a 500-L storage Dewar to a 100-L buffer Dewar and a polarizing-magnet Dewar. Since we were unable to fill the storage Dewar, LHe was directly transferred from a commercial-supply Dewar to the buffer and magnet Dewars. This test also provided the opportunity to check other instruments that require LHe. These include LHe level probes, readouts, and thermal

sensors. The LHe boiling rates in stand-by mode were about 7.5 L/day for the magnet Dewar and about 16 L/day for the buffer Dewar. After this first cold test, we reviewed and established safety procedures for the future runs.



Figure 8.10: (Color online) Preparation for the second cool-down. The left photograph shows the NMR system; the right one shows the electronics rack for the thermal sensors, the LHe level readouts, etc.

Prior to cooling the HIFROST dilution refrigerator, we mounted and assembled it in a vertical position, as shown in Fig. 8.9. The parts that were installed include all the thermal sensors, a new target holder with a  $\text{CD}_2$  target, the temperature monitors for NMR, and a microwave generator. The installation is seen in Fig. 8.10. As we began to pump the helium lines, we found a leak in the  $^3\text{He}$  line and decided to cool the  $^4\text{He}$  line of the refrigerator. In about two hours we

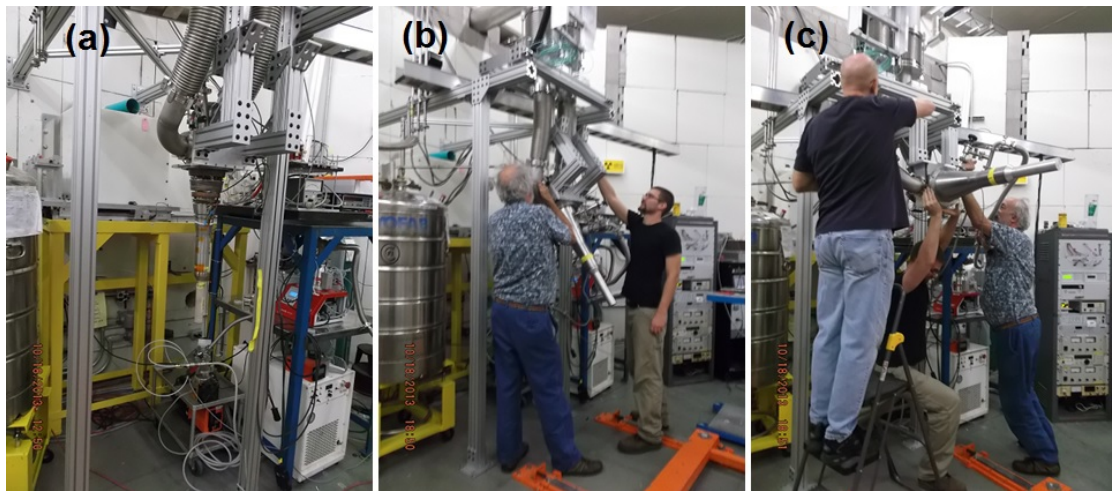


Figure 8.9: (Color online) Preparation of the dilution refrigerator for cool-down. (a) Mounting and assembling the refrigerator in a vertical position; (b) swinging the refrigerator; (c) the refrigerator in its horizontal position.

reached 1 K at the evaporator port of the dilution refrigerator. Since thermal sensors were not working, we used the vapor pressure of  $^4\text{He}$  to estimate the temperature, as seen in Fig. 8.11.

After repairs of the leaks found in the  $^3\text{He}$  pumping line and the thermal sensors, we cooled HIFROST. The goal of the third test was, first, to check all the instruments of the polarizing magnet, microwave, and NMR, and second, to test the dilution capability of the refrigerator. However, due to rapid vaporization of LHe in the buffer Dewar, we had difficulty transferring LHe to the refrigerator. There was also a problem powering up the polarizing magnet through a magnet control unit. We have resolved these problems and plan to have another cool-down at the end of March 2014 to test the refrigerator and

various other instruments for polarization.

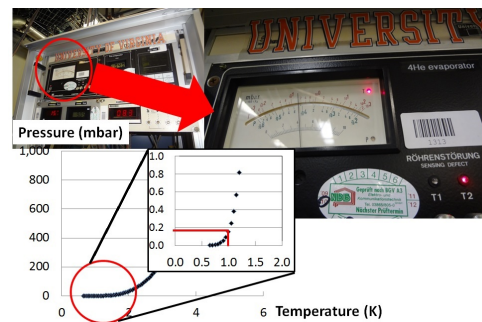


Figure 8.11: (Color online) The measured vapor pressure of  $^4\text{He}$  at the evaporator port of the dilution refrigerator was converted into a temperature. The temperature achieved was determined to be 1 K.

### 8.1.4 A Cryogenic Target for Photonuclear Experiments at HI $\gamma$ S

D.P. KENDELLEN, M.W. AHMED, A. KAFKARKOU, H.R. WELLER, *TUNL*; G. FELDMAN, *George Washington University, Washington, DC*

**We report progress on the design and construction of a cryogenic target for Compton-scattering experiments at HI $\gamma$ S. It will be able to liquefy deuterium, hydrogen, or helium.**

A 0.25 L Kapton-cell cryogenic target has been designed and is being built to liquefy deuterium (LD<sub>2</sub>), hydrogen (LH<sub>2</sub>), or <sup>4</sup>He (LHe). It will be used in Compton-scattering experiments at HI $\gamma$ S to measure the nuclear and nucleon polarizabilities. In the case of deuterium, the electromagnetic polarizabilities of the neutron,  $\alpha_n$  and  $\beta_n$ , can be probed by scattering circularly polarized  $\gamma$ -rays on an unpolarized LD<sub>2</sub> target. Scattered photons will be detected by the HI $\gamma$ S NaI detector array. The LH<sub>2</sub> target will be used to perform model-independent measurements of the proton polarizabilities,  $\alpha_p$  and  $\beta_p$ . Reference [Gri12] gives a review of nucleon polarizability measurements.

A simplified diagram of the cryostat is shown in Fig. 8.12. The main components are a cryocooler to pre-cool the incoming gas, a vacuum can with thermal radiation shields to isolate the components from room temperature, and a condensing volume, which fills the target cell.

We have purchased a Sumitomo Model RDK-415D Gifford-McMahon cryocooler. It has 1.5 W of cooling power at 4.2 K and a base temperature about 3.5 K. Low temperatures are produced through compression and expansion of high-purity helium gas in a closed loop between an external compressor and the cold head. Reference [Rad09] has more detail on the cooling cycle.

Properties of the target liquids are listed in Table 8.1.4 [Pob07]. A 4 K cryocooler is required to cover the full range of temperatures. We will use a temperature controller to keep from freezing LD<sub>2</sub> or LH<sub>2</sub> in the fill or pressure relief lines. To avoid excess stress on the Kapton cell, we plan to condense the target liquid at pressures of about 1 bar.

The liquefaction process begins with room-temperature gas entering through a fill line at the top of the cryostat, shown in Fig. 8.12. From

there the gas is cooled by heat exchangers attached to the two stages of the cryocooler. When filling with helium, the first stage is around 20 to 30 K and the second is at about 4 K.

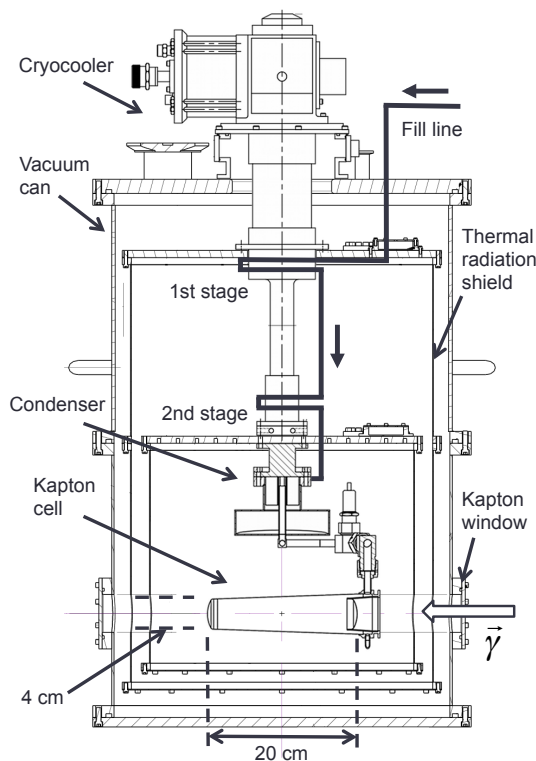


**Figure 8.12: Diagram of the cryogenic target.**

The condenser and cell (Fig. 8.13) were designed in collaboration with the Polarized Target Group at JLab. The incoming gas from the second stage condenses onto a series of copper fins and drips down to the bottom of the target cell through the fill line. The system is designed to promote convective flow and to remove heat from the target liquid efficiently. This minimizes fluctuations in the liquid density and target thick-

ness. Boil-off vapor from the cell rises through the vent line to the condenser's copper fins. It recondenses and drips back down into the fill line. The cell itself is 20 cm long with 4-cm-diameter end caps. It will be built from 0.125 mm thick Kapton film and is formed as the frustum of a cone to encourage bubbles to flow to the vent line.

**Table 8.1: Target Liquid Boiling Points, Melting Points, and Latent Heats at  $P = 1$  bar**

Subst.	$T_b$ (K)	$T_m$ (K)	$L$ (kJ L $^{-1}$ )
$n$ -D $_2$	23.7	18.7	50
$n$ -H $_2$	20.3	14.0	31.8
He	4.21	-	2.56

We have purchased a custom aluminum vacuum can with thermal radiation shields from Precision Cryogenics to house the cryocooler, condenser, and cell. Keeping the apparatus under high vacuum reduces heating from residual gas accommodation. The aluminum shields on the first and second stages, which are covered in aluminized Mylar superinsulation, lower the radiative heat load.

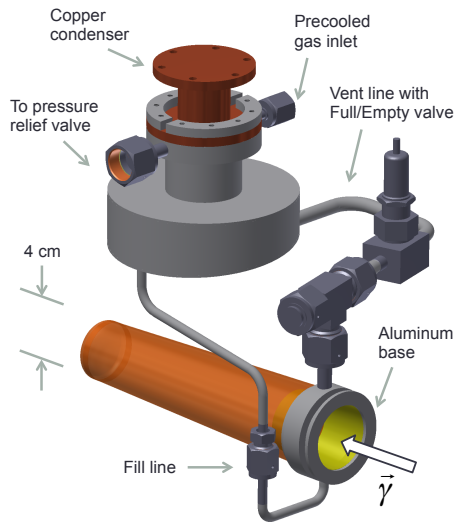


**Figure 8.13: (Color online) Condenser and cell.**

The external heating to the second stage should be a few hundred milliwatts, well within the 1.5 W of cooling power at 4.2 K. The remaining capacity is used to cool and condense the incoming gas. This model of cryocooler can liquefy helium at acceptable rates [SW06] and has the capacity to liquefy H $_2$  and D $_2$  with about 20 W of cooling power at 20 K.

As shown in Figs. 8.12 and 8.13, the incoming beam passes through a Kapton window on the vacuum can, through superinsulation-covered

holes in the two heat shields, and goes directly to a Kapton end-cap through holes in the aluminum base pieces. Scattered photons pass through the two 1-mm-thick aluminum heat shields, several thin layers of superinsulation, and the 3 mm aluminum wall of the vacuum can. The attenuation is less than 5% for photons exiting through these layers.



**Figure 8.14: (Color online) Assembled cryostat.**

We are working with the Duke Physics Instrument Shop to fabricate the condenser and cell. We have tested the cryocooler with the thermal radiation shield on the first stage and have tested a heater and thermometer on the second stage. The apparatus, seen in Fig. 8.14, achieved a base temperature of  $2.3 \pm 0.5$  K. We applied heat to the second stage with a closed-loop proportional-integral-derivative controller and ran at setpoints of 4, 20, and 77 K. The cooling power was 1.4 W at 4.2 K.

Next we will mount and calibrate thermometers, complete the cell and condenser, plan the gas-handling system (including safety measures), and perform test-fills with liquid helium.

[Gri12] H. Griebhammer *et al.*, Prog. Part. Nucl. Phys., **67**, 841 (2012).

[Pob07] F. Pobell, *Matter and Methods at Low Temperatures*, Springer, Berlin, 2007.

[Rad09] R. Radebaugh, J. Phys. Condens. Matter, **21**, 164219 (2009).

[SW06] P. Schmidt-Wellenburg and O. Zimmer, Cryogenics, **46**, 799 (2006).

### 8.1.5 Development of a Tritium Gas Target for a Three-Body Photodisintegration Experiment

F.Q.L. FRIESEN and C.R. HOWELL, *TUNL*;

There are significant challenges associated with the handling and storage of the tritium gas targets for  ${}^3\text{H}(\gamma,p)nn$  measurements. Here we report progress on the development of the targets and on methods for managing and filling them. The cell fabrication procedure has been finalized, and a prototype cell has been built and tested with helium. The system and procedure for filling the cells are under development.

The experiment to study the  ${}^3\text{H}(\gamma,p)nn$  reaction will use approximately 230 Ci of gaseous  ${}^3\text{H}$ , which will be contained in seven target cells constructed using 2.5- $\mu\text{m}$ -thick Havar foils. Dividing the gas volume in this way reduces potential material loss in the event of a foil rupture. The cell fabrication procedure has been finalized, and a prototype cell has been built and tested with helium at 1.04 atm (see Fig. 8.15). No leaks or changes in pressure were observed over a three-month monitoring period. The cells will be pressurized with tritium gas to slightly above atmospheric pressure but no more than 1.07 atm. This will help maintain the shape of the target cells without causing significant stress to the foils. Because the manufacturer of the Havar foils does not guarantee them to be completely free of small holes, quality-control surveys must be performed on each sheet of foil before it is used in target fabrication. A special apparatus has been constructed for certifying pieces of foil as pinhole-free. It works by scanning a laser and shielded photoresistor across the foil surface.

The system and procedure for filling the cells are under development. The key design goals are to reduce the risk of rupturing the containment foils during filling and to fully capture and reclaim tritium in the event of a leak or foil rupture. The target cells cannot withstand large pressure differentials. The filling system accommodates this by simultaneously pumping the target cell and a surrounding chamber to about 15 mTorr, and then filling the target cell slowly while simultaneously bleeding nitrogen into the chamber such that pressure equilibrium is maintained across the target foil (see Fig. 8.16). The tritium will be stored and purified using a temperature-controlled uranium bed. The bed will also be

used to recover excess tritium gas left in the manifold after a filling operation. When the bed is at room temperature, tritium is stored as  $\text{UT}_3$ , and impurities such as  ${}^3\text{He}$  can be safely pumped out [RCT].

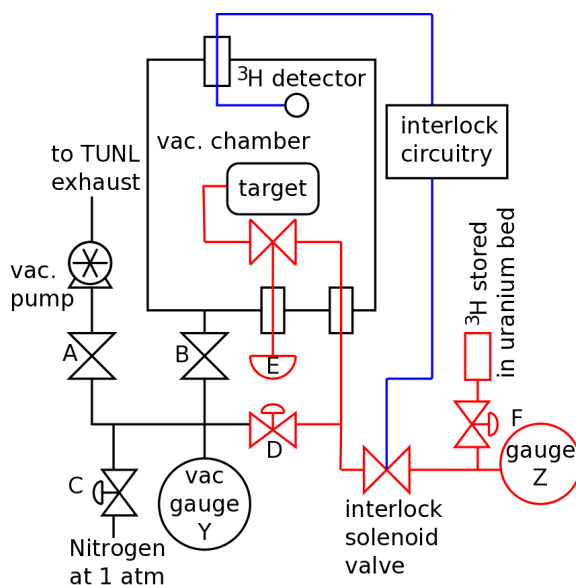


Figure 8.15: (Color online) A photograph of a prototype target cell filled with helium gas to 1.04 atm. The cell is 13 mm in diameter and 10 cm long.

To further mitigate risk of releasing tritium gas into the lab, the entire filling procedure will be carried out inside the fume hood in the neutron-time-of-flight target room. The outer chamber, the uranium bed, and the tritium manifold will be placed inside the fume hood.

A worst-case scenario is for a foil to rupture while being filled. In this event, tritium gas would be released inside the fill chamber, causing the automated interlock system to close the valve connecting the cell to the uranium bed. The bed

can then be cooled, and the interlock valve reopened. This will reclaim the released material from the outer chamber and confine contamination to a relatively small volume. Keeping the interior of the chamber free of oxygen and water by flooding it with nitrogen and thoroughly evacuating it prior to filling operations will minimize the formation of tritiated water in the event of a target leak [Pap82].



**Figure 8.16:** (Color online) Schematic view of the target and filling apparatus. The volume of the tritium manifold is kept at a minimum. Valve E is physically integrated with the target (shown in Fig. 8.15), but the mechanical feed-through which interfaces with it is part of the filling system. The system tested with the prototype target is as depicted, but without gauge Z, the uranium bed, or the interlock.

The targets are constructed with the foil on the inside of the structural frame. This design helps shield the foil from possible damage and reduces the target cell volume not visible to the beam. After being filled with tritium, the targets will be mounted to a single aluminum rail and aligned with respect to each other. The rail will then be aligned to the beam axis. The detector system will be enclosed in a box to provide secondary containment of the tritium gas in the event of a leak. To reduce proton energy loss and the presence of oxygen and water, the box will be flooded with helium and continuously monitored for tritium.

When not being used in an experiment, targets will be kept in a special storage container. The storage container will house the targets in a closed volume connected to an empty, room temperature uranium bed. In the event of a target cell leak, the bed will take up the released tritium gas. This closed volume will be kept inside a larger open volume (likely a length of PVC pipe or similar) connected to the TUNL exhaust system, further reducing the risk of contaminating the lab when the targets are not being actively used.

The detector system will be commissioned using  $^3\text{He}$  filled targets. This will provide an excellent opportunity to certify that the targets behave as expected when used in conjunction with the larger experimental apparatus and the  $\gamma$ -ray beam.

[Pap82] P. J. Papagiannakopoulos and C. E. Easterly, *Int. J. Chem. Kinetics*, **14**, 77 (1982).

[RCT] RCTRITEC, *Uranium Beds*, [www.rctritec.com](http://www.rctritec.com).

## 8.2 Detector Development and Characterization

### 8.2.1 A Recirculation System for Isotopically Enriched Gas Used in the HI $\gamma$ S OTPC

D.P. KENDELLEN, M.W. AHMED, H.R. WELLER, W.R. ZIMMERMAN, *TUNL*; M. GAI, *University of Connecticut at Avery Point, Groton, CT*

**A gas-handling system is being designed to recirculate and store isotopically enriched target gases for use with the HI $\gamma$ S optical time-projection chamber. Using isotopically enriched gases will greatly reduce the background events in measurements of the  $^{16}\text{O}(\gamma,\alpha)^{12}\text{C}$  reaction cross section.**

Stellar helium burning is driven by two major reactions:  $3\alpha \rightarrow ^{12}\text{C}$  (or “triple- $\alpha$ ”) and  $^{12}\text{C}(\alpha,\gamma)^{16}\text{O}$ . The nucleus  $^{12}\text{C}$  is produced in the triple- $\alpha$  reaction and destroyed in the  $^{12}\text{C}(\alpha,\gamma)$  reaction forming  $^{16}\text{O}$ . Hence the  $^{12}\text{C}(\alpha,\gamma)$  reaction determines the carbon-to-oxygen ratio at the end of stellar helium burning—one of the most important parameters of stellar evolution theory. The triple- $\alpha$  reaction rate is well-determined for quiescent helium burning, but the  $^{12}\text{C}(\alpha,\gamma)^{16}\text{O}$  reaction rate is highly uncertain in the region of stellar burning.

Previous measurements of the  $^{12}\text{C}(\alpha,\gamma)^{16}\text{O}$  reaction, based on detecting  $\gamma$  rays [Ass06, Red87], have been limited by a low cross section and high background. Using the HI $\gamma$ S optical time-projection chamber (OTPC), the time-reversed  $^{16}\text{O}(\gamma,\alpha)^{12}\text{C}$  reaction can be studied using  $\text{CO}_2$  and  $\text{N}_2\text{O}$  gas targets at  $\gamma$ -ray beam energies from 9.1 to 10.7 MeV. The HI $\gamma$ S OTPC can measure the complete angular distributions necessary for accurately extracting the E1 and E2 components of the cross section as well as their relative phase  $\phi_{12}$  [Gai10].

The gas used in the HI $\gamma$ S OTPC contains 20%  $\text{N}_2$  as a scintillator. The estimated background count rate from the  $^{14}\text{N}(\gamma,p)$  reaction will likely overwhelm the maximum rate of the detector, which is about 30 Hz. Also, when using  $\text{CO}_2$  target gas, the  $^{12}\text{C}(\gamma,\alpha)$  reaction is the dominant background in when measuring the  $^{16}\text{O}(\gamma,\alpha)$  cross section at beam energies relevant for the astrophysical reaction rate.

In order to remove these background contributions, the experiment will be run using an isotopically enriched target gas of 80%  $^{13}\text{CO}_2$  +

20%  $^{15}\text{N}_2$ . The cost of isotopically-enriched gas dictates the use of a recirculating gas-handling system.

A diagram of the proposed system is shown in Fig. 8.17. In normal circulation, a KNF Neuberger diaphragm pump maintains a pressure of about 100 Torr in the OTPC and compresses the gas mixture to a pressure of 1 to 2 atm. The gas is filtered and purified, then readmitted to the OTPC by a mass flow controller (MFC). The MFC adjusts the flow of gas to the low-pressure side of the loop in order to maintain the OTPC at 100 Torr, as measured by a vacuum gauge.

Operation of the HI $\gamma$ S OTPC requires the use of gas which is free from electronegative impurities, in order to avoid the loss of electrons while they drift towards the multiplication region. For example, in  $\text{CO}_2$ , a 0.1% contamination of  $\text{O}_2$  results in the loss of 10% of the free electrons for each centimeter of drift length [Pov79]. Thus it is essential to keep the target gas free of impurities, particularly  $\text{O}_2$  and  $\text{H}_2\text{O}$ . Matheson sells in-line purifiers which are designed to remove  $\text{O}_2$ ,  $\text{H}_2\text{O}$ , and hydrocarbons from various gases. Inside the purifier,  $\text{O}_2$  in the gas reacts chemically with an active metallic surface, while the  $\text{H}_2\text{O}$  adsorbs onto a molecular sieve. From the manufacturer’s specifications, contaminants are trapped to produce 99.9999% pure gas.

To store the gas after a run, the exhaust of the KNF pump is diverted to a tank. The amount of gas “lost” (left in the OTPC, tubing, etc.) during storage depends upon the ultimate pressure of the diaphragm pump. We have contacted the manufacturer about using the same diaphragm pump for both circulation and storage. If this



## 8.2.2 An Optical Time Projection Chamber for Primordial Deuterium Abundance Studies

A.G. SWINDELL, M. GAI, *University of Connecticut at Avery Point, Groton, CT*; M.W. AHMED, C.R. HOWELL, W.R. ZIMMERMAN, *TUNL*

We are developing an optical avalanche chamber, OPAC2, at HI $\gamma$ S to study the time-reverse of the  ${}^1\text{H}(n,\gamma){}^2\text{H}$  reaction at energies relevant to Big Bang nucleosynthesis. Charge amplification was measured for carbon dioxide and isobutane target gases. The OPAC2 system is being modified to measure the time-projection signal, in order to perform measurements of the photon-beam asymmetry in the  ${}^2\text{H}(\gamma,p)n$  reaction.

Knowledge of the  ${}^1\text{H}(n,\gamma){}^2\text{H}$  cross section holds a key position in predicting the light-element abundances in the standard Big-Bang nucleosynthesis (BBN) framework [No100, Bur99]. The amount of deuterium produced by this reaction is the most sensitive indicator of the primordial baryon density  $\Omega_B h^2$  [Bur99].

While potential-model and effective-field-theory predictions [Are04, Che99] for the total cross section are in agreement within the calculational errors, data in the region of BBN interest are sparse [Nag97]. We will measure the absolute  $np$ -capture-reaction cross section at  $E_n$  between 300 and 3000 keV using the inverse  ${}^2\text{He}(\gamma,p)n$  reaction. We are utilizing a small time-projection chamber, OPAC2 (see Fig. 8.18), to detect the recoiling protons from deuteron photodisintegration and measure the  ${}^2\text{H}(\gamma,p)n$  reaction cross section.

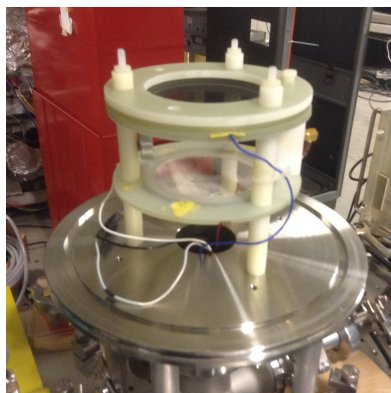


Figure 8.18: (Color online) The OPAC2 detector with the  ${}^{241}\text{Am}$  source and the silicon trigger detector.

OPAC2's design is based on a previous proto-

type detector developed at Braunschweig, Germany for microdosimetry studies [Tit98] and used at the Laboratory for Nuclear Science at Avery Point as a prototype detector [Wei06] for the optical time-projection chamber [Gai10]. The sensitive volume of our detector, which defines the charge-drift region for the ionized electrons, consists of a drift cathode (DC) and a drift anode (DA) made of stainless-steel wire-mesh grids of nearly 80% optical transmission. Each of the drift-region grids are 7.8 cm in diameter and separated by 6.0 cm from each other. Another grid (G2) of the same dimensions and material is placed 0.5 cm above the anode, and defines the charge-multiplication region. The grid arrangement of the OPAC2 detector is shown in Fig. 8.19.

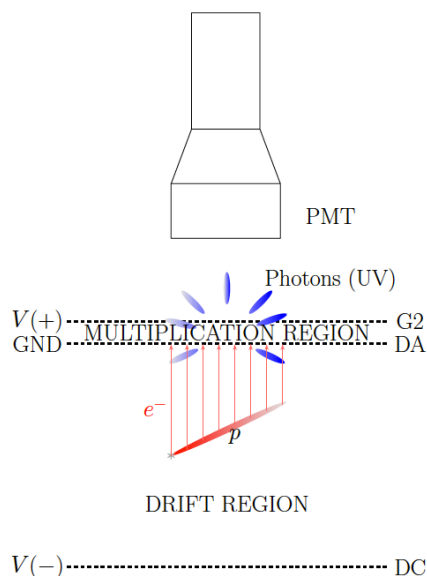


Figure 8.19: (Color online) Schematic diagram of the OPAC2 detector.

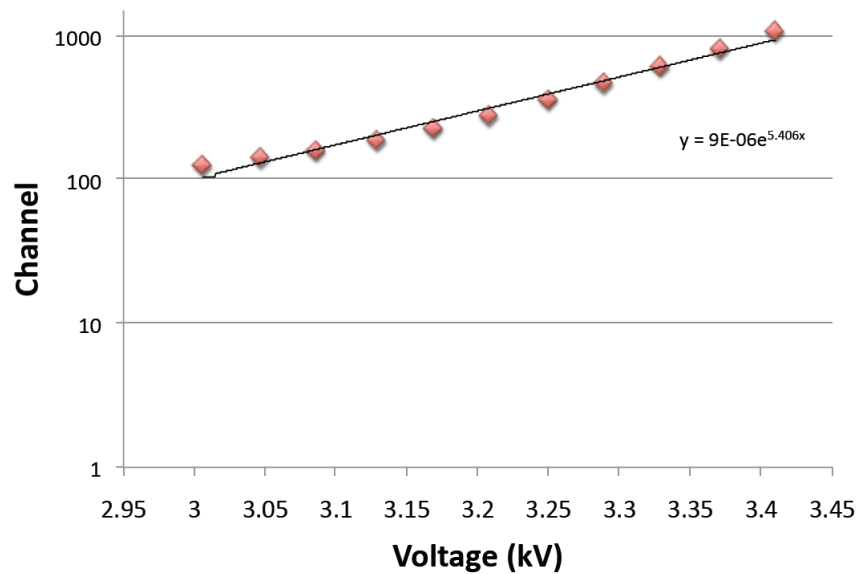


Figure 8.20: (Color online) Charge-gain curve of pure CO<sub>2</sub> at 150 torr measured at Avery Point with a <sup>241</sup>Am source.

Initial electron-charge-amplification measurements were performed for pure CO<sub>2</sub> and isobutane gases using  $\alpha$  particles from an <sup>241</sup>Am source as the ionizing radiation. For the actual measurements, we plan to use a deuterated version of the isobutane. At 150 torr, the  $\alpha$  particles have a range of a few centimeters in pure CO<sub>2</sub>. The electrons drift upward towards the anode, which is held at ground potential. Charge amplification occurs in the region between the anode DA and grid G2, where the potential difference was varied between 3 and 3.4 kV for CO<sub>2</sub>. The amplified charge produces scintillation light in the near-UV range. A schematic view of the chamber operation is shown in Fig. 8.19. The charge amplification curve for CO<sub>2</sub> at 150 torr is shown in Fig. 8.20.

We will use a time-projection technique to distinguish between E1 and M1 proton contributions to the total cross section [Gai10]. To do this, a quartz window, 10 cm in diameter, and a UV-sensitive photomultiplier tube will be installed on top of the chamber enclosure.

- 
- [Are04] H. Arenhovel, Phys. Rev. Lett., **93**, 202301 (2004).
  - [Bur99] S. Burles *et al.*, Phys. Rev. Lett., **82**, 4176 (1999).
  - [Che99] J.-W. Chen and M. J. Savage, Phys. Rev. C, **60**, 065205 (1999).
  - [Gai10] M. Gai *et al.*, J. Instrum, **5**, P12004 (2010).
  - [Nag97] Y. Nagai *et al.*, Phys. Rev. C, **56**, 3173 (1997).
  - [Nol00] K. M. Nollett and S. Burles, Phys. Rev. Lett., **61**, 123505 (2000).
  - [Tit98] U. Titt *et al.*, Nucl. Instrum. Methods, **A416**, 12004 (1998).
  - [Wei06] L. Weissman *et al.*, J. Instrum., **1**, P05002 (2006).

### 8.2.3 Monte Carlo Simulation of the LENA Detector System

C. HOWARD, C. ILIADIS, A.E. CHAMPAGE, *TUNL*;

Many nuclear astrophysics experiments use the singles energy spectrum to measure nuclear cross sections. Using a high purity germanium detector and a NaI(Tl) annulus in coincidence can lower the background, allowing the measurement of smaller cross-sections. In our previous work, our simulation was only able to determine the relative efficiencies of both full-energy peaks. Our present work extends our simulation so that we can predict absolute efficiencies, and both coincidence gate efficiencies.

The LENA detectors were described in Refs. [Row02, Lon06], and a method of coincidence summing corrections was discussed. Exploratory Monte Carlo simulations were performed using the GEANT4 simulation package [Ago03, All06]. These were used only as an aid for interpolating measured efficiencies (full-energy peak and total) of the high purity germanium detector (HPGe) and the NaI(Tl) annulus. They were not accurate enough for predicting absolute efficiencies or for simulating coincidence efficiencies. Our aim here is to obtain these efficiencies, which are needed to fully simulate the LENA detection system for various energy gates.

This report discusses the results obtained for two different photon energy regimes: total decay energy above and below 3.5 MeV. Most astrophysically important fusion reactions emit coincident  $\gamma$ -rays with a total decay energy of up to 15 MeV. If such a cascade is detected using an HPGe-NaI(Tl) spectrometer, a total energy software threshold of 3.5 MeV will reject most of the room background. The example we consider is the  $^{18}\text{O}(p,\gamma)^{19}\text{F}$  reaction. On the other hand, such a spectrometer may also be useful for total  $\gamma$ -ray decay energies below 3.5 MeV. As an example, we discuss measurements using a  $^{22}\text{Na}$  calibration source.

#### Equipment

Figure 8.21 shows the simulated LENA detector geometry. Our HPGe detector is a p-type, closed-end, bulletized HPGe detector (seen at the center of the apparatus) and was originally specified as having a 140% efficiency at 1.33 MeV, relative to a 3-inch $\times$ 3-inch NaI(Tl) detector. According to the manufacturer, the outer contact layer is created by a lithium diffusion process and has a thickness of 0.7 mm. A precise value for

this quantity is important because interactions that occur in this transition layer have a reduced charge collection efficiency compared to the bulk germanium [Bar93]. Comparisons of our simulated and measured efficiencies indicate better agreement if the contact layer thickness is taken to be 1.2 mm. Therefore, we adopted 1.2 mm for all simulations presented in this work.

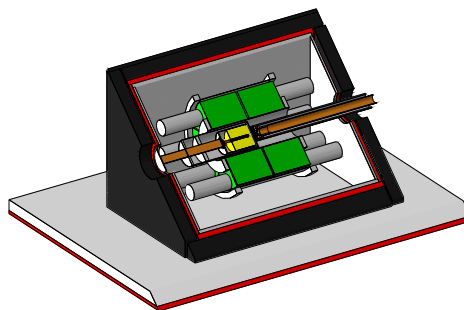


**Figure 8.21:** (Color Online) The LENA detection system as drawn by the simulation code. The HPGe detector is located at the end of the beam line. This is surrounded by the NaI(Tl) annulus with its rings of photomultiplier tubes. The outer box is made up of lead shielding enclosed by plastic-scintillator muon-veto panels. The beam pipe enters from the right.

The NaI(Tl) annulus is made up of 16 optically isolated segments, where each segment signal is read through its own photomultiplier tube. The annulus is positioned such that both the HPGe detector front face and the  $\gamma$ -ray source are located close to the geometric center. The NaI(Tl) annulus is surrounded by an aluminum box, which supports a 10-mm-thick box of lead

**Table 8.2: Comparison of data and simulation count rates for the decay of the 151 keV resonance in the  $^{18}\text{O}(p,\gamma)^{19}\text{F}$  reaction (upper part; units are counts/hour; Gate 1) and for the  $^{22}\text{Na}$  calibration source (last line; units are counts/minute; Gate 2).**

Energy [keV]	Singles		Gated	
	Data	MC	Data	MC
1357	1087(55)	1201(54)	757(42)	783(41)
2354	658(42)	715(42)	458(34)	468(34)
3711	1416(67)	1503(66)	1087(57)	1181(56)
3908	2139(61)	2145(61)	1400(50)	1439(50)
4230	3222(64)	3257(64)	2157(53)	2204(52)
1275	3280(18)	3238(18)	1176(11)	1206(11)

shielding. The lead is surrounded by five 50-mm-thick Bicron BC-408 plastic scintillator plates on all four sides and the top. These plastic scintillators are used as an active veto for events caused by cosmic ray muons. The construction of the scintillator box is detailed in Ref. [Lon06].

## Results

The first example of our coincidence gating is the decay of the 151 keV resonance in the  $^{18}\text{O}(p,\gamma)^{19}\text{F}$  reaction, with a total decay energy of 8137 keV. We can now apply a trapezoidal gate to remove most of the room background. Since the  $Q$ -value of this decay is high, we can remove low energy events—that is, events from decays that have a  $Q$ -value less than about 3.5 MeV. This includes most of the decays from typical room background sources. Figure 8.22 shows the comparison between the data and simulation with the condition for Gate 1 ( $3500 \text{ keV} < E_{\text{HPGe}} + E_{\text{NaI(Tl)}}$ ) applied. The two spectra are virtually indistinguishable. Here  $E_{\text{HPGe}}$  is the energy deposited in the HPGe detector and  $E_{\text{NaI(Tl)}}$  is the energy deposited in the NaI(Tl) annulus. This gate represents a diagonal line from  $E_{\text{HPGe}} = 3500 \text{ keV}$  to  $E_{\text{NaI(Tl)}} = 3500 \text{ keV}$ . Table 8.2 shows the comparison of the count rates for the strongest full energy peaks.

The second example is the positron-emitting  $^{22}\text{Na}$  isotope, which decays with a half-life of 2.6029(8) years and produces 1275 keV  $\gamma$  rays in 99.94% of the decays. In addition, the decay produces an average of 1.807 511 keV annihilation photons per decay. Using Gate 2 ( $944 \text{ keV} < E_{\text{NaI(Tl)}} < 1104 \text{ keV}$ ) we explore a scheme where the 1275 keV  $\gamma$  ray is fully detected in the HPGe detector, and both coincident 511 keV photons are fully absorbed by the NaI(Tl) annulus. The simulation was scaled to the activity of the calibration source. We can then directly compare the full energy peak intensities. The last line of

Table 8.2 shows the comparison of the count rates for the strongest full energy peaks for each case.

In both cases we obtain excellent agreement between the data and the simulations. This work was recently published [How13].

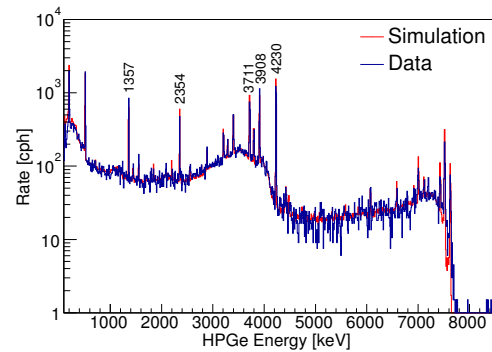


**Figure 8.22: (Color online) Background subtracted data and simulation energy spectra for the decay of the 151 keV resonance in the  $^{18}\text{O}(p,\gamma)^{19}\text{F}$  reaction. The condition for Gate 1 is applied.**

- [Ago03] S. Agostinelli *et al.*, Nucl. Instrum. Methods A, **506**, 250 (2003).
- [All06] J. Allison *et al.*, Nucl. Sci., IEEE Trans., **53**, 270 (2006).
- [Bar93] R. Barlow and C. Beeston, Computer Physics Communications, **77**, 219 (1993).
- [How13] C. Howard, C. Iliadis, and A. E. Champagne, Nucl. Instrum. Methods A, **729**, 254 (2013).
- [Lon06] R. Longland *et al.*, Nucl. Instrum. Methods A, **566**, 452 (2006).
- [Row02] C. Rowland *et al.*, Nucl. Instrum. Methods A, **480**, 610 (2002).

## 8.2.4 Development of a Para-Ortho Deuterium Converter and Raman Spectrometer

R. GOLUB, P.R. HUFFMAN, G.L. MEDLIN, G. PALMQUIST, A.R. YOUNG, *TUNL*; A. COOK, A. HAWARI, E. KOROBKINA, B. WEHRING, *North Carolina State University, Raleigh, NC*

As part of ensuring the performance of the ultracold neutron source at the PULSTAR reactor, a system has been built and tested to prepare deuterium in which a high fraction of the molecules are in the ortho spin state and to analyze this fraction with high precision using Raman spectroscopy.

The ultracold-neutron-(UCN)-source facility being commissioned at the PULSTAR reactor on the campus of North Carolina State University will provide a competitive UCN flux for measurements including the neutron electric dipole moment (EDM),  $\beta$  decay, and material scattering. In addition it will serve as a platform for improving UCN source technology.

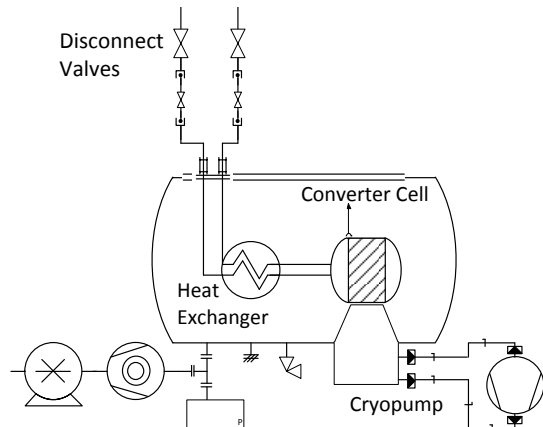


Figure 8.23: Diagram of the converter assembly.

The source utilizes the high leakage of epithermal and thermal neutrons from the reactor core. A heavy-water thermal moderator and solid-methane cold-moderator provide a neutron-flux peak tuned to between 30 and 60 K to optimize performance of the 5 K deuterium UCN converter. As the PULSTAR source is steady-state and lacks a shutter, UCN density is limited by neutron lifetime in the deuterium crystal. This lifetime is dependent, in particular, on the presence of hydrogen and of deuterium in the para spin state. A gas handling system was constructed that can prepare and maintain

very clean deuterium over many operational cycles. Based on the previous work of Lui [Liu03], systems were developed to both prepare deuterium in a very high ortho-fraction and monitor the para-deuterium and hydrogen content to high precision. Ionizing radiation should further lower the para-content. This strategy of maintaining the integrity of the deuterium over a long operational time should allow the source to perform significantly better than the deuterium UCN source at Los Alamos National Laboratory.

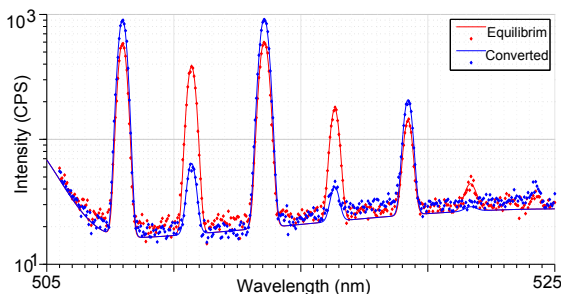


Figure 8.24: (Color online) Comparison of reference and converted samples Raman spectra. The converted spectrum is higher in the first, third, fifth, and seventh peaks characteristic of the ortho state, with much reduced intensity in the second, fourth, and sixth peaks characteristic of the para state. The upper two peaks are quite weak. Note the logarithmic intensity scale.

This para-to-ortho spin converter (see Fig. 8.23) utilizes the paramagnetism of iron hydroxide to catalyze spin flips and quickly reach equilibrium near the triple point of deuterium. The system consists simply of a catalyst-packed U-shaped copper cell mounted to the head of a

cryopump. The ferric hydroxide is manufactured in-house by reacting ammonium hydroxide and iron chloride. The mixture is then dried in a way that produces small granules. We have successfully reached the goal of material with less than 2% of the para-species.

To analyze the ortho/para ratio of a deuterium sample, a focused argon-ion laser induces Raman scattering in a spherical glass sample cell. This light is collected and analyzed in a double-grating spectrometer with a photomulti-

plier tube. The spectrometer can discern the first seven Stokes Raman lines. Figure 8.24 shows spectra taken on equilibrated and converted samples. This system is also sensitive to the Raman scattering of hydrogen and HD species, and it is hoped that the system can also be used to study nitrogen and oxygen.

---

[Liu03] C.-Y. Liu *et al.*, Nucl. Instrum. Methods A, **508** (2003).

## 8.2.5 Detector Characterization and Simulation for a Neutron-Antineutron Oscillation Search

D.G. PHILLIPS II, E.B. DEES, R.W. PATTIE, JR., A.R. YOUNG, B.A. ZECK, *TUNL*; E. RAMBERG, S. STRIGANOV, R. TSCHIRHART, *Fermi National Accelerator Laboratory, Batavia, IL*; C. JOHNSON, R. VAN KOOTEN, *Indiana University, Bloomington, IN*; P. MCGAUGHEY, M. MOCKO, G. MUHRER, S. SJUE, Z. WANG, *Los Alamos National Laboratory, Los Alamos, NM*; L. CASTELLANOS, C.E. COPPOLA, Y. KAMYSHKOV, *University of Tennessee, Knoxville, TN*

**This report describes simulation studies and ongoing characterization of tracking and calorimeter technologies for a modern neutron-antineutron search experiment using a cold neutron beam from a spallation source.**

The discovery of neutrons transforming into antineutrons ( $n\bar{n}$ ) would significantly impact particle physics and cosmology by demonstrating that baryon number ( $\mathcal{B}$ ) is violated. It would imply that the matter in our universe can evolve from the initial  $\mathcal{B}=0$  void predicted by inflation and thereby provide valuable insight into the observed matter-antimatter asymmetry of the universe. By showing  $\mathcal{B}$  is violated by 2 units, its discovery would strongly suggest that the physics of quark-lepton unification and neutrino mass generation is near the TeV scale. If seen at rates observable in a foreseeable next-generation experiment, its effects must be taken into account for any quantitative understanding of the baryon asymmetry of the universe.

The experimental signature of  $n\bar{n}$  annihilation from a free neutron beam is spectacular enough that an essentially “background-free” search is possible, while any positive observation can be turned off by a very small change in the experiment’s ambient magnetic field. An optimized experimental search, NNbarX [Akr], for  $n\bar{n}$  oscillations using free neutrons from a 1 MW spallation target at Fermi National Accelerator Laboratory can improve existing limits on the free-oscillation probability by four orders of magnitude by fully exploiting a new slow-neutron source along with optics technology developed for materials research. The envisioned experiment would deliver a slow-neutron beam through a magnetically-shielded vacuum to a thin carbon target surrounded by an annihilation detector.

The annihilation of an antineutron favors modes with a mix of charged and neutral pions that can be detected using standard tracker and

calorimeter technologies. The spallation geometry of NNbarX is expected to produce a much higher energy background spectrum from protons, neutrons and  $\gamma$  rays than the reactor source of Institut Laue Langevin (ILL), location of the previous  $n\bar{n}$  oscillation search using free neutrons [BCe94]. The ILL experiment eliminated these backgrounds using a curved guide system to couple the cold source to the  $n\bar{n}$  guide. For NNbarX, we will integrate our shielding scheme for fast particles into the design of the source and beamline and will optimize the tracker detectors to differentiate between charged and neutral tracks. The residual fast backgrounds at the detector are a strong function of the guide-tube length, detector threshold, and pulse structure for the proton beam.

According to simulations in MCNPX and MARS [NMo], significant backgrounds in the form of fast neutrons, protons and  $\gamma$  rays will be introduced from the spallation-target geometry. Figure 8.25 shows the production of neutrons and protons from the NNbarX spallation target after traversing a distance of 147 m through a totally evacuated volume with no magnetic field to the entrance of the annihilation detector region. The  $\gamma$  rays can be effectively cut with a veto on the detector correlated with the beam timing. Simulation studies in MCNPX have demonstrated that a Be filter placed in front of the spallation target will eliminate fast protons above 550 MeV.

The primary goal of our simulation campaign is to develop a detector model that allows NNbarX to reach the goal of zero background and optimum signal-event-detection efficiency. Currently, the response of tracker and

scintillator technologies to fast neutrons in Intensity Frontier experiments is not understood. Understanding the response of the NNBarX candidate tracker and calorimeter technologies to fast neutrons would be the key tool for background reduction in NNBarX and extremely useful for detector development in other Intensity Frontier efforts. We are using GEANT4.9.6 to simulate the passage of annihilation-event products through the annihilation detector geometry. Figure 8.26 shows an event display from our preliminary GEANT4 simulation of a  $\pi^+\pi^-2\pi^0$  annihilation event in a detector geometry with a 100  $\mu\text{m}$  thick carbon target, simplified tracker, and a simple polystyrene calorimeter.

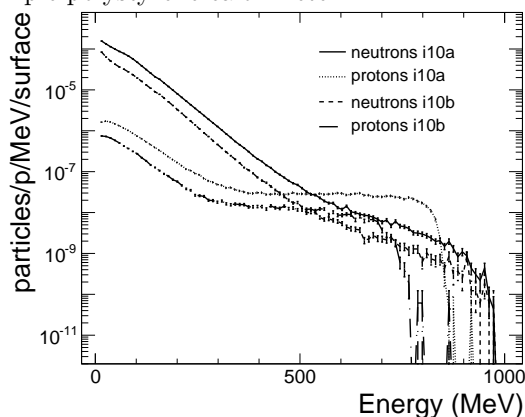


**Figure 8.25:** MCNPX-simulated neutron and proton backgrounds at the entrance of the annihilation detector region. The more intense curves are for the neutron background; the others are for the proton background. The results of two simulations are shown.

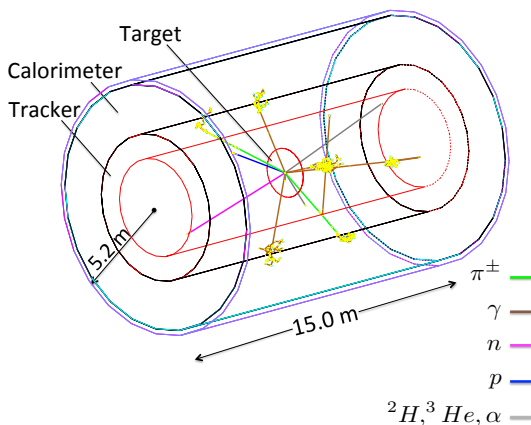


**Figure 8.26:** Preliminary GEANT4 simulation for a  $\pi^+\pi^-2\pi^0$  annihilation event in a generalized NNbarX detector geometry.

Detector characterization studies will be carried out using the 800 MeV proton linear accel-

erator at the Los Alamos Neutron Science Center (LANSCE), which provides a pulsed beam (about 4  $\mu\text{A}$  at 40 Hz) to the spallation target at the WNR facility [SWe93]. Beamlines at fixed angles with respect to the incident proton beam are equipped with shutters and collimators, to provide a maximum fast-neutron-beam intensity of about  $10^6$  n/sec in a 5 cm diameter beam. A test run performed in 2012 was used to validate the DAQ system used for NNbarX-detector characterization, characterization of the response of LANL proportional tubes to fast neutrons (see Fig. 8.27) and to determine that the pulse-beam structure from the LANSCE accelerator allows for the neutron energy to be calculated from the time of flight with an energy resolution of around 0.4% at a few MeV to around 8% at 800 MeV.

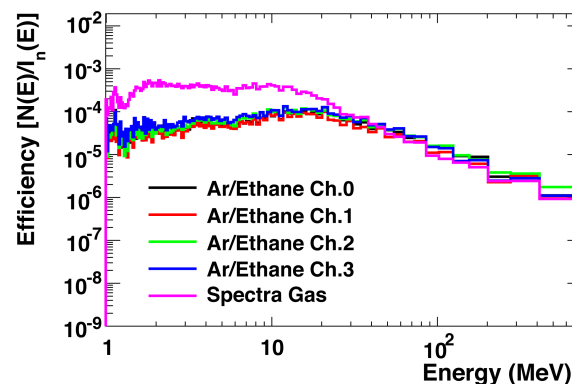


**Figure 8.27:** Neutron detection efficiencies of LANL-constructed proportional tubes for different fill-gas mixtures.

In the coming year, we will further refine our simulation of the annihilation detector geometry to include detailed event reconstruction and perform simulation studies on detector efficiency for all annihilation-event classes. At the end of 2013, another run will be performed at the LANL WNR test site to study the response of NNbarX straw-tube and extruded-polystyrene detector technologies to fast-neutron backgrounds.

[Akr] A. S. Kronfeld *et al.*, arXiv:hep-ex, page 1306.5009.

[BCe94] M. Baldo-Ceolin *et al.*, *Z. Phys. C*, **63**, 409 (1994).

[NMo] [www-ap.fnl.gov/MARS](http://www-ap.fnl.gov/MARS), *MARS Code System*.

[SWe93] S. A. Wender *et al.*, *Nucl. Instrum. Methods A*, **336**, 226 (1993).

## 8.2.6 Characterization of $^{10}\text{B}$ -Lined Proportional Counters and Moderator Design

J.A. SILANO, H.J. KARWOWSKI, *TUNL*

**A  $^{10}\text{B}$ -lined neutron counter was characterized and modeled. A new detector consisting of four neutron counters was designed and optimized for detecting fast neutrons. These detectors are intended as a replacement for  $^3\text{He}$ -based neutron detectors.**

Due to the global  $^3\text{He}$  shortage,  $^3\text{He}$ -based neutron detectors have become prohibitively expensive, and  $^{10}\text{B}$ -lined proportional counters are an emerging, inexpensive replacement technology. In order for these new detectors to be a viable successor to the well-established  $^3\text{He}$ -based counters, it is necessary to fully characterize them. A  $^{10}\text{B}$ -based neutron detector has been designed, built, and characterized at TUNL for operation at the University of Nebraska, Lincoln (UNL), where the Diocles group is developing a novel laser-driven  $\gamma$ -ray-beam source capable of generating photoneutrons.

An SA-B1-0824-101  $^{10}\text{B}$ -lined neutron counter from G.E. Reuter-Stokes was characterized, and a polyethylene moderator for four detector tubes was designed for detecting fast neutrons. The counters are argon-filled, single-wire, cylindrical proportional counters, 2.54 cm in diameter and 71 cm long, with a boron tube-lining enriched to 92% in  $^{10}\text{B}$ . Thermal neutrons interact with the boron layer through the  $^{10}\text{B}(n,\alpha)^7\text{Li}$  reaction, and the reaction products deposit energy in the argon. The thickness of the active boron layer is not provided in the proportional-counter specifications, so it was necessary to determine this value experimentally.

To determine the boron thickness, the efficiency of a single tube was measured using a calibrated  $^{241}\text{AmBe}$  neutron source. A boron counter was placed in an existing polyethylene moderator, 20 cm square and 70 cm long, with the  $^{241}\text{AmBe}$  source located 7.6 cm from the face of the moderator. The counters were simulated with the Monte Carlo code GEANT, and the dependence of the detector efficiency on the thickness of the enriched boron layer was determined. For this work, detection efficiency was defined as the number of detected neutrons divided by the number incident on the face of the detector.

The measured efficiency implied a  $^{10}\text{B}$  thickness of  $0.395 \pm 0.044 \text{ mg/cm}^2$ .

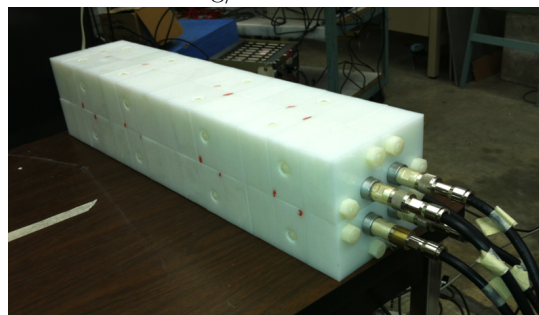


**Figure 8.28:** (Color online) Photograph of the neutron detector. Four proportional counting tubes are set in polyethylene moderator with connected high voltage cables.

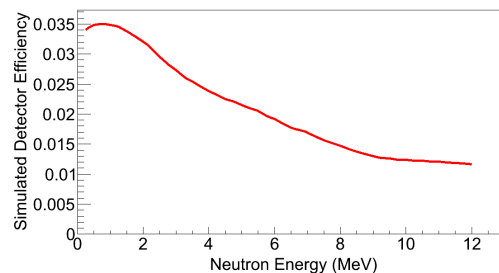


**Figure 8.29:** (Color online) Simulated detector efficiency for high energy neutrons from a monoenergetic point source 3 cm from the face of the detector.

A detector consisting of polyethylene moderator and four boron tubes was designed and simulated in GEANT. The design with the maximum efficiency was a plastic moderator block 15.2 cm square and 71.1 cm long, with proportional counters located 3.2 cm from the center of the block (see Fig. 8.28). The detector was built and tested

with the calibrated  $^{241}\text{AmBe}$  source. The detector efficiency for neutrons from this source was measured to be  $0.026 \pm 0.002$ , agreeing with the simulated efficiency to within 10%. The energy

dependence of the detector efficiency is shown in Fig. 8.29.

This work is supported in part by DTRA Grant No. HDTRA1-11-C-0001.

### 8.2.7 Measurement of the Nab/UCNB Silicon-Detector Response to 15 to 40 keV Protons and Deuterons

A.R. YOUNG, B.A. ZECK, *TUNL*; M. MAKELA, P.L. MCGAUGHEY, A. SALLAS-BACCI, *Los Alamos National Laboratory, Los Alamos, NM*

The detection of recoil protons from neutron  $\beta$  decay is an essential component of the Nab and UCNB experiments. We previously obtained data characterizing the response of the kind of large-area, highly-segmented, thin-dead-layer silicon detectors planned for these experiments. We have since analyzed the data and submitted a publication describing the results. Here we summarize the results of our analysis.

Both the Nab [Poc09] and UCNB [Wil09] experiments seek to perform 0.1% measurements of angular correlations in the decay of free neutrons. The primary physics goal of Nab is to measure the electron-neutrino correlation; the goal of UCNB is to measure the neutrino asymmetry. Both experiments rely on the detection of the recoil proton, with an endpoint energy of 752 eV. The detection scheme for these experiments is to accelerate the protons after decay, so they are incident on the silicon detector at energies greater than 15 keV, with 30 keV the nominal design acceleration.

The design specifications for the Nab/UCNB detectors are unique. They must be large in area (roughly 120 cm<sup>2</sup>), highly segmented (127 segments), and thick (about 2 mm). They must also have very thin dead layers (about 100 nm) and reasonably good timing ( $\Delta t < 5$  ns down to energies of about 10 keV for  $\beta$  particles). Detector technology meeting these specifications was developed by Scott Wilburn's group at LANL together with Micron Semiconductor, Ltd [MS]. A cross-sectional view of the N-type silicon detectors utilized for this study is depicted in Fig. 8.30. Decay events are tagged by  $\beta$  particles detected in delayed coincidence with recoil protons. The resultant timing distribution between the two particles is used to extract the electron-neutrino correlation in Nab. The spin-dependence of the  $\beta$ -proton coincidence distribution is used to extract the neutrino-asymmetry in UCNB. Segmentation serves to define the fiducial volume in both experiments, and to limit the accidental coincidence rate.

In 2012, detectors from the Nab/UCNB program were evaluated at TUNL for their response

to low energy protons and deuterons. For these measurements, one 0.5-mm-thick silicon detector and one 1.0-mm-thick detector were utilized. The detectors were mounted on a frame that could be cooled to about -6° C to reduce leakage current along with the associated parallel noise. One of the central pixels was instrumented with a cold front-end and coupled to a custom amplifier designed for the Nab/UCNB detectors.

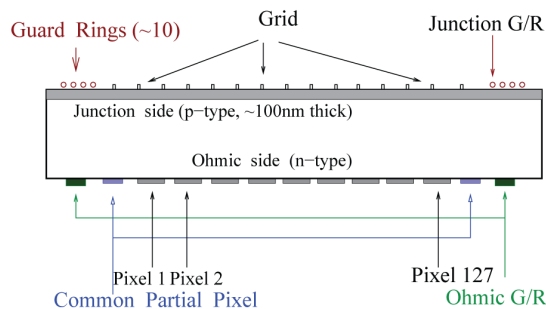


**Figure 8.30:** (Color online) A cross section view of the silicon detector. The silicon wafer is 12 cm in diameter. The planned experiments will be carried out with 2-mm-thick detectors. The 16.6-cm-diameter ceramic disc that is attached on the ohmic side of the silicon wafer is not shown in the figure.

The detectors were mounted in the TUNL low-energy proton accelerator [Hoe06], and data were taken with incident proton and deuteron beams with energies between 15 and 35 keV. The detector response to low energy  $\beta$  particles was calibrated with a <sup>109</sup>Cd conversion-electron source, establishing a noise-threshold of about 6

keV and a linear response to  $\beta$  particles over the energy range of interest. From the calibrated detector response, we determined the detector response shown in Fig. 8.31 and the pulse-height defect or PHD for the detection of protons and deuterons (Fig. 8.32).

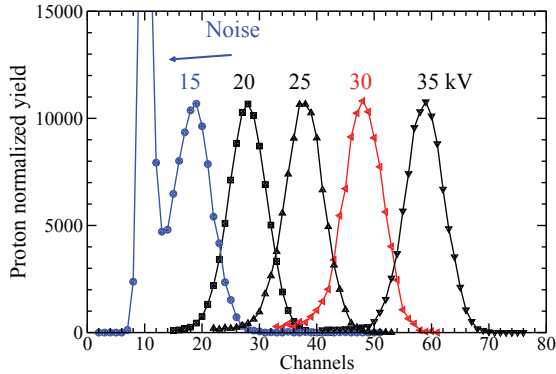


**Figure 8.31:** (Color online) Detection of low energy protons with 1-mm-thick silicon detector at 6°C. The proton acceleration voltage is shown next to each peak. Protons are detected after crossing the detector dead layer. The average energy resolution is 3.2 keV FWHM.

The measured PHD for protons ranged from roughly 7 keV for 20 keV protons to about 9 keV for 35 keV protons. The defect was slightly smaller for deuterons at the same energy. The PHD generically arises from at least three different sources: losses in the dead-layer on the surface of the detector, losses due to nuclear recoil that does not produce collected quasiparticles (electrons or holes), and electron-hole recombination. In our case, the PHD comes almost entirely from dead layer losses. The recombination losses were determined to be negligible, and the nuclear-recoil losses were calculated to be roughly 0.5 keV.

Given our derived value for the PHD due to dead-layer losses, we used stopping-power estimates from various sources to determine a dead-layer thickness for our 1 mm detector. Results ranged from about 70 to 110 nm based on proton PHD data and about 75 to 113 nm based on deuteron PHD data, with the spread in thicknesses due almost entirely to variations in the functional form of the expected stopping power. Figure 8.33 contains a plot of our upper limit for the dead-layer thickness. The measured value

for the dead-layer and the sensitivity to protons provided confirmation of the expected silicon detector performance for proton detection and provided a solid basis for the engineering-design phase of Nab and UCNB.

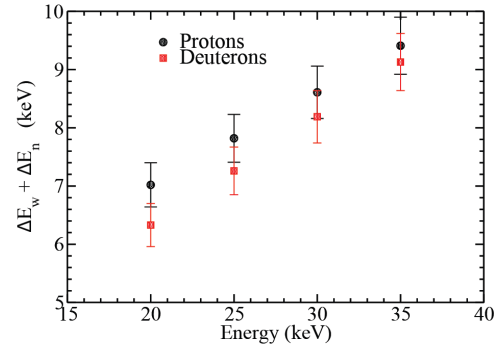


**Figure 8.32:** (Color online) Pulse-height defect of protons and deuterons in the large area, 1-mm-thick, and hexagonally segmented silicon detector's central pixel. The PHD is deduced from Fig. 8.31 for protons.

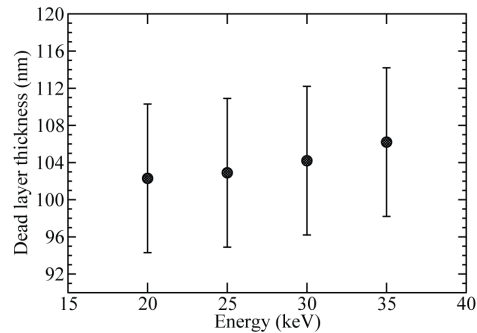


**Figure 8.33:** Upper limit for the deadlayer determined for protons with energies between 20 and 35 keV.

[Hoe06] S. Hoedl *et al.*, *J. Appl. Phys.*, **99** (2006).

[MS] L. Micron Semiconductor, *Micron Semiconductor, Ltd.*, <http://www.micronsemiconductor.co.uk>.

[Poc09] D. Pocanic *et al.*, *Nucl. Instrum. Methods A*, **611** (2009).

[Wil09] S. Wilburn *et al.*, *Revista Mexicana de Física Suplemento*, **55** (2009).

### 8.2.8 Measurement of the Response Matrix of a Large Volume LaBr<sub>3</sub>:Ce Detector at the HI $\gamma$ S Facility

I. MAZUMDAR, M.W. AHMED, A. KAFKARKOU, J.M. MUELLER, L.S. MYERS, H.R. WELLER, W.R. ZIMMERMAN, *TUNL*; M.H. SIKORA, *George Washington University, Washington, DC*

**We report on the first experimental measurement of the response matrix of a large volume, cylindrical LaBr<sub>3</sub>:Ce detector using monochromatic photon beams from HI $\gamma$ S. The measurements were carried out for eight photon energies between 5.5 and 30 MeV, and absolute photo-peak efficiencies were determined at each energy. The photo-peak efficiencies and spectral shapes were well reproduced using GEANT4 simulations.**

The recent discovery of lanthanum-halide crystals marks a major development in the field of scintillator detectors. The production and marketing of the LaCl<sub>3</sub>:Ce and LaBr<sub>3</sub>:Ce crystals have resulted in a flurry of activities to test and characterize their performance [Kum09]. The excellent, roughly 3%, energy resolution of LaBr<sub>3</sub>:Ce is better than any other commercially available scintillator detector. The fast decay time of 35 ns [Dor04], with no intense slow component and afterglow, leads to a time resolution of a few hundred picoseconds [Kum09]. The high density of the crystals (5.08 gm/cm<sup>2</sup>) and the high  $Z$  of lanthanum result in higher detection efficiency than is found with NaI(Tl). These highly attractive properties of LaBr<sub>3</sub> make it suitable for both low- and high-energy  $\gamma$ -ray spectroscopy. We have recently procured a large, 946 cm<sup>3</sup> LaBr<sub>3</sub>:Ce detector to study the suitability of this material for continuum  $\gamma$ -ray spectroscopy at energies up to 40 MeV.

This large-volume detector is an integral assembly of a cylindrical crystal and a photomultiplier tube (PMT), procured from M/S Saint Gobain Inc. The cylindrical B380 crystal is 3.5 in. in diameter and 6 in. in length and is housed in an aluminum casing packed with 5-mm-thick reflector material. The crystal is viewed by a 3.5-in.-diameter Hamamatsu R10233 PMT. All the major properties of this integral assembly have been studied at  $\gamma$ -ray energies from 662 keV up to 22.5 MeV using sources and in-beam reactions [Maz13]. We present the results of our measurements to determine the response matrix of this detector up to 30 MeV using monochromatic photon beams from HI $\gamma$ S.

The cylindrical LaBr<sub>3</sub>:Ce detector was placed

in the path of a highly collimated and attenuated monochromatic photon beam. The spectra were recorded for 5.5, 6.5, 7.5, 9.9, 15, 20, 25, and 30 MeV  $\gamma$ -rays. The absolute photo-peak efficiencies for the different energies were determined after estimates of the background counts under the photo-peaks were subtracted. The total flux of  $\gamma$  rays impinging upon the detector was used in this determination. The line shapes and the efficiencies were also simulated using the GEANT4 package. Figure 8.34 presents the measured  $\gamma$ -ray spectra and the GEANT4 reproductions for sample energies.

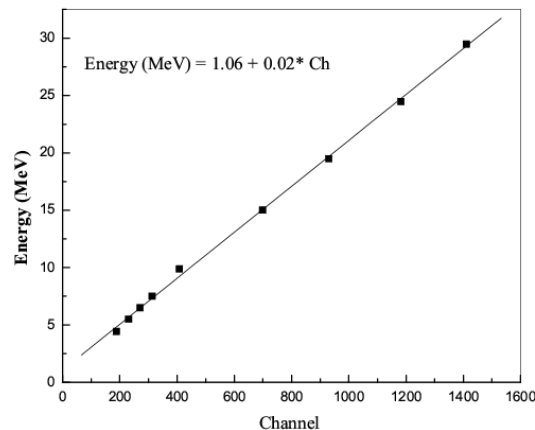


**Figure 8.35: Energy vs. pulse height for all eight energies.**

The energy resolution of the detector at each energy, determined from the FWHM of the photo-peak, is a convolution of the detector resolution and the spread in the beam energy. We

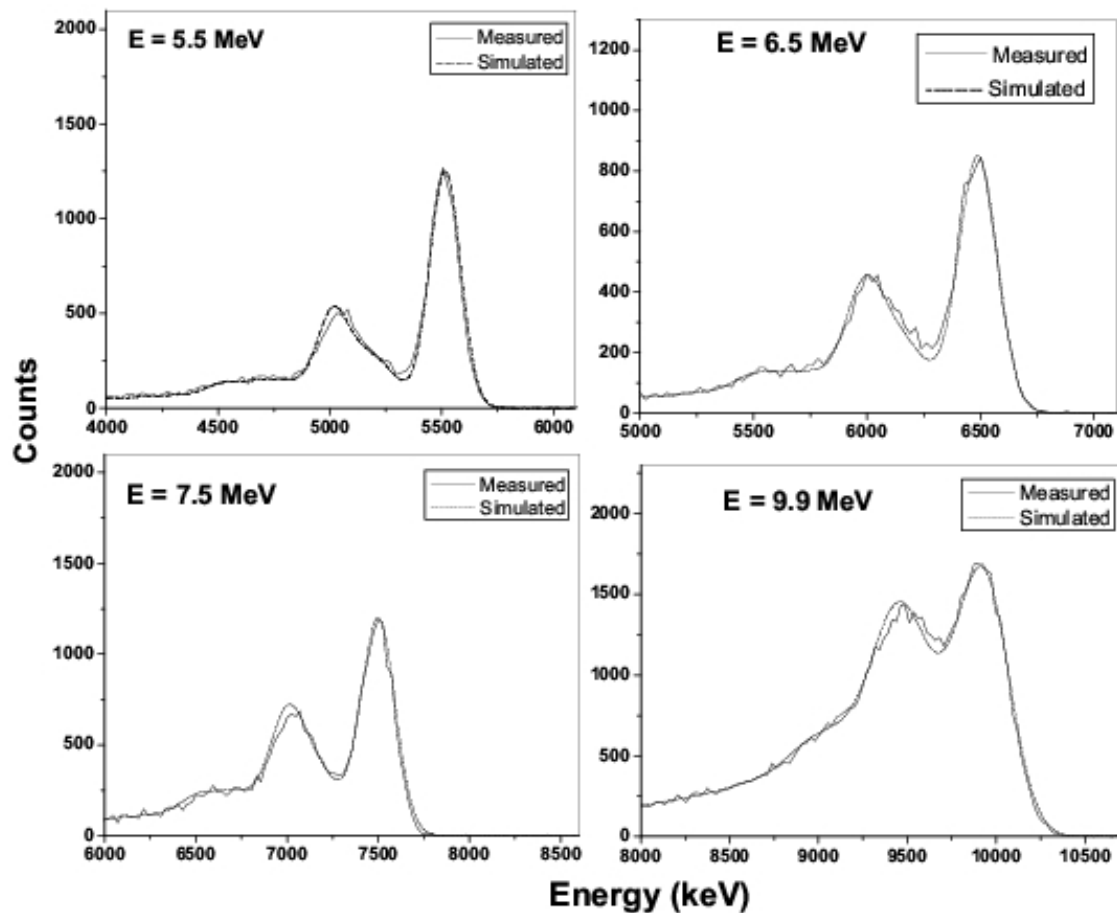


Figure 8.34: Measured  $\gamma$ -ray spectra for 5.5, 6.5, 7.5, and 9.9 MeV. The fine histograms show the data; the smooth curves give the GEANT4 simulations.

made use of the nuclear resonance fluorescence (NRF) reaction on  $^{12}\text{C}$  to measure the intrinsic resolution of the detector. This was achieved by bombarding a thick disk of carbon with 15.1 MeV photons from the HI $\gamma$ S facility. The large-volume LaBr<sub>3</sub>:Ce detector was placed at 90° to the beam direction and at a distance of 30 cm from the center of the target. The 15.1 MeV NRF  $\gamma$ -ray spectrum was measured and the photo-peak was fit, yielding an excellent energy resolution of around 1%. Figure 8.35 shows the very linear response

of the detector to  $\gamma$  rays from 5.5 to 30 MeV.

- [Dor04] P. Dorenbos, J. T. M. de Haas, and C. W. E. Van Eijk, *IEEE Trans. Nucl. Sci.*, **51**, 1289 (2004).
- [Kum09] G. A. Kumar, I. Mazumdar, and D. Gothe, *Nucl. Instrum. Methods A*, **610**, 522 (2009).
- [Maz13] I. Mazumdar *et al.*, *Nucl. Instrum. Methods A*, **705**, 85 (2013).

## 8.3 Facilities

### 8.3.1 Construction of an Ultracold-Neutron-Source Facility at the NC State PULSTAR Reactor

R. GOLUB, P.R. HUFFMAN, G.L. MEDLIN, G. PALMQUIST, A.R. YOUNG, *TUNL*; A. COOK, A. HAWARI, E. KOROBKINA, B. WEHRING, *North Carolina State University, Raleigh, NC*

**We have finished construction and have begun commissioning of an ultracold-neutron-source facility at the PULSTAR reactor on the campus of North Carolina State University. Detailed evaluation of the source’s performance will allow optimization of UCN production. Systematic studies related to nEDM measurements will utilize the source in the near future.**

The ultracold-neutron-(UCN)-source facility being commissioned at the PULSTAR reactor on the campus of North Carolina State University will provide a competitive UCN flux for measurements including the neutron electric dipole moment (nEDM),  $\beta$  decay, and material scattering. In addition it will serve as a platform for improving UCN source technology. In particular, the nEDM collaboration is finalizing plans for a smaller test apparatus that will be operated at the PULSTAR source to research the different techniques needed for the nEDM measurement. There is also the possibility that the source will be used for operating the Los Alamos neutron-lifetime experiment.

The source utilizes the high leakage of epithermal and thermal neutrons from the under-moderated reactor core. The 1-MW-thermal PULSTAR reactor has been upgraded to run at 2 MW, and a license amendment is currently being processed.

One liter of solid ortho-deuterium at a temperature below 5 K serves as the UCN converter material, and this is surrounded by a solid methane cold moderator in a cup-shaped container. The source sits inside a heavy-water thermal moderator. Construction of the heavy-water tank and the cryostat housing the cryogenic methane and deuterium containers has been completed, and the helium liquefier that provides cooling has been tested.

Unlike traditional reactor-based UCN sources, the PULSTAR UCN source was designed to be placed in the former thermal-column facility outside of the reactor pool. A unique graphite-lined port was built to efficiently trans-

port neutrons away from the core. This delivers a majority of the neutron flux to the source while minimizing heating of the source by reactor  $\gamma$  rays. The performance of this neutron transport system was measured directly using activation of cadmium-covered gold foils and a heavy-water tank approximating the source tank. This setup was also modeled using the MCNP code, and this measurement will be used to benchmark the MCNP model of the final source design. Figure 8.36 shows an MCNP plot of the reactor and UCN source geometry.

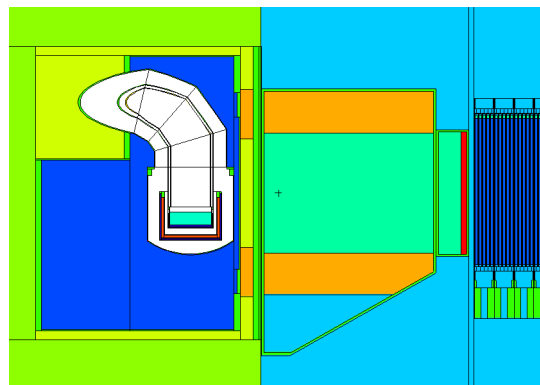


**Figure 8.36: (Color online) MCNP plot of the reactor and UCN source geometry.**

The source is mounted to the thermal-column shield door, allowing it to be easily rolled out of the reactor biological shield, as shown in Fig. 8.37. A replacement shield door that will allow the source to be serviced and tested in situ without an extended shutdown of the reactor is being constructed.

A guide system to transport UCNs from the

source out of the biological shield has been constructed. The guides are six-inch-diameter,  $^{58}\text{Ni}$ -coated quartz tubes, coated using a custom-built e-beam vacuum chamber at Virginia Polytechnic and State University.



**Figure 8.37:** (Color online) Partially assembled heavy-water tank and cryostat on the thermal column door, rolled out of the reactor thermal column void.

To manage and condense methane and deuterium gas, a gas-handling system was designed and built completely out of VCR-stainless-steel components. The cryostat's parallel liquid-helium loops have been tested using liquid nitrogen as a cryogen to condense argon through the

gas handling system in the cryogenic containers. The gas-handling system is shown in Fig. 8.38.

Part of the strategy for the source is detailed modeling and evaluation of its performance, in order to optimize UCN production. The source design allows for the cold-neutron energy at the peak flux to be tuned between 30 and 60 K to optimize UCN production in the deuterium, or for the solid methane moderator to be switched out for a different moderator, such as mesitylene or triphenylmethane. Neutron-scattering kernels for methane and other candidate materials are being examined and updated. In addition, solid nitrogen is being examined as an alternate UCN converter material.



**Figure 8.38:** (Color online) Methane and deuterium gas handling systems.

### 8.3.2 Beamline and Target Chamber for Studies of the ( ${}^3\text{He},n$ ) Reaction

D.R. TICEHURST, D. COMBS, C.R. HOWELL, A.R. YOUNG, *TUNL*

**Cross-section measurements of the ( ${}^3\text{He},n$ ) reaction on several nuclei used in searches for neutrinoless double-beta decay will require a pulsed  ${}^3\text{He}$  beam, a target chamber with a thin window at forward angles to allow the neutrons to escape with low attenuation, and a long flight path for neutron energy measurements with sufficient resolution using time-of-flight. The beamline and target chamber have been installed and are being evaluated.**

Cross-section measurements for the ( ${}^3\text{He},n$ ) two-proton transfer reaction will be carried out on isotopes relevant to experiments that search for neutrinoless double-beta ( $0\nu\beta\beta$ ) decay. The aim of these measurements is to test the BCS ground-state approximation in QRPA calculations of the nuclear matrix element for  $0\nu\beta\beta$  decay. The BCS picture neglects effects in the decay process such as the rearrangement of nucleons beyond the annihilation of two neutrons and the creation of two protons. A phenomenon called pairing vibrations, which are fluctuations about the BCS state, could cause such effects [Bri05]. For instance, in an even-even nucleus near the Fermi surface where the energy gap to the next available single-particle orbital is greater than the pairing energy, excited  $0^+$  states could be due to pairing vibrations [Fre12]. If this is the case, these excited  $0^+$  states should share a substantial fraction of the two-nucleon transfer strength with the ground state of the final nucleus as predicted using the BCS approximation. In this work we evaluate the conjecture of using BCS ground states in QRPA calculations by determining the strength of two-proton transfer to the  $0^+$  excited states relative to the strength to the  $0^+$  ground state of the residual nucleus.

These ( ${}^3\text{He},n$ ) measurements require a long neutron flight-path for precise neutron energy determination via the time-of-flight method. The goal is to have an energy resolution better than 0.5 MeV for neutron energies less than about 25 MeV, thus allowing us to resolve key states in the residual nucleus. The time spread in the pulsed helium beam in the tandem lab was determined in measurements last year to be about 1.1 ns FWHM [Tic12]. The targets will be about 2.5 mg/cm<sup>2</sup> thick. To achieve the desired energy resolution with these parameters, detectors will

be installed to provide a 13 m neutron flight path from the target at angles from 0° to 15° relative to the beam direction.

An existing target chamber was modified for this experiment. The main modification was to remove a section of the chamber wall around 0° and replace it with a 0.5 mm thick piece of stainless steel to reduce the attenuation of the emitted neutrons. The steel was attached to the chamber with A-12 epoxy to form a vacuum-tight seal. The beam stop and suppressor grid were fabricated to sit just behind the target (see Fig. 8.39). The beam stop and the chamber are lined with lead to reduce neutron backgrounds in the detectors due to ( ${}^3\text{He},n$ ) reactions on low-Z materials.

An experiment was conducted in October 2013 to commission the new 70° beamline and to determine the magnitude and sources of neutron background. A pulsed beam of 21 MeV  $\alpha$  particles at a 2.5 MHz repetition rate and a current of 50 pA was delivered to target. A 1.8 mg/cm<sup>2</sup> <sup>nat</sup>Ni target, similar to the germanium and tellurium targets to be used in the experiment, was employed. With this target, the signal-to-background ratio was about 4:1. Placement of additional lead to cover materials that might be exposed to the scattered beam could improve the signal-to-noise ratio by at least a factor of two.

---

[Bri05] D. M. Brink and R. A. Broglia, *Nuclear Superfluidity*, Cambridge University Press, Cambridge, UK, 2005.

[Fre12] S. J. Freeman and J. P. Schiffer, *J. Phys. G.*, **39**, 124004 (2012).

[Tic12] D. R. Ticehurst *et al.*, *TUNL Progress Report*, **LI**, 47 (2012).

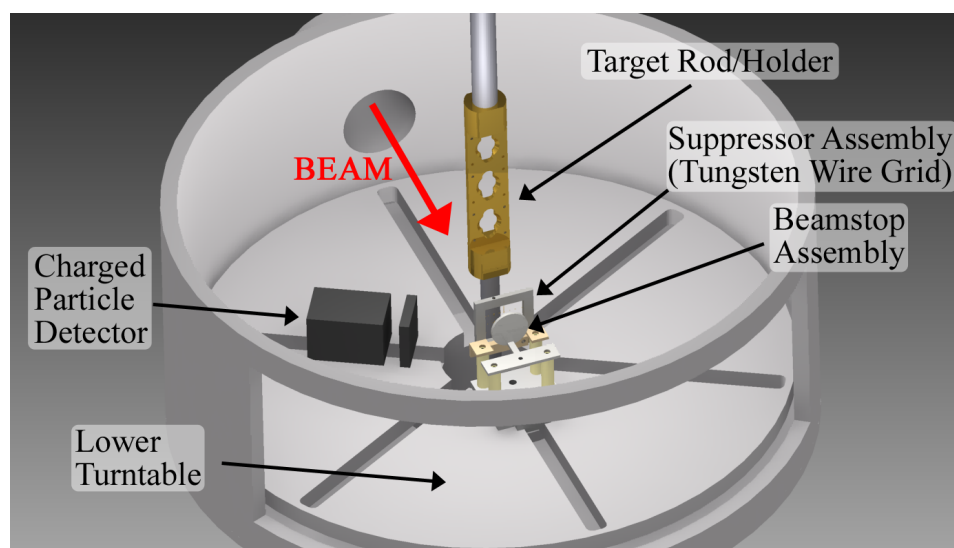


Figure 8.39: (Color Online) A schematic diagram of the target chamber. A target holder sits in the center. A charged particle detector and the suppressor/beamstop assembly are attached to the bottom plate. The top cover of the chamber and the steel neutron window have been removed from the diagram for clarity. All surfaces that could be exposed to scattered helium have been covered with a thin layer of lead.

## 8.4 Data Acquisition Hardware and Software Development

### 8.4.1 Status of the ORCA Data-Acquisition Software

M.A. HOWE, J.F. WILKERSON, *TUNL*; T. BERGMANN, A. KOPMANN, *Karlsruhe Institute of Technology, Karlsruhe, Germany*; M. MARINO, *Technische Universität München, Garching, Germany*

**We describe additions and improvements to ORCA, an object-oriented real-time control-and-acquisition system. ORCA is in use in many laboratories in the US, Canada, and Germany. This year, a number of new VME, ethernet, and serial devices were added to the list of supported hardware, and new features were added to some of ORCA's subsystems.**

The ORCA (object-oriented, real-time control-and-acquisition) software system [How09] is designed for dynamically building flexible and robust data-acquisition systems. It is being used at UNC, TUNL, KURF, Sanford Underground Research Facility (SURF), University of Washington, SNOLAB, LANL, LBNL, Massachusetts Institute of Technology, ORNL, and Karlsruhe Institute of Technology. It is being used in the MAJORANA DEMONSTRATOR (MJD), SNO+, HALO, KATRIN, and Edelweiss experiments, among others. Slow-control systems based on ORCA are monitoring the environmental conditions for MAJORANA at SURF. The ORCA system is under continuous development. New features are added as requested, and the catalog of supported objects continues to grow.

In the last year a number of new serial devices (USB, RS232) were added:

- 5085 Meridian neutron survey meter.
- Agilent 33500 pulser (not all features implemented – used at KATRIN)

Several new VME cards were added:

- CAEN V792N. The existing V792 QDC object was modified to support both the 16- and 32-channel versions of the card.
- CAEN V977. A 16-channel I/O register.
- CAEN V1721. An 8-channel 8-bit 500MHz digitizer.
- CAEN V830. A 250 MHz latching scaler.
- STRUCK 3320. An 8-channel 12-bit 250 MHz digitizer.

The list of newly supported IP devices includes:

- ACP UPS. This object is monitoring the power at MAJORANA.
- Arduino UNO single-board computer. Under ORCA control, the Arduino can be used as an inexpensive data logger and I/O controller.

A few objects were developed specifically for various experiments:

- HALO sentry object. This object watches critical hardware components for various failure modes and attempts to keep the system running by rebooting the VME crate controllers or switching between the backup and main DAQ systems.
- MJD pump-stand monitor and display. A dialog giving an overview of the vacuum system for the string-test-cryostat pump stand.
- 3D calibration scanner. This object links to a VXM two-channel motor controller and shows the operator a 3D view that mirrors the actual radial and vertical positions of the scanning platform. This calibration scanner will be used at UNC and at SURF.
- Edelweiss second-level trigger (SLT). A modified version of the SLT object that was developed for the KATRIN experiment.
- Edelweiss first-level trigger (FLT). A modified version of the KATRIN FLT object.

Some new objects for added to ORCA's slow-control processing system

- An object allowing fixed values to be inserted into the processing data stream. It is useful for defining set points for alarm conditions.
- A rate-of-change object for watching a parameter and outputting a signal based on how fast the value is changing over time.

Some objects and ORCA subsystems had major improvements:

- KATRIN main-controller dialog. A 3D display was added showing parameters such as the data rate of the focal plane detector and veto system. The display can be rotated and scaled in real-time using the mouse.
- Scripts. Script libraries can now be imported, so that scripts can be debugged once and reused. In addition, the scripting language was extended to have script-controlled status and action confirmation dialogs.
- GRETINA. The card's dialog was updated for control of the new features contained in a significant firmware update.
- A firmware loader was added to the RAD7 object. The firmware needed for computer control of the RAD7 is sometimes corrupted because of power glitches. The firmware files have to be purchased from the manufacturer but, if available, they can now be loaded directly from IORCA.

Database improvements:

- Many objects in ORCA are now CouchDB aware. This means that they can post a snapshot of their parameters to a database that can be used for remote monitoring. An application programming interface exists for posting either single documents representing current status or records that go into a long-term history.
- Events such as ORCA-restarts and run-boundaries can now be saved into a CouchDB history database.
- CouchDB Listener. ORCA can now watch for and act on changes to records in a CouchDB.

The release of a new compiler (XCode 4.5) and MacOS operating system (10.8) required a large sweep of the ORCA code-base to eliminate new compiler warnings. The new versions of the XCode static-analysis tools helped to clear a number of long-standing bugs and memory leaks.

In addition to the existing mobile remote-monitoring application IORCA [How10], a number of web-based monitoring tools have been developed. One is a history display that allows a

user to select multiple parameters from an ORCA-created history CouchDB and to display them over any time frame. Various options exist for data display in other time zones and for linear or logarithmic scales. This tool is experiment agnostic.

For MAJORANA, several web-based tools have been developed for displaying experiment-specific information:

- MJD Monitor. A small cross-platform application based on the Processing language for monitoring the environmental conditions at SURF. It was used temporarily until the more sophisticated web-based tools could be developed.
- Vacuum monitor. A web-based application that displays the status of the MAJORANA prototype vacuum system. It shows a schematic of the entire system, including the positions of the gate valves, pressure values, and whatever operational constraints are currently in place. The turbo pump, cryopump, residual gas analyzer, and baratron states are also displayed. A set of time-series plots shows the pressure and heater histories for the past seven days.
- Detector monitor. This tool monitors the MAJORANA preamp controllers and displays a history of the baseline voltages for each detector.
- Environment monitor. All of the environmental parameters (particle counts, radon levels, temperatures, humidities, etc.) that are monitored in the main MAJORANA detector room, the machine shop, and the temporary clean room are displayed with this tool. Histories are also available for display.

At present, the remote monitoring tools for MAJORANA exist as separate applications. Work is underway to consolidate them into one integrated monitoring tool.

A secondary application to ORCA, called ORCAROOT, provides a tool kit to build analysis programs that can decode raw ORCA data streams. As new objects are added to ORCA, new decoders are also added to ORCAROOT to fully support ROOT analysis of data from the new objects.

---

[How09] M. Howe *et al.*, TUNL Progress Report, **XLVIII**, 171 (2009).

[How10] M. Howe *et al.*, TUNL Progress Report, **XLIX**, 214 (2010).

---

## 8.4.2 Addition of 3D Displays in ORCA

---

M.A. HOWE, *TUNL*; L. WENDLANDT, *Grove City College, Grove City, PA*

**We describe the addition of 3D computer visualizations into ORCA. Specifically, we have developed software to convert CAD files into OpenGL and have applied that software to display a 3D model of a detector-calibration stand that will be used both at UNC and at SURF.**

The ORCA software system [How09] is designed primarily for building flexible and robust data-acquisition systems, but it can also be used to control things like stepper motors. ORCA generally displays status and control information using a traditional style of dialog, but if hardware can physically move before or during data acquisition, then tables of numbers may not be sufficient, and real-time visual feedback would be more useful. A picture or an animation allows operators to understand better what is going on, to see quickly if something is positioned incorrectly, and to understand intuitively what kind of data is being generated.

As an example, we are constructing a stand for use in characterizing germanium detectors. One stepper motor moves a collimated radioactive source azimuthally around a detector on a horizontal track, and one moves it vertically up and down using a jack screw. Data are taken at different locations, providing a comprehensive picture of the detector's characterization at different heights and angles. See Sect. 2.1.6 for more details.

To provide an animated model of the characterization stand in ORCA, we use OpenGL, which is a standard cross-platform computer-graphics library that can be used to create 3D models. However, making visualizations directly using OpenGL is difficult. Each shape must be constructed from sets of individually defined vertex points which then have to be grouped into polygon faces. Sometimes predefined primitive shapes such as spheres or cubes can be used, but even then their positions must be carefully specified in relation to the other objects in the model or within a particular transformation scope. In addition, if the model is to look even slightly realistic, each object must have its material properties defined and the light sources must be ar-

ranged. For anything more complex than a few simple objects, doing this process programmatically is tedious, time consuming, and prone to error.

To ease this process, software was developed for taking the existing CAD models that are used in the manufacture of hardware and importing them into formats that can be displayed using OpenGL. Most CAD programs have file export options that allow the raw data of the model to be stored in ASCII formats that are relatively easy for other programs to process. One of the standard formats is an object (.obj) file that defines the geometry of a model as a set of vertexes, normals, texture vertexes, and face groupings. In addition to the raw geometry files, another exported file (.mtl) specifies the materials that make up each object in the model. Each material is defined to have a specific ambient, diffuse, and specular reflectivity.

The object and material definition files are read by ORCA and converted into ORCA OpenGL objects that contain the processed vertexes, face groupings, and material properties. These objects can then be instantiated and displayed in an OpenGL view in an ORCA control dialog. Methods to provide basic functionality to rotate, orient, and scale the displayed objects are provided. A separate class was developed for lighting and shadow effects.

In the case of the detector stand, some parts of it are always stationary so it is necessary to break up the model into the parts that move and those that don't. The stationary parts, like the azimuthal track, are built up programmatically using primitive shapes such as cylinders. CAD files for the vertically and azimuthally moving parts are used to generate two separate objects that can be translated and rotated to positions that match the positions of their real-world coun-

terparts.

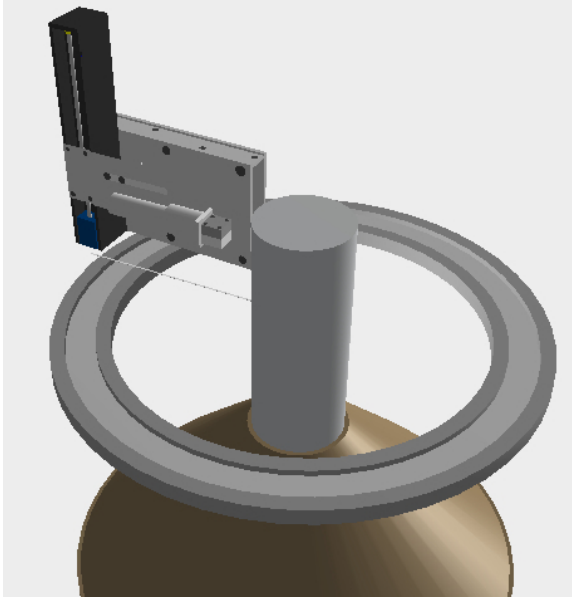


**Figure 8.40:** A screen shot of the detector calibration stand as it appears in its ORCA control dialog. At the center is the detector Dewar surrounded by a horizontal azimuthal track on which runs an assembly holding a collimated source that can also move vertically.

The final result can be seen in Fig. 8.40, which is a screen shot of the ORCA dialog for controlling the calibration stand. The ORCA model is to scale and is based on the technical drawings

for the equipment. For comparison, Fig. 8.41 is a picture of the actual calibration stand that was taken during assembly. The Dewar with its detector will be centered in the circular track.



**Figure 8.41:** A picture of the actual calibration stand as it was nearing completion. The detector Dewar will be centered in the circular track.

---

[How09] M. Howe *et al.*, TUNL Progress Report, **XLVIII**, 171 (2009).



# Appendices

---

- Graduate Degrees Awarded
- Publications
- Invited Talks, Seminars, and Colloquia
- Professional Service Activities

## A.1 Graduate Degrees Awarded

---

### Ph.D. Degrees

---

1. Jeromy R. Tompkins, *Polarized Photofission Fragment Angular Distributions of  $^{232}\text{Th}$  and  $^{238}\text{U}$* , University of North Carolina at Chapel Hill, October 2012  
*Supervisor:* H. J. Karwowski.
2. David P. Kendellen, *Design of Cryogenic Systems for the Neutron Electric Dipole Moment Experiment*, North Carolina State University, November 2012  
*Supervisors:* P. R. Huffman and D. G. Haase
3. Robert W. Pattie Jr., *A Precision Measurement of the Neutron  $\beta$  Asymmetry Using Ultracold Neutrons*, North Carolina State University, December 2012  
*Supervisor:* A. R. Young
4. Sean P. MacMullin, *Elastic and Inelastic Scattering of Neutrons from Neon and Argon: Impact on Neutrinoless Double-Beta Decay and Dark Matter Experimental Programs*, University of North Carolina at Chapel Hill, January 2013  
*Supervisor:* R. Henning
5. Carrie L. Walker, *Neutron Capture Measurements on  $^{97}\text{Mo}$  with the DANCE Array*, North Carolina State University, April 2013  
*Supervisors:* G. E. Mitchell and U. Agvaanluvsan.
6. Padraic S. Finnerty, *A Direct Dark Matter Search with the MAJORANA Low-Background Broad Energy Germanium Detector*, University of North Carolina at Chapel Hill, April 2013  
*Supervisor:* R. Henning
7. Karl W. Schelhammer, *Measurement of the Beta-Decay Lifetime of Magnetically Trapped Ultracold Neutrons*, North Carolina State University, June 2013  
*Supervisor:* P. R. Huffman.
8. William R. Zimmerman, *Direct Observation of the Second  $J^\pi = 2^+$  State in  $^{12}\text{C}$* , University of Connecticut, August 2013  
*Supervisor:* H. R. Weller
9. Stephen Daigle, *Low Energy Proton Capture Study of the  $^{14}\text{N}(p,\gamma)^{15}\text{O}$  Reaction*, University of North Carolina at Chapel Hill, October 2013  
*Supervisor:* A. E. Champagne
10. Jonathan M. Mueller, *Prompt Neutron Polarization Asymmetries in Photofission of Isotopes of Thorium, Uranium, Neptunium, and Plutonium*, Duke University, November 2013  
*Supervisors:* H. R. Weller and M. W. Ahmed

---

**M.S. and M.A. Degrees**

---

1. Kevin J. Wierman, *Evaluation and Implementation of the KATRIN Focal Plane Detector Cosmic Ray Muon Veto*,  
University of North Carolina at Chapel Hill, April 2013  
*Supervisor:* J. F. Wilkerson
2. Kyle Snaveley, *The MAJORANA Parts Tracking Database*,  
University of North Carolina at Chapel Hill, July 2013  
*Supervisor:* R. Henning
3. Forrest Q. Friesen, *Three-Body Photodisintegration of the Triton*,  
Duke University, November 2013  
*Supervisor:* C. R. Howell

## A.2 Publications

The publications co-authored by members of TUNL research groups between September 2012 and November 2013 are tabulated in Table A.1. The papers in refereed journals by TUNL research groups are listed below in chronological order.

Type	No.
Refereed Journal Articles	37
Conference Proceeding Papers	17

**Table A.1: Summary of TUNL publications from September 2012 through November 2013. Among the 37 refereed journal papers, 5 were letters.**

---

### Journal Articles Published

---

1.  $^{40}\text{Ar}(n,p)^{40}\text{Cl}$  Reaction Cross Section Between 9 and 15 MeV, C. Bhatia, S. W. Finch, M. E. Gooden, and W. Tornow, Phys. Rev. C, **86**, 041602 (2012).
2. Evidence for Radiative Coupling of the Pygmy Dipole Resonance to Excited States, C. T. Angell, S. L. Hammond, H. J. Karwowski, J. H. Kelley, M. Krticka, E. Kwan, A. Makinaga, and G. Rusev, Phys. Rev. C, **86**, 051302 (2012).
3. Gamma-Ray Fluxes in Oklo Natural Reactors, C. R. Gould, E. I. Sharapov, and A. A. Sonzogni, Phys. Rev. C, **86**, 054602 (2012).
4. Measurement of Airborne Fission Products in Chapel Hill, NC, USA from the Fukushima Dai-ishi Reactor Accident, S. MacMullin, G. K. Giovanetti, M. P. Green, R. Henning, R. Holmes, K. Vorren, and J. F. Wilkerson, J. Environ. Radioact. **112**, 165 (2012).
5. Neutron-Induced Gamma-Ray Production Cross Sections for the First Excited-State Transitions in  $^{20}\text{Ne}$  and  $^{22}\text{Ne}$ , S. MacMullin, M. Boswell, M. Devlin, S. R. Elliott, N. Fotiades, V. E. Guiseppe, R. Henning, T. Kawano, B. H. LaRoque, R. O. Nelson, and J.M. O'Donnell, Phys. Rev. C, **86**, 067601 (2012).
6. Neutron Scattering from  $^{28}\text{Si}$  and  $^{32}\text{S}$  from 8.0 to 18.9 MeV, Dispersive Optical Model Analyses, and Ground-State Correlations, M. A. Al-Ohali, J. P. Delaroche, C. R. Howell, M. M. Nagadi, A. A. Naqvi, W. Tornow, R. L. Walter, and G. J. Weisel, Phys. Rev. C, **86**, 034603 (2012).
7. Search for Spin-Dependent Short-Range Force Between Nucleons Using Optically Polarized  $^3\text{He}$  Gas, W. Zheng, H. Gao, B. Lalremruata, Y. Zhang, G. Laskaris, W. M. Snow, and C. B. Fu, Phys. Rev. D, **85**, 031505 (2012).
8. Thermonuclear Reaction Rate of  $^{18}\text{O}(p,\gamma)^{19}\text{F}$ , M. Q. Buckner, C. Iliadis, J. M. Cesaratto, C. Howard, T. B. Clegg, A. E. Champagne, and S. Daigle, Phys. Rev. C, **86**, 065804 (2012).
9. A MRPC Prototype for SOLID-TOF in JLab, Y. Wang *et al.* (including H. Gao), JINST **8**, P03003 (2013).
10. Exploring the Multi-Humped Fission Barrier of  $^{238}\text{U}$  via Sub-Barrier Photofission, L. Csige, D. M. Filipescu, T. Glodariu, J. Gulyas, M. M. Gunther, D. Habs, H. J. Karwowski, A. Krasznahorkay, G. C. Rich, and M. Sin, Phys. Rev. C, **87**, 044321 (2013).
11. Fine Structure of the Giant M-1 Resonance in  $^{90}\text{Zr}$ , G. Rusev *et al.* (including A. P. Tonchev, J. H. Kelley, and W. Tornow), Phys. Rev. Lett. **110**, 022503 (2013).

12. *First Determination of an Astrophysical Cross Section with a Bubble Chamber: The  $^{15}\text{N}(\alpha, \gamma)^{19}\text{F}$  Reaction*, C. Ugalde, B. DiGiiovine, D. Henderson, R. J. Holt, K. E. Rehm, A. Sonnenschein, A. Robinson, R. Raut, G. Rusev, A. P. Tonchev, Phys. Lett., **B719**, 74 (2013).
13. *First Measurements of Spin-Dependent Double-Differential Cross Sections and the GDH Integrand from  $^3\text{He}(\vec{\gamma}, n)pp$  at Incident Photon Energies of 12.8 and 14.7 MeV*, G. Laskaris *et al.* (including M. W. Ahmed, H. Gao, H. J. Karwowski, H. R. Weller, and Y. K. Wu), Phys. Rev. Lett. **110**, 202501 (2013).
14. *The High-Efficiency  $\gamma$ -ray Spectroscopy Setup  $\gamma 3$  at HI $\gamma$ S*, B. Löher *et al.* (including J. H. Kelley, A. P. Tonchev, W. Tornow, and H. R. Weller), Nucl. Instrum. Methods A, **723**, 136 (2013).
15. *Laboratory Search for Spin-Dependent Short-Range Force from Axion-Like-Particles Using Optically Polarized  $^3\text{He}$  Gas*, P. H. Chu, A. Dennis, C. B. Fu, H. Gao, R. Khatiwada, G. Laskaris, K. Li, E. Smith, W. M. Snow, H. Yan, and W. Zheng, Phys. Rev. D, **87**, 011105 (2013).
16. *Measurement of  $n - n$  Scattering – The Gamma Ray-Induced Outgassing Complication*, S.L. Stephenson *et al.* (including C. R. Howell, G. E. Mitchell, and W. Tornow), Nucl. Phys. A **895**, 33 (2012).
17. *Measurement of the Neutron  $\beta$ -Asymmetry Parameter  $A_0$  with Ultracold Neutrons*, B. Plaster *et al.* (including A. R. Young), Phys. Rev. C **86**, 055501 (2012).
18. *Measurement of The Elastic Scattering Cross Section of Neutrons from Argon and Neon*, S. MacMullin, M. Kidd, R. Henning, W. Tornow, C. R. Howell, and M. Brown, Phys. Rev. C, **87**, 054613 (2013).
19. *Measurement of the  $^{64}\text{Zn}(n, 2n)^{63}\text{Zn}$  Reaction Cross Section between 12.5 and 14.5-MeV*, C. Bhatia and W. Tornow, J. Phys. G, **40**, 065104 (2013).
20. *Nuclear Physics Detector Technology Applied to Plant Biology Research*, A. G. Weisenberger *et al.* (including C. R. Howell and A. S. Crowell), Nucl. Instrum. Methods A, **718**, 157 (2013).
21. *Nucleosynthesis in Type I X-Ray Bursts*, A. Parikh, J. Jose, G. Sala, and C. Iliadis, Prog. Part. Nucl. Phys., **69**, 225 (2013).
22. *The Design of an Ultra-Low Background Thermosyphon for The Majorana Demonstrator*, E. Aguayo, M. Busch, R. Daniels, J. E. Fast, M. P. Green, and D. J. Reid, Nucl. Instrum. Methods A, **709**, 17 (2013).
23. *The Electric Dipole Response of  $^{76}\text{Se}$  above 4 MeV*, P. M. Goddard *et al.* (including J. H. Kelley, A. P. Tonchev, and W. Tornow), Phys. Rev. C, **88**, 064308 (2013).
24. *The Lead-Glass Electromagnetic Calorimeters for The Magnetic Spectrometers in Hall C at Jefferson Lab*, H. Mkrtchyan *et al.* (including D. Dutta and S. P. Malace), Nucl. Instrum. Methods A, **719**, 85 (2013).
25. *The Production of  $K^+K^-$  Pairs in Proton-Proton Collisions below the Phi Meson Threshold*, Q. J. Ye *et al.* (including H. Gao), Phys. Rev. C, **87**, 065203 (2013).
26. *Unambiguous Identification of the Second  $2^+$  State in  $^{12}\text{C}$  and the Structure of the Hoyle State*, W. R. Zimmerman *et al.* (including M. W. Ahmed, H. R. Weller, and Y. K. Wu), Phys. Rev. Lett., **110**, 152502 (2013).
27.  *$^{136}\text{Xe}(n, 2n)^{135}\text{Xe}$  Cross Section Between 9 and 15 MeV*, C. Bhatia, S. W. Finch, M. E. Gooden, and W. Tornow, Phys. Rev. C, **87**, 011601 (2013).
28. *Reactor On-Off Antineutrino Measurement with KamLAND*, (The KamLAND Collaboration including H.J. Karwowski, D. M. Markoff, and W. Tornow), Phys. Rev. D, **88**, 033001 (2013).

29. *Limit on Neutrinoless  $\beta\beta$  Decay of  $^{136}\text{Xe}$  from the First Phase of KamLAND-Zen and Comparison with the Positive Claim in  $^{76}\text{Ge}$*  (The KamLAND-Zen Collaboration including H.J. Karwowski, D. M. Markoff, and W. Tornow), *Phys. Rev. Lett.*, **110**, 062502 (2013).
30. *Pygmy Dipole Strength in  $^{86}\text{Kr}$  and Systematics of  $N = 50$  Isotones*, R. Schwengner *et al.* (including J. H. Kelley, A. P. Tonchev and W. Tornow), *Phys. Rev. C* **87**, 024306 (2013).
31. *Photon Strength Functions of  $^{155}\text{Gd}$  from Radiative Capture of Resonance Neutrons*, B. Baramsai *et al.* (including G. E. Mitchell), *Phys. Rev. C* **87**, 044609 (2013).
32. *Mean Proton and  $\alpha$ -Particle Widths of the Porter-Thomas Distribution and Astrophysical Applications*, I. Pogrebnyak *et al.* (including C. Iliadis and G.E. Mitchell), *Phys. Rev. C* **88**, 015808 (2013).
33. *Strength of Scissors Mode in Odd Gd Isotopes from Radiative Capture of Resonance Neutrons*, J. Kroll *et al.* (including G. E. Mitchell), *Phys. Rev. C* **88**, 034317 (2013).
34. *The Upscattering of Ultracold Neutrons from the Polymer  $[\text{C}_6\text{H}_{12}]_n$* , E. I. Sharapov *et al.* (including A. R. Young), *Phys. Rev. C* **88**, 064605 (2013).
35. *Detecting Scintillations in Liquid Helium*, P. R. Huffman and D. N. McKinsey, *J. Instrum.*, **8**, C09008 (2013).
36. *Performance of the Los Alamos National Laboratory Spallation-Driven Solid-Deuterium Ultracold Neutron Source*, A. Saunders *et al.* (including A. R. Young), *Rev. Sci. Instrum.* **84**, 013304 (2013).

---

**Journal Articles Accepted**

---

1. *Cross-Section Measurements of the  $^{86}\text{Kr}(g, n)$  Reaction to Probe The  $s$ -Process Branching at  $^{85}\text{Kr}$* , R. Raut *et al.* (including A. P. Tonchev, W. Tornow, C. Iliadis, and J. H. Kelley), accepted for publication in Phys. Rev. Lett., arXiv:1309.4159.
2. *The MAJORANA DEMONSTRATOR Neutrinoless Double-Beta Decay Experiment*, The Majorana Collaboration (including R. Henning, W. Tornow, J.F. Wilkerson, and A.R. Young), accepted for publication in Adv. High Energy Phys., arXiv:1308.1633.
3. *A Segmented, Enriched N-type Germanium Detector for Neutrinoless Double Beta-Decay Experiments*, L.E. Leviner *et al.* (including M.W. Ahmed, W. Tornow, Y.K. Wu, and A.R. Young), accepted for publication in Nucl. Instrum. Methods A, arXiv:1304.5477.
4. *Limits on Tensor Coupling from Neutron  $\beta$ -Decay*, R. W. Pattie, K. P. Hickerson, and A. R. Young, accepted for publication in Phys. Rev. C.
5. *Precision Measurement of the Neutron Beta-Decay Asymmetry*, M. P. Mendenhall *et al.* (including A. R. Young), accepted for publication in Phys. Rev. C.
6. *Measurement and Modeling of Thermal Flow in an Enclosed Tube Containing Superfluid Helium Film*, D. P. Kendellen and D. G. Haase, Accepted for publication in Cryogenics.

---

**Journal Articles Submitted**

---

1. *Nuclear Deformation and Neutron Excess as Competing Effects for Pygmy Dipole Strength*, R. Massarczyk *et al.* (including J.H. Kelley, W. Tornow, and A.P. Tonchev), submitted to Phys. Rev. Lett., arXiv:1311.1974.
2. *Neutron-Antineutron Oscillations: A Snowmass 2013 White Paper*, K. Babu *et al.* (including A.R. Young), arXiv:1310.8593.
3. *Parity Violation in Photonuclear Reactions at HIGS*, M. W. Ahmed *et al.* (including A. E. Champagne, C. R. Howell, P. Huffman, and Y. K. Wu), White Paper submitted to Snowmass 2013: Intensity Frontier, arXiv:1307.8178.
4. *Storage of Ultracold Neutrons in the UCN $\tau$  Magneto-Gravitational Trap*, D. J. Salvat *et al.* (including A. R. Young), submitted to Phys. Rev. C, arXiv:1310.5759.
5. *Measurements of Ultracold Neutron Upscattering and Absorption in Polyethylene and Vanadium*, E. I. Sharapov *et al.* (including A. R. Young), submitted to Phys. Rev. B, arXiv:1306.1261.

---

**Conference Reports and Articles in Conference Proceedings**

---

1. *Background Model for the Majorana Demonstrator Neutrinoless Double-Beta Decay Experiment*, MAJORANA Collaboration (including R. Henning, W. Tornow, J.F. Wilkerson, and A.R. Young), Proceedings of the 24<sup>th</sup> International Conference on Neutrino Physics and Astrophysics (Neutrino 2010), Athens, Greece, June 14 - 19, 2010, Nucl. Phys. Proc. Suppl., **522**, 229 (2012).
2. *Kaon Pair Production in Proton-Proton Collisions at COSY-ANKE*, Q. Ye, MESON 2012 12<sup>th</sup> International Workshop on Production, Properties and Interaction of MESONS, Cracow, Poland, May 31 - June 5, 2012, EPJ Web Conf. **37** 06003 (2012).
3. *The MAJORANA DEMONSTRATOR: Progress Towards Showing the Feasibility of a Tonne-Scale <sup>76</sup>Ge Neutrinoless Double-Beta Decay Experiment*, P. Finnerty for the MAJORANA Collaboration (including R. Henning, W. Tornow, J.F. Wilkerson, and A.R. Young), 18<sup>th</sup> International Symposium on Particles, Strings and Cosmology (PASCOS 2012), Merida, Yucatan, Mexico, June 3 - 8 (2012).
4. *Dark Matter Sensitivities of The Majorana Demonstrator*, G. K. Giovanetti for the MAJORANA Collaboration (including R. Henning, W. Tornow, J.F. Wilkerson, and A.R. Young), 12<sup>th</sup> International Conference on Topics in Astroparticle and Underground Physics (TAUP 2011), Munich, Germany, September 5 - 9 (2011), J. Phys. Conf. Ser. **375**, 012014 (2012).
5. *Studies of Nucleons and Nuclei at TUNL/HIγS: From Hadron Structure to Exploding Stars*, M. W. Ahmed, Proc. Sci. (PoS) **CD12**, 004 (2013).
6. *The Majorana Double Beta Decay Experiment: Present Status*, A.S. Barabash for the MAJORANA Collaboration (including R. Henning, W. Tornow, J.F. Wilkerson, and A.R. Young), 15<sup>th</sup> Lomonosov Conference on Elementary Particle Physics (LomCon), Moscow, Russia, August 18 - 24, 2011.
7. *The MAJORANA DEMONSTRATOR: A Search for Neutrinoless Double-beta Decay of Germanium-76*, S.R. Elliott for the MAJORANA Collaboration (including R. Henning, W. Tornow, J.F. Wilkerson, and A.R. Young), arXiv:1307.7777, Proceedings for the MEDEX 2013 Conference, Prague, Czech Republic, June 11 - 14 (2013), in publication.
8. *Discovering the New Standard Model: Fundamental Symmetries and Neutrinos*, V. Cianciolo *et al.* (including P.R. Huffman and J.F. Wilkerson), arXiv:1212.5190, Fundamental Symmetries and Neutrinos Workshop (FUNSYM), Chicago, IL, August 10 - 11 (2012).
9. *Project X: Physics Opportunities*, A. S. Kronfeld *et al.* (including A. R. Young), prepared in part for the DPF Community Summer Study, arXiv:1306.5009.
10. *Overview of Magnetic Trapping Neutron Lifetime Experiments*, P. R. Huffman, to appear in the proceedings of the *Next Generation Experiments to Measure the Neutron Lifetime*, November 9-10, 2012.
11. *Measuring the Neutron Lifetime with Magnetically Trapped Ultracold Neutrons*, H. P. Mumm *et al.* (including P. R. Huffman), to appear in the proceedings of the *Next Generation Experiments to Measure the Neutron Lifetime*, November 9-10, 2012.
12. *Systematics of the Electric and Magnetic Dipole Response in N=82 Isotones Below the Neutron Separation Energy*, A.P. Tonchev *et al.* (including J.H. Kelley and W. Tornow), in *Capture Gamma-Ray Spectroscopy and Related Topics, Proceedings of the Fourteenth International Symposium*, Guelph, Canada, 28 August - 2 September 2011, Ed. Paul E. Garrett *et al.*, World Scientific, 2013, pp. 192-201.

13. *Dipole Response of  $^{76}\text{Se}$  up to 9 MeV*, V. Werner *et al.* (including A.P. Tonchev, W. Tornow, and J. H. Kelley), in *Capture Gamma-Ray Spectroscopy and Related Topics, Proceedings of the Fourteenth International Symposium*, Guelph, Canada, 28 August - 2 September 2011, Ed. Paul E. Garrett *et al.*, World Scientific, 2013, pp. 421-426.
14. *(n, $\gamma$ ) Experiments on Tin Isotopes*, B. Baramsai *et al.* (including G. E. Mitchell), Conference on Applications of Accelerators in Research and Industry (CAARI12), AIP proceedings 1525, p. 577.
15. *Oklo Phenomenon and Nuclear Data*, E. I. Sharapov, C. R. Gould, and A. A. Sonzogni, Proc. ISINN-20 *Int. Sem. on Interactions of Neutrons with Nuclei*, Joint Institute for Nuclear Research E3-2013-22, Dubna, 2013, p. 245.
16. *Blinding in Experimental Physics*, R. Golub, to appear in the proceedings of the *Next Generation Experiments to Measure the Neutron Lifetime*, November 9-10, 2012.
17. *Eyes Opened, Eyes Closed Comparison of Methods to Measure the Neutron Lifetime*, R. Golub, to appear in the proceedings of the *Next Generation Experiments to Measure the Neutron Lifetime*, November 9-10, 2012.

---

**Abstracts to Meetings and Conferences**

---

1. *Ultracold Neutron Source Technology: Status in 2012*, A.R. Young,  
<http://meetings.aps.org/link/BAPS.2012.DNP.1WC.2>.
2. *Characterization of Large Area, Thick, and Segmented Silicon Detector for Electron and Proton Detection from Neutron Beta Decay Experiments in the Cold and Ultracold Energies*, Americo Salas Bacci *et al.* (including A.R. Young),  
<http://meetings.aps.org/link/BAPS.2012.DNP.NC.3>.
3. *The Design and Testing of a Device to Limit Superfluid Helium Film Flow*, D.G. Haase, Dillon K. Frame, and James R. Rowland,  
<http://meetings.aps.org/link/BAPS.2012.SES.LB.2>.
4. *Modernizing the Fission Basis*, C. Bhatia *et al.* (including C.R. Howell, W. Tornow, and J.H. Kelley),  
<http://meetings.aps.org/link/BAPS.2012.DNP.CE.4>.
5. *Neutron-Induced Reactions on Copper and Zero-Neutrino Double-Beta Decay Searches*, M.E. Gooden, J.H. Kelley, B.A. Fallin, S. Finch, C.R. Howell, G. Rusev, A.P. Tonchev, and W. Tornow,  
<http://meetings.aps.org/link/BAPS.2012.DNP.HE.3>.

## A.3 Invited Talks, Seminars, and Colloquia

---

### Invited Talks, Seminars, and Colloquia

---

1. *Studies of Nuclei at TUNL/HIGS: from Hadron Structure to Exploding Stars*, M. Ahmed, Thomas Jefferson National Accelerator Facility, Chrial Dynamics, August 6, 2012.
2. *The SoLID Program at 12-GeV Jefferson Lab*, H. Gao, Invited talk at the Indiana-Illinois Workshop on Fragmentation Functions, Dec 12-14, 2013.
3. *New Searches on the Neutron Electric Dipole Moment and Spin-Dependent Short-Range Force*, H. Gao, Colloquium, Institute of High Energy Physics, CAS, Beijing, China, Nov. 1, 2013.
4. *Frontiers in Nuclear Physics and Research Experience*, H. Gao, Colloquium, Beijing University of Posts and Telecommunications, Beijing, China, Oct. 31, 2013.
5. *Laboratory Search for Spin-Dependent Short-Range Force from Axion like Particles Using Optically Polarized  $^3\text{He}$  Gas*, H. Gao, invited plenary talk at the 9th Circum-Pan-Pacific Symposium on High Energy Spin Physics, Jinan, China, Oct 28-31, 2013.
6. *New Searches on the Neutron Electric Dipole Moment and Spin-Dependent Short-Range Force*, H. gao, Colloquium, Kuang Yamin Honors School, Nanjing University, Beijing, China, Oct. 27, 2013.
7. *New Searches on the Neutron Electric Dipole Moment and Spin-Dependent Short-Range Force*, H. Gao, Colloquium, Physics Department, Univ. of Notre Dame, Oct. 2, 2013.
8. *Electron-Ion Collider Physics: Transverse Momentum Dependent Parton Distribution Functions (TMDs)*, H. Gao, Invited talk, Weihai Workshop on Electron-Ion Collider, Weihai, China, July 28-30, 2013.
9. *Some aspects of the structure of the nucleon and fundamental symmetries*, H. Gao, Colloquium, China Institute of Atomic Energy, Beijing, China, July 10, 2013.
10. *Three-body photodisintegration of  $^3\text{He}$  with double polarizations at the HIGS Facility*, H. Gao, Invited talk at the 5th Workshop on Hadron Physics in China and Opportunities in US, Huangshan, China, July 2-6, 2013.
11. *Frontiers in Nuclear Physics and Research Experience*, H. Gao, Colloquium, Kuang Yaming School, Nanjing University, Nanjing, China, June 28, 2013.
12. *New searches on parity and time-reversal symmetry violating quantities or interactions*, H. Gao, Colloquium, University of Science and Technology, Hefei, China, June 27, 2013.
13. *Frontiers in Nuclear Physics and Research Experience*, H. Gao, Colloquium, Wuhan Institute of Physics and Mathematics, Chinese Academy of Sciences, Wuhan, China, April 23, 2013.
14. *Frontiers in Nuclear Physics and Research Experience*, H. Gao, Colloquium, Wuhan University, Wuhan, China, April 22, 2013.
15. *TMD Physics with SoLID at 12-GeV Jefferson Lab*, H. Gao, Invited talk at the Second International Conference on QCD and Hadron Physics, Lanzhou, China, March 30 - April 2, 2013.
16. *New Searches on the Neutron Electric Dipole Moment and Spin-Dependent Short-Range Force*, H. Gao, Colloquium, Department of Physics, Tsinghua University, March 14, 2013.
17. *New Searches on the Neutron Electric Dipole Moment and Spin-Dependent Short-Range Force*, H. Gao, Colloquium, Physics Division, Argonne National Laboratory, March 8, 2013.

18. *The Sturtture of the Nucleon - an Exciting Frontier of QCD*, H. Gao, Invited plenary talk at the 84<sup>th</sup> Shuang Qing Lun Tan (Shuangqing Forum) on Research in Haronic Physics: Experiments and Theories, National Natural Science Foundation of China, November 2 - 4, 2012.
19. *Low-Energy Hadron Structure*, H. Gao, Invited talk at Kick-off workshop of the Collaborative Research Center CRC-1044 on The Low-Energy Frontier of the Standard Model, Mainz, Germany, September 3 - 5, 2012.
20. *TMD Experimental Overview*, H. Gao, Invited talk at the International Workshop on Physics Opportunities at an Electron Ion Collider, Bloomington, IN, August 20 - 22, 2012.
21. *New Results from HIGGS*, H. Gao, Invited talk at the Gordon Research Conference on Photonuclear Reactions, Holderness, NH, August 5 - 10, 2012.
22. *Systemtic Errors in the Search for a Neutron EDM*, R. Golub, Internaitonal advisory council for the Munich neutron EDM experiment, Munich, Germany, August 1, 2012.
23. *Blind Analysis*, Workshop on Next Generation Experiments to Measure the Neutron Lifetime, R. Golub, Santa Fe, NM, November 2012.
24. *Nuclear Data and the Oklo Natural Nuclear Reactors*, C. R. Gould, ND2013 International Conference on Nuclear Data for Science and Technology, New York, NY, March 2013.
25. *HIGGS2: Facility and Research Opportunities*, C. R. Howell, Low-Energy Community Meeting, East Lansing, MI, August 2013.
26. *Collaborative Research: ARI-MA: Nuclear Data Measurements Using Gamma Rays*, C. R. Howell, Sixth Annual Academic Research Initiative Grantees Program Review, Leesburg, VA, July 2013.
27. *HIGGS2: Facility and Research*, C. R. Howell, The Fifth Workshop on Hadron Physics in China and Opportunities in US, Huangshan, China, July 2013.
28. *Photo-Induced Precision Cross-Section Measurements on Actinide Nuclei using Monoenergetic and Polarized Photon Beams*, 2013 Stewardship Science Academic Programs Annual Review Symposium, Albuquerque, NM, June 2013.
29. *Measuring the Dynamical Responses of Plants to Changes in Environmental Conditions Using Radioactive Isotopes*, C. R. Howell, Physics department colloquium, George Washington University, Washington, DC, April 2013.
30. *STEM: A Call to Service, Workshop on Promoting Diversity in STEM*, C. R. Howell, George Washington University, Washington, DC, April 2013.
31. *STEM: A Call to Service, Science Pipeline ConNEXTion workshop: Establishing Your Roots in STEM*, C. R. Howell, Davidson, NC, March 2013.
32. *What is the Value of Curiosity-Motivated Research?*, C. R. Howell, Science Pipeline ConNEXTion workshop: Establishing Your Roots in STEM, Davidson, NC, March 2013.
33. *Neutron-Deuteron Breakup: A Probe of the Neutron-Neutron Interaction*, C. R. Howell, The 7<sup>th</sup> International Workshop on Chiral Dynamics, Newport News, VA, August 2012.
34. *Measuring the Neutron Lifetime Using Magnetically Trapped UCN*, P. R. Huffman, Seminar at the University of Kentucky, Lexington, KY, November 14, 2013.
35. *Experiences Using TPB to Detect Scintillations in Liquid Helium*, P. R. Huffman, Invited talk at "Light Detection in Noble Elements", Fermilab, Batavia, IL, May 29-31, 2013.
36. *Overview of Magnetic Trapping Neutron Lifetime Experiments*, P. R. Huffman, Workshop on Next Generation Experiments to Measure the Neutron Lifetime, Santa Fe, NM, November 2012.
37. *Applications of Random Matrix Theory*, G.E. Mitchell, Helmholtz Zentrum Rossendorf, Dresden, Germany, 2012.

38. *Recent Experiments Involving Few-Nucleon Systems*, W. Tornow, 22<sup>nd</sup> European Conference on Few-Body Problems in Physics, Krakow, Poland, September 2013.
39. *Are New Experiments at Low Energies Really Needed to Advance Few-Body Physics?*, W. Tornow, International Workshop on Nuclear Dynamics with Effective Field Theories, Ruhr Universität Bochum, Bochum, Germany, July 2013.
40. *Unsolved Problems in Few-Nucleon Scattering at Low Energies*, W. Tornow, European Center for Theoretical Physics, Trento, Italy, June 2013.
41. *Experimental Study of Photodisintegration Cross Sections on  $^3\text{He}$  and  $^4\text{He}$  at Low Energies*, W. Tornow, Institute for Nuclear Theory, University of Washington, Seattle, November 2012.
42. *Applications of nuclear physics to solving problems of fusion energy production and homeland security*, H. R. Weller, Physics Department Colloquium at the Physics Department of The University of Connecticut, August 30, 2013.
43. *Two Tri-alpha States in  $^{12}\text{C}$* , H. R. Weller, Invited talk at the European Centre for Theoretical Physics (ECT) Reactions Involving  $^{12}\text{C}$ : Nucleosynthesis and Stellar Evolution Workshop, October 7 - 11, 2013.
44. *A New Method for the Precise Determination of the Isovector Giant Quadrupole Resonance in Nuclei*, H. R. Weller, Zakopane Conference on Nuclear Physics 2012, Zakopane, Poland, August-September 2012.
45. *Compton Scattering at the HIGS Facility*, H. R. Weller, Chiral Dynamics Workshop 2012, Newport News, VA, August 2012.
46. *Unambiguous Observation of the Second  $2^+$  State in  $^{12}\text{C}$* , H. R. Weller, seminar, Argonne National Laboratory, Argonne, IL, October 2012.
47. *New Tri-Alpha Structures in  $^{12}\text{C}$* , H. R. Weller, Institute for Nuclear Theory Workshop on Light Nuclei from First Principles, Seattle, WA, October 2012.
48. *Overview of High Intensity Gamma-ray Source – Capabilities and Future Upgrades*, Y. K. Wu, invited talk at 2013 International Workshop on Polarized Sources, Targets and Polarimetry (PSTP2013), the University of Virginia, September 10, 2013.
49. *The HIGS2 Concept – The Next Generation Compton Gamma-ray Source*, Y. K. Wu, invited talk at the HIGS2 Workshop, TUNL and Duke University, June 3, 2013.
50. *Present and Future Compton X-ray and Gamma-ray Sources*, Y. K. Wu, invited talk at Hefei Light Source, University of Science and Technology of China (USTC), May 22, 2013.
51. *Research and Development Program of Polarized, High Intensity Compton  $\gamma$ -ray Sources at Duke University*, Y. K. Wu, invited talk at Hefei Light Source, University of Science and Technology of China (USTC), May 21, 2013.
52. *Ultracold Neutron Source Technology: Status in 2012*, A. R. Young, Invited talk at the 2012 Fall Meeting of the APS Division of Nuclear Physics, Newport Beach, CA, October 24, 2012.
53. *A Detector for  $N$ - $\bar{N}$  Oscillations in the NNBarX experiment: Specifications and Challenges*, A. R. Young, Snowmass on the Mississippi: Community Summer Study, University of Minnesota (Minneapolis-St. Paul), July 31 (2013).
54. *A Detector for  $N$ - $\bar{N}$  Oscillations in the NNBarX experiment: Specifications and Challenges*, A. R. Young, Intensity Frontier Workshop, Argonne National Laboratory, April 25-27 (2013).
55. *Ultracold Neutron Source for Fundamental Neutron Physics*, Frontier Capability Workshop, A. R. Young, Brookhaven National Laboratory, NY, April (2013).

56. *Quantum Mechanics and Ultracold Neutrons*, A. R. Young, Meredith College, Raleigh, NC April (2013).
57. *Ultracold Neutron Sources and Statistics Requirements for a Magnetically Trapped Lifetime Experiment*, A. R. Young, Workshop on Next Generation Experiments to Measure the Neutron Lifetime, Santa Fe, NM, November (2012).
58. *Improved Experimental Searches for Neutron-Antineutron Oscillations*, A. R. Young, NNN-2012 Conference, Fermilab, September (2012).
59. *Angular Correlations Measurements in Neutron Beta-Decay*, A. R. Young, TRIUMF Nuclear Summer School, Vancouver, CA, August (2012).

---

**Seminars at TUNL**

---

1. Hiro Ejiri, RCNP and Osaka University, (October 1, 2012)  
*Experimental Studies of Nuclear Matrix Elements for Double Beta Decays*
2. John Cesaratto, SLAC National Accelerator Laboratory, (October 4, 2012)  
*Controlling Beam Instabilities in CERN's Super Proton Synchrotron*
3. Georg Bollen, Michigan State University and FRIB, (October 18, 2012)  
*Precision Penning Trap Mass Measurements of Rare Isotopes at NSCL Now and at FRIB in the Future*
4. James R. Boyce, Jefferson National Laboratory, (November 1, 2012)  
*Research Beyond the Standard Model (BSM) at Jefferson Lab*
5. Guy Ron, Racah Institute of Physics, Hebrew University of Jerusalem, (November 13, 2012)  
*Lux et Lex: Optical Traps for Decay Studies*
6. Aaron Couture, Los Alamos National Laboratory, (November 15, 2012)  
*Neutron Capture for the Synthesis of the Heavy Elements*
7. Indranil Mazumdar, TUNL & Duke University, (December 6, 2012)  
*Halo World: The Story of Nuclear Halos and the Efimov Effect*
8. Mark Wrobel, Department of Homeland Security, (December 11, 2012)  
*The Academic Research Initiative: Challenges and Opportunities in Research Supporting the Global Nuclear Detection Architecture*
9. Matthias Junker, LUNA LGNS, (December 14, 2012)  
*LUNA: Laboratory for Underground Nuclear Astrophysics at Gran Sasso National Laboratories*
10. Phil Barbeau, Stanford University, (January 31, 2013)  
*Neutrino & Dark Matter Coherent Interactions: New Avenues for Precision Measurements*
11. Ke Han, Lawrence Berkeley National Laboratory, (February 7, 2013)  
*Searching for Neutrino-less Double Beta Decay with a Bolometric Technique*
12. Xin Qian, California Institute of Technology, (February 14, 2013)  
*Overview of the JLab SoLID Physics Program*
13. Nadia Fomin, University of Tennessee Knoxville, (February 19, 2013)  
*Nuclear and Particle Physics with Cold Neutrons*
14. Maxime Brodeur, Michigan State University, (February 21, 2013)  
*Ion Trap Experiments for Nuclear Astrophysics*
15. Kim Palladino, MIT Laboratory for Nuclear Science, (February 28, 2013)  
*It's All About the Recoils: WIMPs*
16. Dave Hornidge, Mount Allison University, (March 14, 2013)  
*Measuring Nucleon Polarizabilities with Real Photons at MAMI*
17. Mei Bai, Collider Accelerator Dept. Brookhaven National Laboratory, (March 21, 2013)  
*Spin Manipulation of Polarized Beams*
18. James Langenbrunner, Los Alamos National Laboratory, (April 11, 2013)  
*Quantifying Complex Inference Uncertainties for Validation*

19. Johann Rafelski, University of Arizona, (May 7, 2013)  
*A New Scheme for  $p+B$  Fusion Reactions*
20. Abhijit Bisoi, Saha Institute of Nuclear Physics, (May 17, 2013)  
*Superdeformation and Alpha-cluster Structure in  $^{35}\text{Cl}$*
21. Mieczyslaw Witold Krasny, CNRS & University Pierre et Marie Curie, (May 28, 2013)  
*High Intensity Photon Beams at CERN?*
22. Carla Frohlich, North Carolina State University, (June 18, 2013)  
*The Neutrino  $p$ -Process: Nuclear Physics and Nucleosynthesis in Core-Collapse Supernovae*
23. Ethan Brown, University of Münster, (June 20, 2013)  
*Searching for Dark Matter with XENON100 and XENON1T*
24. Henryk Witała, Jagiellonian University, (July 25, 2013)  
 *$3N$  Reactions with  $N^3\text{LO}$  Chiral Forces*
25. Zhihong Ye, University of Virginia, (August 14, 2013)  
*Study of Short Range Correlations at Large  $x_{bj}$  via Inclusive Electron-Nucleon Scattering*
26. Nicholas Hirlinger Saylor, Rensselaer Polytechnic and Université Paris-Sud XI, (August 21, 2013)  
*Generalized Parton Distributions and Deeply Virtual Compton Scattering on the Proton*
27. Ulf Meissner, Bonn University & Forschungszentrum Jülich, (August 23, 2013)  
*The Hoyle State and the Fate of Carbon-Based Life*
28. Ulf Meissner, Bonn University & Forschungszentrum Jülich, (August 27, 2013)  
*Effective Field Theories: Lectures 1 and 2*
29. Ulf Meissner, Bonn University & Forschungszentrum Jülich, (August 28, 2013)  
*Effective Field Theories: Lectures 3 and 4*
30. Ingo Wiedenhoever, Florida State University, (September 5, 2013)  
*The Nine Lives of the University Laboratory: Radioactive Beam Experiments at Florida State University*
31. Anton Tonchev, Lawrence Livermore National Laboratory, (September 12, 2013)  
*Modernizing the Fission Basis: Measurement of Fission Product Yields from Fast-Neutron-Induced Fission*
32. Kengo Nakamura, Tohoku University, (September 17, 2013)  
*KamLAND-Zen*
33. Dr. Vitaly Yakimenko, SLAC National Laboratory, (September 17, 2013)  
*Quasi-Monoenergetic Plasma Wakefield Acceleration at FACET*
34. Keith Crum, University of Chicago, (September 26, 2013)  
*Measuring  $\theta_{13}$  in the Double Chooz Experiment*
35. Jordi Casanova, North Carolina State University, (October 10, 2013)  
*Modeling Classical Nova and Type II Supernova Explosions. Multi-Dimensional versus One-Dimensional Models*

---

**Advances in Physics Lectures and Seminars**

---

1. Haiyan Gao, Duke University, (June 6, 2013)  
*Some Aspects of the Structure of the Nucleon and Fundamental Symmetries*
2. Mohammad Ahmed, North Carolina Central University and Duke University, (June 10, 2013)  
*Building Blocks of Nuclei*
3. Mohammad Ahmed, North Carolina Central University and Duke University, (June 10, 2013)  
*NN Interactions and Local Accelerators*
4. Mohammad Ahmed, North Carolina Central University and Duke University, (June 12, 2013)  
*Nuclear Instrumentation*
5. Calvin Howell, Duke University, (June 12, 2013)  
*Cross Sections and Scattering*
6. Constance Kalbach Walker, Duke University, (June 27, 2013)  
*Scientific Writing Part I: It's Not About You!*  
*Scientific Writing Part II: Making it Clear and Easy*
7. Kate Scholberg, Duke University, (July 18, 2013)  
*Neutrinos from the Sky and Through the Earth*

## A.4 Professional Service Activities

---

### Advisory/Fellowship/Review Committees

---

1. Member, LUX Davis Campus Safety Readiness Review Committee, *M. Busch*
2. Convener, Town Meeting on Nuclear Astrophysics, 2012, *A.E. Champagne*
3. Member, 2012 NSAC Subcommittee on the Implementation of the Long Range Plan, *H. Gao*
4. Jefferson Lab Program Advisory Committee, January 2010 – present, *H. Gao*
5. Associate Editor, The European Physical Journal A (EPJA), June 1, 2007 – present, *H. Gao*
6. Associate Editor, Frontiers in Physics, 2011–present, *H. Gao*
7. General Councillor, American Physical Society, 2011–present, *H. Gao*
8. President of International Organization of Chinese Physicists and Astronomers, January 1, 2011–December 31, 2012, *H. Gao*
9. Editorial Board, *Progress in Physics*, Chinese Physical Society, Jan. 2009–present, *H. Gao*
10. Member, Steering Committee for Whitepaper for Electron-Ion Collider Science in US for NSAC Long Range Plan, 2011-2012, *H. Gao*
11. Chair, Prize and Award Committee, American Physical Society, 2013, *H. Gao*
12. Executive Board, American Physical Society, 2013, *H. Gao*
13. Program Advisory Committee, BNL, April 2013 – present, *H. Gao*
14. Executive Committee, Division of Nuclear Physics, American Physical Society, April 2013 – present, *H. Gao*
15. Member, Dean’s Laboratory for Nuclear Science Advisory Committee, MIT, 07/01/2013–present, *H. Gao*
16. Member, Executive Committee, Neutron Electric Dipole Moment Experiment, *R. Golub*
17. Member, AIP/AAPT/APS Task Force on Teacher Preparation in Physics, *D. Haase*
18. Member, Program Committee for the Forum on Education of the APS, *D. Haase*
19. Reviewer, DOE Science Graduate Fellowship Program, *R. Henning*
20. Reviewer, Physical Review Letters, Nuclear Instruments and Methods, Astroparticle Physics, European Journal of Physics, Applied Radiation and Isotopes, and IEEE Transactions on Nuclear Science *R. Henning*
21. Reviewer, Grant Proposals, U.S. Department of Energy, *R. Henning*
22. Chair line, Executive Committee of the Few-Body Topical Group, American Physical Society (APS), 2010–present, *C. R. Howell*
23. Member, Stockpile Stewardship Graduate Fellowship Program Selection Committee, 2010-2013, *C. R. Howell*
24. Member, Selection Committee for the Mellon Mays Dissertation Grant, 2000-present, *C. R. Howell*

25. Member, Majorana Senior Advisory Committee, 2007 - present, *C. R. Howell*
26. Member of the PRC Editorial Board (2011 - present), *C. R. Howell*
27. Member, NSF IRES Review Panel, 2013, *C. R. Howell*
28. Member, Executive Committee for the SNS Fundamental Neutron Physics Beam Line Instrument Development Team, *P. R. Huffman*
29. Member, Executive Committee for the Neutron Electric Dipole Moment Experiment, *P. R. Huffman*
30. Member, International Organizing Committee, Nuclear Astrophysics Town Meeting, October 9-10, 2012, Detroit, MI, *C. Iliadis*
31. Member, Scientific Advisory Committee, Russbach School on Nuclear Astrophysics, March 10-16, 2013, Russbach, Austria, *C. Iliadis*
32. Member, NA-22 LANL Review Panel *Plutonium Isotopics Projects* for the Non-Proliferation agency of DOE, Los Alamos National Laboratory, October 25, 2012, *H. R. Weller*
33. Chair, HIGS PAC Committee, November 2012, *H. R. Weller*
34. Member, NSAC Sub-Committee on Implementation of the 2007 Long Range Plan, 2012, *J. F. Wilkerson*
35. Member, International Neutrino Physics Summer School Organizing Committee, 2012, *J. F. Wilkerson*
36. Member, International CUORE Review Committee (DOE/NSF/INFN), 2011–present, *J. F. Wilkerson*
37. Member, Ad Hoc Publications Committee , American Physical Society Division of Nuclear Physics, 2013, *J.F. Wilkerson*.
38. Member, Ad Hoc Nominations Committee, American Physical Society Division of Nuclear Physics, 2013, *J.F. Wilkerson*.
39. Member, Publications Committee, American Physical Society Division of Nuclear Physics, 2013, *J.F. Wilkerson*.
40. Faculty coordinator, 2013 U.S. Particle Accelerator School at Duke (January 14–25, 2013), *Y. K. Wu*
41. Reviewer, Center grant proposal, National Nuclear Security Administration (NNSA), DoE, 2012, *Y. K. Wu*
42. Convener, Project X Physics Study, Fermilab, Batavia, IL, 2012, *A. R. Young*
43. Member, LANSCE User Group Executive Committee, 2011-2012, *A. R. Young*
44. Co-spokesman, UCNA experiment, *A. R. Young*

---

**Conferences, APS Meetings and Workshops**

---

1. Chair, Slack Service Award Committee, Southeastern Section of the American Physical Society, 2013, *T. Clegg*
2. Co-Chair, 6<sup>th</sup> Workshop on Hadron Physics in China and Opportunities in US, Lanzhou, China, July 21-25, 2013, *H. Gao*
3. Member, International Program Committee ND2013, International Conference on Nuclear Data and Technology, March 2013, *C. Gould*
4. Member, AAPT Book Publications Five-Year Review Committee, *D. Haase*
5. Member, International Advisory Committee, 11<sup>th</sup> Conference on the Intersections of Particle and Nuclear Physics, 2011–2012, *C. R. Howell*
6. Co-chair, Organizing Committee, HIGS2 Workshop, June 2013, Durham, NC, *C. R. Howell*
7. Member, International Program Committee, LUNA MV Workshop, February 6-8, 2013, Gran Sasso, Italy, *C. Iliadis*
8. Member, International Advisory Committee, International Nuclear Physics Conference INPC 2013, Florence, Italy, *W. Tornow*
9. Member, International Advisory Committee, XXII European Conference on Few-Body Problems in Physics, September 2013, Krakow, Poland, *W. Tornow*
10. Member, Organizing Committee, Fundamental Symmetries and Neutrinos Working Group Workshop, 2012, *J.F. Wilkerson*.
11. Chair (2012), APS Division of Nuclear Physics, Tom Bonner Prize Committee, *J. F. Wilkerson*
12. Vice Chair (2013), American Physical Society Division of Nuclear Physics, *J.F. Wilkerson*.
13. Vice Chair (2013), Program Committee, American Physical Society Division of Nuclear Physics, *J.F. Wilkerson*.
14. Member, Organizing Committee of The International Workshop on HIGS2 at Duke University, June 03–04, 2013, *Y.K. Wu*

# Glossary of Acronyms

## Laboratories, Facilities, Experiments and Programs

ANL	Argonne National Laboratory
BNL	Brookhaven National Laboratory
DFELL	Duke Free-Electron Laser Laboratory
DNDO	Domestic Nuclear Detection Office
GV	Gamma-Vault at HI $\gamma$ S
HI $\gamma$ S	High Intensity Gamma-Ray Source
JLAB	Thomas Jefferson Lab National Accelerator Facility
KURF	Kimballton Underground Research Facility
LANL	Los Alamos National Laboratory
LENA	Laboratory for Experimental Nuclear Astrophysics
LLNL	Lawrence Livermore National Laboratory
MJD	MAJORANA DEMONSTRATOR
nEDM	Neutron Electric Dipole Moment
NNSA	National Nuclear Security Administration
ORNL	Oak Ridge National Laboratory
PNNL	Pacific Northwest National Laboratory
UTR	Upstream Target Room at HI $\gamma$ S

## Detectors, Material, Particles, Electronics, Acquisition and Software

DAQ	Data Acquisition
HPGe	High Purity Ge Detector
MCNP	Monte Carlo N-Particle
NaI	Sodium Iodide
ORCA	Object-oriented Real-time Control and Acquisition
PSD	Pulse Shape Discrimination
VME	VERSA module Eurocard

## Calculations, Reactions, and Techniques

FWHM	Full Width at Half Maximum
GDR	Giant Dipole Resonance
NRF	Nuclear Resonance Fluorescence
QCD	Quantum Chromodynamics
QRPA	Quasiparticle Random Phase Approximation

# Index

(Listed by corresponding author)

- Bhike, M., 40, 42, 44, 100, 102, 104  
Busch, M., 22
- Champagne, A.E., 62  
Clegg, T. B., 106  
Combs, D.C., 136  
Cooper, A.L., 140  
Corona, T.J., 54  
Crowell, A.S., 108
- Daigle, S., 60  
Downen, L.N., 138
- Fallin, B., 96  
Finch, S.W., 46, 48  
Fränkle, F.M., 52  
Friesen, F.Q.L., 88, 152
- Gao, H., 86, 92  
Giovanetti, G.K., 30  
Golub, R., 4  
Gooden, M.E., 98  
Gould, C.R., 18
- Haase, D.G., 8  
Howard, C., 158  
Howe, M.A., 174, 176  
Howell, C.R., 110  
Huffman, P.R., 2, 6, 16
- Iliadis, C., 68
- Kafkarkou, A., 72, 74  
Kalbach Walker, C., 76  
Karwowski, H.J., 50  
Kelley, J.H., 112  
Kelly, K.J., 64  
Kendellen, D.P., 10, 150, 154
- Leung, K., 12  
Longland, R., 66
- MacMullin, J., 26  
Mazumdar, I., 168  
Medlin, G.L., 160, 170  
Mikhailov, S.F., 124  
Mitchell, G.E., 78
- O'Shaughnessy, C., 34, 36
- Petersburg, R., 24  
Phillips, D.G. II, 162  
Popov, V.G., 132
- Seo, P.-N., 144, 146, 148  
Shanks, B., 28  
Sikora, M.H., 90  
Silano, J.A., 164  
Swindell, A.G., 156
- Ticehurst, D.R., 172
- Vorren, K., 38
- Westerfeldt, C.R., 134  
Wierman, K.J., 56  
Wu, W.Z., 126  
Wu, Y.K., 116, 118, 120, 122, 128, 130
- Young, A.R., 14, 166
- Zimmerman, W.R., 82, 84  
Zitin, A., 32

# Triangle Universities Nuclear Laboratory

